



# Numerical simulation and modelling of entropy noise in nozzle and turbine stator flows

Ariane Emmanuelli

## ► To cite this version:

Ariane Emmanuelli. Numerical simulation and modelling of entropy noise in nozzle and turbine stator flows. Acoustics [physics.class-ph]. Université Paris Saclay (COMUE), 2019. English. NNT : 2019SACLC067 . tel-02502876

**HAL Id: tel-02502876**

**<https://theses.hal.science/tel-02502876>**

Submitted on 9 Mar 2020

**HAL** is a multi-disciplinary open access archive for the deposit and dissemination of scientific research documents, whether they are published or not. The documents may come from teaching and research institutions in France or abroad, or from public or private research centers.

L'archive ouverte pluridisciplinaire **HAL**, est destinée au dépôt et à la diffusion de documents scientifiques de niveau recherche, publiés ou non, émanant des établissements d'enseignement et de recherche français ou étrangers, des laboratoires publics ou privés.

# Numerical simulation and modelling of entropy noise in nozzle and turbine stator flows

Thèse de doctorat de l'Université Paris-Saclay  
préparée à CentraleSupélec

Ecole doctorale n°579 Sciences mécaniques et énergétiques, matériaux et  
géosciences (SMEMaG)  
Spécialité de doctorat : Acoustique

Thèse présentée et soutenue à Châtillon, le 6 septembre 2019, par

**ARIANE EMMANUELLI**

## Composition du Jury :

Pr. Christophe Bailly LMFA, CNRS et Ecole Centrale de Lyon	Président
Dr. Friedrich Bake DLR	Rapporteur
Pr. Franck Nicoud IMAG, CNRS et Université de Montpellier	Rapporteur
Ing. François Vuillot ONERA	Examineur
Dr. Sébastien Ducruix Laboratoire EM2C, CNRS et CentraleSupélec	Directeur de thèse
Ing. Maxime Huet ONERA	Encadrant
Dr. Alexis Giauque LMFA, CNRS et Ecole Centrale de Lyon	Invité



# Contents

<b>Nomenclature</b>	<b>v</b>
<b>Acknowledgements</b>	<b>1</b>
<b>Introduction</b>	<b>3</b>
<b>1 Literature review of entropy noise</b>	<b>7</b>
1.1 Description of analytical tools for entropy noise . . . . .	8
1.1.1 Reference compact models . . . . .	8
1.1.2 1D models for nozzle flow . . . . .	12
1.1.3 2D modelling . . . . .	17
1.2 Overview of entropy noise generation investigations . . . . .	20
1.2.1 Attenuation of entropy perturbations . . . . .	20
1.2.2 Reference experimental studies of entropy noise . . . . .	22
1.2.3 Fundamental entropy noise generating mechanism . . . . .	24
1.2.4 Interaction with vorticity . . . . .	25
1.2.5 Entropy noise in 3D and complex turbine flow . . . . .	26
<b>2 Description of numerical tools</b>	<b>29</b>
2.1 Computational fluid dynamics code CEDRE . . . . .	30
2.1.1 Equations of motion . . . . .	30
2.1.2 Injection of fluctuations . . . . .	35
2.1.3 Non-reflective boundary conditions . . . . .	36
2.2 Computational aeroacoustics code sAbrinA_v0 . . . . .	37
2.2.1 Fundamental equations . . . . .	38
2.2.2 Boundary conditions for non-reflection and injection of perturbations	39
<b>3 Investigation of entropy noise in nozzle flow</b>	<b>41</b>
3.1 Choice of cases studied . . . . .	42
3.2 Computation of the mean flow field . . . . .	43
3.3 Application of the 2D model . . . . .	44
3.4 Noise levels simulated using CAA . . . . .	45
3.4.1 Choice of sAbrinA_v0 numerical parameters . . . . .	46
3.4.2 CAA simulations . . . . .	47
3.4.3 Choice of post-processing strategy . . . . .	49
3.4.4 Verification of noise levels obtained in the entropic forcing case . . . .	51

3.5	Comparison and analysis of CAA and analytical results . . . . .	55
3.5.1	Comparison of transfer functions and investigation of 2D effects . . .	55
3.5.2	Investigation of the 1D acoustics assumption and of the presence of vorticity . . . . .	59
3.6	Conclusions . . . . .	61
<b>4</b>	<b>Extension of the entropy noise model to 2D stator flow</b>	<b>63</b>
4.1	Formulation of the model's fundamental assumptions and equations . . . . .	64
4.1.1	Choice of the model's assumptions . . . . .	64
4.1.2	Definition of a streamline-attached coordinate system . . . . .	64
4.1.3	Derivation of the model's equations . . . . .	65
4.2	Methodology of the model's resolution process . . . . .	68
4.3	Application of the model . . . . .	72
4.3.1	Compact solution under the assumptions of the model . . . . .	72
4.3.2	Convergence of the model's parameters . . . . .	73
4.4	Conclusions . . . . .	81
<b>5</b>	<b>Investigation of entropy noise in 2D stator flow</b>	<b>83</b>
5.1	Choice of geometry and mean flow simulation . . . . .	84
5.2	Simulation of noise levels using CAA . . . . .	86
5.2.1	Set-up of simulations . . . . .	86
5.2.2	sAbrinA_v0 simulations and post-processing . . . . .	87
5.3	Characterisation of noise levels in the 2D stator . . . . .	89
5.4	Comparison of analytical and numerical transfer functions . . . . .	99
5.5	Conclusions . . . . .	102
<b>6</b>	<b>Investigation of entropy noise in 3D stator flow</b>	<b>105</b>
6.1	ZDES simulation set-up . . . . .	106
6.1.1	Choice of geometry and mesh construction . . . . .	106
6.1.2	Choice of numerical parameters . . . . .	107
6.1.3	Simulation of the flow . . . . .	109
6.2	Characterisation of aerodynamics . . . . .	112
6.2.1	Characterisation of the baseline flow . . . . .	112
6.2.2	Comparison of the mean flows obtained with different forcing types .	115
6.3	Investigation of aeroacoustics . . . . .	117
6.3.1	Verification of hydrodynamic filtering . . . . .	117
6.3.2	Assessment of non-reflective post-processing . . . . .	120
6.3.3	Assessment of the signal-to-noise ratio . . . . .	124
6.3.4	Investigation of noise levels . . . . .	125
6.4	Conclusions . . . . .	131
	<b>Discussion</b>	<b>133</b>
	<b>General conclusions</b>	<b>137</b>
<b>A</b>	<b>Derivation of the Euler equations in a streamline-attached reference frame</b>	<b>139</b>

<b>B Abstract in French</b>	<b>145</b>
<b>List of figures</b>	<b>159</b>
<b>List of tables</b>	<b>165</b>
<b>Bibliography</b>	<b>167</b>



# Nomenclature

## Acronyms

ACARE Advisory Council for Aeronautics Research in Europe

CAA Computational AeroAcoustics

CFL Courant–Friedrichs–Lewy

CPU Central Processing Unit

DCN Direct Combustion Noise

DDES Delayed Detached Eddy Simulation

DES Detached Eddy Simulation

DMM Direct Mode Matching

FFT Fast Fourier Transform

GENCI Grand Équipement National de Calcul Intensif

ICAO International Civil Aviation Organization

ICN Indirect Combustion Noise

LES Large Eddy Simulations

NO<sub>x</sub> Nitric oxides

RANS Reynolds-Averaged Navier-Stokes

RECORD REsearch on COre noise ReDuction

URANS Unsteady Reynolds-Averaged Navier-Stokes

ZDES Zonal Detached Eddy Simulation

## Greek symbols

$\delta_{ij}$  Kronecker delta



$\gamma$	Heat capacity ratio
$\kappa$	Von Kármán constant
$\Lambda$	Acceleration
$\mu$	Chap. 1 and 4: $\mu = [1 + (\gamma - 1)M^2/2]^{-1}$ Chap. 2 and 6: dynamic viscosity
$\mu_t$	Turbulent dynamic viscosity
$\nu$	Chap. 1 and 4: acoustic wave angle Chap. 2 and 6: kinematic viscosity
$\nu_t$	Turbulent kinematic viscosity
$\Omega$	Normalised angular frequency
$\omega$	Angular frequency
$\rho$	Density
$\sigma$	Normalised entropy fluctuations
$\tau$	Chap. 1 and 5: normalised time Chap. 2: stress tensor
$\theta$	Flow angle
$\varphi$	Streamline angle
$\Xi$	Normalised vorticity fluctuation
$\xi$	Vorticity

### Latin symbols

$\mathbf{e}$	Unit vector
$\mathbf{J}$	Jacobian matrix
$\mathbf{K}$	Dimensionless wave vector
$\mathbf{k}$	Wave vector
$\mathbf{N}$	Unit vector in the direction of vorticity
i	Imaginary unit
$\bar{k}$	Kinetic energy of the turbulent field
$A$	Cross-sectional area

$c$	Speed of sound
$c_*$	Critical speed of sound
$c_p$	Heat capacity at constant pressure
$c_v$	Heat capacity at constant volume
$c_x$	Stator axial chord
$D$	Diameter
$d$	Wall distance
$E$	Energy
$e$	Internal specific energy
$f_d$	Function to switch between URANS and LES in ZDES
$K$	Curvature
$l$	Cross-sectional length
$M$	Mach number
$n$	Coordinate perpendicular to streamlines
$P$	Normalised pressure fluctuation
$p$	Pressure
$Pr$	Prandtl number
$q_j$	Heat flux
$R$	Radius of curvature
$r$	Radial coordinate
$s$	Entropy Streamline-attached coordinate
$T$	Temperature
$t$	Time
$U$	Normalised velocity fluctuation
$u$	Velocity
$V_g$	Effective velocity of acoustic propagation

$X$	Normalised axial coordinate
$x$	Axial coordinate
$x^+$	Nondimensional axial distance at the wall
$y$	Coordinate perpendicular to the axial direction
$y^+$	Nondimensional distance to the wall
$Z$	Reduced impedance
$z$	Coordinate perpendicular to both x-y and s-n planes
$z^+$	Nondimensional distance at the wall in the z-direction

### **Subscripts and superscripts**

$-'$	Fluctuating variable
$-^+$	Downstream propagating wave
$-^-$	Upstream propagating wave
$-_0$	Mean variable
$-_1$	Position upstream of geometry
$-_2$	Position downstream of geometry
$-\theta$	Azimuthal component
$-_i$	Variables injected into the domain
$-_n$	Component in the n-direction
$-_r$	Radial component
$-_s$	Component in the direction of streamlines
$-_x$	Axial component
$-_z$	Component in the z-direction
$\dot{-}$	Derivative with respect to the axial direction
$\hat{-}$	Complex amplitude
$\overline{-}$	Cross-section average

# Acknowledgements

Je souhaite tout d'abord remercier les membres du jury de ma thèse de s'être intéressés à mon travail et de s'être déplacés pour la soutenance. Je remercie Friedrich Bake et Franck Nicoud pour leurs rapports sur le manuscrit, Christophe Bailly d'avoir accepté d'être président du jury, François Vuillot d'avoir été examinateur et pour nos discussions sur CEDRE et Alexis Giauque d'avoir participé à la soutenance, mais aussi pour ses conseils dans le cadre d'articles, ainsi que brièvement d'équations. Merci à tous pour vos questions et vos remarques durant la soutenance.

Je tiens aussi à remercier chaleureusement mon encadrant et mon directeur de thèse, Maxime Huet et Sébastien Ducruix. Merci à tout deux pour votre disponibilité tout au long de cette thèse. Maxime, merci pour les discussions de couloir "de deux minutes", pour ta bonne humeur et ton humour, et pour tes corrections dont je suis particulièrement reconnaissante pour leur qualité, exhaustivité et ta réactivité. Sébastien, merci pour tes conseils, techniques mais aussi plus généralement sur la thèse et la suite, et pour ta constante bienveillance. Merci pour les discussions en réunion, pour la complémentarité de vos remarques et malgré cela d'avoir toujours été d'accord !

De nombreuses autres personnes m'ont aidé durant ces années de thèses à l'ONERA. Je pense en particulier à Thomas qui m'a suivi sur la partie CAA. Merci pour ton aide avec les simulations, mais aussi pour les discussions sans fin sur une variété d'autres sujets et plus généralement pour ton implication, y compris dans la vie du labo (même si on attend toujours le laser tag). Je pense aussi à l'équipe CEDRE qui m'a tenue informée de ses derniers développements, à Julien Marty pour ses conseils en matière de ZDES et de turbomachines, à Stéphanie et Majd pour leur aide avec Cassiopée et à Paul pour ses conseils en informatique, ainsi que pour son manuel convivial Tentacule, sans lequel mon manuscrit n'aurait pas la même tête. Merci aux autres qui m'ont conseillé, notamment au sein des unités acoustiques. Je pense aussi à Jun et tout son travail qui a abouti au modèle CHEOPS-Nozzle et qui a permis cette thèse. Enfin, merci à toute la cellule de gestion qui facilite grandement les questions administratives, en particulier Lydie, que je remercie également pour sa disponibilité et sa bonne humeur, et Marie-Line pour les discussions de bout de couloir.

Des calculateurs GENCI ont été utilisés durant cette thèse dans le cadre du projet BREST numéro A0032A10287. J'exprime ma gratitude pour ces moyens de calcul qui m'ont permis de réaliser les simulations ZDES discutées au chapitre 6.

Je profite de ces remerciements pour faire un bon en arrière et mentionner mes professeurs et encadrants de stage à l'ENSICA et à l'ISAE-Supaéro, Xavier Carbonneau, Nicolas Binder et Yannick Bousquet, qui m'ont fait découvrir la recherche et inciter à faire une thèse, et dont je garde de précieux conseils.

Cette thèse s'est déroulée au sein de l'unité SN2A du DAAA à l'ONERA, et je souhaite remercier toute l'équipe des deux unités acoustiques. Je pense à Johan, être social par excellence avec qui j'ai l'impression d'avoir passé bien plus que deux mois à l'ONERA, à la bonne humeur de Iannis, grâce à qui le crawl n'a (presque) plus de secrets pour moi, à Jun, le thésard originel de la team combustion, à Fernando et ses histoires de lapins et de paella. Il y a Mathieu, que je pourrais citer comme on me l'a présenté en parlant de ses gâteaux ou du calcul mental mais dont je préfère parler de l'enthousiasme, et la cool attitude de Tobias, instigateur des afters inter-branches, puis des Friday Beers. J'en profite pour remercier nos collègues doctorants en matériaux ! Je pense à mes voisins de couloir : David le savoyard, Sofiane, qui a eu la gentillesse de m'offrir la Rolls des chaises et Paul avec qui la musique a rempli le couloir. Il y a aussi les belles discussions avec Antoine, allant des élections à l'oisiveté, en passant par les échecs avec Adil, confrère des frustrations et des joies dictées par sAbrinA, v0 pour les intimes. Je n'oublie pas les stagiaires qui ont périodiquement peuplés le couloir A8d, en particulier Rafael, grand amateur de gingembre avec qui la team combustion s'est officialisée, et qui a mis l'ambiance (et du bruit!) dans le couloir avec Régis, chef du chapon-carottes. Merci aussi à toute la team piscine - j'ai une pensée émue pour la Joy Machine – et à la team escalade, avec qui j'ai beaucoup appris, ri et partagé des amandes et des noix de cajou. Il est difficile d'être exhaustif, mais je souhaite vraiment remercier toute l'équipe acoustique à l'ONERA, dont chacun participe à sa façon à l'ambiance conviviale qui y règne, lors des fameux pots mais aussi au quotidien.

Merci aussi à l'ASCO Voile et à toutes les personnes qui participent à son fonctionnement de m'avoir fait découvrir l'habitable puis la régate, ce magnifique voilier Pandora et des endroits exceptionnels. Merci aussi pour les belles rencontres, y compris Stéphane grâce à qui j'ai pu m'occuper d'un cours à l'EPF et que je remercie.

J'aimerais également remercier mes amis, les meilleurs pour se changer les idées et se déconnecter de la thèse, et Julien, notamment pour ses virées malakoffiotes. Merci à ceux qui sont venus fêter la soutenance ! Enfin, merci de tout coeur à ma famille de m'avoir aidé durant cette thèse mais aussi pendant mes études, et de m'avoir permis de travailler face au mirabellier et à l'île du milieu.

# Introduction

Noise pollution in the vicinity of airports is becoming a more and more pressing concern as air traffic increases. According to the International Civil Aviation Organization (ICAO), the passenger-kilometre indicator increased by 70% between 2007 and 2017 [ICAO, 2017]. The Advisory Council for Aeronautics Research in Europe (ACARE) was established to guide and encourage aeronautical research in Europe. They set ambitious goals for 2050, including a 65 % reduction in the perceived noise emissions of aircraft relative to the year 2000 [ACARE, 2017]. Engines are responsible for a significant amount of aircraft noise through several noise generating mechanisms. Fan and jet noise are the dominant sources, but they have been greatly reduced in the past decades, thereby increasing the relative contribution of internal noise sources, called core noise.

As well as contributing to the noise emitted by the aircraft overall, core noise can interact with the flame in the engine's combustion chamber, which can be instrumental in the onset of highly destructive thermo-acoustic instabilities. Security margins are necessary to avoid the latter, but they lead to increased emissions, in particular of nitric oxides ( $\text{NO}_x$ ) which reduce air quality and cause acid rain. Their particularly harmful impact on the environment explains why ACARE's objective for the reduction of  $\text{NO}_x$  emissions by 2050 is as high as 90 % [ACARE, 2017]. A greater understanding of core noise could help reduce the risk of combustion instabilities and  $\text{NO}_x$  emissions.

One of the main sources of internal noise is combustion noise, which is made up of two distinct phenomena: direct (DCN) and indirect (ICN) combustion noise [Dowling and Mahmoudi, 2015, Huet et al., 2016, Ihme, 2017]. DCN is generated by the unsteady heat release rate of the flame in the combustion chamber [Candel et al., 2009, Hassan, 1974]. On the other hand, ICN is due to the acceleration of heterogeneities produced by combustion through the rest of the engine, notably turbine stages and nozzles. These perturbations can be either compositional, vortical or temperature fluctuations which can be assimilated to entropy, and they generate compositional [Magri et al., 2016, Rolland et al., 2018], vortex [Kings, 2014] and entropy noise [Morgans and Durán, 2016] respectively. The latter is the subject of this PhD.

There is a need to better understand the generation mechanism of entropy noise, as it affects both the sound levels globally emitted by aircraft engines and thermo-acoustic instabilities in the combustion chamber. There is also a need for the development of cost effective and accurate tools for use in an industrial context, to enable entropy noise to be taken into account during engine design stages. Indeed, experimental and numerical methods currently available for the study of entropy noise are complex and costly, because of extreme operating conditions, chemical reactions, heat exchange, complex flow and acoustic reflection. Among

other challenges, this leads to difficulties to separate direct and indirect combustion noise or to make temperature measurements experimentally, while costly simulations are necessary to capture acoustic fluctuations numerically. This motivates the development of semi-analytical methods which constitute an interesting additional tool to better understand entropy noise, and which may become a cost-effective alternative for engineering developments.

The theory of entropy noise was established in the 1970s, when Marble and Candel [1977] developed a model for nozzle configurations. They used conservation principles applied to one-dimensional perturbed flow. The model was formulated under the compact assumption, which stipulates that the dimension of the geometry is small compared to wavelengths. This model provides simple solutions for subsonic or supersonic nozzle flow, with or without a shock, and serves as a reference. However, the compact limit, which is only valid at near-zero frequencies, is unrealistic for entropy noise applications. Marble and Candel [1977] also analysed the supercritical non-compact case, but the model remained limited by linear velocity profile and one-dimensional flow assumptions, which prevented the full deformation of the flow and entropy perturbations from being taken into account. Moase et al. [2007] and Huet and Giauque [2013a] later generalised this model to non-compact and non-linear cases in the presence of a shock, while Giauque et al. [2012] extended it to subcritical flow.

In order to consider mean flow and entropy wave deformation, Zheng [Zheng, 2016, Zheng et al., 2015] recently developed a two-dimensional semi-analytical model for entropy noise in nozzle flow. He took radial variations of the mean flow and entropy perturbations into account, while acoustic fluctuations were considered one-dimensional. This model highlights the significance of two-dimensional effects on entropy noise. To validate it, Zheng used Large Eddy Simulation (LES) which is well-suited to simulate entropy noise. However, its assumptions are not the same as the model's, which explains noise level discrepancies compared to the analytical results. The latter were indeed overestimated in comparison to LES.

Around the time Marble and Candel [1977] developed their model for entropy noise in nozzle flow, Cumpsty and Marble [1977] formulated a similar compact model for turbine configurations. It was based on Marble and Candel's model and the actuator disk theory. For both stator and rotor rows, jump conditions were used to relate acoustic, entropic and vortical fluctuations just upstream and downstream of the blades. Comparison to experimental data gave promising results. This model provides a simple reference solution for turbine configurations, but like Marble and Candel's model, the compact assumption is unrealistic.

Durán and Moreau [2013a] developed a model by using Cumpsty and Marble's model [1977] in blade passages and by estimating the attenuation of the two-dimensional entropy wave in between blade rows. They built on the work of Leyko et al. [2010, 2014] and Durán et al. [2013] who focused on isolated stator and rotor configurations respectively. Bauerheim et al. [2016] verified the analytical results for a full turbine stage numerically using LES. These studies highlighted the impact of entropy wave distortion on noise levels. In addition, this model was integrated into the chain CHORUS, which models both the combustion chamber and turbine stages. This powerful tool allows to compute both direct combustion noise and the entropy noise generated by perturbations convected from the combustion chamber within the model. However, the compact assumption is maintained in blade passages. It may need to be relaxed in view of its impact in nozzle flow and of the significance of flow distortion in turbomachinery.

There have been few analytical studies in turbine flow compared to the nozzle case, but

in recent years, several numerical and experimental investigations of entropy noise in turbine configurations have been carried out to better understand the noise generating mechanism. This is one of the objectives of the FP7-European project RECORD (REsearch on COre noise ReDuction). A turbine stage is studied experimentally at Politecnico di Milano within this project. Using the same geometry, entropy noise was investigated numerically by several institutions, constituting a benchmark allowing the improvement of numerical methods to predict entropy noise [Pinelli et al., 2015]. The flow within the turbine stage was first characterised aerodynamically [Gaetani et al., 2007a,b, 2010, Persico et al., 2012], and it has been analysed acoustically more recently [Bake et al., 2016, Gaetani and Persico, 2017, Holewa et al., 2017, Knobloch et al., 2016, 2017]. Due to the complexity of turbine flow and the entropy noise generation mechanism, further investigations are required to fully understand the latter.

As explained in previous paragraphs, early work on entropy noise led to the development of reference compact models for entropy noise in both nozzle and turbine flow. In more recent years, experimental [Bake et al., 2009b, De Domenico et al., 2017] and numerical [Leyko et al., 2011, Moreau et al., 2018, Mühlbauer et al., 2009] investigations have led to greater understanding of entropy noise in nozzle flow, although studies are under-way to further investigate the complex noise generating mechanism. Several one-dimensional solutions have been formulated for this geometry [Durán and Moreau, 2013b, Giauque et al., 2012, Goh and Morgans, 2011, Huet and Giauque, 2013a, Moase et al., 2007, Stow et al., 2002], as well as two-dimensional models for both radial [Zheng, 2016, Zheng et al., 2015] and circumferential [Dowling and Mahmoudi, 2015, Durán and Morgans, 2015] directions. Zheng highlighted the impact of radial flow variations on entropy noise, but his model requires further validation. Once this is achieved, it could be extended to turbine configurations, which have been studied less extensively than nozzles due to the complexity of the flow, even though they are responsible for most of the entropy noise. Though few analytical studies have been carried out for turbine flow, and the compact assumption has not fully been relaxed, both numerical [Becerril Aguirre, 2017, Ceci et al., 2019, Wang et al., 2016] and experimental [Beard et al., 2009, Persico et al., 2012] projects have recently flourished in an effort to understand entropy noise generation in turbine stages.

In this context, the aim of this study is to increase the understanding of entropy noise in isolated turbine stator flow and to extend the two-dimensional model for nozzle flow developed by Zheng to stator configurations.

To achieve this, this PhD includes the following chapters. First, a brief literature review including the description of the models used in this PhD is presented in chapter 1, and numerical tools are detailed in chapter 2. Chapter 3 focuses on the case of the nozzle. A Computational AeroAcoustics (CAA) method is set up to investigate entropy noise by comparison with analytical tools, in particular Zheng’s model [2016]. The CAA simulations serve as a reference case to validate the latter under similar assumptions. Entropy noise is computed with CAA and the two-dimensional model using the same mean flow field in both cases. The generated noise is also compared to existing one-dimensional compact and non-compact models in order to further investigate two dimensional effects of the flow on entropy noise in nozzles.



Once Zheng’s semi-analytical model [2016] is rigorously validated, it can be extended to isolated stator geometries as a first step towards the more complex full turbine stage configurations. This is the objective of chapter 4. The model’s fundamental equations are derived after choosing the assumptions and the coordinate system best suited to stator flow. Their implementation can then be updated to account for the new reference frame and equations, as well as specific features of the stator geometry, including its 2D-planar nature. The model is finally applied to a geometry using both Euler and RANS mean flow fields, and the convergence of estimated noise levels with its main parameters is verified. The model’s results are compared to a modified version of Cumpsty and Marble’s compact model [1977].

These analytical developments are used together with a CAA approach similar to the one discussed in chapter 3 to investigate entropy noise and acoustic scattering through a two-dimensional turbine stator in chapter 5. The same Euler and RANS mean flows are used for both analytical and numerical methods in this chapter. Firstly, the CAA simulations are described and then used to characterise entropy noise in stator flow under simplifying assumptions by analysing both perturbed flow fields and overall noise levels. The differences obtained with Euler and RANS mean flows are highlighted. Then, the results of the 2D semi-analytical model are compared to those of CAA as well as compact solutions, in order to determine the model’s accuracy and limits, and to investigate the effect of some of its assumptions.

Finally, after having investigated two-dimensional stator flow, chapter 6 deals with a more realistic three-dimensional case. The aim of this chapter is to determine whether three-dimensionality and viscosity have a significant impact on entropy noise in stator flow. To do so, a Zonal Detached Eddy Simulation (ZDES) is set up. First, the aerodynamics of the flow are characterised to verify both their agreement with expectations and whether they are affected by the entropic and acoustic excitations injected into the domain. Next, aeroacoustics are analysed. Filtering of aerodynamics, numerical reflections and signal-to-noise ratios are verified. Entropy noise levels and acoustic scattering are then analysed and compared to those obtained in the two-dimensional stator in chapter 5.

# Chapter 1

## Literature review of entropy noise

### Contents

---

<b>1.1</b>	<b>Description of analytical tools for entropy noise . . . . .</b>	<b>8</b>
1.1.1	Reference compact models . . . . .	8
1.1.1.1	Compact model for nozzle flow . . . . .	8
1.1.1.2	Compact model for turbine stator flow . . . . .	10
1.1.2	1D models for nozzle flow . . . . .	12
1.1.2.1	1D model MARCAN . . . . .	13
1.1.3	2D modelling . . . . .	17
1.1.3.1	2D model CHEOPS-Nozzle . . . . .	17
<b>1.2</b>	<b>Overview of entropy noise generation investigations . . . . .</b>	<b>20</b>
1.2.1	Attenuation of entropy perturbations . . . . .	20
1.2.2	Reference experimental studies of entropy noise . . . . .	22
1.2.3	Fundamental entropy noise generating mechanism . . . . .	24
1.2.4	Interaction with vorticity . . . . .	25
1.2.5	Entropy noise in 3D and complex turbine flow . . . . .	26

---

## 1.1 Description of analytical tools for entropy noise

This section presents a review of analytical methods developed to estimate entropy noise. The response of a nozzle to acoustic fluctuations was first investigated analytically by Tsien [1952] and Crocco [1953] for rocket applications. Based on this, Candel [1972] studied the passage of an entropic perturbation through a nozzle in the context of turbojet engines. He found it to be a significant noise source, motivating further investigations. This was confirmed by Morfey [1973] and Marble [1973]. The former used the concept of "excess density", density fluctuations not associated with acoustic waves, to explain entropy noise, while Marble [1973] concluded the nozzle can be considered acoustically compact, that is of small dimension compared to the wavelengths. Cumpsty [1975] used this assumption to estimate the contribution of the turbine to the so-called "excess noise".

These studies led to the development of compact models for both nozzle and turbine configurations, detailed in § 1.1.1. The model for nozzle flow was used as a basis for many one-dimensional tools described in § 1.1.2. Further developments allowed to consider 2D flow in the circumferential or radial directions, as detailed in § 1.1.3. The two compact solutions, a one-dimensional model and a two-dimensional model which are used in this PhD are described in detail.

### 1.1.1 Reference compact models

The compact analytical solutions for nozzle and turbine flow developed by Marble and Candel [1977] and Cumpsty and Marble [1977] respectively are presented in this section. They share the following assumptions:

- ideal and calorifically perfect fluid.
- inviscid and adiabatic assumptions, so that the flow is supposed isentropic.
- small perturbations, to allow linearisation of equations.
- compactness: wavelengths are considered large compared to the geometry's characteristic length.

#### 1.1.1.1 Compact model for nozzle flow

As well as the assumptions listed above, Marble and Candel's solution [Marble and Candel, 1977] assumes one-dimensional axial flow. Under the compact assumption, the nozzle is reduced to a discontinuity between positions 1 upstream and 2 downstream. Matching conditions can be written for continuity, stagnation temperature and entropy, which are conserved

throughout the nozzle in isentropic flow.

$$\left( \frac{1}{M} \frac{u'}{c_0} + \frac{\rho'}{\rho_0} \right)_1 = \left( \frac{1}{M} \frac{u'}{c_0} + \frac{\rho'}{\rho_0} \right)_2 \quad (1.1)$$

$$\begin{aligned} & \left( \frac{1}{1 + \frac{(\gamma-1)}{2} M^2} \left[ \gamma \left( \frac{p'}{\gamma p_0} \right) - \frac{\rho'}{\rho_0} + (\gamma-1) M \frac{u'}{c_0} \right] \right)_1 \\ &= \left( \frac{1}{1 + \frac{(\gamma-1)}{2} M^2} \left[ \gamma \left( \frac{p'}{\gamma p_0} \right) - \frac{\rho'}{\rho_0} + (\gamma-1) M \frac{u'}{c_0} \right] \right)_2 \end{aligned} \quad (1.2)$$

$$s'_1 = s'_2 \quad (1.3)$$

where mean and fluctuating parts of variables are noted  $\cdot_0$  and  $\cdot'$  respectively.  $\gamma$  is the heat capacity ratio,  $c_0$  the mean speed of sound and  $M = M_0$  is the mean Mach number for which the subscript is omitted. Assuming harmonic solutions, the pressure, axial velocity and entropic fluctuations  $p'$ ,  $u'$  and  $s'$  can be expressed, in normalised form:

$$\frac{p'}{\gamma p} = P^+ \exp(i\omega t) + P^- \exp(i\omega t) \quad (1.4)$$

$$\frac{u'}{c} = P^+ \exp(i\omega t) - P^- \exp(i\omega t) \quad (1.5)$$

$$\frac{s'}{c_p} = \sigma \exp(i\omega t) \quad (1.6)$$

In order for Eqs. 1.1 and 1.2 to involve pressure, velocity and entropy fluctuations only, density perturbations can be expressed  $\rho' = \frac{\rho_0 p'}{\gamma p_0} - \frac{\rho_0 s'}{c_p}$ . Then, expressing the primitive variables in wave form leads to relations involving the entropy perturbations  $\sigma$  and the regressive and progressive acoustic fluctuations  $P^-$  and  $P^+$ , both upstream and downstream, i.e. at positions 1 and 2. These equations are directly applicable for subsonic flow, which this paragraph concentrates on, as supercritical configurations are not investigated in this PhD.

Different cases are considered. Entropy noise results from the acceleration of entropy perturbations through the nozzle, but acoustic waves are also scattered, either as a result of entropy noise or from other sources upstream or downstream of the nozzle. In order to estimate entropy noise,  $\sigma$  is imposed at the inlet, and no acoustic waves propagate towards the nozzle, so that  $P_1^+ = P_2^- = 0$ . The acoustic waves generated in the nozzle  $P_1^-$  and  $P_2^+$  can be expressed in the form of transfer functions, which give the noise levels corresponding to a certain entropy wave  $\sigma$ :

$$\left[ \frac{P_1^-}{\sigma_1} \right] = - \left( \frac{M_2 - M_1}{1 - M_1} \right) \frac{\frac{1}{2} M_1}{1 + \frac{\gamma-1}{2} M_1} \quad (1.7)$$

$$\left[ \frac{P_2^+}{\sigma_1} \right] = \left( \frac{M_2 - M_1}{1 + M_2} \right) \frac{\frac{1}{2} M_2}{1 + \frac{\gamma-1}{2} M_1 M_2} \quad (1.8)$$

Secondly, acoustic excitation from upstream is considered, and the wave  $P_1^+$  is imposed while

$\sigma_1 = P_2^- = 0$ . The resulting acoustic waves  $P_1^-$  and  $P_2^+$  then write:

$$\left[ \frac{P_1^-}{P_1^+} \right] = \left( \frac{M_2 - M_1}{1 - M_1} \right) \left( \frac{1 + M_1}{M_2 + M_1} \right) \frac{1 - \frac{\gamma-1}{2} M_1 M_2}{1 + \frac{\gamma-1}{2} M_1 M_2} \quad (1.9)$$

$$\left[ \frac{P_2^+}{P_1^+} \right] = \left( \frac{2M_2}{1 + M_2} \right) \left( \frac{1 + M_1}{M_2 + M_1} \right) \frac{1 + \frac{\gamma-1}{2} M_2^2}{1 + \frac{\gamma-1}{2} M_1 M_2} \quad (1.10)$$

Finally, the wave  $P_2^-$  is imposed to acoustically force the system from downstream. Other incoming fluctuations are set to zero, so that  $\sigma_1 = P_1^+ = 0$ . The corresponding transfer functions write:

$$\left[ \frac{P_1^-}{P_2^-} \right] = \left( \frac{2M_1}{M_1 + M_2} \right) \left( \frac{1 - M_2}{1 - M_1} \right) \frac{1 + \frac{\gamma-1}{2} M_1^2}{1 + \frac{\gamma-1}{2} M_1 M_2} \quad (1.11)$$

$$\left[ \frac{P_2^+}{P_2^-} \right] = - \left( \frac{M_2 - M_1}{1 + M_2} \right) \left( \frac{1 - M_2}{M_2 + M_1} \right) \frac{1 - \frac{\gamma-1}{2} M_1 M_2}{1 + \frac{\gamma-1}{2} M_1 M_2} \quad (1.12)$$

In the case of a choked nozzle, the wave  $P_2^-$  cannot be imposed and is an extra unknown. A fourth equation is therefore needed, and the mass flow rate expressed at the throat where  $M=1$  is used. Relations for the transfer functions in acoustically and entropy forced cases can then be written. Moase et al. [2007] and Huet [2016] modified the model's boundary conditions so the wave  $P_2^-$  could be imposed, in cases with or without a shock. With three unknowns, only three equations are required once again, and Eq. 1.3 is dropped since entropy is not conserved through shocks.

### 1.1.1.2 Compact model for turbine stator flow

The model developed by Cumpsty and Marble [1977] to estimate entropy noise and acoustic scattering in a compact stator is presented in this section. A sketch of the problem is presented in Fig 1.1. Similarly to Eqs. 1.1-1.3 in the previous section but assuming 2D flow, the matching conditions between the inlet at 1 and the downstream position 2 for mass-flow rate, stagnation temperature and entropy write:

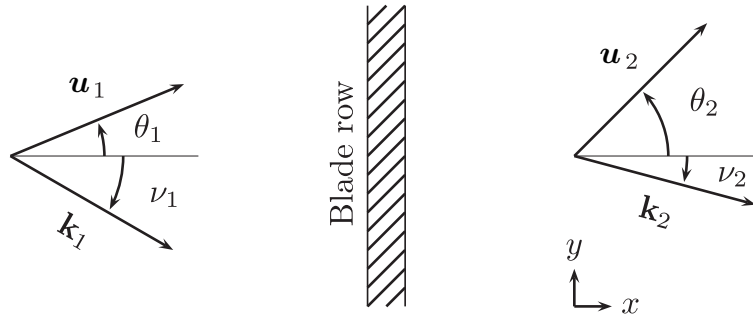


Figure 1.1: Sketch of the configuration considered in Cumpsty and Marble's [1977] compact model. This figure is adapted from Leyko et al. [2014].

$$\begin{aligned} \left(\frac{p'}{\gamma p_0}\right)_1 + \frac{1}{M_1} \left(\frac{|\mathbf{u}'|}{c_0}\right)_1 - \theta'_1 \tan \theta_1 - \left(\frac{s'}{c_p}\right)_1 &= \left(\frac{p'}{\gamma p_0}\right)_2 + \frac{1}{M_2} \left(\frac{|\mathbf{u}'|}{c_0}\right)_2 \\ &\quad - \theta'_2 \tan \theta_2 - \left(\frac{s'}{c_p}\right)_2 \end{aligned} \quad (1.13)$$

$$\begin{aligned} \frac{1}{1 + \frac{\gamma-1}{2} M_1^2} \left[ \left(\frac{p'}{\gamma p_0}\right)_1 + M_1 \frac{|\mathbf{u}'|}{c_0} + \frac{1}{\gamma-1} \left(\frac{s'}{c_p}\right)_1 \right] &= \frac{1}{1 + \frac{\gamma-1}{2} M_2^2} \\ \left[ \left(\frac{p'}{\gamma p_0}\right)_2 + M_2 \frac{|\mathbf{u}'|}{c_0} + \frac{1}{\gamma-1} \left(\frac{s'}{c_p}\right)_2 \right] \end{aligned} \quad (1.14)$$

$$\left(\frac{s'}{c_p}\right)_1 = \left(\frac{s'}{c_p}\right)_2 \quad (1.15)$$

where  $\theta$  is the flow angle and  $|\mathbf{u}'|$  the total velocity fluctuation. A fourth equation is necessary to solve the system and the Kutta condition is used:

$$\theta'_2 = 0 \quad (1.16)$$

In a generalised form, it can be written:

$$\theta'_2 = \alpha \theta'_1 \quad (1.17)$$

The fluctuations at the stator outlet can then be related to those at the inlet by expressing Eqs 1.15-1.17 in matrix form:

$$\mathbf{E}_1 \begin{pmatrix} s'/c_p \\ |\mathbf{u}'|/c_0 \\ p'/\gamma p_0 \\ \theta' \end{pmatrix}_1 = \mathbf{E}_2 \begin{pmatrix} s'/c_p \\ |\mathbf{u}'|/c_0 \\ p'/\gamma p_0 \\ \theta' \end{pmatrix}_2 \quad (1.18)$$

with

$$\mathbf{E}_1 = \begin{bmatrix} 1 & 0 & 0 & 0 \\ -1 & 1/M_1 & 1 & -\tan \theta_1 \\ \mu_1/(\gamma-1) & M_1 \mu_1 & \mu_1 & 0 \\ 0 & 0 & 0 & \alpha \end{bmatrix} \quad (1.19)$$

and

$$\mathbf{E}_2 = \begin{bmatrix} 1 & 0 & 0 & 0 \\ -1 & 1/M_2 & 1 & -\tan \theta_2 \\ \mu_2/(\gamma-1) & M_2 \mu_2 & \mu_2 & 0 \\ 0 & 0 & 0 & 1 \end{bmatrix} \quad (1.20)$$

where  $\mu = [1 + (\gamma-1)M^2/2]^{-1}$ . Next, consider harmonic entropy, vorticity and both upstream and downstream propagating acoustic waves  $\sigma = s'/c_p$ ,  $\Xi = \xi'/\omega$  and  $P^\pm = p'_\pm/(\gamma p)$  respectively, where  $p'_\pm$  are the pressure fluctuations associated to the progressive or regressive

acoustic waves. They can be written in the form  $w = A \exp[i(\omega t - \mathbf{k} \cdot \mathbf{x})]$ , where  $A$  is the wave's amplitude,  $\omega$  the angular frequency and  $\mathbf{k}$  the wave vector. Using the linearised Euler equations, these waves can be related to the primitive variable fluctuations:

$$\begin{pmatrix} s'/c_p \\ |\mathbf{u}'|/c_0 \\ p'/\gamma p_0 \\ \theta' \end{pmatrix} = \mathbf{P} \begin{pmatrix} \sigma \\ \Xi \\ P^+ \\ P^- \end{pmatrix} \quad (1.21)$$

where

$$\mathbf{P} = \begin{bmatrix} 1 & 0 & 0 & 0 \\ 0 & -i \frac{\sin(\nu_\xi - \theta)}{K_\xi} & \frac{K_+ \cos(\nu_+ - \theta)}{1 - MK_+ \cos(\nu_+ - \theta)} & \frac{K_- \cos(\nu_- - \theta)}{1 - MK_- \cos(\nu_- - \theta)} \\ 0 & 0 & 1 & 1 \\ 0 & -i \frac{\sin(\nu_\xi - \theta)}{MK_\xi} & \frac{K_+ \sin(\nu_+ - \theta)}{M[1 - MK_+ \cos(\nu_+ - \theta)]} & \frac{K_- \sin(\nu_- - \theta)}{M[1 - MK_- \cos(\nu_- - \theta)]} \end{bmatrix} \quad (1.22)$$

with  $\nu$  the wave angle and  $\mathbf{K} = \mathbf{k}c/\omega$  the dimensionless wave vector. Finally, combining Eqs. 1.18 and 1.21, the waves upstream and downstream of the stator are related by:

$$\mathbf{E}_1 \mathbf{P}_1 \begin{pmatrix} \sigma \\ \Xi \\ P^+ \\ P^- \end{pmatrix}_1 = \mathbf{E}_2 \mathbf{P}_2 \begin{pmatrix} \sigma \\ \Xi \\ P^+ \\ P^- \end{pmatrix}_2 \quad (1.23)$$

The waves travelling into the nozzle are imposed, while outgoing waves are not known. The only unknown in the left-hand side term of Eq. 1.23 is therefore  $P_1^-$  which travels upstream, while only  $P_2^-$  is known in the right-hand term. In order to gather the unknowns into one term, in the case of a single blade row, the vectors' last terms can be permuted and the matrices modified accordingly, yielding:

$$\begin{pmatrix} \sigma_2 \\ \Xi_2 \\ P_2^+ \\ P_1^- \end{pmatrix} = \mathbf{A}_o^{-1} \mathbf{A}_i \begin{pmatrix} \sigma_1 \\ \Xi_1 \\ P_1^+ \\ P_2^- \end{pmatrix} \quad (1.24)$$

Assuming incoming waves are plane and the Kutta condition is satisfied, leading to  $\alpha = 0$  in Eq. 1.17, this equation can be solved to obtain thermo-acoustic and acoustic transfer functions to estimate entropy noise and acoustic scattering. Leyko et al. [2014] also provide expressions for the latter. As well as describing the compact model in detail, Leyko et al. [2014] verified its results numerically, as did Mishra and Bodony [2013].

### 1.1.2 1D models for nozzle flow

Based on Marble and Candel's [1977] compact solution, Huet and Giauque [2013a] extended the compact model to non-linear perturbations in subcritical and supercritical nozzles in the absence of a shock. They derived both second-order and full non-linear solutions. By comparing them, they found non-linearity to be negligible in subcritical converging nozzles and

the supercritical case with no shock. In subsonic diverging nozzles however, they concluded high-order non-linearities may significantly affect the regressive acoustic wave. Huet [2016] completed this model in the case of supercritical nozzles with shocked flow regimes. Comparison of the second order model to numerical simulations showed that, with a large Mach number at the inlet, non-linear effects on the downstream propagating acoustic wave resulting from entropic excitation are significant and harmonics of the forcing frequency become predominant.

De Domenico et al. [2019] also proposed an extension of Marble and Candel's [1977] model for which the isentropic assumption is relaxed. The model can be used to estimate entropy noise and acoustic scattering through orifice plates and non-isentropic nozzles with subsonic-to-sonic throat conditions, given a static pressure loss parameter. Results matched experimental data. De Domenico et al. [2019] showed taking pressure loss into account has a non-negligible effect on the transfer functions of orifice-plates or non-isentropic nozzles in the presence of flow separation.

Marble and Candel [1977] extended their model to non-compact solutions for supercritical nozzles with a linear velocity profile. Alternatively, Stow et al. [2002] and Goh and Morgans [2011] proposed an equivalent nozzle length by correcting the phase of the transfer functions using the asymptotic expansion of the LEE. Moase et al. [2007] and Giauque et al. [2012] also extended Marble and Candel's model to non-compact frequencies, but using a piecewise linear velocity profile assumption. They concentrated on choked nozzles and supersonic diffusers and on subsonic nozzles respectively. As proposed by Marble and Candel [1977], linearised Euler equations are reduced to an hypergeometric differential equation in each linear-velocity element, solved numerically, and jump conditions are used at discontinuities. § 1.1.2.1 details the model in the subsonic case, which is used in this PhD. Giauque et al. [2013] combined the model with an optimisation algorithm to minimise or maximise entropy noise in a nozzle by modifying its shape. Durán and Moreau [2013b] used a different method to estimate entropy noise in non-compact nozzles in subsonic and choked conditions, with or without a shock. They solved the linearised Euler equations in the frequency domain using Marble and Candel's flow invariants and the Magnus expansion [Magnus, 1954]. They found good agreement with Giauque et al. [2012] in subsonic flow. In the supersonic case, Durán and Moreau [2013b] used jump conditions based on the Rankine-Huguenot equation at shocks, like Stow et al. [2002] and Moase et al. [2007].

### 1.1.2.1 1D model MARCAN

The one-dimensional model MARCAN was developed to account for non-compact nozzles of arbitrary shape [Giauque et al., 2012, Huet, 2013b], based on the work of Marble and Candel [1977] and Moase et al. [2007]. Similar assumptions as those detailed above for the compact models are made:

- Viscous effects are neglected.
- The flow is adiabatic and the undisturbed flow is isentropic.
- The gas is ideal and calorifically perfect, so that  $\gamma$ ,  $c_p$  and  $c_v$  are constant.
- Perturbations are small, allowing the linearisation of equations.



Under these assumptions and using the equations for continuity, momentum and entropy in a perturbed form, pressure, velocity, density and entropy fluctuations  $p'$ ,  $u'$ ,  $\rho'$  and  $\sigma'$  are described by the following equations:

$$\frac{p'}{\gamma p} - \frac{\rho'}{\rho} = \frac{s'}{c_p} \quad (1.25)$$

$$\left[ \frac{\partial}{\partial t} + u \frac{\partial}{\partial x} \right] \left( \frac{p'}{\gamma p} \right) + u \frac{\partial}{\partial x} \left( \frac{u'}{u} \right) = 0 \quad (1.26)$$

$$\left[ \frac{\partial}{\partial t} + u \frac{\partial}{\partial x} \right] \left( \frac{u'}{u} \right) + \frac{c^2}{u} \frac{\partial}{\partial x} \left( \frac{p'}{\gamma p} \right) + \left( 2 \frac{u'}{u} - (\gamma - 1) \frac{p'}{\gamma p} \right) \frac{du}{dx} = \frac{du}{dx} \frac{s'}{c_p} \quad (1.27)$$

Assuming a harmonic regime of angular frequency  $\omega$ , the normalised pressure, velocity and entropy fluctuations are expressed:

$$\frac{p'}{\gamma p}(x) = P(x)e^{i\omega t} \quad (1.28)$$

$$\frac{u'}{u}(x) = U(x)e^{i\omega t} \quad (1.29)$$

$$\frac{s'}{c_p}(x) = \sigma(x)e^{i\omega t} \quad (1.30)$$

Furthermore, the normalised entropy perturbation  $\sigma(x)$  writes:

$$\sigma(x) = S e^{-i\omega t} \quad (1.31)$$

with  $g(x) = \int^x d\zeta/u\zeta$ . Introducing these normalised fluctuations into Eqs. 1.26-1.27 and using the isentropic flow relation  $c^2 + u^2(\gamma - 1)/2 = c_*^2(\gamma + 1)/2$ , in which the critical speed of sound  $c_*$  is used as a reference, it comes:

$$i\omega P + u\dot{P} + u\dot{U} = 0 \quad (1.32)$$

$$i\omega U + u\dot{U} + \left( \frac{\gamma + 1}{2} \frac{c_*^2}{u} - u \frac{\gamma - 1}{2} \right) \dot{P} + (2U - (\gamma - 1)P) \frac{du}{dx} = \frac{du}{dx} \sigma \exp[-i\omega g(x)] \quad (1.33)$$

where  $\dot{\phantom{x}}$  represents the derivative with respect to  $x$ .

Assuming a linear velocity profile in the nozzle, the acceleration  $\Lambda = \Delta U/\Delta x = du/dx$  is constant and the velocity can be expressed  $u = \Lambda x$ . With the change of variables  $\tau = \Lambda t$ ,  $\Omega = \omega/\Lambda$  and  $X = (\Lambda x/c_*)^2$  and after some algebra, Eqs. 1.32-1.33 are recast to:

$$X(1 - X)P'' - X \left( 2 + \frac{2i\Omega}{\gamma + 1} \right) P' - \frac{(2 + i\Omega)i\Omega}{2(\gamma + 1)} P = -S \frac{i\Omega}{2(\gamma + 1)} \left( \frac{X}{X^1} \right)^{-i\Omega/2} \quad (1.34)$$

$$(2 + i\Omega)U = -(\gamma + 1)(1 - X)P' + (\gamma - 1 + i\Omega)P + S \left( \frac{X}{X^1} \right)^{-i\Omega/2} \quad (1.35)$$

where  $-'$  now stands for the derivative with respect to  $X$  and  $X^1$  is the nondimensional abscissa on the left. Resolution of Eq. 1.34 provides the pressure fluctuation  $P$  and Eq. 1.35

can then be used to compute the velocity fluctuation  $U$ . Equation 1.34 is a non-homogeneous hypergeometric differential equation of the form:

$$X(1-X)F'' + (c - (a+b+1)X)F' - abF = RS \quad (1.36)$$

with

$$R = -\frac{i\Omega}{2(\gamma+1)} \left( \frac{X}{X^1} \right)^{-i\Omega/2} \quad (1.37)$$

$$a = \frac{1}{2} \left( 2i\frac{\Omega}{\gamma+1} + 1 + \sqrt{-4 \left( \frac{\Omega}{\gamma+1} \right)^2 + 2\frac{\Omega^2}{\gamma+1} + 1} \right) \quad (1.38)$$

$$b = \frac{1}{2} \left( 2i\frac{\Omega}{\gamma+1} + 1 - \sqrt{-4 \left( \frac{\Omega}{\gamma+1} \right)^2 + 2\frac{\Omega^2}{\gamma+1} + 1} \right) \quad (1.39)$$

$$c = 0 \quad (1.40)$$

Two solutions of the homogeneous counterpart of Eq. 1.36 are:

$$Y_1(X) = {}_2F_1(a, b; a+b+1; 1-X) \quad (1.41)$$

$$Y_2(X) = X {}_2F_1(a+1, b+1; 2; X) \quad (1.42)$$

where  ${}_2F_1(a, b; c; X)$  is the hypergeometric function. The particular solution  $Y_p$  writes:

$$Y_p(X) = [I(X)Y_1(X) + J(X)Y_2(X)] S \quad (1.43)$$

with

$$I(X) = -\int_{X^1}^X \frac{R(\xi)Y_2(\xi)}{X(1-X)W(Y_1, Y_2)(\xi)} d\xi \quad (1.44)$$

$$J(X) = \int_{X^1}^X \frac{R(\xi)Y_1(\xi)}{X(1-X)W(Y_1, Y_2)(\xi)} d\xi \quad (1.45)$$

using the Wronskian of the functions  $Y_1$  and  $Y_2$ , obtained using Abel's identity:

$$W(Y_1, Y_2)(X) = \frac{Y_1(X^1)Y_2'(X^1) - Y_1'(X^1)Y_2(X^1)}{(1-X^1)^{-(a+b+1)}} \quad (1.46)$$

In the case of a nozzle of arbitrary shape, it is discretised into elements, noted  $k$ , in which the velocity profile is assumed to be linear. In such subcritical or supercritical elements, outside of the sonic throat, velocity, pressure and entropy perturbations are expressed:

$$P_k(X) = \beta_k^1(X)A_k + \beta_k^2(X)B_k + d_k(X)S_k \quad (1.47)$$

$$U_k(X) = \alpha_k^1(X)A_k + \alpha_k^2(X)B_k + c_k(X)S_k \quad (1.48)$$

$$\sigma_k(X) = S_k \left( \frac{X}{X_k^1} \right)^{-i\Omega_k/2} \quad (1.49)$$

where  $A_k$ ,  $B_k$  and  $S_k$  are unknowns and

$$\beta_k^1 = Y_1^k \quad (1.50)$$

$$\beta_k^2 = Y_2^k \quad (1.51)$$

$$d_k = Y_p^k \quad (1.52)$$

$$\alpha_k^1 = \frac{\gamma - 1 + i\Omega}{2 + i\Omega} Y_1^k - \frac{(\gamma + 1)(1 - X)}{2 + i\Omega} (Y_1^k)' \quad (1.53)$$

$$\alpha_k^2 = \frac{\gamma - 1 + i\Omega}{2 + i\Omega} Y_2^k - \frac{(\gamma + 1)(1 - X)}{2 + i\Omega} (Y_2^k)' \quad (1.54)$$

$$c_k = \frac{\gamma - 1 + i\Omega}{2 + i\Omega} Y_p^k - \frac{(\gamma + 1)(1 - X)}{2 + i\Omega} (Y_p^k)' + \frac{1}{2 + i\Omega_k} \left( \frac{X}{X_k^1} \right)^{-i\Omega_k/2} \quad (1.55)$$

If the nozzle is discretised into  $n$  elements,  $2n$  constants  $(A_k, B_k)$  must be determined to solve the linear system of Eqs. 1.47-1.48. Considering  $p'$  and  $u'$  are continuous between two elements leads to  $2(n - 1)$  equations. Nozzle boundary conditions provide the last two equations. It is assumed the domain extremities are non-reflective, and entropy and upstream or downstream propagating acoustic waves may be injected to generate entropy noise or acoustic scattering. In subcritical flow, pressure and velocity fluctuations at the nozzle boundaries are related by the reduced impedance coefficient  $Z$ , which is equal to  $-1$  at the nozzle inlet and  $1$  at the outlet. One can write:

$$P - ZMU = 2P_0 \quad (1.56)$$

where  $P_0$  is the acoustic forcing, either from upstream  $P_0 = P_1^+$  or from the nozzle outlet  $P_0 = P_n^-$ . Using Eqs. 1.47-1.49 and imposing the entropy fluctuation  $\sigma_0$  at the inlet directly, the boundary conditions are expressed:

$$S_1 = \sigma_0 \quad (1.57)$$

$$\nu_1^1 A_1 + \nu_1^2 B_1 + \nu_1^3 S_1 = 2P_1^+ \quad (1.58)$$

$$\nu_n^1 A_n + \nu_n^2 B_n + \nu_n^3 S_n = 2P_n^- \quad (1.59)$$

where

$$\nu_1^1 = \beta_1^1(X_1^1) - Z_1 M_1 \alpha_1^1(X_1^1) \quad (1.60)$$

$$\nu_1^2 = \beta_1^2(X_1^1) - Z_1 M_1 \alpha_1^2(X_1^1) \quad (1.61)$$

$$\nu_1^3 = d_1(X_1^1) - Z_1 M_1 c_1(X_1^1) \quad (1.62)$$

$$\nu_n^1 = \beta_n^1(X_n^2) - Z_n M_n \alpha_n^1(X_n^2) \quad (1.63)$$

$$\nu_n^2 = \beta_n^2(X_n^2) - Z_n M_n \alpha_n^2(X_n^2) \quad (1.64)$$

$$\nu_n^3 = d_n(X_n^2) - Z_n M_n c_n(X_n^2) \quad (1.65)$$

with  $X_n^2$  is the nondimensional abscissa on the right of element  $n$ .

In the case of supercritical flow with a normal shock, jump conditions are used to describe the reflection and transmission occurring at the shock in the same way as described by Moase et al. [2007]. They are applied to the nozzle element  $k$  in which the shock is assumed to be.

### 1.1.3 2D modelling

Two-dimensional flow variations and their effect on entropy noise have been studied from an analytical point of view in both the circumferential and radial directions. Stow et al. [2002] extended Marble and Candel's [1977] compact model to supersonic flows containing circumferential modes. They made the thin annular nozzle assumption for which variations in the radial direction are small compared to those in the circumferential direction. Dowling and Mahmoudi [2015] developed exact solutions for acoustic, entropy and vorticity waves in the presence of circumferential modes in compact annular ducts for very low Mach numbers. The one-dimensional model of Durán and Moreau [2013b] developed from the invariant method was extended to annular configurations for subsonic and choked flow by Durán and Morgans [2015]. Zheng [Zheng, 2016, Zheng et al., 2015] developed a semi-analytical model to take the radial evolution of both the mean flow and entropy perturbations in nozzles into account. It is presented in detail in § 1.1.3.1 as it is used and extended in this PhD.

Few analytical solutions for entropy noise in turbine geometries have been developed since Cumpsty and Marble's [1977] compact model due to the complexity of the flow. Leyko et al. [2010], Livebardon et al. [2016] and Bauerheim et al. [2016] associated an attenuation function to Cumpsty and Marble's compact solution to estimate entropy noise in several turbine stages. The attenuation function accounts for the distortion of the entropy wave in between blade rows, but the flow in the inter-blade passage remains compact. Tam et al. [2013] used an equivalent nozzle to model a full auxiliary power unit from combustor to turbine outlet, while Tam and Parrish [2014] proposed a source function to model the entropy noise generated around a single blade, and which could be integrated to a future model for entropy noise in a turbine row. Guzmán-Iñigo et al. [2018] analytically described the noise generated by the interaction of entropy perturbations with an isolated blade. The latter was assumed to be acoustically compact, but no restrictions were made on the entropy wave. Only uniform flow was considered.

#### 1.1.3.1 2D model CHEOPS-Nozzle

The model CHEOPS-Nozzle [Zheng, 2016, Zheng et al., 2015] was developed to estimate entropy noise in nozzle flow. A simplified version detailed by Emmanuelli et al. [2020] is presented in this section. This model is compared to CAA simulations in chapter 3 and then used as a basis for developments with turbine stator configurations in chapter 4. It is based on the Euler equations and obeys the following assumptions:

- all viscous terms are neglected, verifying the Euler equations,
- pressure and velocity fluctuations are solely due to acoustics, thereby neglecting vorticity fluctuations,
- swirl is neglected, leading to  $u_\theta = 0$  m/s.
- the mean flow is considered 2D-axisymmetric, with variations in the axial and radial directions,

- acoustic waves are considered one-dimensional throughout the domain, as radial modes are cut-off by the duct and azimuthal modes are neglected, assuming all fields are 2D-axisymmetric,
- perturbations are small, allowing the linearisation of equations.

In order to estimate entropy noise, the entropy fluctuations  $s'$  need to be computed throughout the domain, as well as the pressure and velocity fluctuations  $p'$  and  $u'$  which characterise the resulting one-dimensional acoustic waves. As entropy is purely convected, it can be computed numerically from mean flow quantities. This leaves two unknowns, so that two equations are needed. Mass conservation and momentum in the main direction of the flow are chosen.

In its integral form, the continuity equation can be written:

$$\frac{\partial}{\partial t} \int_V \rho dV = \int_A [\rho u_x](x) dA - \int_A [\rho u_x](x + dx) dA \quad (1.66)$$

where  $V$  is the control volume, which is closed by the area  $A$ , other than the geometry's walls. The radially dependent flow variables are reduced to one-dimensional quantities by averaging over each section of area  $A$  using the formula:

$$\bar{z} = \frac{1}{A} \int_A z dA \quad (1.67)$$

and after some simplifications, Eq. (1.66) reduces to:

$$\frac{\partial \bar{\rho}}{\partial t} + \frac{\partial \bar{\rho} u_x}{\partial x} = -\frac{1}{A} \bar{\rho} u_x \frac{dA}{dx} \quad (1.68)$$

where  $u_x$  is the velocity in the axial direction. Axial momentum on the other hand, can be written:

$$\frac{\partial u_x}{\partial t} + u_x \frac{\partial u_x}{\partial x} + u_r \frac{\partial u_x}{\partial r} = -\frac{1}{\rho} \frac{\partial p}{\partial x} \quad (1.69)$$

Both these equations are linearised using flow variable decomposition into mean and perturbed quantities, such as  $f = f_0 + f'$ . Because of the one-dimensional acoustics assumption, the radial velocity fluctuation  $u'_r = 0$  m/s and sectional averaging of acoustic fluctuations amounts to  $\bar{u}'_x = u'_x$  and  $\bar{p}' = p'$ . In addition, the equations are given in terms of entropy and pressure fluctuations,  $s'$  and  $p'$ , rather than density perturbations  $\rho'$ . The continuity and momentum equations in the direction of the flow then write:

$$\begin{aligned} A \left( \frac{1}{c_0^2} \right) \frac{\partial p'}{\partial t} + \frac{d}{dx} \left[ A \left( \frac{\bar{u}_{0x}}{c_0^2} \right) \right] p' + \left[ A \left( \frac{\bar{u}_{0x}}{c_0^2} \right) \right] \frac{\partial p'}{\partial x} + \frac{dA \bar{\rho}_0}{dx} u'_x + A \bar{\rho}_0 \frac{\partial u'_x}{\partial x} \\ = \frac{\partial}{\partial x} \left[ A (\bar{\rho}_0 u_{0x}) \frac{s'}{c_p} \right] + A \frac{\partial}{\partial t} \left( \bar{\rho}_0 \frac{s'}{c_p} \right) \end{aligned} \quad (1.70)$$

$$\begin{aligned} \frac{\partial u'_x}{\partial t} + u'_x \left( \frac{\partial \bar{u}_{0x}}{\partial x} \right) + \bar{u}_{0x} \frac{\partial u'_x}{\partial x} + \left( \frac{1}{\rho_0} \right) \frac{\partial p'}{\partial x} + \left[ \frac{u_{0x}}{\gamma p_0} \frac{\partial u_{x0}}{\partial x} + \frac{u_{0r}}{\gamma p_0} \frac{\partial u_{x0}}{\partial r} \right] p' \\ = \left[ u_{0x} \frac{\partial u_{x0}}{\partial x} + u_{0r} \frac{\partial u_{x0}}{\partial r} \right] \frac{s'}{c_p} \end{aligned} \quad (1.71)$$

Next, the harmonic regime is considered in order to eliminate terms involving temporal derivatives. Under this condition, fluctuations can be written in the form:

$$u'_x(x, t) = \hat{u}(x)e^{i\omega t} \quad (1.72)$$

$$p'(x, t) = \hat{p}(x)e^{i\omega t} \quad (1.73)$$

$$\frac{s'}{c_p}(x, t) = \hat{\sigma}(x)e^{i\omega t} \quad (1.74)$$

where  $\hat{u}$ ,  $\hat{p}$  and  $\hat{\sigma}$  are the complex amplitudes of the velocity, pressure and normalised entropy fluctuations. The angular frequency is noted  $\omega = 2\pi f$ , with  $f$  the frequency. The mass conservation and momentum equations, Eqs. 1.70-1.71, can ultimately be written:

$$\begin{aligned} \left( A \left( \frac{1}{c_0^2} \right) i\omega + \frac{d}{dx} \left[ A \left( \frac{\overline{u_{0x}}}{c_0^2} \right) \right] \right) \hat{p} + \left[ A \left( \frac{\overline{u_{0x}}}{c_0^2} \right) \right] \frac{\partial \hat{p}}{\partial x} + \frac{dA\bar{\rho}_0}{dx} \hat{u} + A\bar{\rho}_0 \frac{\partial \hat{u}}{\partial x} \\ = \frac{d}{dx} \left[ A(\overline{\rho_0 u_{0x}}) \hat{\sigma} \right] + Ai\omega \overline{\rho_0 \hat{\sigma}} \end{aligned} \quad (1.75)$$

$$\begin{aligned} \left[ \frac{u_{0x}}{\gamma p_0} \frac{\partial u_{x0}}{\partial x} + \frac{u_{0r}}{\gamma p_0} \frac{\partial u_{x0}}{\partial r} \right] \hat{p} + \left( \frac{1}{\rho_0} \right) \frac{\partial p'}{\partial x} + \left[ i\omega + \left( \frac{\partial \overline{u_{0x}}}{\partial x} \right) \right] \hat{u} + \overline{u_{0x}} \frac{\partial \hat{u}}{\partial x} \\ = \left[ \overline{u_{0x} \frac{\partial u_{x0}}{\partial x} + u_{0r} \frac{\partial u_{x0}}{\partial r}} \right] \hat{\sigma} \end{aligned} \quad (1.76)$$

Equations 1.75-1.76 form a system of two equations and two unknowns  $\hat{u}$  and  $\hat{p}$ .

Its numerical resolution is summarised by Fig. 1.2, and it is only briefly described in this paragraph because it is close to the process detailed in chapter 4, in the case of a turbine stator. The mean flow is an input of the problem which needs to be computed externally, typically using CFD. It must be interpolated onto a 2D-structured mesh with constant axial

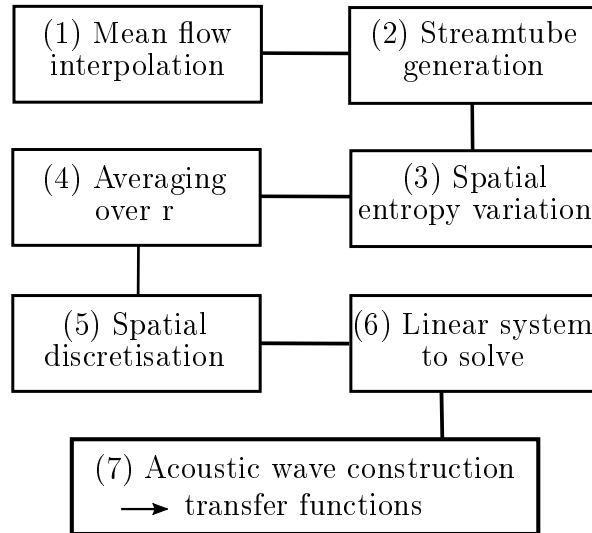


Figure 1.2: Resolution process of CHEOPS-Nozzle.

planes to allow cross-sectional averaging. Streamlines are generated by the model and used to rediscrétise the mesh in the radial direction. Entropy perturbations are also an input to Eqs. 1.75-1.76, but they are computed within the model using a time-marching method and the streamlines' properties. Once the two-dimensional variations of both the mean flow and the entropy fluctuations are taken into account, they can be sectionally averaged so Eqs. 1.75-1.76 can be solved. Second order spatial discretisation is applied along the axial direction. Finally, the linear system is closed using non-reflective acoustic boundary conditions, and the numerical resolution of the resulting matrix yields the pressure and velocity fluctuations required to compute the nozzle's transfer functions.

## 1.2 Overview of entropy noise generation investigations

The existence of entropy noise was established analytically in the 70s [Candel, 1972, Marble, 1973, Morfey, 1973], and it has been studied extensively following more recent evolutions of civil aircraft engines. As well as highlighting the significance of non-compact and two-dimensional flows, the analytical studies presented in section 1.1 suggest non-linearity and non-isentropic flow can affect entropy noise. The noise generation mechanism is discussed in more detail in the present section, which constitutes an overview of the current knowledge of entropy noise.

### 1.2.1 Attenuation of entropy perturbations

Acoustic waves are considered to propagate with little variation in constant-section ducts such as longitudinal combustors. However, between viscous effects and potential turbulent velocity fluctuations, entropy perturbations are affected by the flow as they are convected in the combustor and up to the first turbine stage, even before they are accelerated in the turbine stages or the nozzle [Morgans and Durán, 2016]. Sattelmayer [2003] was the first to investigate this, in the context of combustion instabilities, and developed an analytical approach to take dispersion arising from spatially varying mean velocity into account. This model showed dispersion was so strong it could render entropy noise negligible in realistic conditions. More recently, Morgans et al. [2013] simulated the advection of entropy waves in turbulent channel flow. Shear dispersion of entropy perturbations proved dominant, while dissipation remained negligible. Furthermore, they concluded the probability density function of an entropy spot used by Sattelmayer [2003] in his model is better approximated by a Gaussian than a rectangle. Using this Gaussian model, Morgans et al. [2013] found the entropy wave at the exit of typical combustors to be strong enough to generate significant acoustic fluctuations, despite shear dispersion. Giusti et al. [2017] showed entropy perturbations decay with wavelength and propagation distance using experimental and numerical data. They also proposed a new model to compute entropy transfer functions. They concluded shear dispersion is dominant at low Helmholtz number (ratio between the propagation distance and the wavelength) while turbulent mixing and diffusion could play a role at high Helmholtz number in constant-section ducts. However, this study was not led in realistic flow conditions, which Xia et al. [2018] aimed to do using low Mach number LES of a real gas turbine combustor. The computed decay in entropy is illustrated in Fig. 1.3. This study

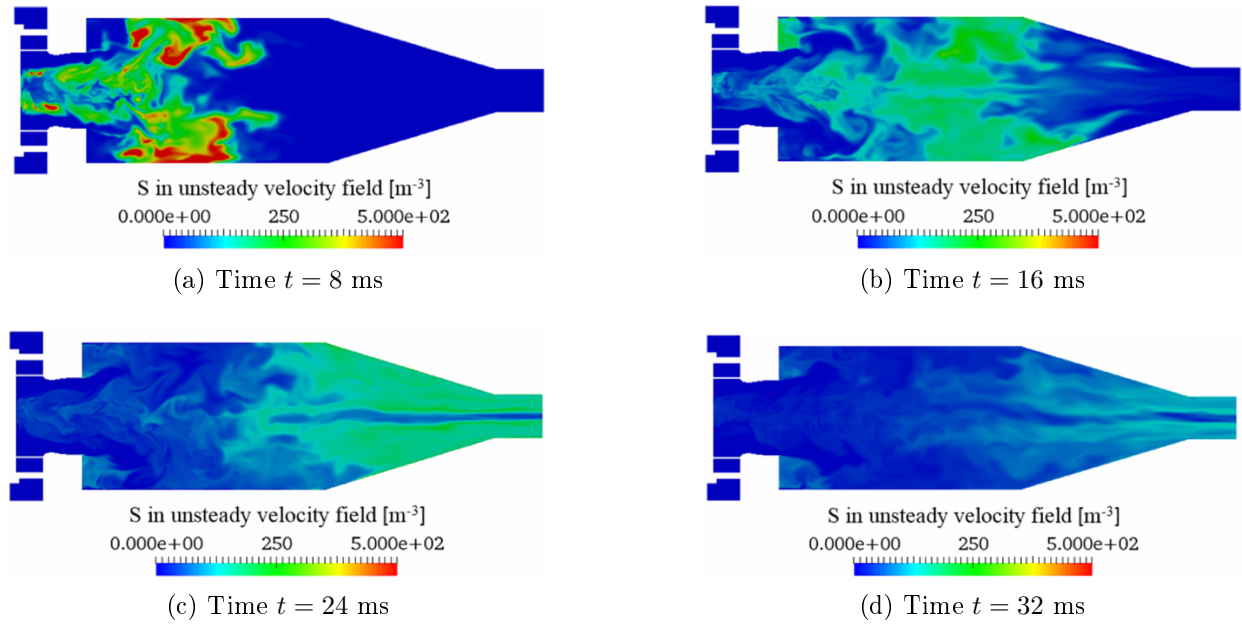


Figure 1.3: Contours of reduced entropy concentration,  $S$ , on a symmetry plane of  $z = 0$ , at four time instants after the impulsive entropy source injection into the time-varying combustor flow-field [Xia et al., 2018].

showed advection was dominant in the transport of entropy perturbations, while thermal diffusion and viscous production could be neglected. It also indicated both mean flow fields and large-scale unsteady flow features must be considered. Furthermore, while entropy is generally considered a passive scalar, Hosseinalipour et al. [2017] suggested that not only are entropy perturbations affected by the flow, but they can also have an impact on flow hydrodynamics as they decay.

The attenuation of entropy perturbations has not only been investigated in combustors and channel flow, but also in nozzles and turbine stages in which they are accelerated. Using numerical simulation, Becerril Aguirre [2017] and Moreau et al. [2018] concluded entropy perturbations are dispersed through nozzles with hardly any dissipation, like for ducts discussed in the previous paragraph. They found dispersion in the DLR EWG geometry is weak, in particular since the forcing frequency is low, and hot spots are only attenuated in the duct downstream of the nozzle, after propagation over a sufficiently long distance. Bauerheim et al. [2016], Durán and Moreau [2012], Leyko et al. [2010] and Livebardon et al. [2016] concluded attenuation of the entropy wave is also due to shear dispersion in turbine configurations, and Mahmoudi et al. [2018] investigated entropy dispersion using data from a real engine, the Rolls-Royce ANTLE, as well as modelling. This study also showed dispersion has a strong impact on combustion noise levels and it indicated turbulent mixing could have a significant effect on the decay of entropy perturbations in the combustor.



### 1.2.2 Reference experimental studies of entropy noise

Following the early theoretical studies described in the beginning of section 1.1, experimental campaigns were led to verify the presence of entropy noise. Zukoski and Auerbach [1976] first demonstrated its existence experimentally. Around the same time, Bohn [1977, 1979] suggested the two-dimensionality of entropy spots was negligible at sufficiently low frequencies, while Muthukrishnan [1977] found entropy noise was dominant on direct combustion noise at high exit Mach number, but results were inconclusive due to limitations in the experimental set-up and post-processing at the time.

More recently, these limitations were overcome by Bake et al. [2009b], who led an extensive experimental study of entropy noise in a non-reactive nozzle at DLR [Bake et al., 2007, 2008, 2009a,b]. This experiment was motivated by the renewed interest in entropy noise due to fan and jet noise reduction. The test-section was a converging-diverging nozzle with straight ducts upstream and downstream, as represented in Fig. 1.4a. In both subsonic and transonic choked conditions, pulses of increased temperature were convected through the nozzle by use of an electrical heating device installed upstream of the nozzle and allowing variations in hot spot shape. This set-up allowed to isolate the contribution of entropy noise to combustion noise, and rigorously prove its existence in a controlled setting for the first time. Bake et al. [2009b] highlighted the complexity of the phenomena and the significance of reflections. They also used numerical simulations with two different methods, URANS and CAA (LEE), increasing confidence in the results. These computations allowed to identify the sources of entropy noise [Bake et al., 2009b, Mühlbauer et al., 2009], which were orders of magnitude larger than direct noise.

This EWG experimental study constitutes a reference case which motivated several numerical and analytical investigations. For example, Ullrich et al. [2014a] used CAA simulations to compute this case in subsonic and supersonic conditions, while Lourier et al. [2014] focused on subsonic flow with URANS. Both were in agreement with experimental results. Analytically, the EWG configuration was investigated by Leyko et al. [2009, 2011] in the compact supersonic case together with numerical simulations, and they found entropy noise was dominant over direct noise. On the contrary, in subsonic conditions and at non-zero frequencies, Durán and Moreau [2013b] concluded direct noise was predominant, while Giauque et al. [2012] also suggested direct noise could be significant in these conditions using Howe’s [2010] analytical results. Based on the methods used by Leyko et al. [2011] and Durán and Moreau [2013b] as well as both Euler and LES simulations, Becerril Aguirre [2017] stressed the importance of accurate modelling of both the heating device and acoustic reflections at the inlet and outlet of the rig to properly reproduce experimental results. By doing so, he was able to show indirect noise dominates the transmitted noise measured in subsonic flow during the EWG experiment, which confirms Lourier et al.’s [2014] numerical results, as also detailed by Moreau et al. [2018].

Investigation of the EWG data led to the development of the Hot-Acoustic Test rig [Knobloch et al., 2015a,b], a new facility built at DLR within the European FP7-project RECORD to increase understanding of entropy noise generation by providing additional test cases. It is sketched in Fig. 1.4b. Unlike the previous experiment, cold air spots are injected into a hot mean flow. Knobloch et al. [2015b] measured no significant entropy noise in the subsonic regime. This contradicts results obtained using the EWG set-up, but Knobloch

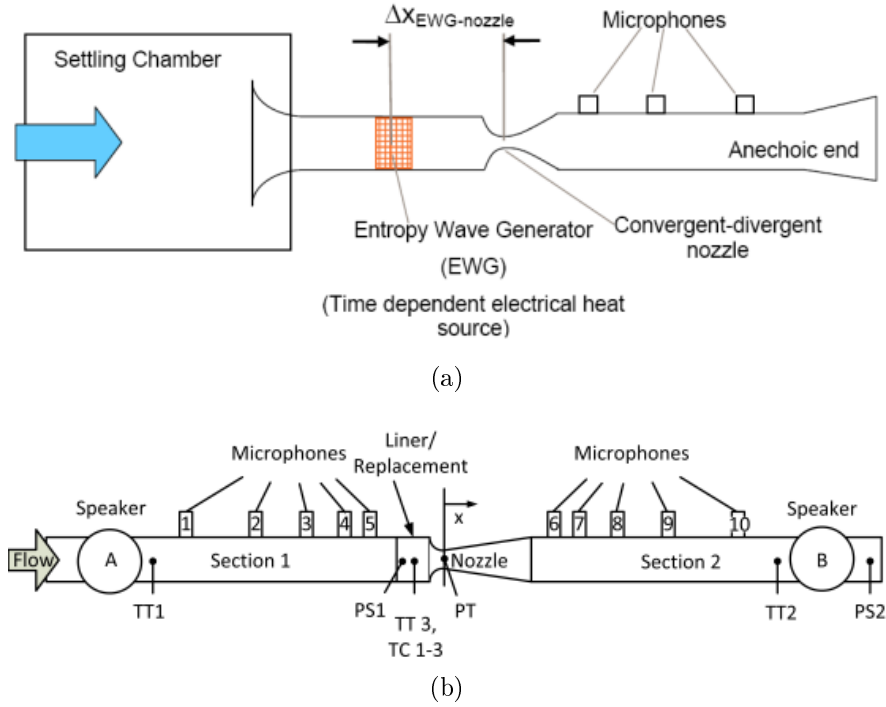


Figure 1.4: Sketches of the (a) EWG [Bake et al., 2007] and (b) HAT [Knobloch et al., 2015a] test-facilities at DLR.

et al. [2015b] suggest entropy noise may have been masked by background noise as low forcing amplitudes were used. The DLR EWG study also encouraged experimental studies in other institutions, such as Cambridge [De Domenico et al., 2017, 2018, 2019, Rolland et al., 2017, 2018]. With both test-facilities, reflections were found to affect pressure fluctuations significantly, making measurements particularly complex. At Cambridge, experimental and analytical methods were developed to account for reflections in the separation of direct and indirect noise, allowing the comparison of both combustion noise contributions to existing models.

Investigation of the more complex turbine geometries were also led as part of the European RECORD project. A test-rig of a high-pressure turbine stage was set-up at Politecnico di Milano [Persico et al., 2012]. Entropy perturbations were generated by a custom built injection system [Gaetani et al., 2015] and the sound fields were measured upstream and downstream of the stage, at both subsonic and supersonic operating points. Several studies aimed at investigating entropy noise in this geometry numerically [Bake et al., 2016, Gaetani and Persico, 2017, Holewa et al., 2017, Knobloch et al., 2016, 2017], constituting a benchmark to improve entropy noise simulation capabilities [Pinelli et al., 2015]. The Rolls Royce high-pressure turbine stage MT1 was also used to investigate entropy noise experimentally [Beard et al., 2009] and numerically [Becerril Aguirre, 2017, Papadogiannis et al., 2016, Wang et al., 2016]. Finally, some investigations using real engine data have also been led to better understand the significance of entropy noise [Miles, 2009, 2010, Pardowitz et al., 2014, Tam and Parrish, 2015]

### 1.2.3 Fundamental entropy noise generating mechanism

Chu and Kovásznyai [1958] analysed the interaction between acoustic, vortical and entropic modes, which are independent in uniform flow and interact in the presence of a velocity gradient. This provides an explanation for entropy noise: the interaction between accelerated entropy perturbations and acoustic waves. This corresponds to the momentum equation used by Marble and Candel [1977] to develop their compact solution, with acoustic propagation on the left-hand side and the entropy source on the right-hand side of the equation. Tam and Parrish [2018] aimed at providing a more physical explanation of entropy noise generation by studying the convection of a positive density pulse through a nozzle. They concluded that in the case of a positive velocity gradient, the front of entropy perturbations are accelerated first, thereby stretching the entropy spot and leading to rarefaction of gas and a pressure drop. They suggested rarefaction waves are then emitted downstream to maintain pressure balance. When an entropy perturbation is decelerated, following the same principal, compression waves radiate ahead. Tam and Parrish [2014] also provided a detailed description of the noise generated by the passage of an entropy line pulse past a single turbine blade, simulated using CAA. As shown in Fig. 1.5, this simplified configuration generates multiple noise sources as the pulse is deformed along the blade, highlighting its complexity compared to nozzle flow.

Parametric studies have been led to evaluate the effect of some basic parameters on entropy noise in nozzle flow. Tam and Parrish [2018] confirmed entropy noise increases with the mean velocity gradient, which drives entropy noise generation. On the other hand, both Bake et al. [2009b] and Knobloch et al. [2015a,b] verified that larger temperature differences between injected perturbations and the mean flow lead to more intense entropy noise, using the DLR EWG and HAT experimental facilities respectively. Knobloch et al. [2015a,b] also measured larger entropy noise when they increased the injection mass flow of cold spots,

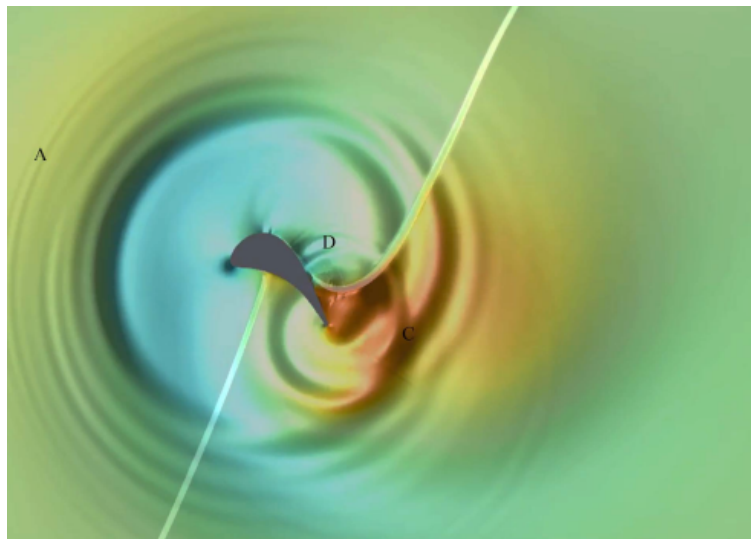


Figure 1.5: Snapshot showing the pressure field generated as an entropy line pulse is convected through a fixed turbine blade. In this figure, red is compression (high pressure) and blue is rarefaction (low pressure). [Tam and Parrish, 2014]

while Bake et al. [2009b] studied the effect of Mach number. They found its increase led to larger entropy noise levels, but only up to a Mach number of about 0.6 at the throat, at which point the peak pressure fluctuation reached a plateau. Using URANS simulations, they showed that the strength of the acoustic source increases with Mach number, and does not reach a maximum like the measured peak pressure fluctuation. They were able to identify the entropy noise source distributions at different Mach numbers [Bake et al., 2009b, Mühlbauer et al., 2009]. There was a dominant source near the throat and a sink just downstream, the strength of which grew with Mach number. Bake et al. [2009b] explained the peak pressure fluctuation plateau at larger Mach numbers by the increased superposition of acoustic waves of opposite amplitude. In addition, Howe [2010] suggested that in the event of flow separation, correlation between vortex sound and entropy noise could reduce the overall noise emitted and explain the plateaued peak pressure fluctuations.

### 1.2.4 Interaction with vorticity

Not only do entropy or vorticity perturbations generate noise in the presence of a velocity gradient, but accelerated entropy waves can also lead to vorticity, which in turn leads to additional acoustic fluctuations in the form of vortex sound [Kings, 2014, Kings and Bake, 2010, Kings et al., 2016].

Using analytical methods in nozzle configurations, Howe [2010] showed the indirect noise generated by the vorticity resulting from the acceleration of entropy perturbations affects entropy noise at low frequency. The coupling between entropy perturbations and vorticity was also investigated by Ullrich et al. [2014b] in the DLR EWG nozzle using CAA with RANS and the Linearised Navier-Stokes Equations (LNSE). Entropic and resulting vortical source mechanisms were identified by isolating the terms of the LNSE. In accordance with section 1.2.1, this study showed viscous dissipation had a limited impact on the evolution of entropy through the nozzle, which was affected by mean flow and heat conduction principally. On the other hand, Ullrich et al. [2014b] found shear-layer interactions and instabilities, baroclinic effects in the convergent part of the nozzle and the presence of a shock to be the main reasons for vorticity. Furthermore, they showed acoustic excitation also leads to some vorticity production in the nozzle, affecting its reflection properties. Durán and Morgans [2015] identified entropy-generated vorticity analytically in the case of an annular nozzle, with numerical verification. They concluded it came from the baroclinic torque in the vorticity equation. Their results indicate the sound generated by this vorticity is small compared to entropy noise. On the other hand, like Howe [2010], Becerril Aguirre [2017] found that the acceleration of entropy perturbations through a nozzle generates vorticity at very low frequency. Using LES of the subsonic EWG experiment, he showed the generated vorticity was maximal in the azimuthal direction and negligible in the axial direction. Note this study considered plane entropy waves which may lead to lower vorticity levels than more realistic hot-spots. Like Ullrich et al. [2014b], Becerril Aguirre [2017] pointed out vorticity is not only produced by accelerated entropy perturbations, but also by flow dynamics. He also observed that entropy modes are converted to vorticity modes in the MT1 turbine stage.

### 1.2.5 Entropy noise in 3D and complex turbine flow

The analytical studies presented in section 1.1 show nozzle flow cannot be considered compact to accurately estimate entropy noise. They also suggest two-dimensional variations of the flow cannot be neglected. Becerril Aguirre [2017] highlighted the fact two-dimensional nozzle flow affects entropy noise by the scattering of entropy perturbations into higher order modes, as discussed in section 1.2.1, and that vorticity generated by three-dimensional unsteady flow produces non-negligible noise at low frequency, in particular in case of flow separation or because of transition to turbulence at the nozzle throat [Howe, 2010]. Using numerical simulation, Leyko et al. [2011] concluded three-dimensional effects were negligible in the DLR EWG case, which is close to the compact limit with very low forcing frequency. On the other hand, Zheng [2016] found that entropy noise in nozzle flow computed by his two-dimensional model is over-predicted compared to three-dimensional LES, although much less than using a one-dimensional solution.

Turbine flow presents added complexity compared to nozzle configurations, in particular because of inherent three-dimensionality, strong turning of the flow, secondary vortices, wakes and rotor-stator interactions. Recent studies have sought to understand their effect on entropy noise, as well as the impact of the latter on the mean flow.

Becerril Aguirre [2017] simulated the flow in the 3D transonic MT1 high-pressure turbine stage using LES and forcing the flow with non-planar hot streaks. He found the baseline flow produced entropy perturbations by both the motion of unsteady shock waves and conversion of vorticity to entropic modes. Because of this, comparison of the entropy forced case to analytical methods neglecting 3D and viscous effects showed the model underestimated the stage's transmission coefficient.

Papadogiannis et al. [2016] and Wang et al. [2016] also used LES to compute the flow in the MT1 turbine stage, forced with plane entropic waves, as illustrated in Fig. 1.6. Despite non-linear interactions and broadband turbulence, they found the Blade Passing Frequency (BPF) and pulsating modes were the most significant, and equally so. The authors highlighted the 3D effects of the flow on the entropy wave, which was highly distorted. They suggested it was unlikely to produce more noise in the following stage, while the transmitted acoustic wave's amplitude remained comparable to 2D results. On the other hand, the reflected wave

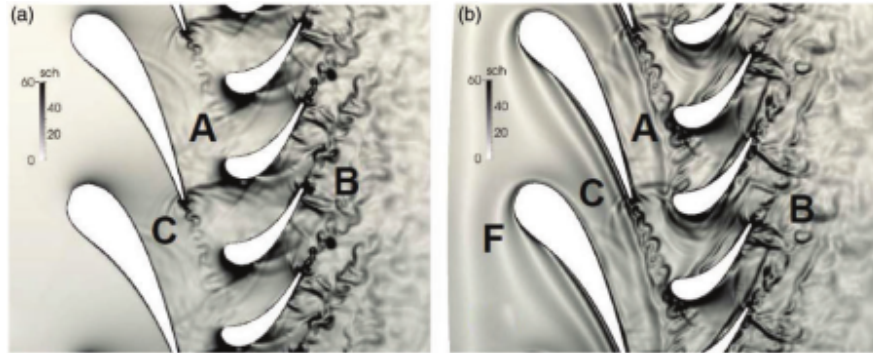


Figure 1.6:  $\|\nabla\rho\|/\rho$  of an instantaneous solution at mid-span without (a) and with (b) an entropy pulse. [Papadogiannis et al., 2016, Wang et al., 2016]

was weaker than in 2D.

This evolution of entropic and acoustic waves was also noted by Ceci et al. [2019], who forced a 2D-extruded turbine stator with a plane entropy wave in off-design transonic conditions using LES. In addition, this study showed entropy noise affected trailing edge shock dynamics, which were characterised by the frequency of the entropy wave. Chandramouli et al. [2017] studied the effect of entropy forcing with a plane wave on vortex shedding in the same stator flow using 2D-URANS and LES. They found that while the vortex shedding frequency remained unchanged, its pattern was amplified by the entropy forcing, becoming thicker.

Holewa et al. [2017] simulated entropy noise in the high-pressure turbine stage used for the European RECORD project with harmonic balance, a cost-effective CFD method in the frequency domain. Vorticity was neglected in an effort to isolate the impact of temperature inhomogeneity, and hot-streaks were injected. The forced simulations led to less noise than when no streaks were injected. The effect of hot-streak amplitude, diameter, and radial and azimuthal positions were investigated. Acoustic waves generated by streak-rotor interactions were identified, and the authors suggested they could either be due to the convection of entropy perturbations through the rotor or to the velocity field variations induced by the acceleration of hot-streaks through the stator.

Gaetani and Persico [2017] investigated the effect of hot streaks on the thermal and aerodynamic behaviour of the high-pressure turbine used for the European RECORD project. In accordance with previous studies, they found the hot-streaks are significantly attenuated through the stator, in particular when they are injected at the leading-edge, taking the shape of the wake. They confirmed this is also the case which degrades the performance of the machine the most, as suggested by An et al. [2009]. Finally, they found that while the over-speed induced by the hot-streaks has limited effect on the incidence at the rotor leading edge, there are additional vorticity cores at the top and bottom of the hot streak which could have a significant impact in the rotor passage.



# Chapter 2

## Description of numerical tools

*A CFD and a CAA solver are used for this PhD, both of which are developed at ONERA. Two types of simulations are performed with the CFD code CEDRE. Euler and RANS mean flow fields are computed as inputs for both semi-analytical modelling and CAA simulation. CEDRE is also used to simulate the unsteady Navier-Stokes equations to take more complex flow into account. The CFD solver CEDRE is presented in section 2.1 and the CAA code sAbrinA\_v0 is described in section 2.2.*

### Contents

---

<b>2.1</b>	<b>Computational fluid dynamics code CEDRE . . . . .</b>	<b>30</b>
2.1.1	Equations of motion . . . . .	30
2.1.1.1	Navier-Stokes equations . . . . .	30
2.1.1.2	Euler equations . . . . .	31
2.1.1.3	RANS equations . . . . .	31
2.1.1.4	Large eddy simulation . . . . .	32
2.1.1.5	Overview of DES97 and DDES . . . . .	33
2.1.1.6	Zonal Detached Eddy Simulation . . . . .	34
2.1.2	Injection of fluctuations . . . . .	35
2.1.3	Non-reflective boundary conditions . . . . .	36
<b>2.2</b>	<b>Computational aeroacoustics code sAbrinA_v0 . . . . .</b>	<b>37</b>
2.2.1	Fundamental equations . . . . .	38
2.2.2	Boundary conditions for non-reflection and injection of perturbations	39
2.2.2.1	Radiation and outflow boundary conditions . . . . .	39
2.2.2.2	Injection of entropic or acoustic perturbations . . . . .	40

---



## 2.1 Computational fluid dynamics code CEDRE

The ONERA in-house code CEDRE (Calcul d'Ecoulements Diphasiques et Réactifs pour l'Énergétique) [Reffloch et al., 2011] is made of several solvers allowing it to address multi-physics problems. The Navier-Stokes solver CHARME is used in the context of this PhD. Both steady and unsteady solutions are considered, with respectively pseudo-transient and implicit second order Runge-Kutta time schemes. In space, second order upwind discretisation is applied. These simulations call for different forms of the equations of motion with different treatment of turbulence as described in § 2.1.1. To investigate entropy noise, perturbations are injected into the computational domain according to § 2.1.2, while the non-reflective boundary conditions detailed in § 2.1.3 are carefully applied to limit contamination of the flow field by spurious noise reflection.

### 2.1.1 Equations of motion

#### 2.1.1.1 Navier-Stokes equations

The Navier-Stokes equations describe the dynamics of a moving fluid by relating velocity  $u_i$ , static pressure  $p$ , density  $\rho$  and temperature  $T$ , which evolve with time  $t$  and following the spatial coordinates  $x_i$ . They include three equations resulting from conservation of mass, momentum and energy respectively. Assuming three-dimensional, compressible, unsteady flow, they can be written in their conservative form as follows:

$$\frac{\partial \rho}{\partial t} + \frac{\partial}{\partial x_j}(\rho u_j) = 0 \quad (2.1)$$

$$\frac{\partial}{\partial t}(\rho u_i) + \frac{\partial}{\partial x_j}(\rho u_i u_j) = \frac{\partial}{\partial x_j}(-p \delta_{ij} + \tau_{ij}) \quad (2.2)$$

$$\frac{\partial}{\partial t}(\rho E) + \frac{\partial}{\partial x_j}(\rho E u_j) = \frac{\partial}{\partial x_j}(-p u_j + \tau_{ij} u_i - q_j) \quad (2.3)$$

where  $\delta_{ij}$  is the Kronecker delta. The stress tensor is a diffusion term which is expressed:

$$\tau_{ij} = -\frac{2}{3}\mu \frac{\partial u_k}{\partial x_k} \delta_{ij} + \mu \left( \frac{\partial u_i}{\partial x_j} + \frac{\partial u_j}{\partial x_i} \right) \quad (2.4)$$

where  $\mu$  is the molecular dynamic viscosity. Energy and heat flux, which appear in the energy equation (Eq. 2.3) along with the stress tensor, follow the relations:

$$E = e + \frac{1}{2}u_i u_i = e_{ref}(T_{ref}) + \int_{T_{ref}}^T c_v dT + \frac{1}{2}u_i u_i \quad (2.5)$$

$$q_j = -\frac{\mu c_p}{Pr} \frac{\partial T}{\partial x_j} \quad (2.6)$$

with internal specific energy  $e$ , temperature  $T$ , heat capacity at constant volume  $c_v$ , heat capacity at constant pressure  $c_p$  and the Prandtl number  $Pr$ . Note heat capacity at constant pressure  $c_p$  is considered variable in the CEDRE simulations in this PhD.

### 2.1.1.2 Euler equations

The Euler equations are a simplification of the Navier-Stokes equations for which all viscous and thermal diffusion terms are assumed negligible. Conservation of mass, momentum and energy then leads to:

$$\frac{\partial \rho}{\partial t} + \frac{\partial}{\partial x_j}(\rho u_j) = 0 \quad (2.7)$$

$$\frac{\partial}{\partial t}(\rho u_i) + \frac{\partial}{\partial x_j}(\rho u_i u_j) = -\frac{\partial}{\partial x_j}(p \delta_{ij}) \quad (2.8)$$

$$\frac{\partial}{\partial t}(\rho E) + \frac{\partial}{\partial x_j}(\rho E u_j) = -\frac{\partial}{\partial x_j}(p u_j) \quad (2.9)$$

These unsteady equations are solved by the code CEDRE with a pseudo transient time scheme, but only the steady solution towards which they converge is used in this PhD to provide mean flow information to both semi-analytical models and CAA simulations.

### 2.1.1.3 RANS equations

When the resolution of the full Navier-Stokes equations is required, taking into account all viscous terms unlike the Euler equations, one finds oneself confronted to the problem of resolution of turbulent scales, as they are necessarily smaller than grid size in high Reynolds flows and because of computational cost considerations. A solution is the use of turbulence based models which dissociate scales that can be resolved and those which require modelling. Aerodynamic variables are then decomposed into resolved and modelled components noted  $\bar{\cdot}$  and  $\cdot'$  respectively.

Making use of the Reynolds-Averaged Navier-Stokes (RANS) equations amounts to such a decomposition. In this case, the filter is Reynolds decomposition into one mean resolved part, and another fluctuating modelled component so that  $f = \bar{f} + f'$ . After averaging, the continuity, momentum and energy equations in the compressible RANS form can be written:

$$\frac{\partial \bar{\rho}}{\partial t} + \frac{\partial}{\partial x_j}(\bar{\rho} \bar{u}_j) = 0 \quad (2.10)$$

$$\frac{\partial}{\partial t}(\bar{\rho} \bar{u}_i) + \frac{\partial}{\partial x_j}(\bar{\rho} \bar{u}_i \bar{u}_j) = \frac{\partial}{\partial x_j}(-\bar{p} \delta_{ij} + \bar{\tau}_{ij} + \bar{\tau}_{ij,RANS}) \quad (2.11)$$

$$\frac{\partial}{\partial t}(\bar{\rho} \bar{E}) + \frac{\partial}{\partial x_j}(\bar{\rho} \bar{E} \bar{u}_j) = \frac{\partial}{\partial x_j}(-\bar{p} \bar{u}_j + \bar{\tau}_{ij} \bar{u}_i - \bar{q}_j + \bar{\tau}_{ij,RANS} \bar{u}_i + \bar{q}_{tj,RANS}) \quad (2.12)$$

Reynolds averaging introduces correlation terms which require modelling, namely Reynolds stress and turbulent heat flux, respectively expressed:

$$\bar{\tau}_{ij,RANS} = -\overline{\rho u'_i u'_j} \quad (2.13)$$

$$\bar{q}_{tj,RANS} = -\overline{(\rho e' + p) u'_j} \quad (2.14)$$

Reynolds stress accounts for the enhanced mixing observed in turbulent flows and it is the focus of turbulence models. It can either be solved directly, typically via Reynolds stress

models, or approximated using first order ones. The latter make use of a constitutive law such as the Boussinesq approximation, whereby the turbulent eddy-viscosity  $\mu_{t,RANS}$  is introduced to represent the momentum associated with eddies. It is a function of the flow, rather than of the characteristics of the fluid itself:

$$\bar{\tau}_{ij,RANS} = \mu_{t,RANS} \left( \frac{\partial \bar{u}_i}{\partial x_j} + \frac{\partial \bar{u}_j}{\partial x_i} - \frac{2}{3} \frac{\partial \bar{u}_k}{\partial x_k} \delta_{ij} \right) - \frac{2}{3} \bar{k} \delta_{ij} \quad (2.15)$$

where  $\bar{k} = (1/2) \overline{u'_i u'_i}$  is the kinetic energy of the turbulent field. The turbulence models used in the context of this PhD fall under this first order model category. The turbulent viscosity concept can also be used to model the turbulent heat flux:

$$\bar{q}_{tj,RANS} = - \frac{\mu_{t,RANS} c_p}{Pr_{t,RANS}} \frac{\partial \bar{T}}{\partial x_j} \quad (2.16)$$

The only term left to be estimated by turbulence models is the turbulent viscosity. In the same way as with the Euler equations, RANS mean flow is computed to serve as an input to semi-analytical models and CAA simulations. The two-equation  $k-\omega$  SST turbulence model [Menter, 1994] is chosen for its good behaviour in the presence of coarsely meshed boundary layers. As detailed at the end of this section, the RANS equations also appear in the ZDES formulation. This time, the one-equation Spalart-Allmaras model [Spalart and Allmaras, 1994] is chosen for its good balance between simplicity and effectiveness. Although all turbulence scales are modelled, making use of the RANS equations allows to take some viscosity into account, in particular the effect of boundary layers, while keeping computational costs low.

#### 2.1.1.4 Large eddy simulation

Large Eddy Simulation (LES) is an alternative method for separation of turbulent scales into resolved and modelled components. This time, the filter applied to obtain the resolved variables is a low-pass spatio-temporal filter which makes use of convolution as follows:

$$\bar{f}(\vec{x}, t) = G(\vec{x}, t) \star f(\vec{x}, t) = \int_{\Omega} \int_{-\infty}^{+\infty} G_{\bar{\Delta}, \bar{T}}(\vec{x} - \vec{\xi}, t - \tau) \cdot f(\vec{\xi}, t) d\vec{\xi} d\tau \quad (2.17)$$

where  $\bar{\Delta}$  and  $\bar{T}$  are the cut-off length and time respectively. There are several definitions of such filters, but in practice, filtering is often achieved implicitly through mesh size. Such a model leads to resolution of large turbulent scales, while the ones requiring modelling are often considered small enough to be case-independent. LES therefore makes much less assumptions than RANS simulations by resolving the main unsteady features of the flow. The equations of motion resulting from this separation of turbulent scales are very similar to the RANS equations (Eqs. 2.10-2.12) with, in addition to varying definitions of the resolved variables  $\bar{f}$ , different modelled terms: the sub-grid scale tensor  $\bar{\tau}_{ij,LES}$  and the turbulent heat flux  $\bar{q}_{tj,LES}$ . In the same way as for the RANS equations, these terms can be modelled using the turbulent viscosity concept given by the Boussinesq approximation:

$$\bar{\tau}_{ij,LES} = \bar{\rho}(\bar{u}_i \bar{u}_j - \bar{u}_i \bar{u}_j) = \mu_{t,LES} \left[ \frac{2}{3} \frac{\partial \bar{u}_k}{\partial x_k} \delta_{ij} - \left( \frac{\partial \bar{u}_i}{\partial x_j} + \frac{\partial \bar{u}_j}{\partial x_i} \right) \right] + \frac{1}{3} \bar{\tau}_{kk,LES} \delta_{ij} \quad (2.18)$$

$$\bar{q}_{tj,LES} = - \frac{\partial}{\partial x_j} (\bar{\rho} \bar{e} \bar{u}_j - \bar{\rho} \bar{e} \bar{u}_j) - \left( \bar{p} \frac{\partial \bar{u}_i}{\partial x_i} \bar{p} \frac{\partial \bar{u}_i}{\partial x_i} \right) = - \frac{\mu_{t,LES} c_p}{Pr_{t,LES}} \frac{\partial \bar{T}}{\partial x_j} \quad (2.19)$$

Again, only modelling of  $\mu_t$  remains for the computation of modelled scales. The first of this type of method was the Smagorinsky model [Smagorinsky, 1963] which is widely used. Other approaches exist, in particular scale similarity models based on the interaction between the largest unresolved scales and the smallest resolved ones. They present improved correlation but omit non-linear interactions and are under-dissipative. This situation led to the development of mixed models taking advantage of both turbulent viscosity and scale similarity models.

### 2.1.1.5 Overview of DES97 and DDES

This section describes the Detached Eddy Simulation (DES97) formulation which is a hybrid RANS/LES approach which was first proposed by Spalart et al. [1998] in 1997. While it is not used directly in this PhD, the ZDES technique described in the following section 2.1.1.6 is based on this method.

The DES97 formulation aims at associating the RANS equations to attached regions of the flow and LES to fully turbulent detached flow. This allows significant cost reduction compared to full LES, as RANS near-wall regions admit much larger cell aspect ratios [Sagaut et al., 2013]. As described in previous paragraphs, RANS and LES are two scale-separation formulations of similar structure, with different cut-off lengths associated to varying definitions of turbulent viscosity  $\mu_t$  under the Boussinesq approximation. Switching between them then amounts to a change of cut-off scales. To do so, DES97, inspired by the Spalart-Allmaras RANS model, is based on the transport equation of a pseudo viscosity  $\tilde{\nu}$ . It is related to turbulent kinematic viscosity  $\nu_t$  and turbulent dynamic viscosity  $\mu_t = \rho\nu_t = \rho f_{v1}\tilde{\nu}$ , where  $f_{v1}$  is a correlation function dependent on flow variables. The transport equation is expressed:

$$\frac{D\tilde{\nu}}{Dt} = c_{b1}\tilde{S}\tilde{\nu} + \frac{1}{\sigma} [\nabla \cdot ((\nu + \tilde{\nu})\nabla\tilde{\nu}) + c_{b2}(\nabla\tilde{\nu})^2] - c_{w1}f_w \left[ \frac{\tilde{\nu}}{\tilde{d}} \right]^2 \quad (2.20)$$

$\sigma$ ,  $c_{b1}$ ,  $c_{b2}$  and  $c_{w1}$  are constants and  $f_w$  is a near wall correlation function.  $\tilde{S}$  is the vorticity magnitude, modified to maintain a log-layer behaviour and the molecular kinematic viscosity is noted  $\nu$ . Finally,  $\tilde{d}$  is a modified distance to the wall, which gives this model its specificity. It is defined as  $\tilde{d} = \min(d_w, C_{DES}\Delta)$ , where  $d_w$  is the wall distance,  $C_{DES} = 0.65$  and  $\Delta = \Delta_{max} = \max(\Delta x, \Delta y, \Delta z)$ . This amounts to a modification of the destruction term allowing the RANS model to be reduced to a LES subgrid scale model in detached flow.

However, the switch between RANS and LES modes is not precise, and it does not imply an instantaneous change in resolution levels, which results in incorrect simulation of the flow and in particular model-stress depletion (MSD) and grid induced separation (GIS). As a consequence, [Spalart et al., 2006] proposed Delayed Detached Eddy Simulation (DDES) to delay the switch to LES mode by redefining the modified length  $\tilde{d}$  so that

$$\tilde{d}_{DDES} = d_w - f_d \max(0, d_w - C_{DES}\Delta) \quad (2.21)$$

where

$$f_d = 1 - \tanh[(8r_d)^3] \quad (2.22)$$

$$r_d = \frac{\nu_t + \nu}{\sqrt{U_{i,j}U_{i,j}}\kappa^2 d_w^2} \quad (2.23)$$

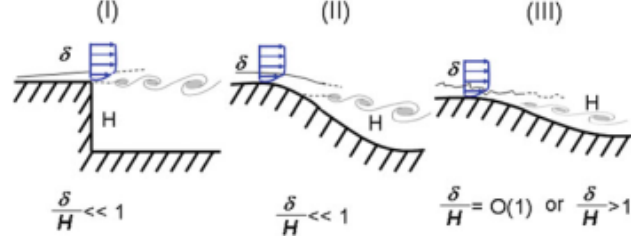


Figure 2.1: Classification of flow problems associated with ZDES modes. I: separation fixed by the geometry, II: separation induced by a pressure gradient on a curved surface, III: separation strongly influenced by the dynamics of the incoming boundary layer [Deck, 2012].

$U_{i,j}$  is the velocity gradient and  $\kappa$  is the von Karman constant. Then  $r_d$  is equal to one in the logarithmic layer and tends to zero at the edge of the boundary layer, so that  $f_d$  is zero in the boundary layer and one elsewhere, amounting to DES97.

### 2.1.1.6 Zonal Detached Eddy Simulation

Zonal Detached Eddy Simulation (ZDES) aims at further reducing the occurrence of MSD and GIS. It allows the user to define RANS and DES zones, clarifying the role of each region of the computational domain. The user can also choose from three DES modes tailored to the flow categories shown in Fig. 2.1. In addition, the use of subgrid length scales not only dependent on grid size, like  $\Delta_{vol}$ , but also on flow characteristics, namely  $\Delta_\omega$ , prevents the delay of instabilities in the shear layer, which can lead to late transition to turbulent flow [Deck, 2012]. These length scales are expressed:

$$\Delta_{vol} = (\Delta x \Delta y \Delta z)^{1/3} \quad (2.24)$$

$$\Delta_\omega = \sqrt{N_x^2 \Delta y \Delta z + N_y^2 \Delta z \Delta x + N_z^2 \Delta x \Delta y} \quad (2.25)$$

where  $\mathbf{N} = \boldsymbol{\omega}/\|\boldsymbol{\omega}\|$  is the unit vector which gives the direction of vorticity  $\boldsymbol{\omega}$ , and  $\Delta x$ ,  $\Delta y$  and  $\Delta z$  are grid sizes in the x, y and z directions respectively.

The ZDES length scale is defined as

$$\tilde{d}_{ZDES} = \begin{cases} d_w & \text{in RANS mode} \\ \tilde{d}_{DES}^{I,II,III} & \text{in DES mode} \end{cases} \quad (2.26)$$

In RANS mode, the original one-equation Spalart-Allmaras model is normally used. The hybrid length scale is noted  $\tilde{d}_{DES}^{I,II,III}$  and corresponds to flow types I, II or III in Fig. 2.1. The associated DES modes are briefly described in the following.

**Mode I** The problem considered here is a flow in which separation is fixed by the geometry, such as a forward facing step. The length scale chosen for this mode corresponds to DES97 which is well adapted to massively separated flows. It writes:

$$\tilde{d}_{DES}^I = \min(d_w, C_{DES} \tilde{\Delta}_{DES}^I) \quad (2.27)$$

where the subgrid length scale is

$$\tilde{\Delta}_{DES}^I = \Delta_{vol} \text{ or } \Delta_\omega \quad (2.28)$$

Mode II In this case, the separation point is unknown a priori which corresponds to DDES, and following Eq. 2.21 the length scale is defined as:

$$\tilde{d}_{DES}^{II} = d_w - f_d \max \left( 0, d_w - C_{DES} \tilde{\Delta}_{DES}^{II} \right) \quad (2.29)$$

where the subgrid length scale writes:

$$\tilde{\Delta}_{DES}^{II} = \begin{cases} \Delta_{max} & \text{if } f_d < f_{d0} \\ \Delta_{vol} \text{ or } \Delta_{\omega} & \text{if } f_d > f_{d0} \end{cases} \quad (2.30)$$

$f_{d0}$  is a user-defined function which it is advised to set to 0.8. This guaranties shielding of the boundary layer for  $f_d < 0.8$ , which corresponds to DDES, while transition to DES mode is accelerated by the use of  $\Delta_{vol}$  or  $\Delta_{\omega}$  closer to the edge of the RANS zone, reducing the delay of instabilities in shear layers.

Mode III This mode is of interest when boundary layer turbulence cannot be modelled completely, for example in the presence of synthetic turbulence convected inside the boundary layer. The DES mode is used in the mid-to-upper region of the boundary layer and smaller turbulent structures are resolved than with other modes, while RANS is selected for the zone closest to the wall, keeping computational costs down compared to full LES. The position of the RANS/DES interface originally needed to be known a priori, but improvements [Renard and Deck, 2015] allow this mode to be used in general cases.

### 2.1.2 Injection of fluctuations

To study entropy noise and the scattering of acoustic waves, injection of perturbations into the computational domain is needed. In CEDRE, this is achieved with the tool CILEPI which allows spatial and temporal variation of boundary conditions. Here, three types of temporal variations are considered: a) entropic through the inlet, b) acoustic also from upstream, and c) acoustic through the outlet of the domain. They are imposed analytically in the linear regime (small perturbations) as detailed in Tab. 2.1. Note only the axial velocity noted  $u$  is considered,  $c_0$  is the mean speed of sound and  $\gamma$  is the specific heat capacity ratio. For the simulations using CILEPI in this PhD, velocity and static temperature are chosen as inlet boundary conditions, while static pressure is set downstream. In case a) the entropy perturbation is used in its normalised form  $\sigma = s'/c_p$ . The relation between entropy and temperature is straightforward and comes from the definition of entropy, while it leads to no pressure or velocity fluctuations so that the inlet velocity remains constant. On the other hand, the acoustic waves are isentropic pressure and velocity perturbations. For b), the desired wave can be expressed in terms of velocity fluctuations with the impedance relation for a plane progressive wave  $p'/u' = \rho_0 c_0$ . The isentropic relation is used to impose temperature. Finally, the acoustic perturbation can be imposed directly as pressure fluctuations in case c).

In chapter 6, the injection of these three types of fluctuations is made in three different simulations, but with a unique mesh and forced at the same frequencies. Because of their lower convection speed compared to acoustic waves, entropy fluctuations are more critical in terms of mesh discretisation. A test case was conducted at ONERA [Huet and Vuillot, 2017]

Wave type	a) upstream entropic $\sigma$	b) upstream acoustic $P_1^+$	c) downstream acoustic $P_2^-$
Velocity $u$	$u = u_0$	$u = u_0 + \frac{p'}{\rho_0 c_0}$	–
Temperature $T$	$T = T_0(1 + \sigma)$	$T = T_0 + \frac{\gamma-1}{\gamma} \frac{T_0}{p_0} p'$	–
Pressure $p$	–	–	$p = p_0 + p'$

Table 2.1: Variables imposed at the boundaries of the domain using CILEPI for three fluctuation types: entropic at the inlet, acoustic at the inlet, acoustic at the outlet.

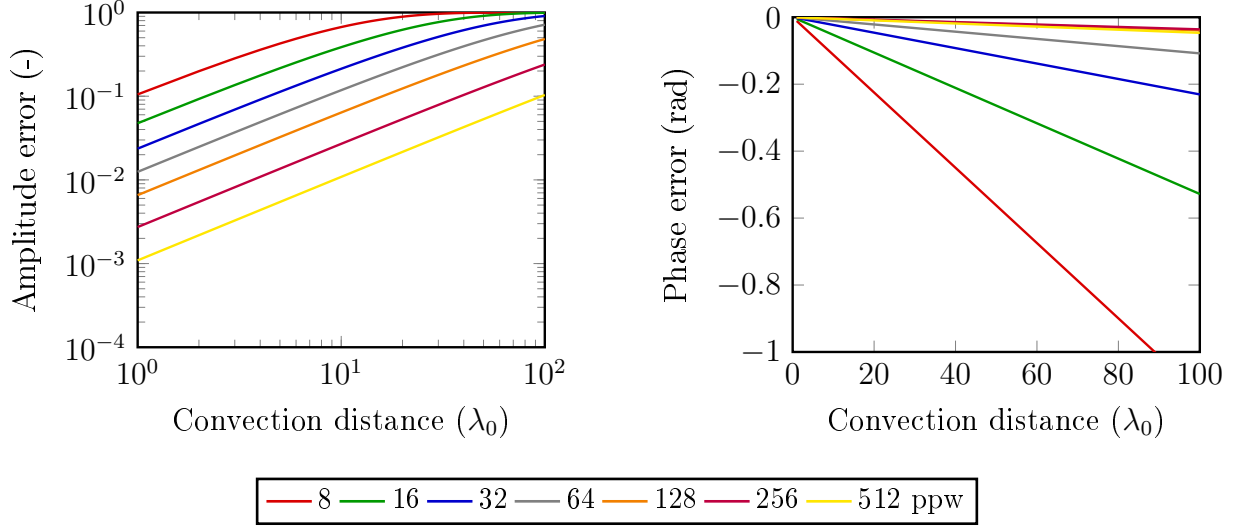


Figure 2.2: Amplitude and phase error over the distance convected and for a range of entropy wave spatial discretisation [Huet and Vuillot, 2017].

to estimate the number of points per wavelength (ppw) required for negligible mesh induced dissipation and dispersion of a planar entropy wave for such cases. The Euler equations were solved in a 3D duct made of tetrahedra with a time-step adjusted for a CFL of around 0.8. The same second order schemes as those applied for ZDES in this PhD were used both in space and time. The entropy fluctuation was convected over a distance of  $10\lambda_0$ , where  $\lambda_0$  is the theoretical wavelength, in all cases except for 256 and 512 ppw for which the distance was reduced to  $5\lambda_0$ . The resulting error in amplitude and phase of the wave is given in Fig. 2.2 for different numbers of points per wavelength. In chapter 6, these results allow to choose grid sizes which ensure an entropy wave amplitude error of less than two percent.

### 2.1.3 Non-reflective boundary conditions

Non-reflective boundary conditions play a critical role in the correct simulation of aeroacoustic phenomena and different formulations have been developed. Unlike those classically found in the literature, the boundary conditions implemented in CEDRE consist of the direct relaxation of the variables at the boundaries of the computational domain [Huet and Courbet, 2016].

This is achieved with the relation:

$$\frac{\partial w_b}{\partial t} = f(w_m - w_b) \quad (2.31)$$

where  $w_b$  is the variable at the boundary,  $w_m$  is the modelled objective value and  $f$  is the relaxation frequency. This relation is used for each of the variables, which are either relaxed towards the imposed value or treated as a function of the rest of the flow when they are not part of the boundary condition considered. The requirement that the flux must be equal on either side of the boundary is not necessarily satisfied in these conditions, so that a separate assumption must be made on the flux. In CEDRE, by default the same uncentered flux model as the one used at cell boundaries within the domain is applied. The same principle prevails for non-reflection whether the boundary conditions are set to constants or to varying values using the tool CILEPI presented in § 2.1.2.

It can be shown analytically that these non-reflective boundary conditions result in acoustic transfer functions with the amplitudes and phases given in Tab. 2.2. These correspond

	Amplitude	Phase
Inlet TF $P^-/P^+$	$\frac{1}{\sqrt{1+\omega_*^2}}$	$-\tan^{-1}(\omega_*)$
Outlet TF $P^+/P^-$	$\frac{1}{\sqrt{1+\omega_*^2}}$	$\pi - \tan^{-1}(\omega_*)$

Table 2.2: Amplitude and phase of the acoustic transfer functions at the inlet and at the outlet, with  $\omega_* = 2\omega/\tilde{f}$  where  $\tilde{f}$  is the relaxation frequency of the variables not imposed at the boundary.

to first order low-pass filters, so that the non-reflective character of the boundary is most efficient at high frequencies. At the cut-off frequency, where  $\omega_* = 1$ , the amplitude of the transfer function is equal to 1/2 for both inlet and outlet boundaries. The (quasi) non-reflective behaviour of the boundary conditions has been verified numerically at ONERA in 1D and 2D for planar acoustic and entropic waves [Huet and Courbet, 2016]. It has also been shown that the pressure fluctuations resulting from a 2D vortex crossing the boundary remain in the region close to it and do not propagate in the computational domain. Finally, a 3D case with a spherical wave exiting the domain was tested without significant reflection.

## 2.2 Computational aeroacoustics code sAbrinA\_v0

The Computational aeroacoustics (CAA) code sAbrinA\_v0 is used to investigate entropy noise in both nozzle and 2D stator configurations in this PhD (cf. chapters 3 and 5). Aerodynamic mean flow fields are required as inputs to the simulations and are computed with the CFD code CEDRE, described in § 2.1. The code sAbrinA\_v0, which is developed at ONERA, is time-accurate and solves the full or linearised Euler equations in their conservative form with perturbed flow decomposition [Redonnet, 2010, Redonnet et al., 2001]. A 6<sup>th</sup> order spatial scheme is applied onto a structured mesh with 10<sup>th</sup> order explicit filtering and a 3rd order explicit Runge-Kutta scheme is used in time. The equations resolved by sAbrinA\_v0 and the boundary conditions used for both non-reflection and wave injection are presented in this section.



### 2.2.1 Fundamental equations

The code sAbrinA\_v0 is based on the Euler equations in their conservative form. In the case of a perfect, compressible fluid with no heat or mass transfer, they can be written as follows:

$$\frac{\partial \mathbf{U}}{\partial t} + \frac{\partial \mathbf{F}}{\partial x} + \frac{\partial \mathbf{G}}{\partial y} + \frac{\partial \mathbf{H}}{\partial z} = \mathbf{0} \quad (2.32)$$

where  $\mathbf{U}$  is the vector  $(\rho, \rho u, \rho v, \rho w, \rho E)^T$  and  $\mathbf{F}$ ,  $\mathbf{G}$ ,  $\mathbf{H}$  are flux vectors in the directions  $x$ ,  $y$  and  $z$ . Unlike CEDRE simulations, the heat capacity at constant pressure  $c_p$  is kept constant in sAbrinA\_v0, which allows the total energy  $E$  to be expressed:

$$E = \frac{||\mathbf{u}||^2}{2} + \frac{1}{\gamma - 1} \frac{p}{\rho} \quad (2.33)$$

with the velocity vector  $\mathbf{u} = (u, v, w)^t$ . The flux vectors can then be written:

$$\mathbf{F} = \begin{pmatrix} \rho u \\ \rho u^2 + p \\ \rho uv \\ \rho uw \\ u \left( \frac{1}{2} \rho ||\mathbf{u}||^2 + \frac{\gamma}{\gamma-1} p \right) \end{pmatrix}, \quad \mathbf{G} = \begin{pmatrix} \rho v \\ \rho uv \\ \rho v^2 + p \\ \rho vw \\ v \left( \frac{1}{2} \rho ||\mathbf{u}||^2 + \frac{\gamma}{\gamma-1} p \right) \end{pmatrix},$$

$$\mathbf{H} = \begin{pmatrix} \rho w \\ \rho uw \\ \rho vw \\ \rho w^2 + p \\ w \left( \frac{1}{2} \rho ||\mathbf{u}||^2 + \frac{\gamma}{\gamma-1} p \right) \end{pmatrix} \quad (2.34)$$

The flow variables is decomposed a mean part  $\bar{\cdot}$  and a fluctuating part  $\cdot'$ :

$$\rho = \bar{\rho} + \rho' \quad , \quad \mathbf{u} = \bar{\mathbf{u}} + \mathbf{u}' \quad , \quad p = \bar{p} + p'$$

resulting in the system:

$$\left[ \frac{\partial \bar{\mathbf{U}}}{\partial t} + \frac{\partial \bar{\mathbf{F}}}{\partial x} + \frac{\partial \bar{\mathbf{G}}}{\partial y} + \frac{\partial \bar{\mathbf{H}}}{\partial z} \right] + \left[ \frac{\partial \mathbf{U}'}{\partial t} + \frac{\partial \mathbf{F}'}{\partial x} + \frac{\partial \mathbf{G}'}{\partial y} + \frac{\partial \mathbf{H}'}{\partial z} \right] = \mathbf{0} \quad (2.35)$$

where the mean and fluctuating components of the flux vectors can be obtained from equations 2.34. Since mean flow variables are directly input into the code, the first term of this equation does not need to be resolved. The perturbed part is separated into linear and non-linear terms, so that either the full or the linear equations can be used. The linear equations are chosen in this PhD.

## 2.2.2 Boundary conditions for non-reflection and injection of perturbations

CAA solvers are characterised by high-order schemes both in space and time to allow the propagation of small amplitude acoustic fluctuations. These schemes are weakly dissipative and dispersive, which makes them highly sensitive to parasite numerical reflection. To investigate entropy noise and its scattering, both entropy and acoustic waves need to be injected, while acoustic and hydrodynamic perturbations must be able to exit the domain without spurious acoustic wave generation. Both these objectives are met using boundary conditions developed by Tam [1998], Tam and Dong [1996], Tam and Webb [1993] and presented in this section.

### 2.2.2.1 Radiation and outflow boundary conditions

To write Tam et al.'s non-reflective boundary conditions, perturbations are decomposed into three mode types which can be considered independently in the linear regime: acoustic, entropic and hydrodynamic. The first propagate at the flow velocity plus or minus the speed of sound, while the others are simply convected by the flow.

The radiation boundary conditions allow acoustic waves to cross the boundary with minimum reflection. They were developed from the asymptotic solution of the linearised Euler equations in the case of an acoustic wave, which involves perturbations in all physical variables, and can be expressed as follows:

$$\left( \frac{1}{V_g} \frac{\partial}{\partial t} + \frac{\partial}{\partial r} + \frac{1}{\alpha r} \right) \begin{pmatrix} \rho' \\ \mathbf{u}' \\ p' \end{pmatrix} = 0 \quad (2.36)$$

In three dimensions  $\alpha = 1$  and  $\alpha = 2$  for two-dimensional flow, while the radius is noted  $r$ . The variable  $V_g$  stands for the effective velocity of acoustic propagation, and it is defined as the vector sum of the mean flow velocity and the ray velocity:  $V_g = \bar{\mathbf{u}} \cdot \mathbf{e}_r + \sqrt{\bar{c}^2 - (\bar{\mathbf{u}} \cdot \mathbf{e}_\theta)^2 - (\bar{\mathbf{u}} \cdot \mathbf{e}_\varphi)^2}$ . This expression takes into account the velocity angle and in particular whether acoustic waves are regressive or progressive. Theoretically, the origin of the spherical coordinate system  $(r, \theta, \varphi)$  is the location of the acoustic source, but the boundary conditions are not sensitive to its position. For the simulations in this PhD, it is positioned far upstream or downstream of the computational domain because only plane waves in duct flow are considered at the boundaries.

The outflow boundary conditions were formulated to let not only acoustic waves, but also entropy and vorticity exit the boundary. To do so, the asymptotic solutions of the linearised Euler equations for entropy, vorticity and acoustic waves were used in a similar way as for the radiation boundary conditions, which leads to the expression:

$$\begin{cases} \frac{\partial \rho'}{\partial t} + \bar{\mathbf{u}} \cdot \nabla \rho' = \frac{1}{\bar{c}^2} \left( \frac{\partial p'}{\partial t} + \bar{\mathbf{u}} \cdot \nabla p' \right) \\ \frac{\partial \mathbf{u}'}{\partial t} + \bar{\mathbf{u}} \cdot \nabla \mathbf{u}' = \frac{-1}{\bar{\rho}} \nabla p' \\ \frac{1}{V_g} \frac{\partial p'}{\partial t} + \frac{\partial p'}{\partial r} + \frac{p'}{\alpha r} = 0 \end{cases} \quad (2.37)$$

Pressure fluctuations  $p'$  are considered purely acoustic, so that the corresponding equation remains unchanged, while the expressions for density and velocity perturbations  $\rho'$  and  $\mathbf{u}'$  depend on these pressure fluctuations.

### 2.2.2.2 Injection of entropic or acoustic perturbations

The injection of three types of waves is considered in this PhD to compute entropy noise and the scattering of acoustic waves through the computational domain:

1. acoustic forcing from upstream, which requires both the injection and exit through the inlet of acoustic fluctuations only.
2. entropic forcing from upstream, which leads to the injection of entropic perturbations and the exit of acoustics through the inlet.
3. acoustic forcing from downstream, for which only acoustic fluctuations are injected, but which necessitates the exit of both acoustic and hydrodynamic modes.

For entropy forcing, density fluctuations  $\rho'_i$  are injected, while all variables must be considered for the injection of an acoustic wave:  $p'_i$ ,  $\rho'_i$  and  $u'_i$ . Density and velocity perturbations depend on  $p'_i$ , and can be expressed in the case of plane waves in the linear regime:  $\rho'_i = p'_i/c_0^2$  and  $u'_i = \pm p'_i/(\rho_0 c_0)$ , where the sign depends on the regressive or progressive nature of the wave.

The first two cases, for which perturbations are injected from upstream and only acoustic waves exit the boundary, can easily be addressed using the radiation boundary conditions. In the linear regime, one can consider computed variables are the direct sum of the incoming and outgoing perturbations, so that for a variable  $f$ ,  $f_{out} = f - f_{in}$ . Substituting this expression into the radiation boundary conditions Eq. 2.36 leads to the following inflow boundary conditions allowing the exit of acoustic waves:

$$\left( \frac{1}{V_g} \frac{\partial}{\partial t} + \frac{\partial}{\partial r} + \frac{1}{\alpha r} \right) \begin{pmatrix} \rho' \\ \mathbf{u}' \\ p' \end{pmatrix} = \left( \frac{1}{V_g} \frac{\partial}{\partial t} + \frac{\partial}{\partial r} + \frac{1}{\alpha r} \right) \begin{pmatrix} \rho'_i \\ \mathbf{u}'_i \\ p'_i \end{pmatrix} \quad (2.38)$$

The third injection type considered, for which all modes exit the domain, corresponds to the outflow boundary conditions. However, acoustic waves are injected following Eq. 2.38 in this case as well, because adapting the outflow conditions is less straightforward. The passage of entropy and vorticity through this type of boundary increases the possibility of numerical error, but this formulation is expected to be sufficient in the absence of strong vortical modes.

## Chapter 3

# Investigation of entropy noise in nozzle flow

*The objective in this chapter is to investigate entropy noise in nozzle flow using CAA and by comparison with existing analytical models. Special attention is given to two-dimensional effects. The 2D model CHEOPS-Nozzle described in section 1.1.3.1 is considered for validation and to discuss some of its assumptions [Emmanuelli et al., 2017, 2020].*

*First, the mean flow is simulated, as both CAA and the model require it as an input to account for flow variations. It is described in § 3.2, which follows the definition of the configurations considered, in § 3.1. Next, entropy noise levels are obtained in § 3.3 under simplifying assumptions via CHEOPS-Nozzle. The CAA approach presented in § 3.4 is a second method to obtain entropy noise levels, under similar assumptions as the model with two major differences: acoustic fluctuations are not assumed one-dimensional and vorticity is taken into account. Investigation of these assumptions allows increased understanding of entropy noise, and CAA can be used to validate the model as they are both based on the Euler equations. The transfer functions given by CAA and CHEOPS-Nozzle, but also by other existing models, can then be compared in § 3.5 to determine the significance of two-dimensional effects on entropy noise and to analyse the resulting flow and noise levels.*

## Contents

<b>3.1</b>	<b>Choice of cases studied . . . . .</b>	<b>42</b>
<b>3.2</b>	<b>Computation of the mean flow field . . . . .</b>	<b>43</b>
<b>3.3</b>	<b>Application of the 2D model . . . . .</b>	<b>44</b>
<b>3.4</b>	<b>Noise levels simulated using CAA . . . . .</b>	<b>45</b>
3.4.1	Choice of sAbrinA_v0 numerical parameters . . . . .	46
3.4.2	CAA simulations . . . . .	47
3.4.3	Choice of post-processing strategy . . . . .	49
3.4.3.1	Evaluation of the entropic and acoustic waves in the ducts . . . . .	49
3.4.3.2	Non-reflective post-processing . . . . .	51
3.4.4	Verification of noise levels obtained in the entropic forcing case . . . . .	51
<b>3.5</b>	<b>Comparison and analysis of CAA and analytical results . . . . .</b>	<b>55</b>
3.5.1	Comparison of transfer functions and investigation of 2D effects . . . . .	55
3.5.2	Investigation of the 1D acoustics assumption and of the presence of vorticity . . . . .	59
<b>3.6</b>	<b>Conclusions . . . . .</b>	<b>61</b>

## 3.1 Choice of cases studied

The configurations of interest which will be studied both with CAA and CHEOPS-Nozzle are described in this section. A typical converging-diverging nozzle is considered at a subsonic operating point. To fully investigate entropy noise in this nozzle configuration, three forcing types illustrated in Fig. 3.1 are considered: the injection of entropy fluctuations, to compute entropy noise levels, as well as the injection in separate simulations of acoustic waves from upstream and downstream. These two latter cases allow to verify the behaviour of the propagation and scattering of the acoustic waves through the domain, in particular as noise sources other than entropy noise are present in engines. In the first case shown in Fig. 3.1a, the entropy perturbations are noted  $\sigma = s'/c_p$ . As they are accelerated from position 1 at the inlet to the outlet noted 2, entropy noise is generated in the form of acoustic perturbations propagating upstream and downstream respectively, and which are noted  $P_1^-$  and  $P_2^+$  once normalised:  $P^\pm = p^\pm/(\gamma p_0)$ . The transfer functions  $[P_1^-/\sigma_1]$  and  $[P_2^+/\sigma_1]$  are used to describe these waves, generated by the acceleration of a certain fluctuation  $\sigma_1$  through the domain. Figures 3.1b and Fig. 3.1c illustrate acoustically forced cases in which the waves  $P_1^+$  and  $P_2^-$  are injected through the inlet and the outlet respectively. Both cases result in waves  $P_1^-$  and  $P_2^+$  propagating upstream and downstream respectively, as with entropic forcing. These waves can also be characterised using transfer functions:  $[P_1^-/P_1^+]$  and  $[P_2^+/P_1^+]$  for upstream acoustic excitation and  $[P_1^-/P_2^-]$  and  $[P_2^+/P_2^-]$  for forcing from downstream. The range of frequencies at which these waves are excited is chosen between 0 and 1000 Hz in accordance with previous studies of entropy noise in this configuration [Zheng, 2016]. More

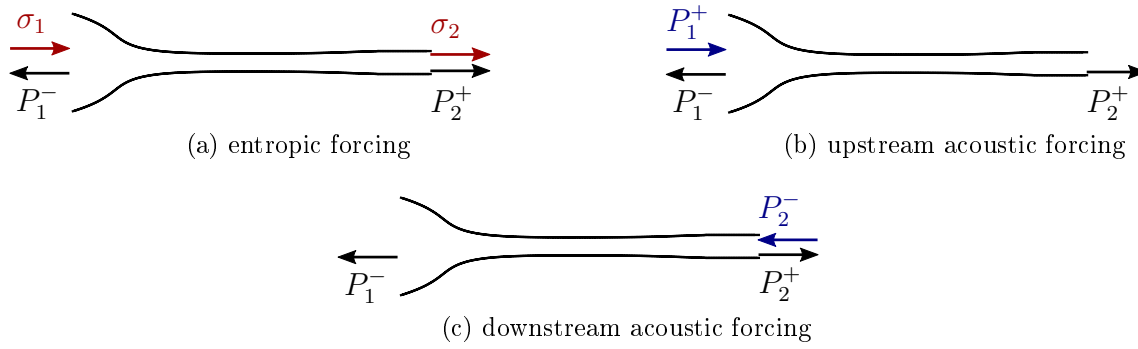


Figure 3.1: Diagrams of the waves involved for each forcing type in the subsonic case.

generally, entropy noise has been found to be most important in the low to mid-frequency range [Dowling and Mahmoudi, 2015].

## 3.2 Computation of the mean flow field

As both CAA and CHEOPS-Nozzle require a mean flow field as an input, its simulation and characteristics are described in this section. First, a nozzle geometry is chosen, before discretisation of the domain and resolution of the Euler equations using the CFD code CEDRE described in section 2.1.

The converging-diverging nozzle considered is based on a geometry designed to maximise indirect combustion noise as part of the DISCERN project [Giauque et al., 2013] and studied experimentally at CentraleSupélec in the framework of the EU project RECORD [Bake et al., 2016, Knobloch et al., 2016, 2017]. The version used for this work and which is shown in Fig. 3.1 was modified to avoid flow separation in the divergent section and allow numerical investigation of entropy noise. A 2D-axisymmetric section of the nozzle is considered here, as nozzle flow is largely 2D-axisymmetric in nature and 3D effects are not considered in this chapter. This also reduces computational cost. The nozzle itself is 185 mm long, its radius is of 29.5 mm at the inlet, 5.49 mm at the throat and 6.96 mm at the outlet. Two 100 mm long ducts are added upstream and downstream of the nozzle respectively for post-processing reasons.

An unstructured mesh is built with the software Centaur. Five quadrilateral layers are created along the axisymmetric axis of the nozzle for better behaviour of the code. Their thickness is 0.08 mm with a stretching of 1. As the computational costs remain low with this 2D domain, a mesh originally designed for RANS simulations with  $y^+ < 1$  can be used. To meet this condition, 30 quadrilateral layers are applied along the wall of the nozzle with stretching of 1.05 and initial thickness of 0.05 mm in the upstream duct, 0.015 mm at the throat and 0.02 mm downstream. The rest of the domain is filled with tetrahedra of 0.08 mm in size. This amounts to a 980,000 node mesh made of 170,500 quadrilaterals and 1.6 million triangles. This mesh is significantly finer than those onto which the flow is interpolated for CHEOPS-Nozzle and CAA in § 3.3 and § 3.4, reducing the possibility for error.

The CFD code CEDRE is used to solve the Euler equations in adiabatic conditions, which

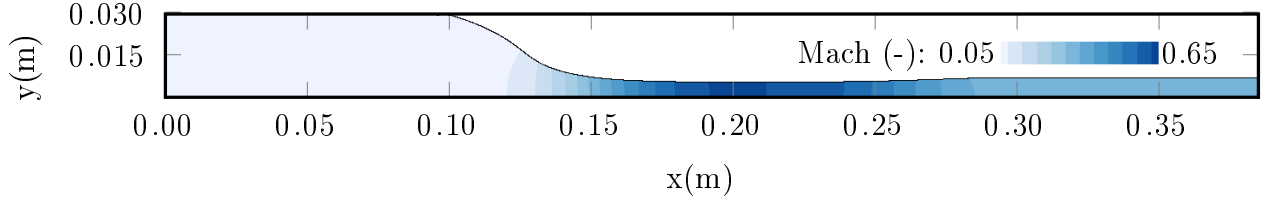


Figure 3.2: Contour of the Mach number in the nozzle.

corresponds to assumptions made in both the CAA approach and CHEOPS-Nozzle. A subsonic operating point is selected to simplify the analysis, and boundary conditions are set in consequence. At the inlet, conditions are chosen to be representative of those at the exit of a typical combustion chamber with a static temperature of 1300 K and an axial velocity of 12,53 m/s. In the same spirit, the heat capacity ratio is set to 1.315 throughout the domain. At the outlet, the static pressure is set to atmospheric levels at 101325 Pa, which is likely to correspond to the conditions in the event of an experimental study. Second order discretisation is applied in space and a first order pseudo transient scheme is used in time. Convergence of the resulting flow is verified, with a relative mass flow rate error smaller than  $8.10^{-5}\%$  and residual errors having reached a plateau after decreasing by several orders of magnitude. Figure 3.2 shows the Mach number throughout the 2D-axisymmetric domain. For this subsonic operating point, the Mach number reaches a maximum of 0.66 at the throat, it is quite low upstream at 0.02 and equals to 0.34 downstream.

### 3.3 Application of the 2D model

In this section, the 2D semi-analytical model CHEOPS-Nozzle described in § 1.1.3.1 is applied to the DISCERN nozzle. This low-order model is characterised by simplifying assumptions which make for a more straightforward analysis, including 1D acoustics and negligible viscosity. In addition, short restitution times allow entropy noise levels to be estimated at a large number of frequencies. To be able to process flow variables as described in § 1.1.3.1, the semi-analytical model requires a 2D structured mesh and planes of constant axial positions, for sectional averaging. The mean flow field computed in § 3.2 is then interpolated onto the mesh. Errors in the interpolation are limited by the fact the CFD mesh is much finer than the one built for the model.

CHEOPS-Nozzle is run for the three forcing types described in § 3.1 over the whole frequency range of interest: 0 to 1000 Hz with a step of 10 Hz. Fig. 3.3 gives transfer-function amplitudes obtained with a varying number of streamlines and the different mesh sizes given in Tab. 3.1. Only the amplitudes of the transfer functions resulting from the entropic forcing case are shown here for conciseness, as it is the most critical configuration, and the other cases are discussed in § 3.5. It is important to verify proper discretisation of the flow is guaranteed by sufficiently small grid size, but also enough streamtubes for discretisation in the radial direction. These streamlines are used as part of the model's resolution process as explained in section 1.1.3.1. Good convergence of the transfer functions and reasonable computational cost were found using 50 streamtubes and the scale 6 mesh, which is made

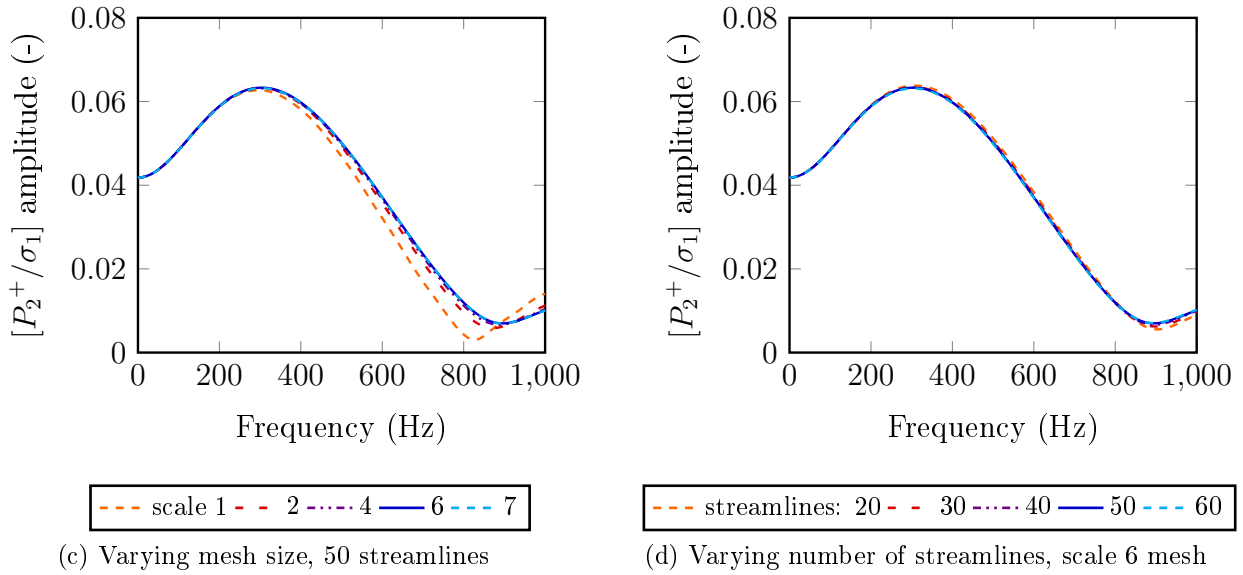


Figure 3.3: Amplitude of the transfer function  $[P_2^+/\sigma_1]$  computed using CHEOPS-Nozzle for a varying mesh size or number of streamlines.

Table 3.1: Number of nodes in the axial and radial directions for the different scales considered for mesh convergence in the semi-analytical model.

Scale	1	2	4	6	7
Nodes - axial direction	671	1341	2529	3433	4001
Nodes - radial direction	37	74	153	217	251

of 750,000 elements. Under these conditions, the computation time using one processor of a desktop computer is of approximately 20 minutes for 101 frequencies.

### 3.4 Noise levels simulated using CAA

In this section, entropy noise is simulated using CAA which is an alternative method to CHEOPS-Nozzle with similar assumptions, with two major differences:

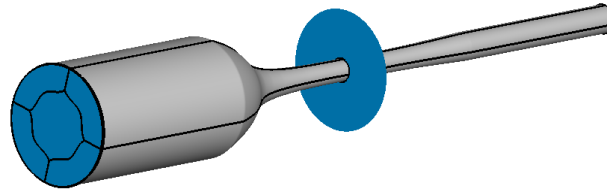
- acoustic fluctuations are not assumed one-dimensional,
- vorticity is taken into account.

This is interesting in view of further investigation of entropy noise, while also allowing validation of the model.

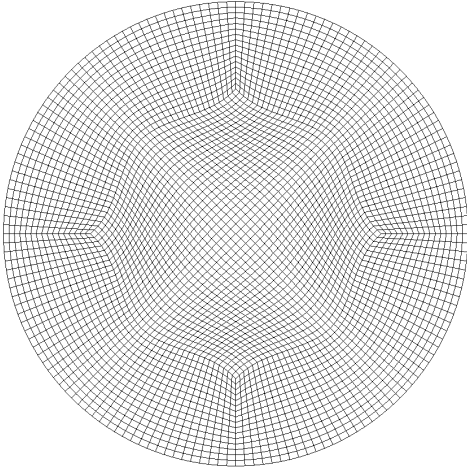


### 3.4.1 Choice of sAbrinA\_v0 numerical parameters

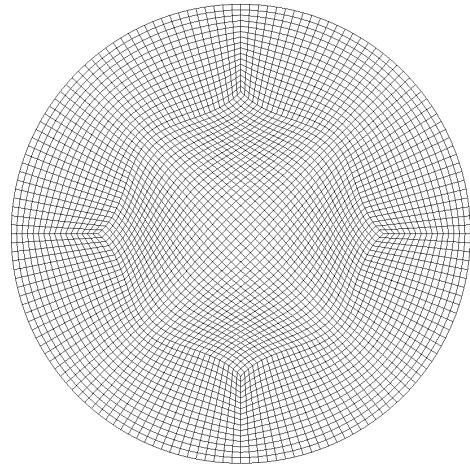
As 2D-axisymmetric simulations are not available in sAbrinA\_v0 and it uses finite difference, a 3D structured mesh adapted to the CAA code is built. The 3D geometry is split into five domains in the axial direction as shown on Fig. 3.4a. Notice upstream and downstream ducts have been appended to the 3D nozzle geometry in the same way as the 2D-axisymmetric configuration in section 3.2. The center domain allows to maintain a homogeneous mesh rather than having smaller cells in the center of each cross-section. It is designed to ensure domain corners are right angles insofar as possible to avoid mesh-induced errors on the simulated flow. This topology, which is maintained throughout the domain, is illustrated for two different cross-section areas in Fig. 3.4b and 3.4c, which also show the mesh.



(a) 3D geometry with plane positions



(b)  $x = -0.10$  m,  $D = 0.060$  m



(c)  $x = 0.10$  m,  $D = 0.011$  m

Figure 3.4: CAA geometry and structured mesh. (b) and (c) have different scales.

It is made of constant axial position planes for easier post-processing. The axial grid size is set to guarantee at least 16 points per entropic wavelength in the upstream duct, which corresponds to the most critical conditions with low convection velocity. Radial discretisation is chosen in consequence for mesh homogeneity with reasonable aspect ratios, which is sufficient to capture radial gradients of the flow. In total, this amounts to a 2.5 million node mesh. Care is also taken to maintain grid stretching, which sAbrinA\_v0 is sensitive to, below about 1.05. In the same way as for CHEOPS-Nozzle, the mean flow described in section 3.2 is interpolated onto the CAA mesh and used as an input to the code. Using the

same flow for the two methods reduces the possibility of error when comparing the resulting transfer functions. After rotating the 2D-axisymmetric mean flow field to match the 3D CAA domain, second order interpolation is performed.

For the three forcing types described in section 3.1, the linear Euler equations are then solved in the time domain with a linearised perturbation form of the conservative variables made of the mean flow and a disturbance field, as explained in chapter 2. The use of boundary conditions developed by Tam and Webb [1993] and Tam and Dong [1996] for both non-reflection and injection of perturbations into the domain is also detailed in chapter 2. The lower end of the frequency range is limited to 100 Hz for CAA because of increased computational cost at low frequency, stemming from larger time periods and the need for a longer signal. To limit numerical cost, multi-harmonic simulations are achieved by injecting waves excited at frequencies in the 100 to 1000 Hz range with a step of 100 Hz. Their amplitudes are set to 1% of the mean quantity associated to each wave: density, the injection of which can be assimilated to an entropy perturbation, and pressure for acoustic waves. The resulting signals are computed with a 50 Hz step to verify the noise levels obtained are not polluted. Harmonic cases are also simulated at 100 and 1000 Hz with entropic excitation of the flow in order to verify the good behaviour of the multi-harmonic computations and to facilitate analysis of the simulated flow. A time step of  $8.10^{-8}$  seconds is chosen ensuring the CFL number reaches a maximum at 0.73, which is within the required limits for the computation of acoustic sources and recommended within sAbrinA\_v0.

#### 3.4.2 CAA simulations

Simulations are run using 220 processors to reach reasonable computational times and for a good balance in point distribution, with a maximum of 2.86% difference in the number of points per processor. In the following, verifications of the simulations are made taking the multi-harmonic entropy-forced case as an example. Figure 3.5 represents both the injected analytical density wave, which can be assimilated to entropy, and the density fluctuations measured on the nozzle axis in the inlet plane. They are in good agreement, showing the signal is correctly injected into the domain. Convergence of the computations is verified by checking the periodicity of signals which is illustrated in Fig. 3.6. It shows pressure fluctuations measured in the middle of the outlet plane of the domain. Figure 3.6a represents the full signal on which the transient part of the simulation is visible. Figure 3.6b on the other hand gives the last two periods of the signal, superimposed, and clearly shows the periodicity of the fluctuations. This was also verified for other quantities and shows good convergence of the simulation. The limited dissipation of entropy through the nozzle is established by noting the ratio of entropy fluctuations at the outlet and at the inlet of the domain reaches a minimum of 97% at 1000 Hz, the highest forcing frequency. It was also verified the amplitude computed at frequencies between the ones excited (50 Hz, 150 Hz etc.) are negligible, which shows background noise does not pollute the signal, as expected in the linear regime. The computational costs of the transient simulations is about 3,000 CPU hrs in acoustically forced cases and 6,000 CPU hrs with entropic excitation, while the steady-state simulations during which signals are stored cost 6,000 CPU hrs, which corresponds to two time periods at 100 Hz. Computational costs weren't optimised as they are reasonable, and the transient part of simulations could be significantly reduced in cases with acoustic

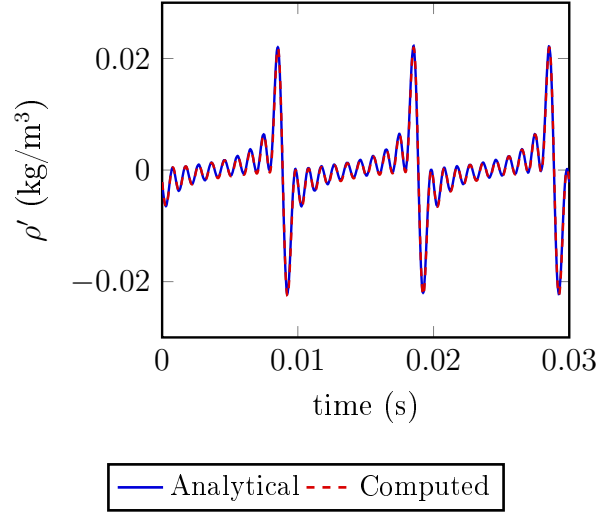


Figure 3.5: Density fluctuations injected into the computational domain in the entropy-forced case.

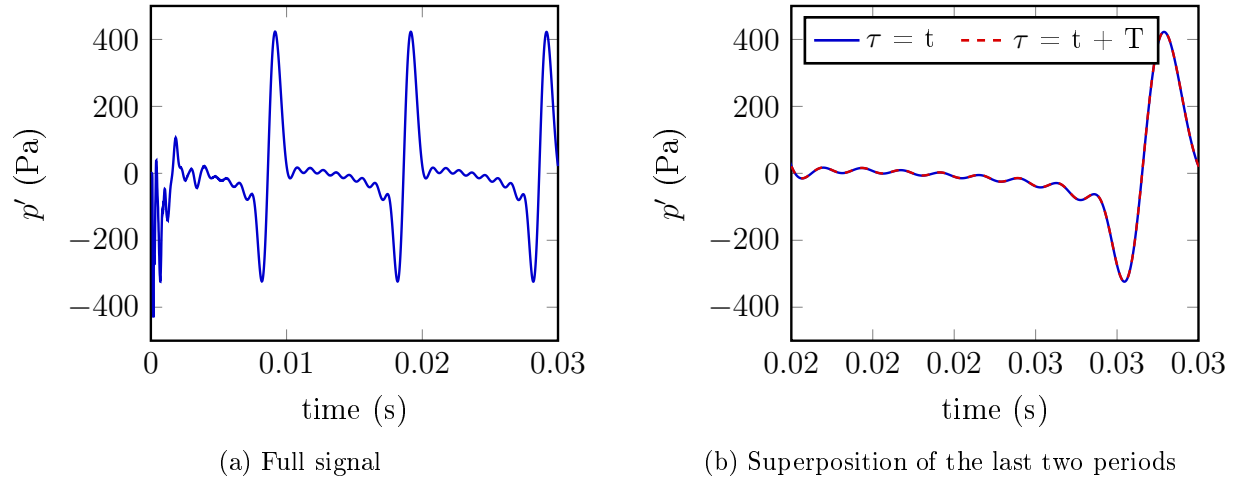


Figure 3.6: Pressure fluctuations measured in the entropic forcing case on the nozzle axis in the exit plane.

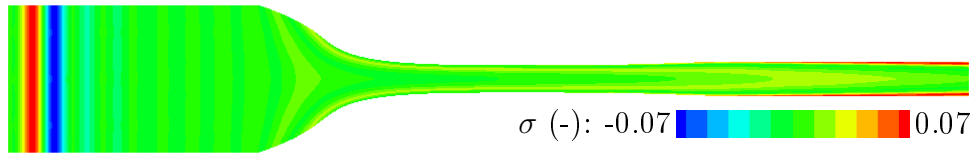


Figure 3.7: Contour of normalised entropy fluctuations in an axial plane in the multi-harmonic entropy-forced case.

excitation, while the data storage part of the harmonic simulation at 1000 Hz requires much shorter signals than at 100 Hz.

Figure 3.7 shows a normalised entropy fluctuation contour resulting from the multi-harmonic simulation with entropic forcing. As shown more clearly in Fig. 3.5, entropy waves for each frequency considered are injected in phase to allow the amplitude to be equal to zero at the beginning of the simulation for smoother injection into the domain. This explains the peak on the colour contour, which also shows plane waves are correctly injected upstream before being distorted by the flow through the nozzle.

### 3.4.3 Choice of post-processing strategy

#### 3.4.3.1 Evaluation of the entropic and acoustic waves in the ducts

Fluctuations  $p'$ ,  $u'$  and  $\rho'$  resulting from sAbrinA\_v0 simulations in the time domain are processed both to obtain transfer functions and to ensure they are not polluted by numerical reflection, which is the object of this section.

In order to compute the entropic transfer functions  $[P_1^-/\sigma_1]$  and  $[P_2^+/\sigma_1]$ , normalised entropy disturbances  $\sigma$  are required. They can be computed from the available fluctuations with the relation:

$$\sigma = \frac{s'}{c_p} = \frac{p'}{\rho_0 c_0^2} - \frac{\rho'}{\rho_0} \quad (3.1)$$

Fast Fourier Transform (FFT) is then applied to obtain these perturbations in the frequency domain. It is less straightforward to obtain the acoustic waves as both  $P^-$  and  $P^+$  components are required, whereas only the full perturbations are given by sAbrinA\_v0. Wave separation must therefore be applied to these fluctuations. As a first step,  $u'$  and  $p'$  are averaged over each section assuming acoustic waves are one-dimensional in the ducts. In doing so, some hydrodynamic perturbations and potential numerical errors are filtered by area averaging [Polifke et al., 2006]. Next, two methods are applied for the wave separation *stricto sensu*, which allows to verify no errors are made at this post-processing step. The first is the use of the Riemann invariants, also applied for wave separation in CHEOPS-Nozzle. They are given by:

$$P^\pm = \frac{1}{2} \left( \frac{p'}{\gamma \bar{p}_0} \pm \frac{\bar{\rho}_0 c_0}{\gamma \bar{p}_0} u' \right) \quad (3.2)$$

They are only valid under the assumption of purely acoustic fluctuations  $p'$  and  $u'$ , and have been adapted to 2D flow by sectional averaging of mean variables. This can be verified by

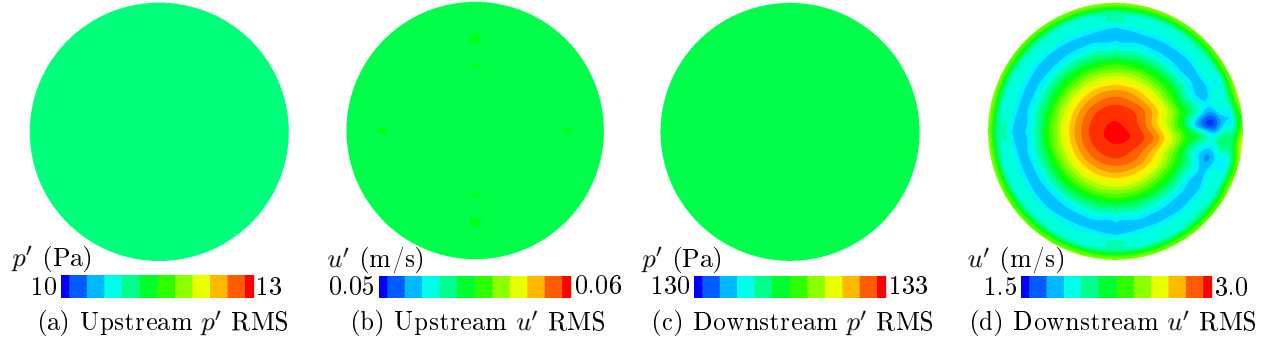


Figure 3.8: RMS values of pressure and velocity fluctuations  $p'$  and  $u'$  in upstream and downstream ducts.

visualising the RMS value of these perturbations in Fig. 3.8. It shows both  $p'$  and  $u'$  are one dimensional upstream, but only  $p'$  is downstream. The values of these one-dimensional fluctuations follow the impedance relation for a plane progressive wave  $p'/u' = \rho_0 c_0$  and they can be considered purely acoustic. On the other hand, velocity fluctuations in the downstream duct (Fig. 3.8d) are not only multi-dimensional but also of amplitudes which seems to indicate the presence of vorticity. This implies the flow does not fill the conditions required to apply the Riemann invariants downstream. Note the non-axisymmetry of Fig. 3.8d is due to a numerical error related to the division of the mesh into five domains.

The second approach used for wave separation of the fluctuations resulting from sAb-rinA\_v0 is a Direct Mode Matching (DMM) method in the harmonic regime. It was chosen because only purely acoustic pressure fluctuations are involved, so that the presence of vorticity is of no consequence, and it is described by the following equations:

$$p' = p'^+ + p'^- \quad (3.3)$$

$$\frac{\partial p'}{\partial x} = -ik_x^+ p'^+ - ik_x^- p'^- \quad (3.4)$$

where  $p'^-$  and  $p'^+$  are the pressure fluctuations propagating upstream and downstream respectively, and the wavenumbers are expressed as:

$$k_x^+ = \frac{\omega}{u_0 + c_0}, \quad k_x^- = \frac{\omega}{u_0 - c_0} \quad (3.5)$$

where  $\omega$  is the angular frequency. The derivatives are evaluated using a finite difference scheme using 5 axial positions. The linear system can then be solved for  $p'^+$  and  $p'^-$  and FFT is applied to move to the frequency domain. The pressure fluctuations are normalised and noted  $P^+$  and  $P^-$ .

Wave separation is applied at several axial positions, over which fluctuations are averaged after phase-shifting to a reference plane. This reduces the possibility of error, which can in particular be introduced by the finite difference scheme used to compute derivatives with DMM. In addition, this amounts to characteristic filtering of potential hydrodynamic components of the perturbations [Kopitz et al., 2005]. This step is more efficient the greater the

number of planes and the further away from one another they are. 20 planes are used both in the upstream and downstream ducts, four of which are only used for finite difference in the case of DMM. Care is taken to position the planes far enough from the nozzle to avoid the effect of the flow. The inlet and outlet are chosen as the reference planes for phase shifting, which corresponds to the convention in CHEOPS-Nozzle. This also allows the use of the resulting waves to evaluate numerical reflection at the boundaries.

### 3.4.3.2 Non-reflective post-processing

Once the normalised fluctuations  $\sigma$ ,  $P^+$  and  $P^-$  are obtained in the frequency domain, a simple non-reflective post-processing method is applied. It makes use of data resulting from the three multi-harmonic simulations considered, with entropic, upstream acoustic and downstream acoustic forcing respectively. The following system of six equations and six unknowns can be solved to obtain the non-reflective transfer functions:

$$P_1^-(\sigma_1) = \left[ \frac{P_1^-}{\sigma_1} \right] \sigma_1(\sigma_1) + \left[ \frac{P_1^-}{P_1^+} \right] P_1^+(\sigma_1) + \left[ \frac{P_1^-}{P_2^-} \right] P_2^-(\sigma_1) \quad (3.6)$$

$$P_2^+(\sigma_1) = \left[ \frac{P_2^+}{\sigma_1} \right] \sigma_1(\sigma_1) + \left[ \frac{P_2^+}{P_1^+} \right] P_1^+(\sigma_1) + \left[ \frac{P_2^+}{P_2^-} \right] P_2^-(\sigma_1) \quad (3.7)$$

$$P_1^-(P_1^+) = \left[ \frac{P_1^-}{\sigma_1} \right] \sigma_1(P_1^+) + \left[ \frac{P_1^-}{P_1^+} \right] P_1^+(P_1^+) + \left[ \frac{P_1^-}{P_2^-} \right] P_2^-(P_1^+) \quad (3.8)$$

$$P_2^+(P_1^+) = \left[ \frac{P_2^+}{\sigma_1} \right] \sigma_1(P_1^+) + \left[ \frac{P_2^+}{P_1^+} \right] P_1^+(P_1^+) + \left[ \frac{P_2^+}{P_2^-} \right] P_2^-(P_1^+) \quad (3.9)$$

$$P_1^-(P_2^-) = \left[ \frac{P_1^-}{\sigma_1} \right] \sigma_1(P_2^-) + \left[ \frac{P_1^-}{P_1^+} \right] P_1^+(P_2^-) + \left[ \frac{P_1^-}{P_2^-} \right] P_2^-(P_2^-) \quad (3.10)$$

$$P_2^+(P_2^-) = \left[ \frac{P_2^+}{\sigma_1} \right] \sigma_1(P_2^-) + \left[ \frac{P_2^+}{P_1^+} \right] P_1^+(P_2^-) + \left[ \frac{P_2^+}{P_2^-} \right] P_2^-(P_2^-) \quad (3.11)$$

where the forcing type is given in parenthesis.

### 3.4.4 Verification of noise levels obtained in the entropic forcing case

In this section, elements of the CAA simulations and their post-processing are verified. Only the entropic forcing case is considered for conciseness and because it is the most critical. The amplitudes of the corresponding transfer functions,  $[P_1^-/\sigma_1]$  and  $[P_2^+/\sigma_1]$ , are presented in Fig. 3.9.

Two different meshes are tested. The coarsest is made of 2.2 million points and the second is 1.5 times finer in all directions resulting in a 7.5 million element mesh. Fig. 3.9 shows the resulting transfer functions are in very good agreement, so that the coarser mesh is adopted for the other simulations. The transfer functions obtained through harmonic simulations are

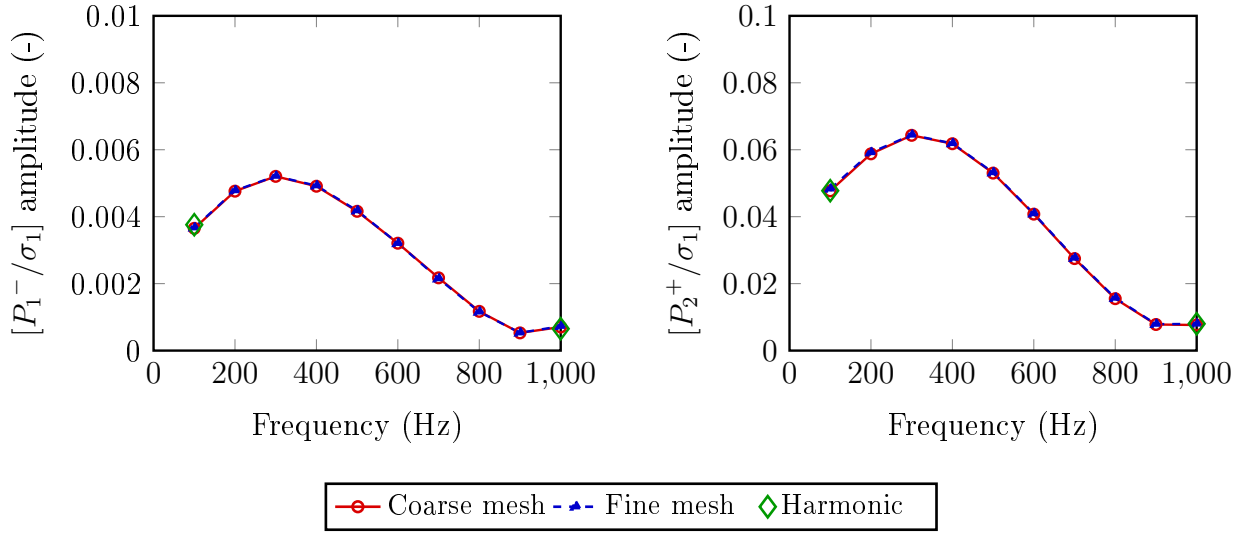


Figure 3.9: Amplitude of the transfer functions resulting from entropic forcing  $[P_1^-/\sigma_1]$  (left) and  $[P_2^+/\sigma_1]$  (right) computed using CAA with a baseline 2.2 million node mesh, a mesh 1.5 times finer in all directions with 7.5 million elements and harmonic simulations.

also given and correspond well to the multi-harmonic simulation as expected in the linear regime.

The consistency of two methods used for acoustic wave separation is determined. Figure 3.10 gives entropic transfer function amplitudes resulting from the use of Riemann invariants and DMM. As expected they concur upstream, validating the wave separation post-processing step. Recall conditions for the use of the Riemann invariants are not met downstream of the nozzle, where velocity fluctuations are not purely acoustic. Figure 3.10b nevertheless shows transfer function amplitudes obtained with the Riemann invariants match those computed using DMM. This can be explained by the signal filtering steps of post-processing which eliminate the vortical component of the velocity fluctuations. It was verified the transfer function amplitudes computed at each of the axial positions considered correspond to Fig. 3.10b. The characteristic filtering resulting from averaging over these positions is therefore not responsible for the good behaviour of the Riemann invariants, which must be due to averaging over each axial plane. This is shown in Fig. 3.11 which gives the evolution of  $p'$  and  $u'$  resulting from both averaging over a plane in the middle of the downstream duct and computed at a point on the nozzle axis in the same plane. It also gives the velocity fluctuation  $u'$  computed from  $p'$  using the impedance relation for a plane progressive wave  $p'/u' = \rho_0 c_0$ . While the signals at a point on the axis and averaged over the plane are equal for  $p'$ , they are not for  $u'$ . However, the velocity fluctuation averaged over the plane is equal to the value calculated from  $p'$ . This shows area averaging is an effective filtering method, and in this case it results in purely acoustic velocity fluctuations and accurate wave separation using the Riemann invariants.

The role of non-reflective post-processing is also evaluated. First, reflection coefficients are evaluated in Fig. 3.12a in the entropy-forced case, but also with acoustic excitations in

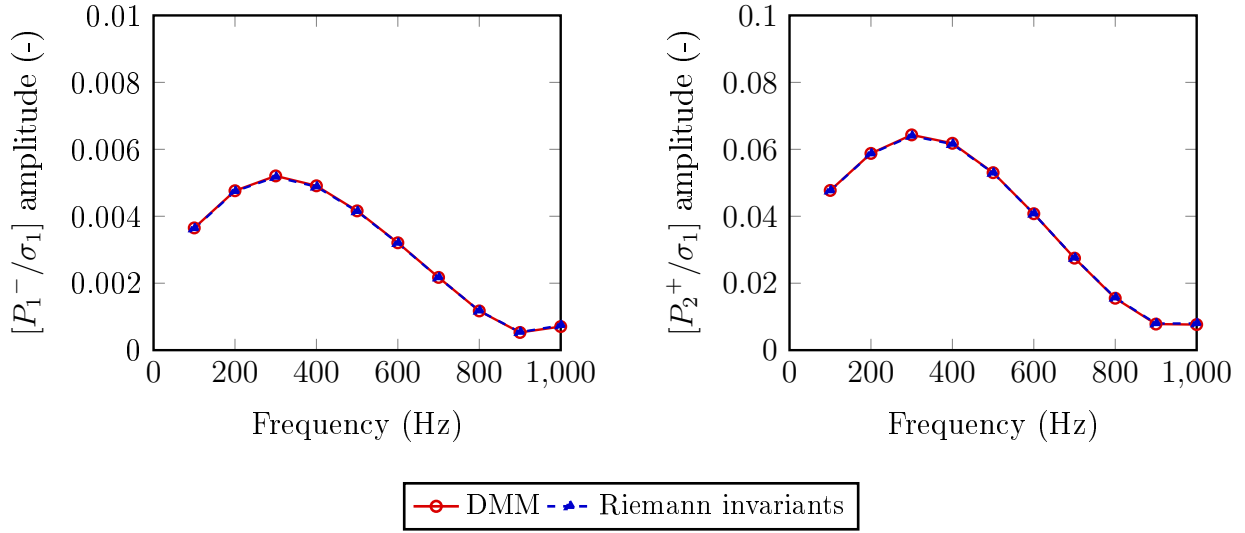


Figure 3.10: Amplitude of the transfer functions resulting from entropic forcing  $[P_1^-/\sigma_1]$  (left) and  $[P_2^+/\sigma_1]$  (right) computed using CAA and both the Riemann invariants and DMM for acoustic wave separation.

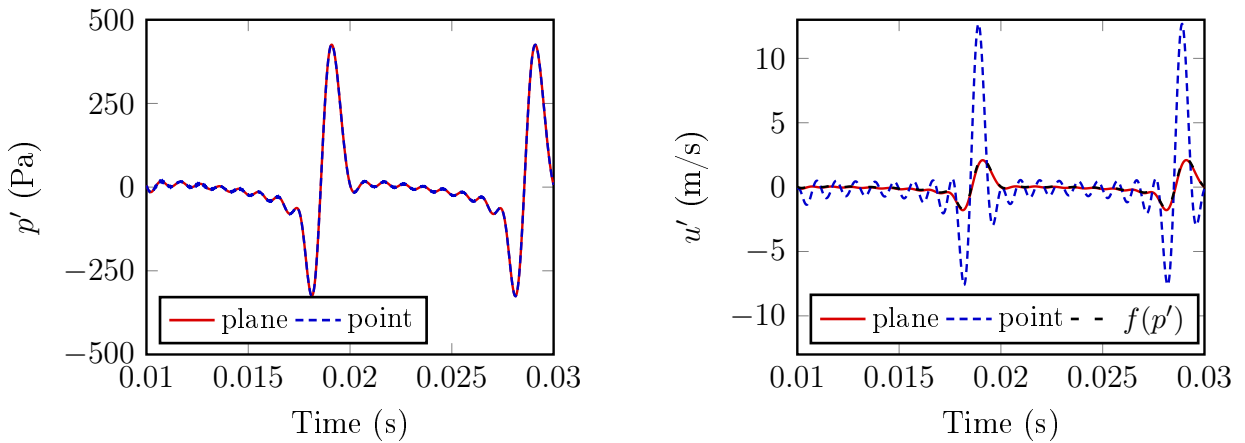


Figure 3.11: Pressure and velocity fluctuations computed as part of the multi-harmonic entropy-forced simulation both at a point of the nozzle axis in the middle of the downstream duct and averaged over the plane, and acoustic velocity fluctuations computed from the impedance relation for a plane progressive wave  $u' = p'/(\rho_0 c_0)$ .



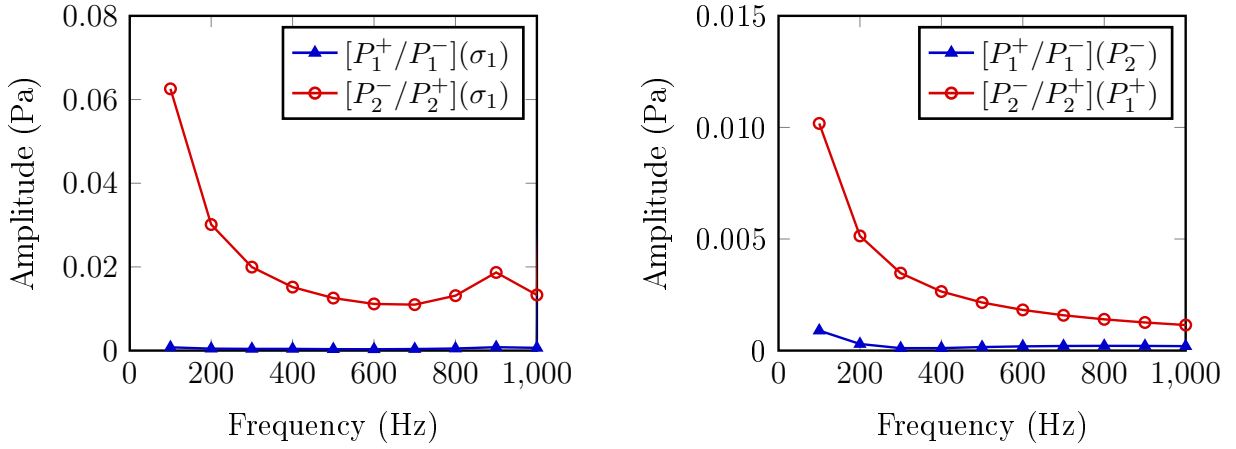


Figure 3.12: Reflection coefficients obtained for the (a) entropy-forced simulation and (b) the two computations with acoustic forcing. Excitation types are given in brackets.

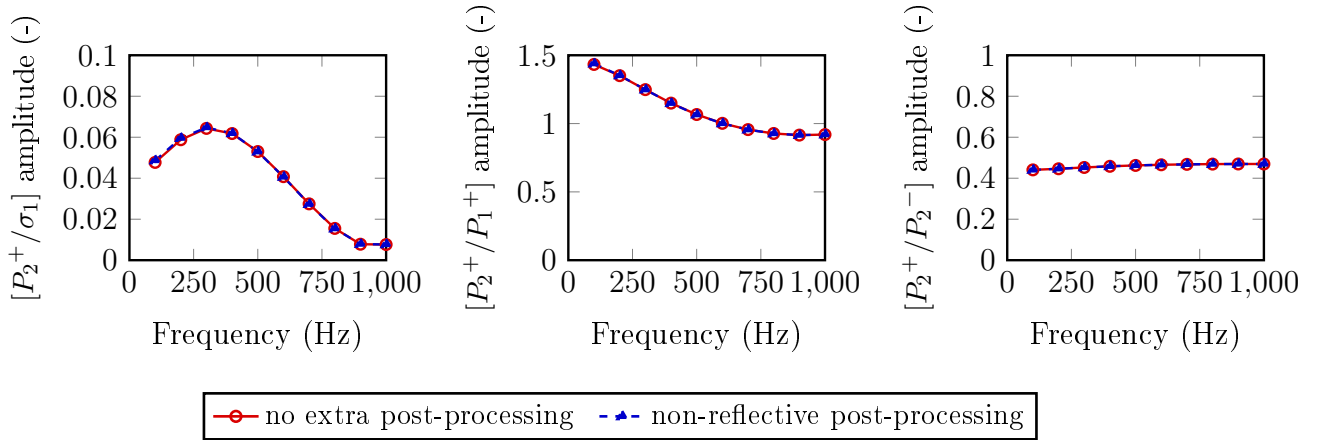


Figure 3.13: Amplitude of the transfer functions  $[P_2^+/\sigma_1]$ ,  $[P_2^+/P_1^+]$  and  $[P_2^+/P_2^-]$  computed with and without non-reflective post-processing.

Fig. 3.12b. For the latter, the reflection coefficient cannot be evaluated at the boundary where an acoustic wave is injected, and only one is shown in each case. Reflection coefficients are quite low, reaching a maximum of 6% at 100 Hz downstream with entropy forcing and at only 1% downstream for upstream acoustic excitation, while upstream reflection coefficients appear negligible. Next, the amplitude of the downstream transfer function is plotted in Fig. 3.13 for all three forcing types with and without using the non-reflective post-processing described in the previous section. They are in good agreement, confirming reflection is low in all three cases. Recall from section 2.2.2 the boundary conditions used to inject an acoustic wave  $P_2^-$  downstream do not guarantee the correct exit of entropic and vortical perturbations, as they are formulated to let acoustic waves cross the boundary. Figure 3.13 shows this

does not lead to significant spurious noise or affect computed noise levels. Furthermore, this low reflection indicates the simulation of all three forcing types, required for non-reflective post-processing, is not necessary for this type of simulation if only one excitation type is investigated.

## 3.5 Comparison and analysis of CAA and analytical results

The aim of this section is to analyse entropy noise and scattering of acoustic waves in the nozzle, in particular by comparison of data obtained through CAA, CHEOPS-Nozzle and other existing analytical tools. The role of 2D effects is notably investigated.

### 3.5.1 Comparison of transfer functions and investigation of 2D effects

The case in which an entropy wave is injected into the domain and accelerated to generate entropy noise is considered first. The thermo-acoustic transfer functions  $[P_1^-/\sigma_1]$  and  $[P_2^+/\sigma_1]$  which give the noise levels generated by a certain entropy wave are computed using the two two-dimensional methods detailed in previous sections, CAA and CHEOPS-Nozzle, but also a one-dimensional and a compact model from the literature, as shown in Fig. 3.14. The entropy noise given by CAA is maximal around 300 Hz and becomes relatively low in the upper end of the frequency range. Also note the transmitted acoustic wave  $P_2^+$  exhibits noise levels about ten times greater than its regressive counterpart  $P_1^-$ . The compact solution is computed using Marble and Candel's model [1977]. It is in good agreement with CAA, but it is only valid for very low frequencies which are not realistic, while the amplitude of the transfer functions obtained with CAA quickly evolves. The model MARCAN which was developed at ONERA provides a one-dimensional estimation of the transfer functions. It captures the evolution of the amplitude with frequency but only in a limited low frequency range, as amplitudes are grossly overestimated for both transfer functions from about 200 Hz. The 2D-model CHEOPS-Nozzle allows to overcome this, since its estimated noise levels are in good accordance with CAA. The amplitude of  $[P_1^-/\sigma_1]$  is nevertheless overestimated by the model at high frequency, above about 800 Hz, which could be due to the model's assumptions which differ from CAA : considering acoustic waves are one-dimensional and neglecting vorticity. Overall, one can consider CHEOPS-Nozzle gives a good estimate of the entropy noise generated in the DISCERN nozzle.

This comparison highlights the significance of radial effects on entropy noise, taken into account by CAA and CHEOPS-Nozzle. They can be due to the two-dimensionality of either the mean flow or the entropy wave. Figure 3.15 gives one-dimensional mean flow quantities along the nozzle axis, as well as two-dimensional values averaged over each section in the same way as for CHEOPS-Nozzle. There are only slight differences between the 1D and 2D averaged values, so that two-dimensional mean flow effects don't appear to be responsible for the lower entropy noise levels. On the other hand, the normalised entropy fluctuation contours used by the one-dimensional and two-dimensional models and presented in Fig. 3.16 differ significantly. It seems the two-dimensional nature of this entropy wave leads to source

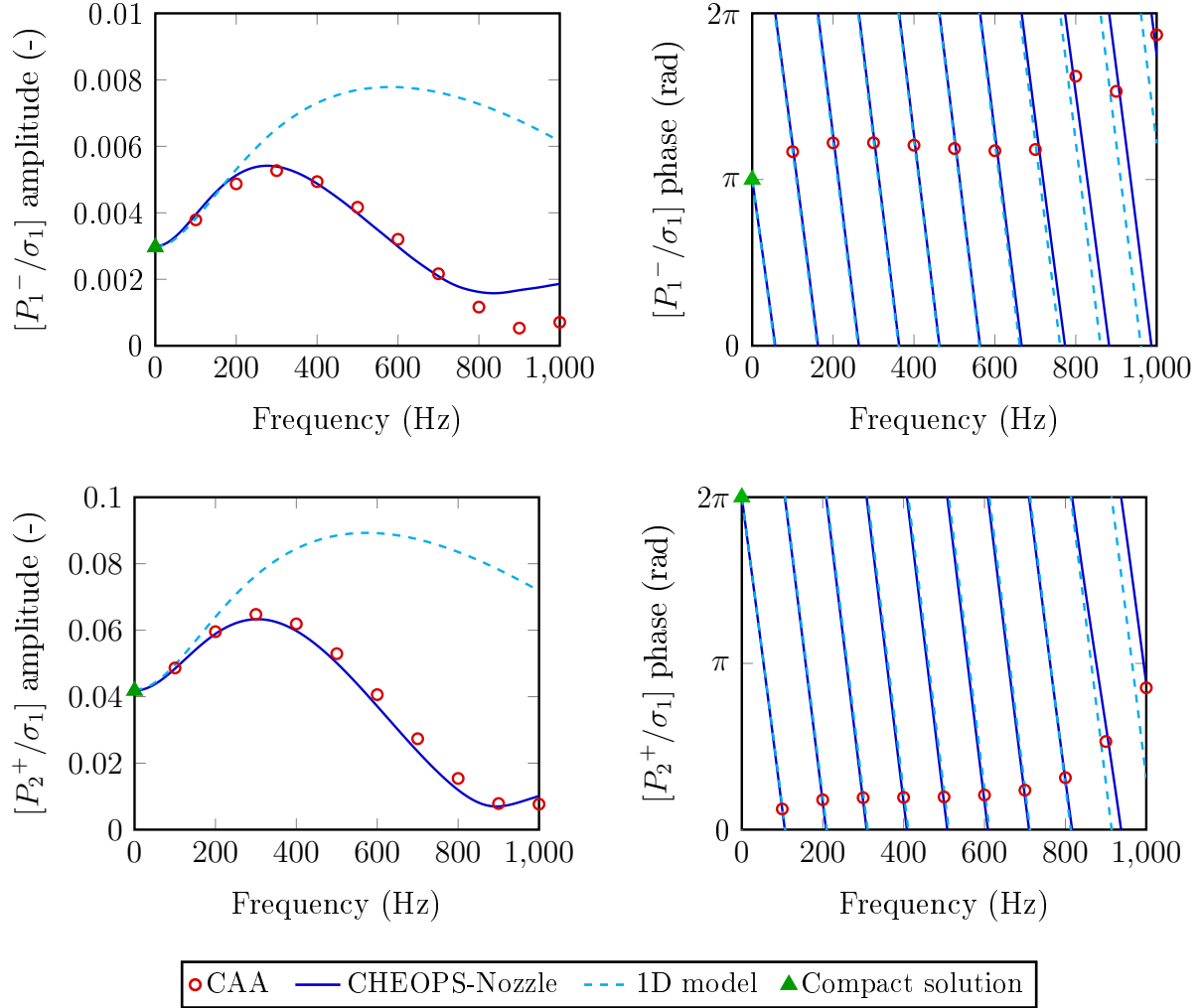


Figure 3.14: Amplitude and phase of the transfer functions resulting from entropic forcing  $[P_1^-/\sigma_1]$  (top) and  $[P_2^+/\sigma_1]$  (bottom) computed using CAA, CHEOPS-Nozzle, the one-dimensional model MARCAN [Giauque et al., 2012, Huet et al., 2016] and Marble and Candel's compact solution [1977].

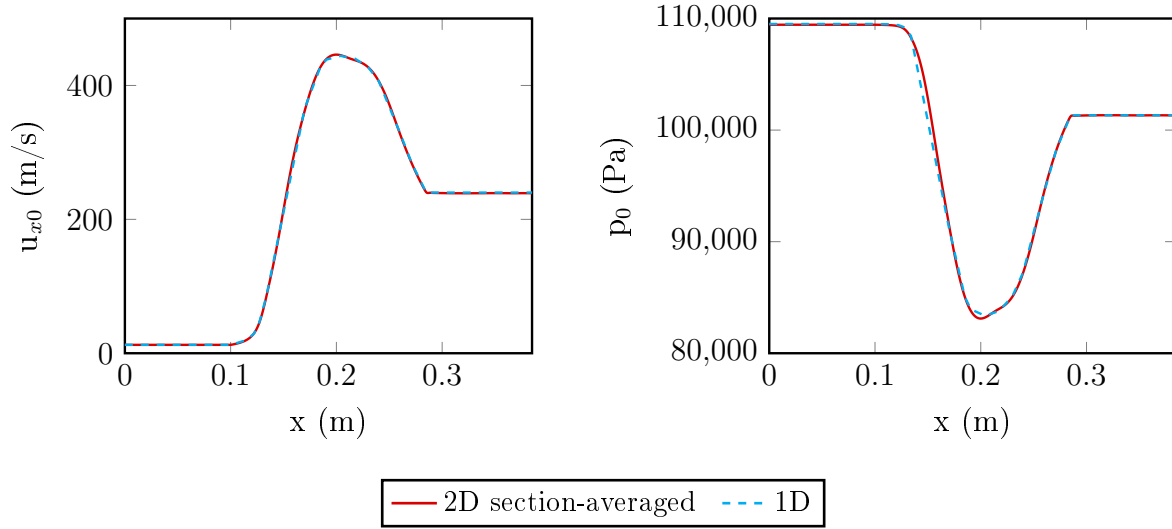


Figure 3.15: Mean axial velocity (left) and pressure (right) profiles used by the 2D model CHEOPS-Nozzle after sectional averaging and by the 1D model MARCAN [Giauque et al., 2012, Huet et al., 2016].

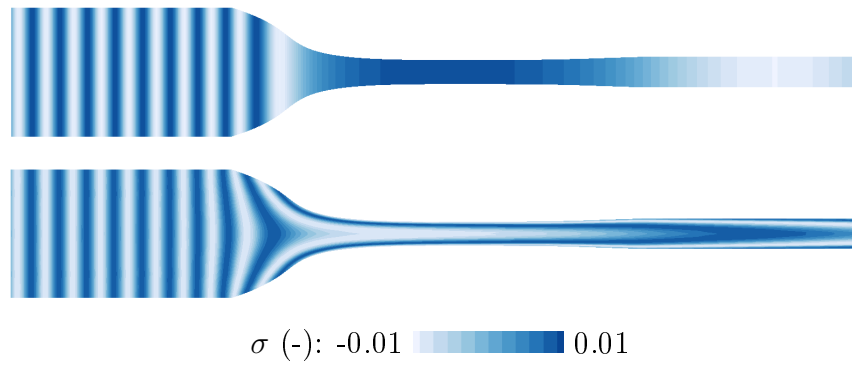


Figure 3.16: Contour of the normalised entropy fluctuations  $\sigma$  inside the nozzle in 1D (top) and 2D (bottom) for harmonic forcing at 1000 Hz.

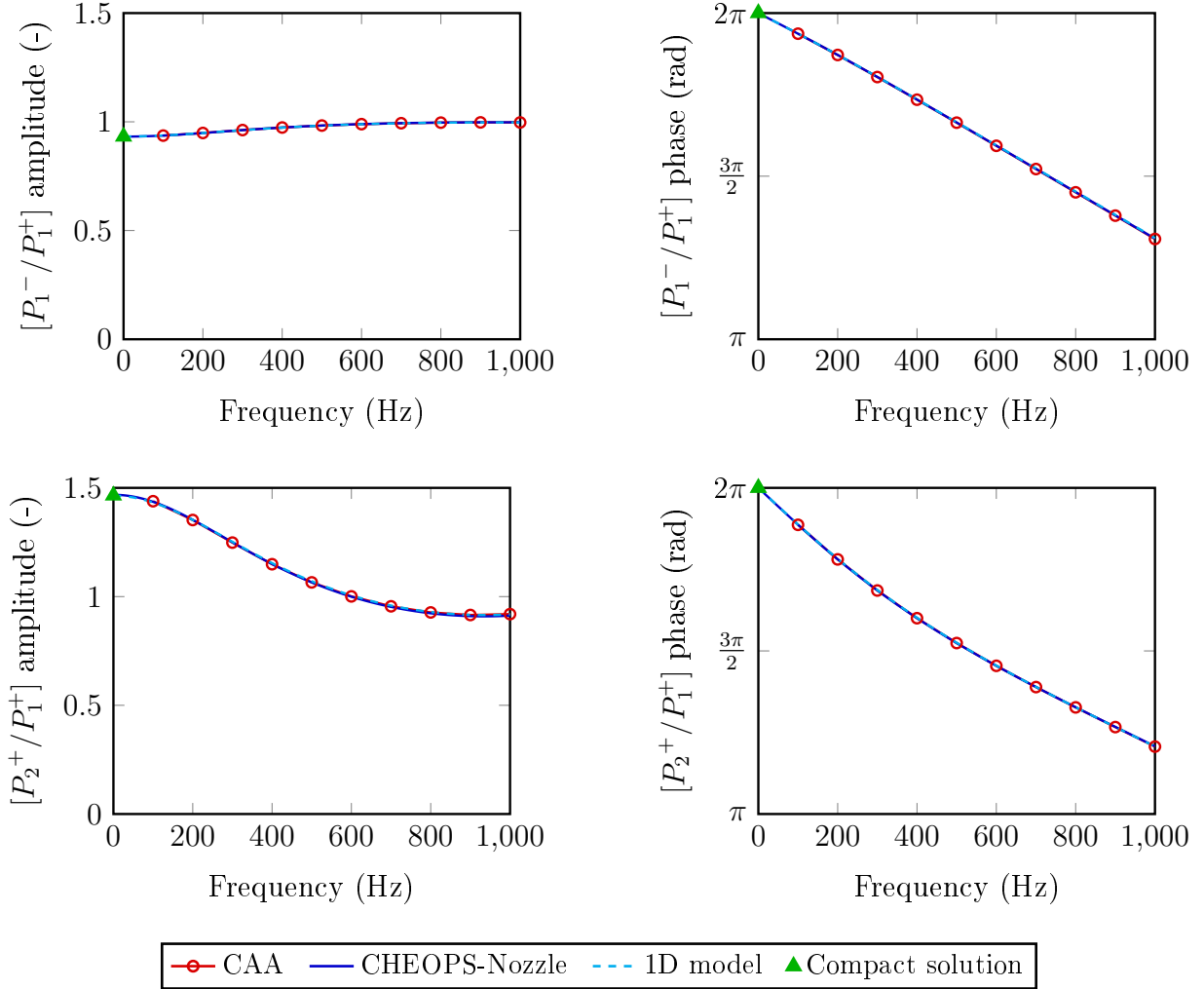


Figure 3.17: Amplitude and phase of the transfer functions resulting from upstream acoustic forcing  $[P_1^-/P_1^+]$  (top) and  $[P_2^+/P_1^+]$  (bottom) computed using CAA, CHEOPS-Nozzle, the 1D model MARCAN [Giauque et al., 2012, Huet et al., 2016] and Marble and Candel's compact solution [1977].

decorrelation as it is accelerated through the nozzle at sufficiently high frequencies, which explains the reduction in entropy noise levels in two dimensions.

Transfer functions resulting from upstream and downstream acoustic excitation are represented in Fig. 3.17 and Fig. 3.18 respectively in order to describe the propagation and scattering of acoustic waves through the nozzle. Like for the entropy-forced case, noise levels estimated by CHEOPS-Nozzle agree with both CAA and Marble and Candel’s compact solution [1977], confirming the good behaviour of the model. Here, data from the one dimensional model MARCAN is also in agreement with the 2D results. This highlights the one-dimensional nature of the propagation and scattering of acoustic waves through the nozzle. Note  $P_1^+$  excitation results in larger wave amplitudes than  $P_2^-$  forcing, which can be explained by the difference in upstream and downstream Mach numbers using energy budgets [Huet, 2018]. In addition, the waves computed on the side where disturbances are injected, corresponding to  $[P_1^-/P_1^+]$  and  $[P_2^+/P_2^-]$ , seem close to the compact limit. This can be verified by evaluating the acoustic wavelengths, which are between 2.5 and 5 times the length of the nozzle. As an example, this remains well under the criteria of a wavelength at least 10 times larger than the axial length proposed by Bauerheim et al. [2016] in the case of a 2D stator.

### 3.5.2 Investigation of the 1D acoustics assumption and of the presence of vorticity

Comparison of the two-dimensional methods also allows discussion of CHEOPS-Nozzle’s assumptions. Recall the CAA approach makes assumptions similar to those of the model, only without assuming that all acoustic waves are one-dimensional or that vorticity is negligible. In regards to the 1D acoustics assumption, the acoustic transfer functions (Figs. 3.17 and 3.18) showed propagation and scattering of acoustic waves is one-dimensional. This is consistent with the 1D acoustics assumption made for post-processing of CAA data in the ducts upstream and downstream of the nozzle. However, it does not necessarily imply the behaviour of the acoustic source is one-dimensional. On the contrary, Fig. 3.19 shows axial pressure fluctuations resulting from simulations excited with entropy waves at 100 and 1,000 Hz are multi-dimensional in the convergent section, where entropy is accelerated. The fact CAA and CHEOPS-Nozzle result in noise levels that are very close despite their different assumptions indicates this effect is not significant. However, it is a possible explanation for the discrepancies in  $[P_1^-/\sigma_1]$  amplitude noted at high frequency.

Now concentrating on the negligible vorticity assumption, recall the presence of vorticity was established in the downstream duct in § 3.4.3. Figure 3.20 shows velocity fluctuation contours at 100 and 1,000 Hz display vortical levels from the region of the throat. The acceleration of entropy perturbations is responsible for their presence, as established in the literature [Durán and Morgans, 2015]. The question is whether this leads to significant vortical noise compared to entropy noise levels. Howe [2010] finds the latter are reduced by the vorticity noise generated and Becerril Aguirre [2017] suggests they are increased at low frequency, while others do not register significant effects of induced vorticity. Here, the closeness of transfer functions obtained using CAA and CHEOPS-Nozzle indicates the vorticity generated by the acceleration of entropy does not lead to significant acoustic fluctuations compared to entropy noise. Like the 1D acoustics assumption, this could nevertheless contribute to the

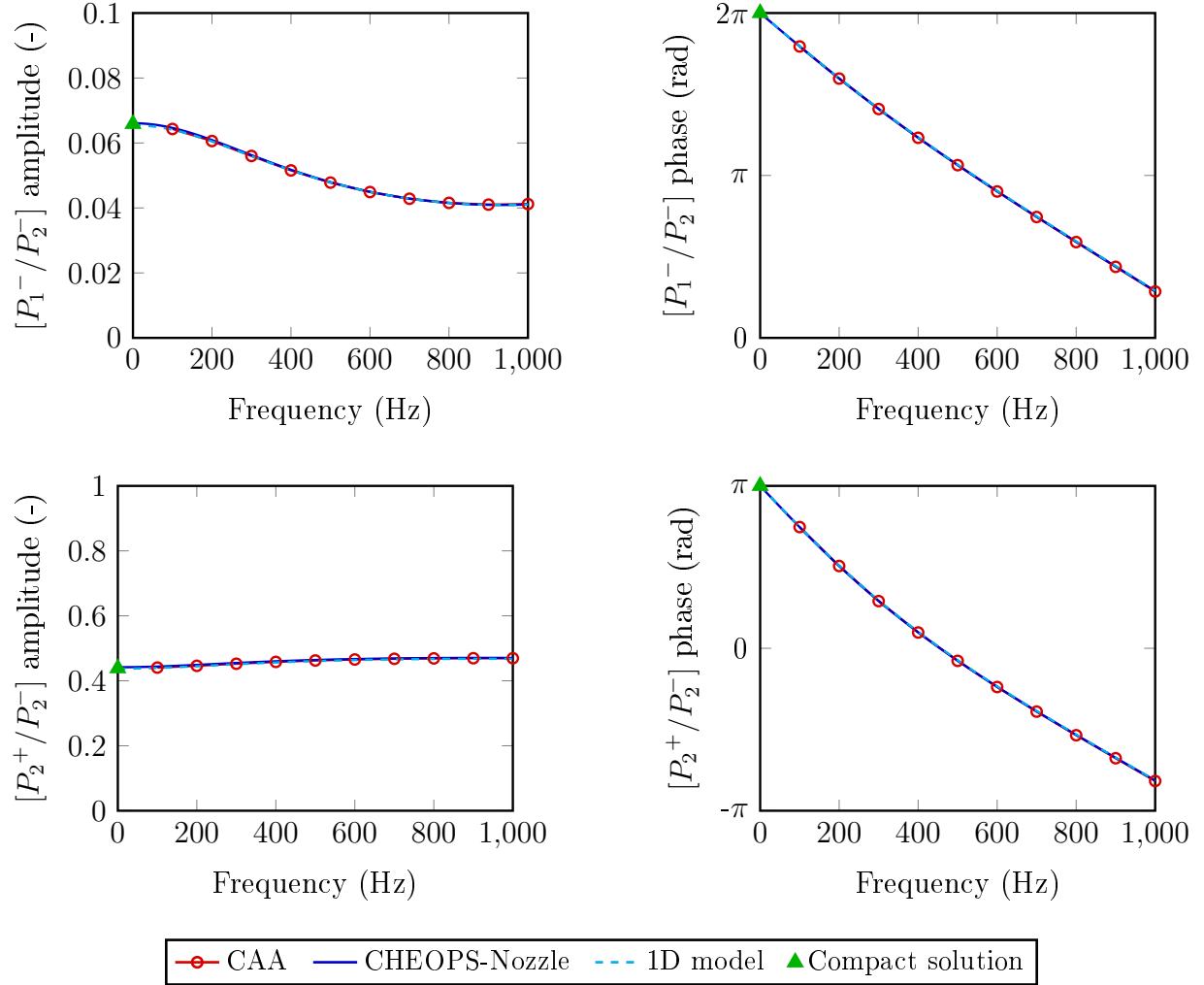


Figure 3.18: Amplitude and phase of the transfer functions resulting from downstream acoustic forcing  $[P_1^-/P_2^-]$  (top) and  $[P_2^+/P_2^-]$  (bottom) computed using CAA, CHEOPS-Nozzle, the 1D model MARCAN [Giauque et al., 2012, Huet et al., 2016] and Marble and Candel's compact solution [1977].

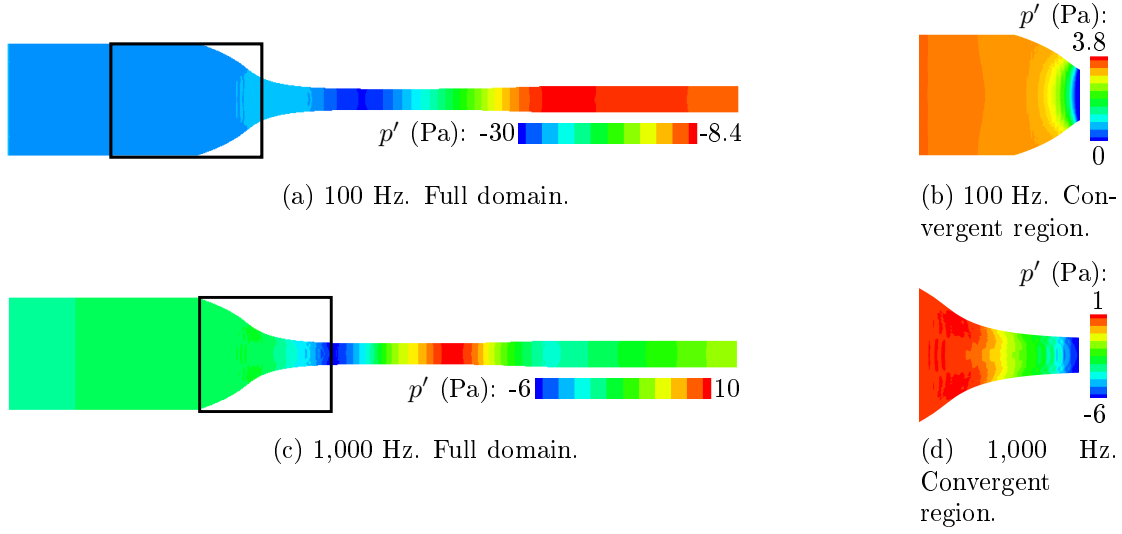


Figure 3.19: Pressure fluctuation contours in an axial plane with entropic excitation at 100 and 1,000 Hz respectively. Figures (b) and (d) show the convergent regions of the nozzle with reduced colour contour range.

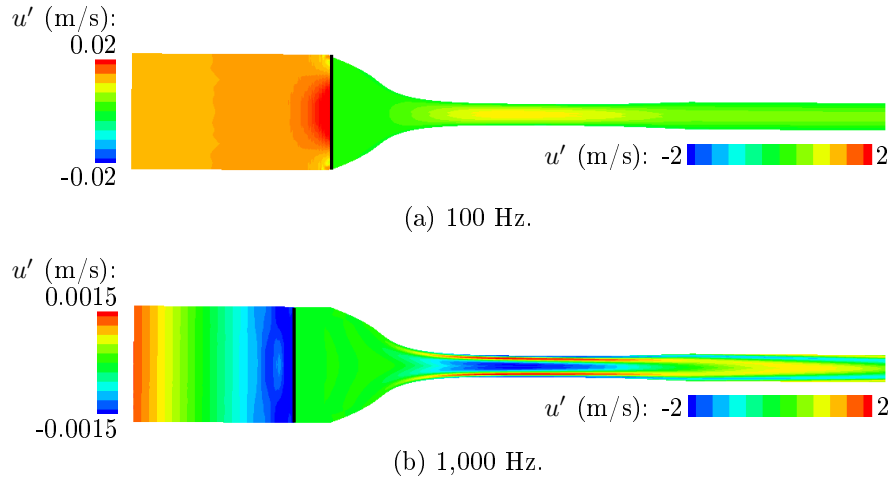


Figure 3.20: Axial velocity fluctuation contours in an axial plane of the nozzle with entropic excitation at 100 and 1,000 Hz. Different colour contour ranges are used upstream and downstream.

difference in  $[P_1^-/\sigma_1]$  amplitude at high frequency.

## 3.6 Conclusions

This chapter presents the investigation of entropy noise in nozzle flow with simplifying assumptions. To this end, a CAA approach with non-reflective post-processing, which can easily be adapted to other configurations, is set up. In addition, the existing 2D model CHEOPS-



Nozzle described in section 1.1.3.1 is applied, as well as the 1D model MARCAN Giauque et al. [2012], Huet et al. [2016] and Marble and Candel’s compact solution [1977]. Comparison of the entropy noise levels resulting from these methods allowed to highlight the significance of 2D effects. In addition, although acoustic waves are found to be multi-dimensional at the throat, it showed acoustic waves can be considered one-dimensional throughout the nozzle in this case. The presence of vorticity induced by the acceleration of the entropy wave was also evidenced, as well as its negligible contribution to indirect combustion noise for the configuration considered. Finally, the comparison of transfer functions resulting from CHEOPS-Nozzle and CAA, the fundamental equations and assumptions of which are similar, allowed mutual validation of the two methods. With some understanding of entropy noise in nozzle flow and the validation of CHEOPS-Nozzle, the model can be extended to 2D stator configurations in the following chapter.

# Chapter 4

## Extension of the entropy noise model to 2D stator flow

*In this chapter, the two-dimensional model for entropy noise CHEOPS-Nozzle presented in § 1.1.3.1 is extended to two-dimensional isolated turbine stator configurations. The resulting model is called CHEOPS-Stator. Section 4.1 presents its fundamental equations, derived under simplifying assumptions and using a two-dimensional streamline-attached reference frame. The steps of the model's resolution process, allowing these equations to be solved, are described in section 4.2. Noise-level convergence with CHEOPS-Stator's parameters is then verified in section 4.3 and results are compared to Cumpsty and Marble's compact model [1977], adapted under the same assumptions as CHEOPS-Stator.*

### Contents

---

<b>4.1</b>	<b>Formulation of the model's fundamental assumptions and equations . . . . .</b>	<b>64</b>
4.1.1	Choice of the model's assumptions . . . . .	64
4.1.2	Definition of a streamline-attached coordinate system . . . . .	64
4.1.3	Derivation of the model's equations . . . . .	65
<b>4.2</b>	<b>Methodology of the model's resolution process . . . . .</b>	<b>68</b>
<b>4.3</b>	<b>Application of the model . . . . .</b>	<b>72</b>
4.3.1	Compact solution under the assumptions of the model . . . . .	72
4.3.2	Convergence of the model's parameters . . . . .	73
<b>4.4</b>	<b>Conclusions . . . . .</b>	<b>81</b>

---

## 4.1 Formulation of the model's fundamental assumptions and equations

The mathematical description of CHEOPS-Stator is established in this section, by adapting CHEOPS-Nozzle's assumptions to the two-dimensional isolated stator case in § 4.1.1, and by making use of the streamline-attached coordinate system adapted to this configuration and described in § 4.1.2. Finally, the fundamental equations of the model are derived in § 4.1.3.

### 4.1.1 Choice of the model's assumptions

Simplifying assumptions are made in this section to enable semi-analytical resolution of the governing equations. They are adapted from CHEOPS-Nozzle to take the specificities of two-dimensional isolated stator configurations into account.

- Two-dimensional planar mean flow is considered, with variations in the axial and azimuthal directions, which is a major difference compared to CHEOPS-Nozzle as nozzle flow is intrinsically axisymmetric.
- Inviscid conditions are adopted by making use of the Euler equations.
- Pressure and velocity fluctuations are supposed solely due to acoustics, which implies that vorticity fluctuations are neglected.
- Acoustic waves are considered one-dimensional. Radial modes are neglected by making the 2D-planar mean flow assumption, while azimuthal modes are assumed to be cut-off by the periodicity of the stator channel.
- Perturbations are presumed small, allowing linearisation of the model's equations.

### 4.1.2 Definition of a streamline-attached coordinate system

The use of a streamline-attached reference frame accounts for flow deviation by the stator and leads to the simplification of the model's equations. The coordinate system  $(\vec{e}_s, \vec{e}_n)$  is an orthogonal curvilinear mobile reference frame which follows a streamline of local angle  $\varphi$  from the x-axis of the Cartesian coordinate system  $(\vec{e}_x, \vec{e}_y)$ . The angle  $\varphi$  is positive in the counter-clockwise direction as illustrated in the sketch Fig. 4.1. Being an orthogonal coordinate system, the axis is perpendicular to the streamlines in the  $n$ -direction.

Projection of  $(\vec{e}_s, \vec{e}_n)$  is needed onto a Cartesian coordinate system  $(\vec{e}_x, \vec{e}_y)$  in which acoustic fluctuations are sought:

$$\vec{e}_s = \cos \varphi \vec{e}_x + \sin \varphi \vec{e}_y \quad (4.1)$$

$$\vec{e}_n = -\sin \varphi \vec{e}_x + \cos \varphi \vec{e}_y \quad (4.2)$$

It can be applied to velocity vectors directly:

$$u_s = \cos \varphi u_x + \sin \varphi u_y \quad (4.3)$$

$$u_n = -\sin \varphi u_x + \cos \varphi u_y \quad (4.4)$$

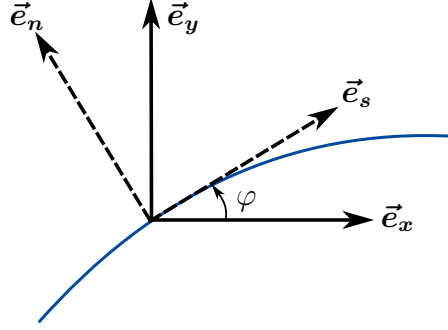


Figure 4.1: Unit vectors of the Cartesian coordinate system ( $\vec{e}_x, \vec{e}_y$ ) and the mobile coordinate system ( $\vec{e}_s, \vec{e}_n$ ) at a point along a streamline.

Derivatives also need to be projected and the chain rule leads to:

$$\begin{pmatrix} \frac{\partial}{\partial s} \\ \frac{\partial}{\partial n} \end{pmatrix} = \mathbf{J} \begin{pmatrix} \frac{\partial}{\partial x} \\ \frac{\partial}{\partial y} \end{pmatrix} = \begin{bmatrix} \frac{\partial x}{\partial s} & \frac{\partial y}{\partial s} \\ \frac{\partial x}{\partial n} & \frac{\partial y}{\partial n} \end{bmatrix} \begin{pmatrix} \frac{\partial}{\partial x} \\ \frac{\partial}{\partial y} \end{pmatrix} \quad (4.5)$$

where the matrix  $\mathbf{J}$  is the Jacobian matrix. Simplified expressions of its terms are used. Only rotation is considered, neglecting axes curvature and assuming they are locally straight, which leads to more straightforward mathematical expressions and numerical implementation. The Jacobian terms write:

$$\frac{\partial x}{\partial s} = \cos \varphi \quad \frac{\partial y}{\partial s} = \sin \varphi \quad \frac{\partial x}{\partial n} = -\sin \varphi \quad \frac{\partial y}{\partial n} = \cos \varphi \quad (4.6)$$

They will be used in the next section to write equations for acoustic fluctuations to be computed in Cartesian coordinates.

### 4.1.3 Derivation of the model's equations

The model's equations are derived from the Euler equations in this section. They involve entropy, pressure and velocity fluctuations. The first are computed within CHEOPS-Stator and are then input into the equations' source terms, while the latter two are to be computed. Under the assumption of purely acoustical one-dimensional perturbations, only the axial velocity component is considered. There are therefore only two unknowns, requiring the use of two equations.

First, the continuity equation in the x-direction is considered. The derivation based on this equation is the same as for CHEOPS-Nozzle. It is detailed in section 1.1.3.1 and leads to:

$$\begin{aligned} \left( l \left( \frac{1}{c_0^2} \right) i\omega + \frac{d}{dx} \left[ l \left( \frac{\overline{u_{x0}}}{c_0^2} \right) \right] \right) \hat{p} + \left[ l \left( \frac{\overline{u_{x0}}}{c_0^2} \right) \right] \frac{\partial \hat{p}}{\partial x} + \frac{d\overline{\rho_0}}{dx} \hat{u} + l\overline{\rho_0} \frac{\partial \hat{u}}{\partial x} \\ = \frac{d}{dx} [l\overline{\rho_0 u_{x0} \hat{\sigma}}] + l\overline{\rho_0} \hat{\sigma} i\omega \end{aligned} \quad (4.7)$$

where  $\hat{u}$ ,  $\hat{p}$  and  $\hat{\sigma}$  are the complex amplitudes of the velocity, pressure and normalised entropy fluctuations and the angular frequency is given by  $\omega = 2\pi f$ , where  $f$  is the frequency. Unlike

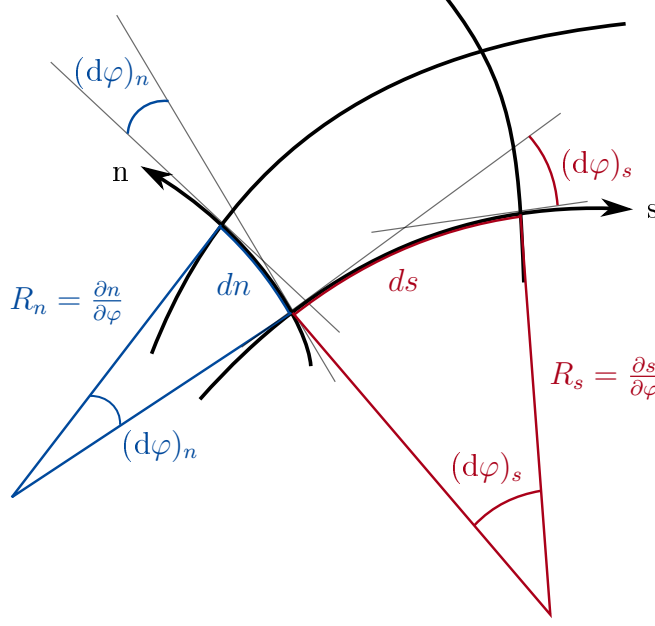


Figure 4.2: Sketch showing the radii of curvature  $R_s$  and  $R_n$  in the  $s$  and  $n$  directions respectively.

the nozzle for which variables are averaged over areas,  $\bar{\bullet}$  stands for the average over  $x$ -constant lines of size  $l$  here, in the 2D planar stator case. The distance  $l$  is equal to the size of the blade passage in the region of the blade and to the distance between periodic boundaries upstream and downstream of the stator.

The second equation is the momentum equation in the  $s$ -direction, which is the direction of the flow in the streamline-attached coordinate system  $(s, n)$  presented in section 4.1.2. The derivation of the Euler equations in this reference frame is detailed in appendix A. It leads to the following equation for momentum in the  $s$ -direction:

$$\frac{\partial u_s}{\partial t} + u_s \frac{\partial u_s}{\partial s} + u_n \frac{\partial u_s}{\partial n} + u_n (u_s K_s - u_n K_n) = -\frac{1}{\rho} \frac{\partial p}{\partial s} \quad (4.8)$$

where  $K_s$  and  $K_n$  are curvatures in directions  $s$  and  $n$  respectively. They are defined as:

$$K_s = \frac{1}{R_s} = \frac{\partial \varphi}{\partial s} \quad (4.9)$$

$$K_n = \frac{1}{R_n} = \frac{\partial \varphi}{\partial n} \quad (4.10)$$

with  $R_s$  and  $R_n$  the radii of curvature illustrated in Fig. 4.2. As perturbations are assumed small, Eq. 4.8 can be linearised by separating pressure, velocity and density into mean and fluctuating parts so that  $f = f_0 + f'$ . This introduces the perturbations needed to compute acoustic and entropy waves in the stator. Noting the mean velocity in the direction perpendicular to streamlines  $u_{n0} = 0$  m/s and  $\frac{1}{\rho_0 + \rho'} = \frac{1}{\rho_0} \left(1 - \frac{\rho'}{\rho_0}\right)$  to first order, the momentum

equation in the s-direction can be expressed:

$$\frac{\partial u'_s}{\partial t} + u_{s0} \frac{\partial u'_{s0}}{\partial s} + u_{s0} \frac{\partial u'_s}{\partial s} + u'_s \frac{\partial u_{s0}}{\partial s} + u'_n \frac{\partial u_{s0}}{\partial n} + u'_n u_{s0} K_s = \frac{1}{\rho_0} \left( \frac{\rho'}{\rho_0} \right) \frac{\partial p_0}{\partial s} - \frac{1}{\rho_0} \left( \frac{\partial p_0}{\partial s} + \frac{\partial p'}{\partial s} \right) \quad (4.11)$$

Using the fact the mean flow satisfies Eq. 4.8, terms involving mean variables can be cancelled out:

$$\frac{\partial u'_s}{\partial t} + u_{s0} \frac{\partial u'_s}{\partial s} + u'_s \frac{\partial u_{s0}}{\partial s} + u'_n \frac{\partial u_{s0}}{\partial n} + u'_n u_{s0} K_s = \frac{1}{\rho_0} \left( \frac{\rho'}{\rho_0} \right) \frac{\partial p_0}{\partial s} - \frac{1}{\rho_0} \frac{\partial p'}{\partial s} \quad (4.12)$$

Next, density perturbations  $\rho'$  are expressed in terms of pressure and entropy fluctuations  $p'$  and  $s'$  following  $\rho' = \frac{\rho_0 p'}{\gamma p_0} - \frac{\rho_0 s'}{c_p}$ . The entropy fluctuations thus introduced are the source of entropy noise. The right-hand side of Eq. 4.12 becomes:

$$\left( \frac{p'}{\gamma \rho_0 p_0} - \frac{s'}{\rho_0 c_p} \right) \frac{\partial p_0}{\partial s} - \frac{1}{\rho_0} \frac{\partial p'}{\partial s} = \left( \frac{p'}{c_0^2 \rho_0^2} - \frac{s'}{\rho_0 c_p} \right) \frac{\partial p_0}{\partial s} - \frac{1}{\rho_0} \frac{\partial p'}{\partial s} \quad (4.13)$$

Because acoustic perturbations are assumed one-dimensional and to propagate in the x-direction, pressure and velocity fluctuations and their derivatives are sought in the Cartesian coordinate system  $(\vec{e}_x, \vec{e}_y)$ . Following Eqs. 4.3-4.4 and noting  $u'_y = 0$  m/s because of the 1D acoustics assumption, velocity fluctuations become:

$$u'_s = \cos \varphi u'_x + \sin \varphi u'_y = \cos \varphi u'_x \quad (4.14)$$

$$u'_n = -\sin \varphi u'_x + \cos \varphi u'_y = -\sin \varphi u'_x \quad (4.15)$$

Equations 4.6 are used to express velocity and pressure fluctuation derivatives, which can also be simplified:

$$\frac{\partial u'_x}{\partial s} = \frac{\partial u'_x}{\partial x} \frac{\partial x}{\partial s} + \frac{\partial u'_x}{\partial y} \frac{\partial y}{\partial s} = \frac{\partial u'_x}{\partial x} \frac{\partial x}{\partial s} \quad (4.16)$$

$$\frac{\partial u'_x}{\partial n} = \frac{\partial u'_x}{\partial x} \frac{\partial x}{\partial n} + \frac{\partial u'_x}{\partial y} \frac{\partial y}{\partial n} = \frac{\partial u'_x}{\partial x} \frac{\partial x}{\partial n} \quad (4.17)$$

$$\frac{\partial p'}{\partial s} = \frac{\partial p'}{\partial x} \frac{\partial x}{\partial s} + \frac{\partial p'}{\partial y} \frac{\partial y}{\partial s} = \frac{\partial p'}{\partial x} \frac{\partial x}{\partial s} \quad (4.18)$$

After projection, combining Eq. 4.12 and Eq. 4.13 leads to the following equation:

$$\cos \varphi \frac{\partial u'_x}{\partial t} + \left[ \cos \varphi \frac{\partial u_{s0}}{\partial s} - \sin \varphi \frac{\partial u_{s0}}{\partial n} - 2 \sin \varphi K_s u_{s0} \right] u'_x + \left[ \cos \varphi u_{s0} \frac{\partial x}{\partial s} \right] \frac{\partial u'_x}{\partial x} - \frac{1}{c_0^2 \rho_0^2} \frac{\partial p_0}{\partial s} p' + \frac{1}{\rho_0} \frac{\partial x}{\partial s} \frac{\partial p'}{\partial x} = -\frac{1}{\rho_0} \frac{\partial p_0}{\partial s} \frac{s'}{c_p} \quad (4.19)$$

After dividing by  $\cos \varphi$ , the terms of the momentum equation are reduced to 1D variables to be able to solve the final system of equations. Equation 4.19 becomes:

$$\frac{\partial u'_x}{\partial t} + \left[ \frac{\partial u_{s0}}{\partial s} - \tan \varphi \frac{\partial u_{s0}}{\partial n} - 2 \tan \varphi K_s u_{s0} \right] u'_x + \left[ u_{s0} \frac{\partial x}{\partial s} \right] \frac{\partial u'_x}{\partial x} - \frac{1}{\cos \varphi c_0^2 \rho_0^2} \frac{\partial p_0}{\partial s} p' + \frac{1}{\cos \varphi \rho_0} \frac{\partial x}{\partial s} \frac{\partial p'}{\partial x} = -\frac{1}{\cos \varphi \rho_0} \frac{\partial p_0}{\partial s} \frac{s'}{c_p} \quad (4.20)$$

Finally, the harmonic regime is considered in order to express the equations in the frequency domain and eliminate temporal derivatives. Under this condition, fluctuations can be written in the form:

$$u'_x(x, t) = \hat{u}(x)e^{i\omega t} \quad (4.21)$$

$$p'(x, t) = \hat{p}(x)e^{i\omega t} \quad (4.22)$$

$$\frac{s'}{c_p}(x, y, t) = \hat{\sigma}(x, y)e^{i\omega t} \quad (4.23)$$

The momentum equation in the s-direction can ultimately be written:

$$\left[ i\omega + \frac{\partial u_{s0}}{\partial s} - \tan \varphi \frac{\partial u_{s0}}{\partial n} - 2 \tan \varphi K_s u_{s0} \right] \hat{u}(x) + \left[ u_{s0} \frac{\partial x}{\partial s} \right] \frac{\partial \hat{u}(x)}{\partial x} - \frac{1}{\cos \varphi c_0^2 \rho_0^2} \frac{\partial p_0}{\partial s} \hat{p}(x) + \frac{1}{\cos \varphi \rho_0} \frac{\partial x}{\partial s} \frac{\partial \hat{p}(x)}{\partial x} = - \frac{1}{\cos \varphi \rho_0} \frac{\partial p_0}{\partial s} \hat{\sigma}(x, y) \quad (4.24)$$

Equations 4.7 and 4.24 form a system of equations which can be solved numerically for the pressure and velocity fluctuations  $\hat{p}(x)$  and  $\hat{u}(x)$ , following the resolution process presented in the next section.

## 4.2 Methodology of the model's resolution process

The resolution process of CHEOPS-Stator is close to that of the model for nozzle flow CHEOPS-Nozzle, which is briefly described in section 1.1.3.1. It is made of the steps given in Fig. 4.3 and described in this section. Steps 1-3 involve the processing of the input variables of Eqs. 4.7 and 4.24. Steps 4-5 then prepare the system of equations to be solved numerically in step 6, before post-processing in step 7.

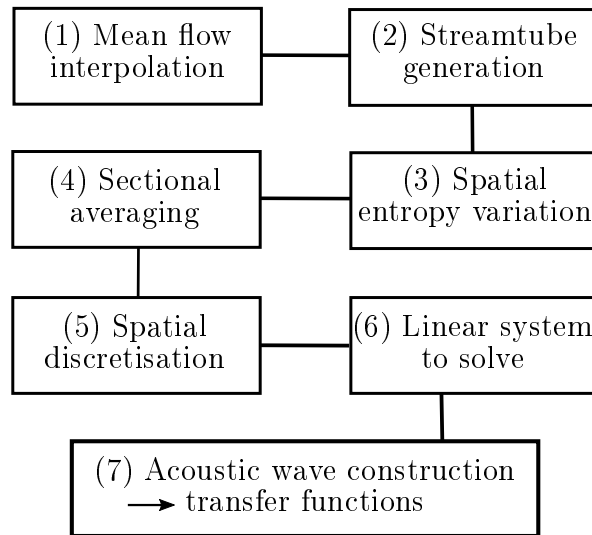


Figure 4.3: Resolution process of CHEOPS-Stator.

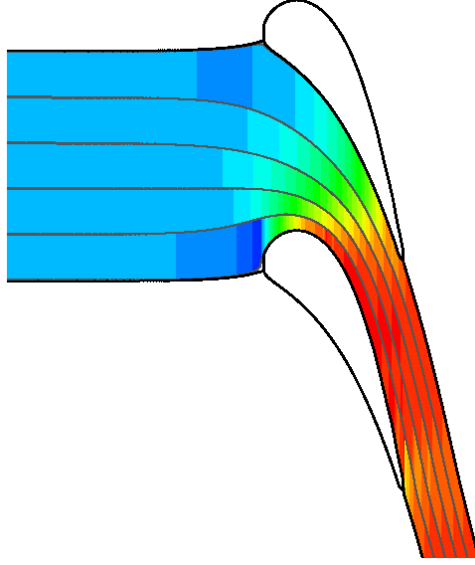


Figure 4.4: Velocity interpolated by CHEOPS-Stator onto a mesh made of five streamtubes delimited by streamlines (grey lines). The blade and stagnation streamlines are represented by thicker black lines.

(1) The model uses two-dimensional mean flow fields as an input. They can be obtained by any method, typically Computational Fluid Dynamics (CFD): Euler simulation, RANS, or even time-averaged LES for instance. These fields must be interpolated by the user onto a 2D-structured mesh made of one domain for the resolution process to be possible. The use of an x-constant mesh is also required for line averaging in step 4.

(2) Streamlines are generated either externally or by using a time marching method. Figure 4.4 shows an example with five streamtubes. This step amounts to a re-discretisation of the flow, affecting the shape of the domain, which follows the streamlines. The bottom and top boundaries are very close to the blade, as shown in Fig. 4.4, but they are not flush with it and they do not go through the stagnation points. This is because the first streamlines to fully circumvent the blade on either side of it are used. A sufficiently large number of streamtubes must be used in order to capture the azimuthal variations of the mean flow accurately. They are arranged so that the blade is out of the domain for easier averaging over full sections in step 4. The result is a new mesh made of the streamlines and the original axial positions. Flow variables are finally interpolated onto it and cell-centred.

(3) As entropy is a quantity convected by the mean flow without attenuation or distortion in subsonic flow governed by the Euler equations, the entropy fluctuations are transported numerically using the mean velocity by integration along each streamtube:

$$\frac{s'}{c_p}(l, t) = \frac{s'}{c_p} \left( l = 0, t - \int_0^l \frac{d\zeta}{\|u(\zeta)\|} \right) \quad (4.25)$$



assuming velocity is constant between two axial positions. It follows sufficient discretisation of the mesh is required in the axial direction, as well as the use of a large enough number of streamtubes.

(4) With both mean flow variables and entropy fluctuations computed in two dimensions to take azimuthal variations into account, sectional averaging is applied to obtain the system of two equations Eqs. 4.7 and 4.24 with two unknowns  $\hat{u}(x)$  and  $\hat{p}(x)$ , assumed to be one-dimensional.

(5) In order to solve the linear system numerically, second-order spatial discretisation is applied in the axial direction. The equations are evaluated at the centre of each element  $c_k$ , bounded by nodes  $k$  and  $k+1$ , while the unknowns are sought at the nodes of the axial grid. Then, using the relations:

$$f_{c_k} = \frac{f_{k+1} + f_k}{2} \quad (4.26)$$

$$\frac{\partial}{\partial x} f_{c_k} = \frac{f_{k+1} - f_k}{\Delta x_{c_k}} \quad (4.27)$$

where  $\Delta x_{c_k}$  is the size of element  $c_k$  in the axial direction, the continuity and momentum equations (Eqs. 4.7 and 4.24) become:

$$\lambda_{c_k}^1 \hat{p}_k + \lambda_{c_k}^2 \hat{u}_k + \lambda_{c_k}^3 \hat{p}_{k+1} + \lambda_{c_k}^4 \hat{u}_{k+1} = \hat{S}_{c_k}^C \quad (4.28)$$

$$\phi_{c_k}^1 \hat{p}_k + \phi_{c_k}^2 \hat{u}_k + \phi_{c_k}^3 \hat{p}_{k+1} + \phi_{c_k}^4 \hat{u}_{k+1} = \hat{S}_{c_k}^M \quad (4.29)$$

where  $\hat{p}_k$  and  $\hat{u}_k$  are the pressure and velocity fluctuation amplitudes evaluated at node  $k$ ,  $\lambda_{c_k}^j$  and  $\phi_{c_k}^j$  are cell-centred coefficients at element  $c_k$  which depend on the mean flow variables, and  $\hat{S}_{c_k}^C$  and  $\hat{S}_{c_k}^M$  the source terms, also evaluated at the center of  $c_k$ . These coefficients can be expressed as:

$$\lambda_{c_k}^1 = \left( \frac{1}{2} \left[ l \left( \frac{1}{c_0^2} \right) i\omega + \frac{d}{dx} \left[ l \left( \frac{u_{x0}}{c_0^2} \right) \right] \right] - \frac{l}{\Delta x} \left( \frac{u_{x0}}{c_0^2} \right) \right)_{c_k} \quad (4.30)$$

$$\lambda_{c_k}^2 = \left( \frac{1}{2} \frac{dl\bar{\rho}_0}{dx} - \frac{l\bar{\rho}_0}{\Delta x} \right)_{c_k} \quad (4.31)$$

$$\lambda_{c_k}^3 = \left( \frac{1}{2} \left[ l \left( \frac{1}{c_0^2} \right) i\omega + \frac{d}{dx} \left[ l \left( \frac{u_{x0}}{c_0^2} \right) \right] \right] + \frac{l}{\Delta x} \left( \frac{u_{x0}}{c_0^2} \right) \right)_{c_k} \quad (4.32)$$

$$\lambda_{c_k}^4 = \left( \frac{1}{2} \frac{dl\bar{\rho}_0}{dx} + \frac{l\bar{\rho}_0}{\Delta x} \right)_{c_k} \quad (4.33)$$

$$\phi_{c_k}^1 = \left( \frac{1}{2} \left[ -\frac{1}{\cos \varphi \rho_0^2 c_0^2} \frac{\partial p_0}{\partial s} \right] - \frac{1}{\Delta x} \left[ \frac{1}{\cos \varphi \rho_0} \frac{\partial x}{\partial s} \right] \right)_{c_k} \quad (4.34)$$

$$\phi_{c_k}^2 = \left( \frac{1}{2} \left[ i\omega + \left( \frac{\partial u_{s_0}}{\partial s} - \tan \varphi \frac{\partial u_{s_0}}{\partial n} - 2 \tan \varphi K_s u_{s_0} \right) \right] - \frac{1}{\Delta x} \left[ \frac{\partial x}{\partial s} u_{s_0} \right] \right)_{c_k} \quad (4.35)$$

$$\phi_{c_k}^3 = \left( \frac{1}{2} \left[ -\frac{1}{\cos \varphi \rho_0^2 c_0^2} \frac{\partial p_0}{\partial s} \right] + \frac{1}{\Delta x} \left[ \frac{1}{\cos \varphi \rho_0} \frac{\partial x}{\partial s} \right] \right)_{c_k} \quad (4.36)$$

$$\phi_{c_k}^4 = \left( \frac{1}{2} \left[ i\omega + \left( \frac{\partial u_{s_0}}{\partial s} - \tan \varphi \frac{\partial u_{s_0}}{\partial n} - 2 \tan \varphi K_s u_{s_0} \right) \right] + \frac{1}{\Delta x} \left[ \frac{\partial x}{\partial s} u_{s_0} \right] \right)_{c_k} \quad (4.37)$$

$$\hat{S}_{c_k}^C = \left( \frac{d}{dx} \left[ l(\rho_0 u_{x_0} \hat{\sigma}) \right] + li\omega(\rho_0 \hat{\sigma}) \right)_{c_k} \quad (4.38)$$

$$\hat{S}_{c_k}^M = \left( -\frac{1}{\cos \varphi \rho_0} \frac{\partial p_0}{\partial s} \hat{\sigma} \right)_{c_k} \quad (4.39)$$

Notice the acoustic source terms  $\hat{S}_{c_k}^C$  and  $\hat{S}_{c_k}^M$  given by Eqs. 4.38-4.39 cancel out in the case of uniform flow.

(6) Boundary conditions are needed to close the system of Eqs. 4.28-4.29. Physically, they represent the acoustic waves entering the domain from the inlet and the outlet. Under the condition the pressure and velocity fluctuations  $\hat{p}$  and  $\hat{u}$  are purely acoustical, which is one of the model's assumptions, these waves are given by the Riemann invariants:

$$P_1^+ = \frac{1}{2} \left( \frac{\hat{p}}{\gamma \bar{p}_0} + \frac{\bar{\rho}_0 c_0}{\gamma \bar{p}_0} \hat{u} \right)_1 \quad (4.40)$$

$$P_n^- = \frac{1}{2} \left( \frac{\hat{p}}{\gamma \bar{p}_0} - \frac{\bar{\rho}_0 c_0}{\gamma \bar{p}_0} \hat{u} \right)_n \quad (4.41)$$

These relations allow the user to set reflection coefficients, which can be interesting for comparison with numerical or experimental data with non-negligible spurious reflections. They are also used to acoustically excite the system. In practice, the flow is either forced acoustically from upstream, from downstream or excited with the entropy fluctuations  $\hat{\sigma}$ , which appear in Eqs. 4.38-4.39, and boundaries are considered to be non-reflective. Combining Eqs. 4.40-4.41 with Eqs. 4.28-4.29 results in a linear system of  $2n$  equations with  $2n$  unknowns which can be solved numerically for the pressure and velocity fluctuations  $\hat{p}$  and  $\hat{u}$ .

It is finally recast in matrix form:

$$\begin{pmatrix} \left(\frac{1}{2\gamma\bar{p}_0}\right)_1 & \left(\frac{\overline{\rho_0 c_0}}{2\gamma\bar{p}_0}\right)_1 & 0 & \dots & \dots & \dots & \dots & \dots & \dots & \dots \\ \lambda_{c_1}^1 & \lambda_{c_1}^2 & \lambda_{c_1}^3 & \lambda_{c_1}^4 & 0 & \dots & \dots & \dots & \dots & \dots \\ \phi_{c_1}^1 & \phi_{c_1}^2 & \phi_{c_1}^3 & \phi_{c_1}^4 & 0 & \dots & \dots & \dots & \dots & \dots \\ \dots & \dots & \dots & \dots & \dots & \dots & \dots & \dots & \dots & \dots \\ \dots & \dots & 0 & \lambda_{c_k}^1 & \lambda_{c_k}^2 & \lambda_{c_k}^3 & \lambda_{c_k}^4 & 0 & \dots & \dots \\ \dots & \dots & 0 & \phi_{c_k}^1 & \phi_{c_k}^2 & \phi_{c_k}^3 & \phi_{c_k}^4 & 0 & \dots & \dots \\ \dots & \dots & \dots & \dots & \dots & \dots & \dots & \dots & \dots & \dots \\ \dots & \dots & \dots & \dots & \dots & 0 & \lambda_{c_{n-1}}^1 & \lambda_{c_{n-1}}^2 & \lambda_{c_{n-1}}^3 & \lambda_{c_{n-1}}^4 \\ \dots & \dots & \dots & \dots & \dots & 0 & \phi_{c_{n-1}}^1 & \phi_{c_{n-1}}^2 & \phi_{c_{n-1}}^3 & \phi_{c_{n-1}}^4 \\ \dots & \dots & \dots & \dots & \dots & \dots & \dots & 0 & \left(\frac{1}{2\gamma\bar{p}_0}\right)_n & -\left(\frac{\overline{\rho_0 c_0}}{2\gamma\bar{p}_0}\right)_n \end{pmatrix} \begin{pmatrix} \hat{p}_1 \\ \hat{u}_1 \\ \dots \\ \hat{p}_k \\ \hat{u}_k \\ \hat{p}_{k+1} \\ \hat{u}_{k+1} \\ \dots \\ \hat{p}_n \\ \hat{u}_n \end{pmatrix} = \begin{pmatrix} P_1^+ \\ \hat{S}_{c_1}^C \\ \hat{S}_{c_1}^M \\ \dots \\ \hat{S}_{c_k}^C \\ \hat{S}_{c_k}^M \\ \dots \\ \hat{S}_{c_{n-1}}^C \\ \hat{S}_{c_{n-1}}^M \\ P_n^- \end{pmatrix} \quad (4.42)$$

(7) The resulting acoustic fluctuations are separated into upstream and downstream propagating contributions, again using the Riemann invariants:

$$P_1^- = \frac{1}{2} \left( \frac{\hat{p}}{\gamma\bar{p}_0} - \frac{\overline{\rho_0 c_0}}{\gamma\bar{p}_0} \hat{u} \right)_1 \quad (4.43)$$

$$P_n^+ = \frac{1}{2} \left( \frac{\hat{p}}{\gamma\bar{p}_0} + \frac{\overline{\rho_0 c_0}}{\gamma\bar{p}_0} \hat{u} \right)_n \quad (4.44)$$

In this normalised form, noise levels can readily be expressed as transfer functions.

## 4.3 Application of the model

CHEOPS-Stator is applied to a 2D-planar stator based on the geometry used for the European-FP7 project RECORD [Bake et al., 2016, Knobloch et al., 2016, 2017], which will be described in detail in chapter 5. Convergence of acoustic and thermo-acoustic transfer functions with a varying number of streamtubes and mesh size is verified in § 4.3.2, where noise levels are also compared to a compact model. The latter is adapted from Cumpsty and Marble's model [1977] to neglect vorticity, like CHEOPS-Stator, as presented in § 4.3.1.

### 4.3.1 Compact solution under the assumptions of the model

The compact model developed by Cumpsty and Marble [1977] and described in section 1.1.1.2 is adapted to CHEOPS-Stator's assumptions in this paragraph. The terms involving vorticity are neglected and the equation for the perturbed flow angle  $\theta'$  is dismissed. Indeed,  $\theta'$  can be expressed in terms of the total velocity fluctuation  $u'$ :

$$\frac{u'_y}{u_{y0}} = \frac{u'}{u_0} + \frac{\theta'}{\tan\theta} \quad (4.45)$$

where the velocity component in the azimuthal direction  $u'_y$  is neglected following CHEOPS-Stator's one-dimensional acoustics assumption. The angle  $\theta'$  is then expressed:

$$\theta' = -\tan\theta \frac{u'}{u_0} = -\frac{\tan\theta}{M} \frac{u'}{c_0} \quad (4.46)$$

The term involving  $\theta'$  remaining in the continuity equation is expressed in terms of  $u'$ , and Cumpsty and Marble's compact model, modified assuming negligible vorticity, can be written:

$$\mathbf{E}_1 \mathbf{P}_1 \begin{pmatrix} w^s \\ w^+ \\ w^- \end{pmatrix}_1 = \mathbf{E}_2 \mathbf{P}_2 \begin{pmatrix} w^s \\ w^+ \\ w^- \end{pmatrix}_2 \quad (4.47)$$

where

$$\mathbf{E} = \begin{bmatrix} 1 & 0 & 0 \\ -1 & (1 + \tan^2\theta)/M & 1 \\ \mu/(\gamma - 1) & M\mu & \mu \end{bmatrix} \quad (4.48)$$

$$\mathbf{P} = \begin{bmatrix} 1 & 0 & 0 \\ 0 & \frac{K_+ \cos(\theta)}{1 - MK_+ \cos(\theta)} & \frac{K_- \cos(\theta)}{1 - MK_- \cos(\theta)} \\ 0 & 1 & 1 \end{bmatrix} \quad (4.49)$$

where symbols have the same meaning as in section 1.1.1.2. The second row of  $\mathbf{P}$  is simplified using an acoustic wave angle of zero, following the one-dimensional acoustics assumption. This formulation of the compact solution is compared to CHEOPS-Stator in the following section.

### 4.3.2 Convergence of the model's parameters

This section aims at verifying that the number of streamlines and the axial mesh size chosen for CHEOPS-Stator are sufficient for accurate discretisation of the flow. In addition, the resulting transfer functions are compared to the compact solution based on Cumpsty and Marble's model [1977] and discussed in the previous paragraph.

CHEOPS-Stator is run with both a Euler and a RANS mean flow. Discussion is limited to the convergence of the transfer functions in this section, and these flow fields are detailed in chapter 5. Figures 4.5 and 4.6 show the evolution of acoustic transfer functions with the number of streamtubes in the case of Euler mean flow with excitation from the inlet and the outlet respectively. Recall the number of streamtubes drives the azimuthal discretisation of the mesh used by CHEOPS-Stator. Full convergence is reached with 100 streamtubes. Figure 4.7, which exhibits similar results for entropic forcing, shows the use of only 50 streamtubes is sufficient in this case. A similar trend is found for the transfer functions obtained with a RANS mean flow field and represented in Figs. 4.8-4.10. Full convergence is also reached with 100 streamtubes in the case of acoustic forcing, and just 25 streamtubes are needed with entropic excitation. With both mean flow types, the transfer functions are also computed using 100 streamtubes and a mesh twice as refined as the baseline mesh in the axial direction. The baseline and refined meshes are made of  $2681 \times 241$  and  $5361 \times 241$  cells respectively. Sufficient axial discretisation is necessary for the accurate evaluation of

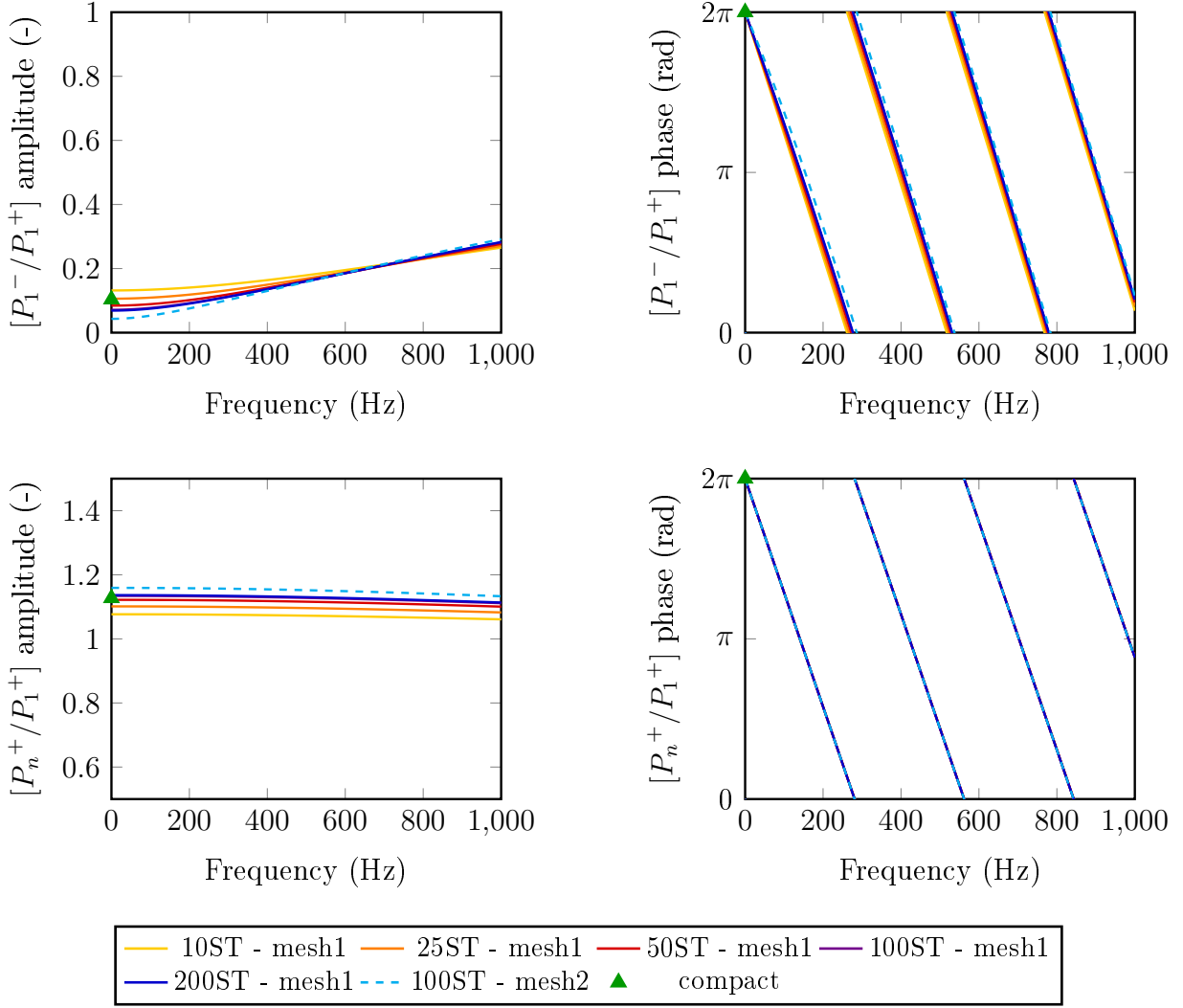


Figure 4.5: Amplitude and phase of the transfer functions  $[P_1^-/P_1^+]$  and  $[P_n^+/P_1^+]$  computed using CHEOPS-Nozzle for a varying number of streamlines and mesh size with Euler mean flow. Transfer functions obtained using Cumpsty and Marble's compact solution [1977] assuming negligible vorticity are also represented.

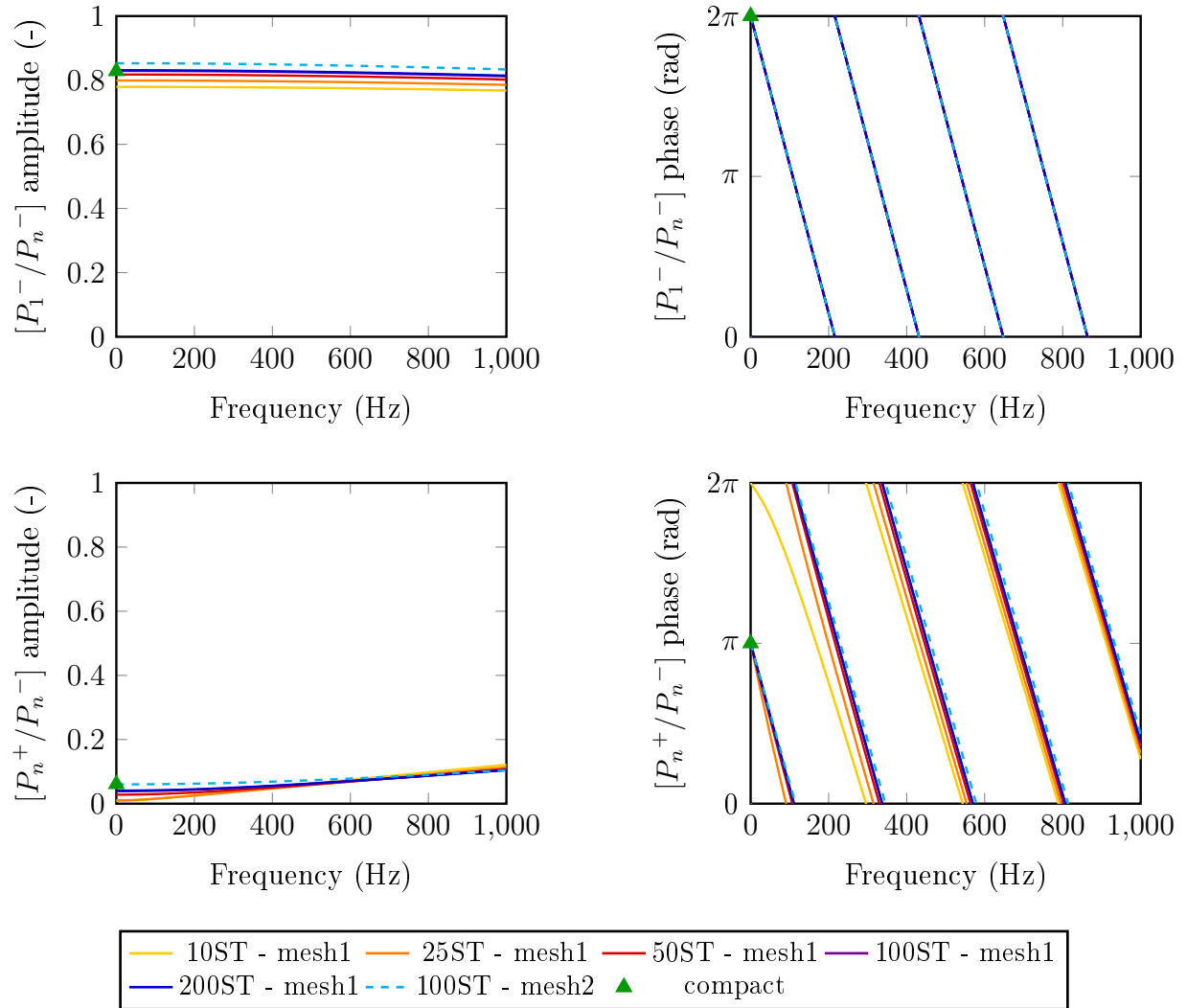


Figure 4.6: Amplitude and phase of the transfer functions  $[P_1^-/P_n^-]$  and  $[P_n^+/P_n^-]$  computed using CHEOPS-Nozzle for a varying number of streamlines and mesh size with Euler mean flow. Transfer functions obtained using Cumpsty and Marble's compact solution [1977] assuming negligible vorticity are also represented.

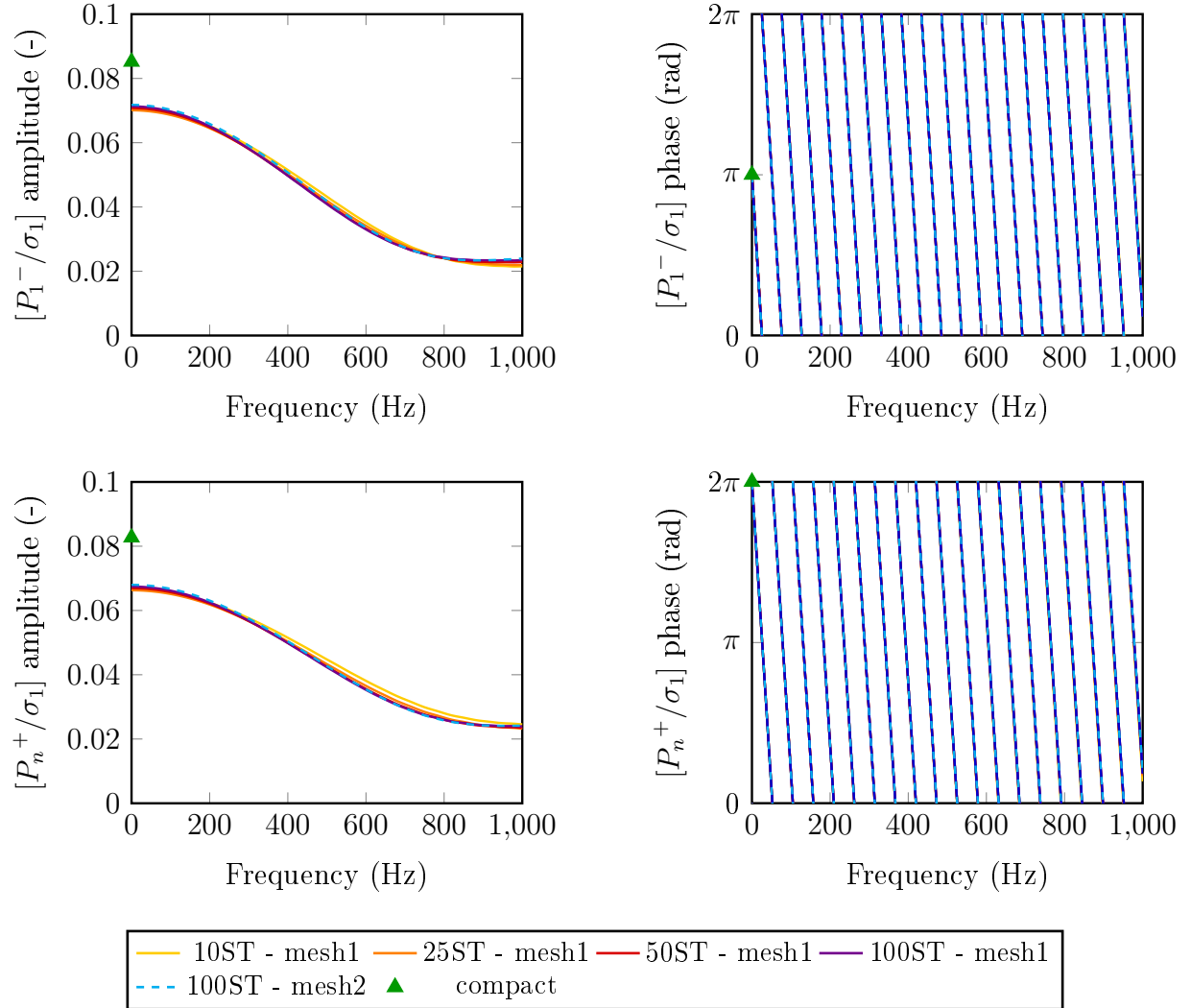


Figure 4.7: Amplitude and phase of the transfer functions  $[P_1^-/\sigma_1]$  and  $[P_n^+/\sigma_1]$  computed using CHEOPS-Nozzle for a varying number of streamlines and mesh size with Euler mean flow. Transfer functions obtained using Cumpsty and Marble's compact solution [1977] assuming negligible vorticity are also represented.

derivatives in particular. The use of the two meshes leads to small differences in transfer functions for acoustic forcing with Euler mean flow, but they are considered small enough for this study. With entropic excitation and all forcing types with RANS mean flow, transfer functions resulting from both meshes are in very good agreement, so that the baseline mesh is retained for comparison with the computational results in the next chapter. As it is already quite refined, it could be optimised for reduced computational cost. The model is run on one desktop processor, and the CPU cost for each mesh-streamtube combination is given in Tab. 4.1. It corresponds to the computation of the transfer functions at 101 frequencies, so that using 50 streamtubes and the baseline mesh leads to a cost of 20 seconds per frequency. As illustrated in Figs. 4.5-4.10, the evolution of the transfer functions with the number of streamtubes is slow from about 25 streamtubes, so that for an optimised computational cost fewer streamtubes than required for full convergence could be employed with only slightly diminished accuracy.

		Number of streamtubes				
		10	25	50	100	200
Mesh size	2681×241	8 min	17 min	33 min	3.7 hrs	9.4 hrs
	5361×241				18.5 hrs	

Table 4.1: Cost of the computation of transfer functions by CHEOPS-Stator, for one forcing type and 101 frequencies, using different mesh sizes and numbers of streamtubes.

The formulation of Cumpsty and Marble’s model [1977] discussed in § 4.3.1 is used to verify the transfer functions obtained in the compact limit with a Euler mean flow. Cumpsty and Marble’s solution is based on the Euler equations and no such model is available in the case of RANS mean flow. Figures 4.5 and 4.6 show CHEOPS-Stator compares well to the analytical solutions resulting from acoustic excitation. This suggests the approximation of the Jacobian terms in Eqs. 4.6, which omits the effect of curvature, does not have a significant impact of the solutions. In the entropic case, CHEOPS-Stator underestimates the amplitudes corresponding to the upstream and downstream propagating acoustic waves by 16% and 18% respectively. The Jacobian terms are not involved in the entropy noise source term on the right-hand side of Eq. 4.24, which indicates their approximation is not the reason for these discrepancies. Indeed, they only appear in terms accounting for the propagation and scattering of acoustic waves, so that an error in the Jacobian terms would affect both entropic and acoustic transfer functions. CHEOPS-Stator’s one-dimensional acoustics assumption could also be responsible for the discrepancies. In theory, the flow in the blade passage does not affect noise levels in the compact limit, but variations in the blade passage are taken into account by CHEOPS-Stator regardless of the frequency. If one-dimensional acoustics in the blade passage is too strong an assumption, it could lead to errors which could explain the gap in amplitude of entropic transfer functions between CHEOPS-Stator and Cumpsty and Marble’s modified model. This point is further discussed in chapter 5.



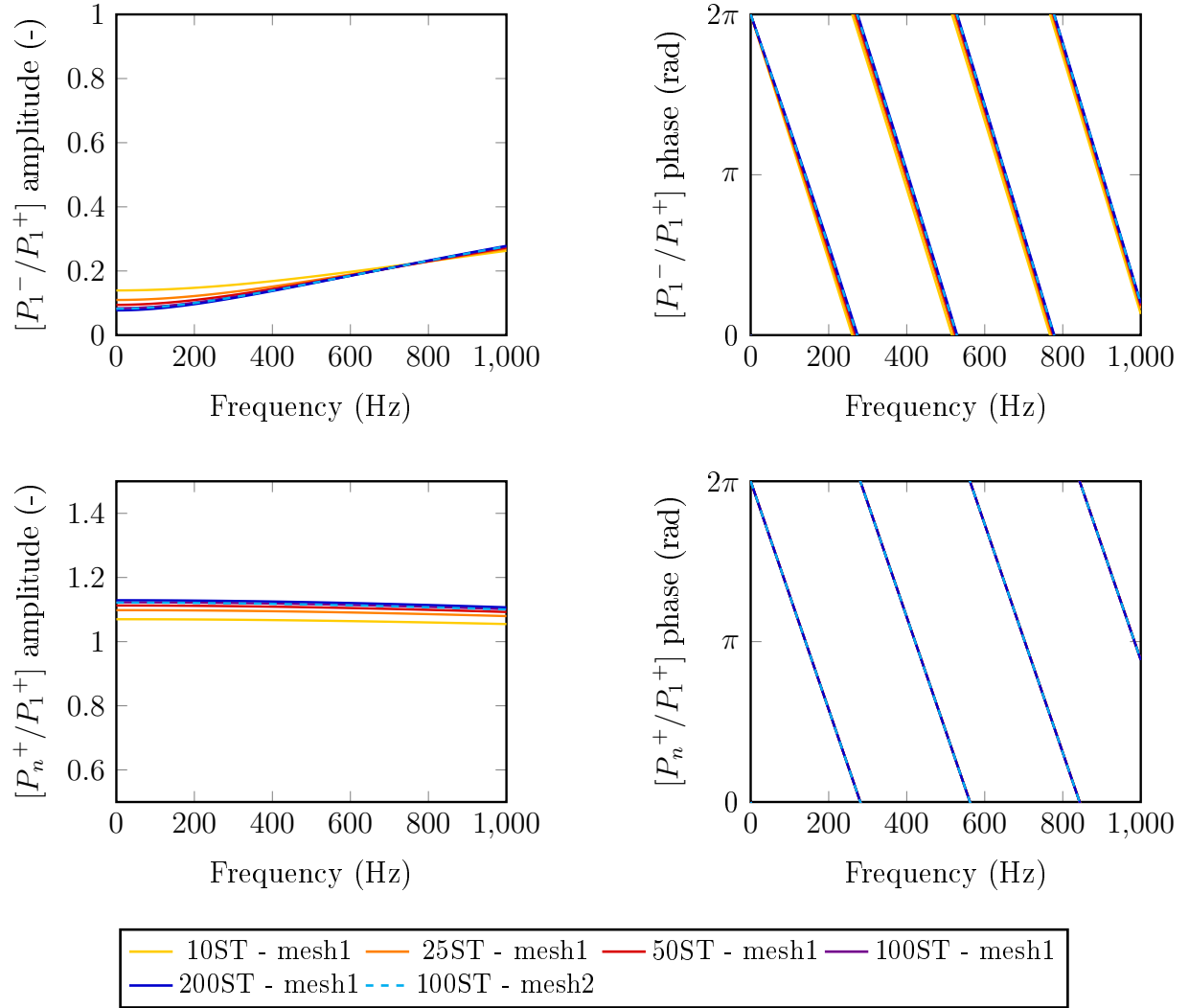


Figure 4.8: Amplitude and phase of the transfer functions  $[P_1^-/P_1^+]$  and  $[P_n^+/P_1^+]$  computed using CHEOPS-Nozzle for a varying number of streamlines and mesh size with RANS mean flow.

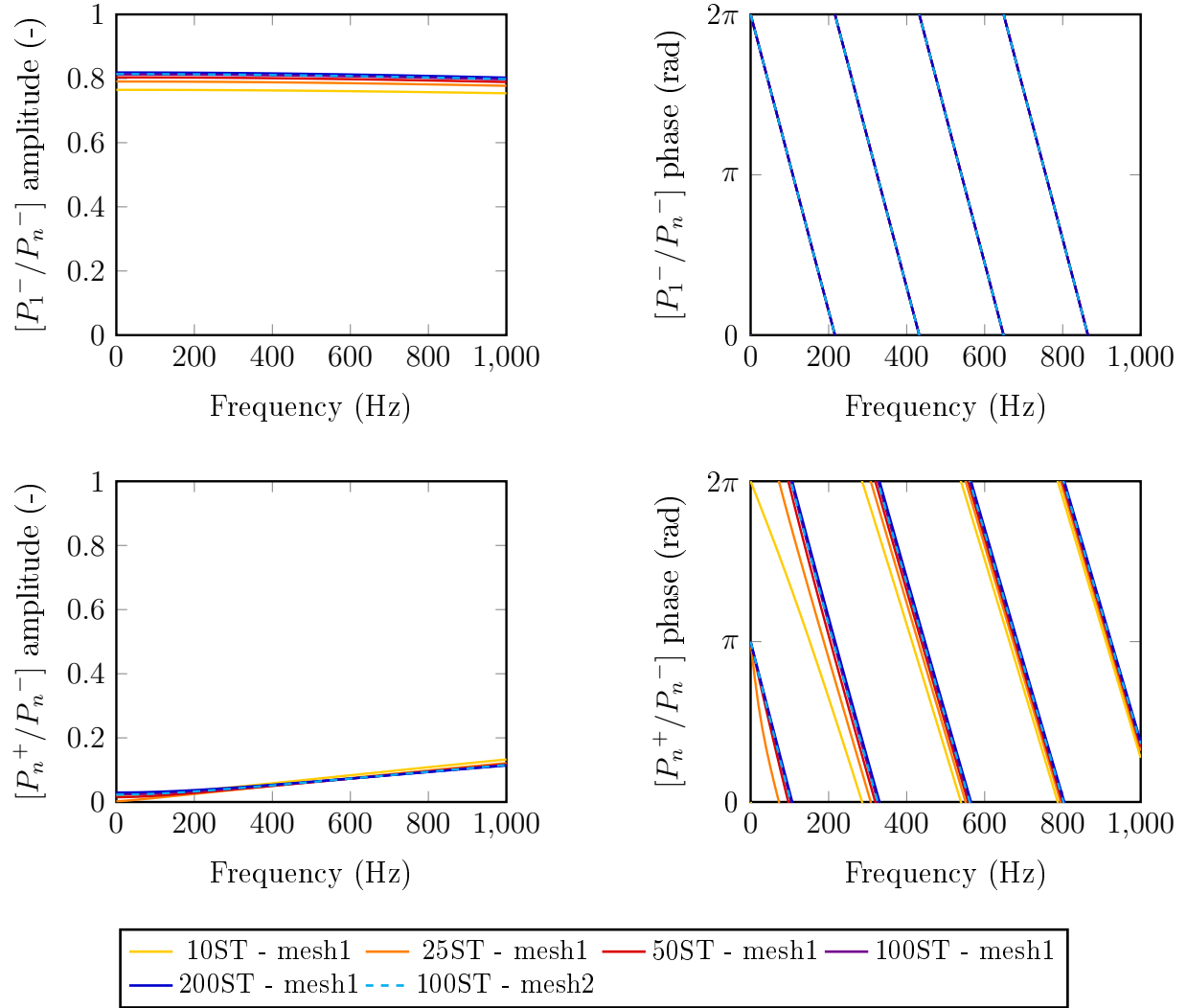


Figure 4.9: Amplitude and phase of the transfer functions  $[P_1^-/P_n^-]$  and  $[P_n^+/P_n^-]$  computed using CHEOPS-Nozzle for a varying number of streamlines and mesh size with RANS mean flow.

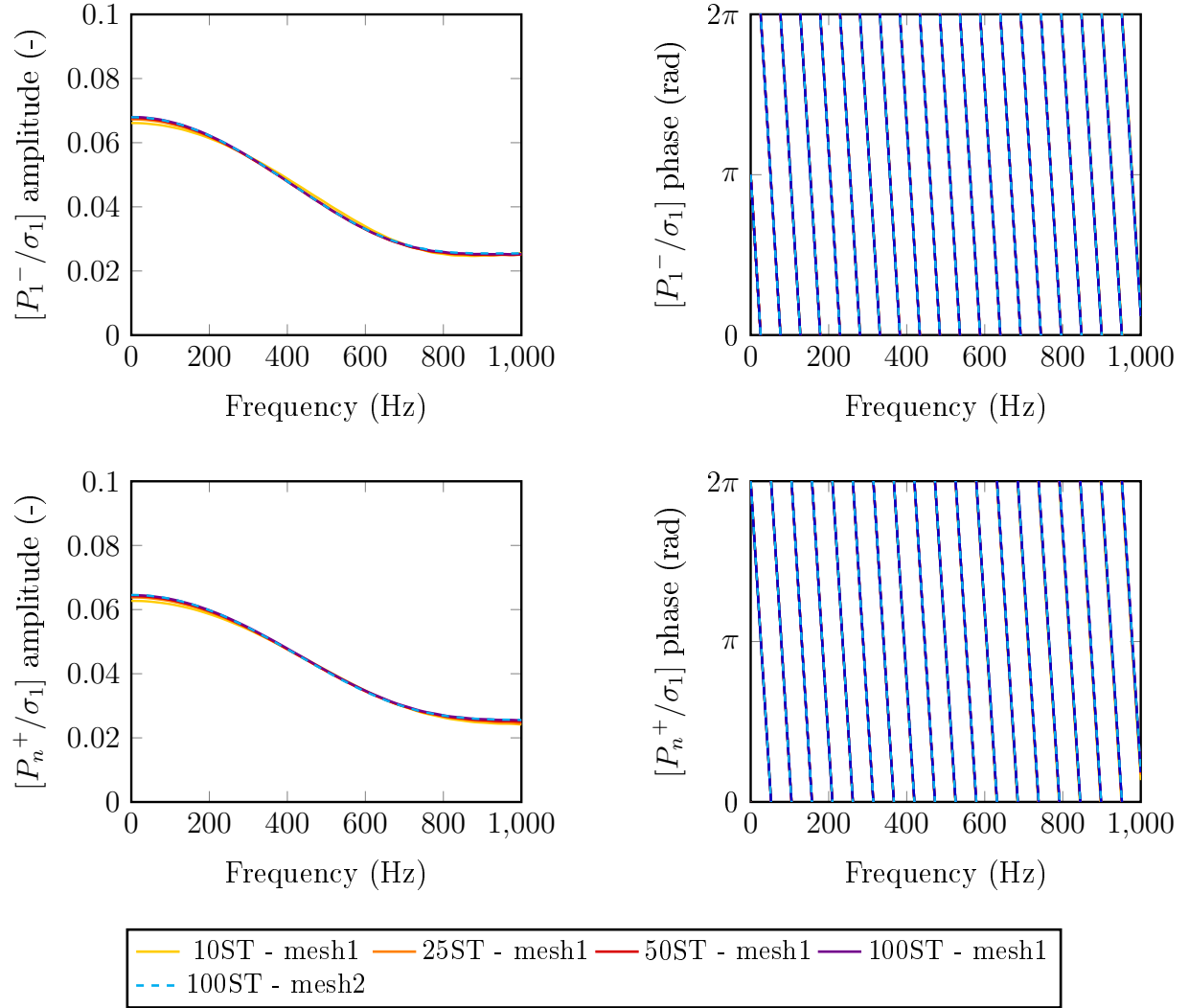


Figure 4.10: Amplitude and phase of the transfer functions  $[P_1^-/\sigma_1]$  and  $[P_n^+/\sigma_1]$  computed using CHEOPS-Nozzle for a varying number of streamlines and mesh size with RANS mean flow.

## 4.4 Conclusions

This chapter presents the semi-analytical model CHEOPS-Stator for the estimation of entropy noise and acoustic scattering through 2D planar stator flow, which is adapted from the model for nozzle configurations described in section 1.1.3.1. It is derived from the Euler equations expressed in a mobile curvilinear reference frame. After the description of the model's equations and resolution process, the accurate discretisation of the numerical domain is verified through a convergence study of the modelled transfer functions. Then, the resulting noise levels are compared to those given by a version of Cumpsty and Marble's compact model [1977] modified to neglect vorticity, in the case of a Euler mean flow. Transfer functions are in very good agreement for acoustic forcing, while they are slightly underestimated by the 2D model in the entropic case. This could be due to CHEOPS-Stator's one-dimensional acoustics assumption, which is discussed in more detail in chapter 5. The latter focuses on the analysis of entropy noise and acoustic scattering in 2D stator configurations using CAA.



# Chapter 5

## Investigation of entropy noise in 2D stator flow

*This chapter aims at investigating entropy noise in isolated 2D stator flow and at building a reference case for comparison with the two-dimensional model CHEOPS-Stator presented in chapter 4. To this end, after choosing an appropriate geometry, both Euler and RANS computations are used to obtain mean flow fields in § 5.1. They act as inputs to the CAA simulations detailed in § 5.2, and the resulting noise levels are discussed in § 5.3 with the analytical compact solution of Cumpsty and Marble [1977]. Lastly, in § 5.4, CHEOPS-Stator is compared to the CAA simulations.*

### Contents

<b>5.1</b>	<b>Choice of geometry and mean flow simulation . . . . .</b>	<b>84</b>
<b>5.2</b>	<b>Simulation of noise levels using CAA . . . . .</b>	<b>86</b>
5.2.1	Set-up of simulations . . . . .	86
5.2.2	sAbrinA_v0 simulations and post-processing . . . . .	87
<b>5.3</b>	<b>Characterisation of noise levels in the 2D stator . . . . .</b>	<b>89</b>
<b>5.4</b>	<b>Comparison of analytical and numerical transfer functions . . . .</b>	<b>99</b>
<b>5.5</b>	<b>Conclusions . . . . .</b>	<b>102</b>

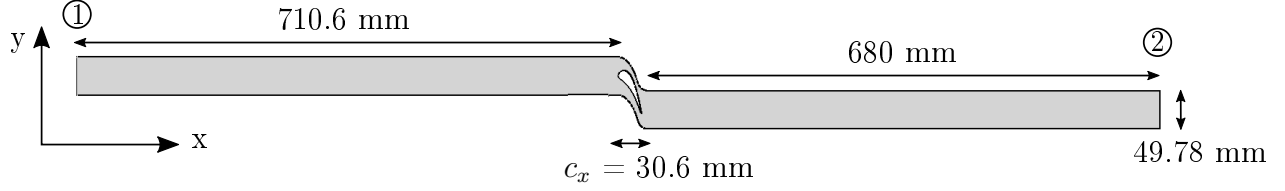


Figure 5.1: Geometry used to simulate two-dimensional isolated stator flow with computational domain dimensions.

## 5.1 Choice of geometry and mean flow simulation

The chosen geometry is based on the stator used for the European-FP7 project RECORD [Bake et al., 2016, Knobloch et al., 2016, 2017], during which entropy noise was studied in a full turbine stage using the high-pressure turbine test-rig at Politecnico di Milano for both subsonic and supersonic operating points. The subsonic conditions are used in this study. The domain is made of a 2D profile extracted at 50% of the 3D blade height, with lateral periodic boundaries corresponding to the distance between two blades. Ducts of length of about 20 axial chords are added upstream and downstream for post-processing. The domain and its dimensions are shown in Fig. 5.1. The inlet is noted 1 and the outlet 2, which corresponds to position  $n$  in the previous chapter.

The mean flow is computed in this domain to serve as an input to CAA simulations. The CFD code CEDRE, which was also used to compute the mean flow in the nozzle in chapter 3, is this time used to provide two sets of mean flow fields by solving both the Euler and RANS equations. The former lead to the simplest case by omitting all viscous terms, and it is the most natural choice for use with the CAA code sAbrinA\_v0, as well as with the low-order model presented in chapter 4, since both approaches are based on the Euler equations. Using the RANS equations allows to partly take viscosity into account, in particular through the presence of boundary layers.

A single unstructured mesh is built to simulate both mean flows using Centaur. Low computational cost in two-dimensions allows the use of a mesh with  $y^+ < 1$ , for the RANS simulation. To this end, 35 quadrilateral layers are built at the wall with an initial thickness of 0.002 mm and stretching of 1.1. The rest of the domain is filled with triangles. Their size is set to 0.3 mm in the region of the blade and of the first two wake crossings of the periodic domain, and it reaches 5 mm at the duct extremities. This results in a 340,000 node mesh made of about 47,000 quadrilaterals and 580,000 triangles. Boundary conditions are chosen in adequation with the subsonic cold operating point used for the RECORD project. The inlet temperature is set to 322 K, the inlet velocity to 42 m/s in the axial direction and the outlet pressure is 109216 Pa for both Euler and RANS flows, leading to slightly different operating points due to the presence of boundary layers in the latter. The specific heat capacity ratio is kept constant at 1.4. Spatial discretisation is of second order, and a pseudo-transient first order implicit scheme is used in time. The  $k-\omega$  SST turbulence model is chosen for the RANS case. The simulation of each of the two mean flows costs 3,500 CPU hrs and 60 processors are used. Convergence is verified with a relative mass flow rate error smaller than  $2.2 \times 10^{-5}$  and  $1.6 \times 10^{-7}$  for Euler and RANS flows respectively, and plateaued

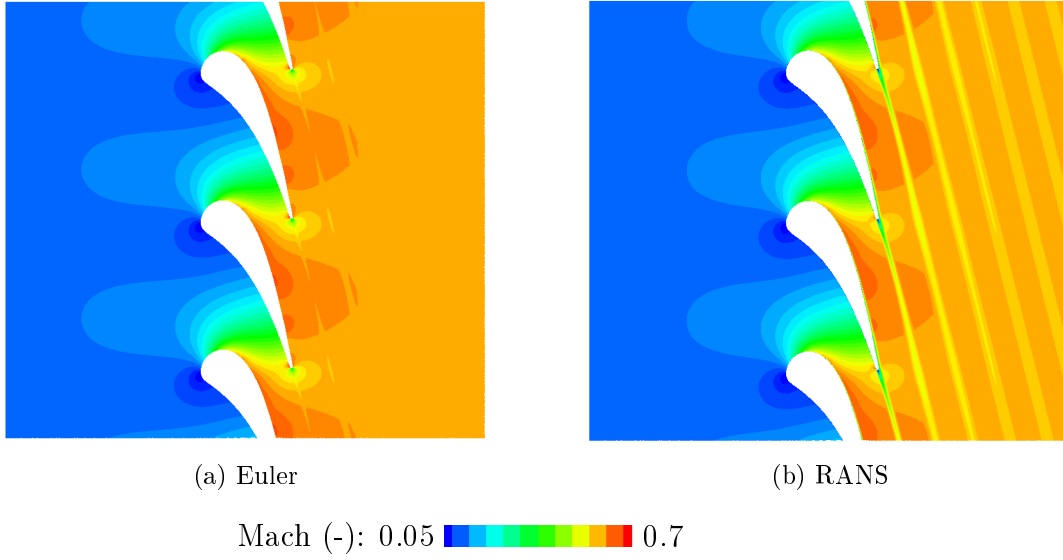


Figure 5.2: Mach number contours of Euler and RANS mean flow fields.

residual errors having decreased by several orders of magnitude.

Figure 5.2 shows Mach number contours resulting from both Euler and RANS simulations. They appear quite close overall, but the wake is much more pronounced in the RANS case and boundary layers are present. These are mainly visible on the suction side of the blade towards the trailing edge, where they are the thickest. The Mach number is maximal at 0.662 with the Euler equations and 0.654 with RANS. Acceleration is also represented in Fig. 5.3

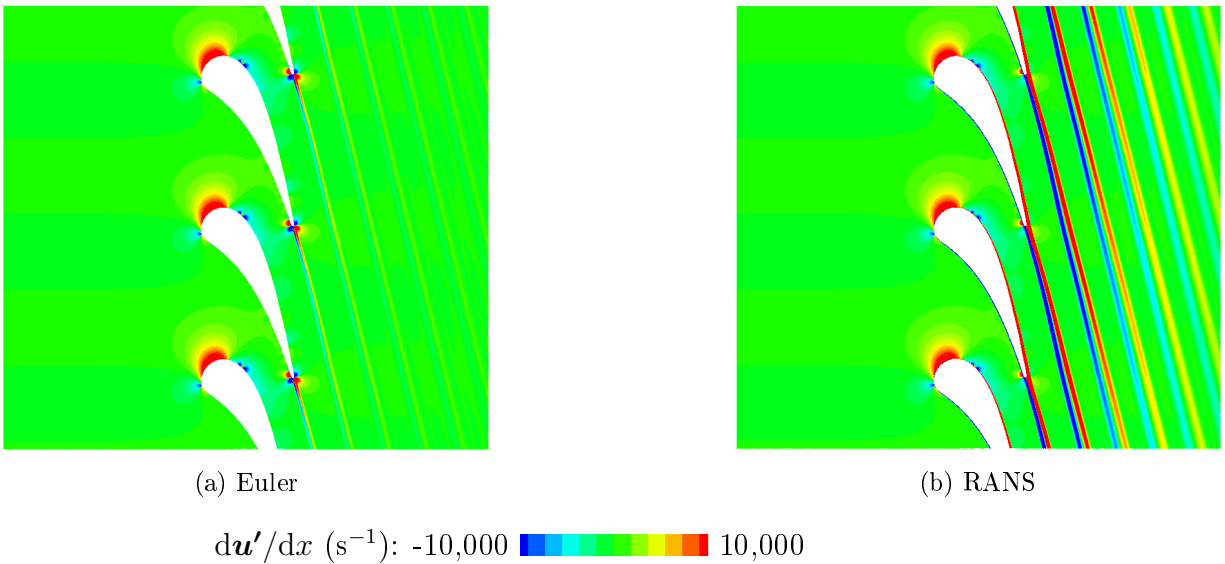


Figure 5.3: Acceleration contours of Euler and RANS mean flow fields.



for both flow types. It highlights the presence of the boundary layers and a thicker wake in the RANS case, and shows the regions of largest acceleration are close to the leading edge on the blade's pressure side and at the trailing edge. No significant differences are visible between Euler and RANS in these regions other than those induced by the boundary layers at the trailing edge.

## 5.2 Simulation of noise levels using CAA

The code `sAbrinA_v0` is used to compute noise levels with both the Euler [Emmanuelli et al., 2018] and RANS mean flow fields presented in the previous section. The simulations are forced by the injection of the three types of plane waves detailed in section 3.1: an entropy perturbation  $\sigma_1$  from upstream, an acoustic wave  $P_1^+$  also injected through the inlet and an acoustic wave  $P_2^-$  propagating from downstream.

### 5.2.1 Set-up of simulations

A structured mesh is built in the 8 domains represented in Fig. 5.4a. X-constant planes are used in the ducts for post-processing reasons. The mesh is dimensioned to have at least 20 points per acoustic or entropic wavelength, which is sufficient to propagate waves without significant numerical error in amplitude or phase. This results in a 260,000 node mesh. It is filtered to be smooth at domain boundaries, as illustrated in Fig. 5.4b at the intersection of the domains on the suction side of the blade. The mean flow fields are interpolated onto this mesh. As the CAA grid is coarse in the near-wall region compared to the size of the boundary layers present in the RANS case, values at the first node at the wall are made equal to those at the second one on the suction side of the blade and near the trailing edge on the

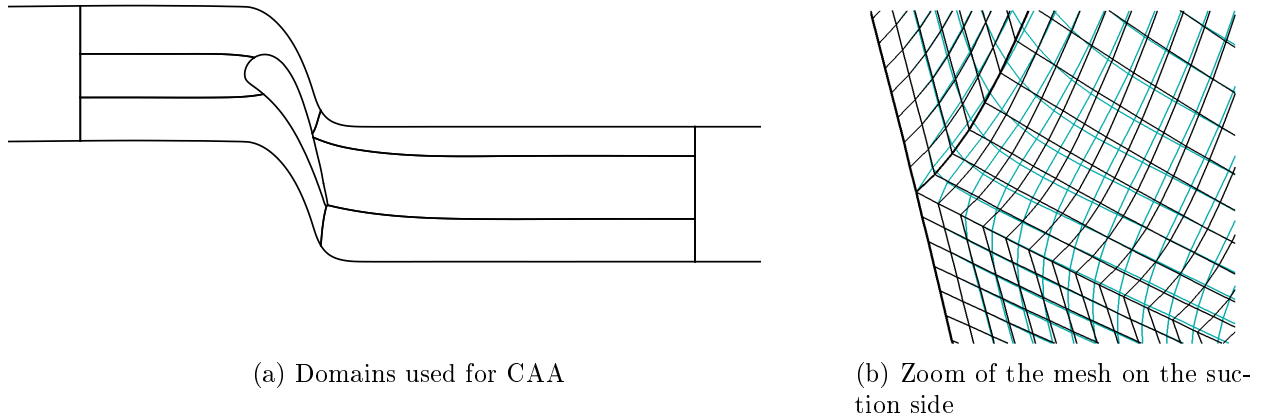


Figure 5.4: Sketch of the domains used for CAA and zoom of the mesh at the intersection of the domains on the suction side of the blade, showing both unfiltered (black) and filtered (blue) meshes.

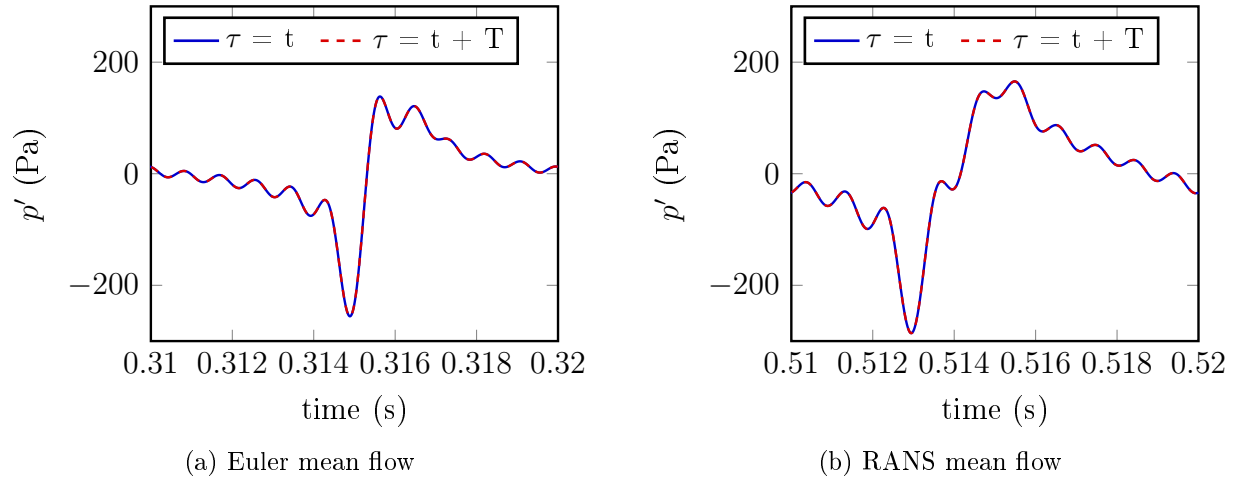


Figure 5.5: Pressure fluctuations measured over two time periods  $T$  at a point near the exit of the domain in the entropic forcing case with both Euler and RANS mean flows.

pressure side in order to avoid excessive gradients leading to numerical instabilities. In the same way as for the nozzle in chapter 3, sAbrinA\_v0 is then used to solve the linearised Euler equations with the non-reflective boundary conditions developed by Tam et al. [Tam and Dong, 1996, Tam and Webb, 1993], injecting waves excited at frequencies between 100 and 1,000 Hz with a step of 100 Hz, with amplitudes equal to 1% of the associated mean flow quantity. The waves corresponding to each frequency are in phase in multi-harmonic cases, like for the nozzle. In this case, the time step is set to  $1.67 \times 10^{-7}$  second, yielding to a maximal CFL number of 0.78.

### 5.2.2 sAbrinA\_v0 simulations and post-processing

Multi-harmonic simulations are run on 12 processors for the three forcing types, as well as harmonic simulations excited at 100, 400 and 1,000 Hz. Convergence of the simulations is verified by ensuring pressure signals measured at a point close to the exit of the domain are periodic, as shown in Fig. 5.5. Only signals from the entropy-forced multi-harmonic simulations with both Euler and RANS mean flow are represented for conciseness, but they are found to be periodic in all cases. It was also verified fluctuations are negligible at 50 Hz, 150 Hz etc, as expected in the linear domain. The cost of each simulation is about 1,000 CPU hrs, but it could be greatly reduced as simulation time was deliberately long to make sure full convergence was reached despite the length of the ducts on either side of the stator. The resulting normalised entropy perturbations  $\sigma$  are shown in Fig. 5.6 in the entropy-forced case with the Euler mean flow. The peak of the injected planar wave is clearly visible and the rest of the fluctuations does not appear on the figure as each frequency is excited with the same phase. The deformation of the entropy wave through the blade passage is studied using harmonic simulations in section 5.3.

The same post-processing strategy as the one presented in section 3.4.3 in the case of the nozzle is used for the 2D stator. Both Direct Mode Matching (DMM) and the Riemann

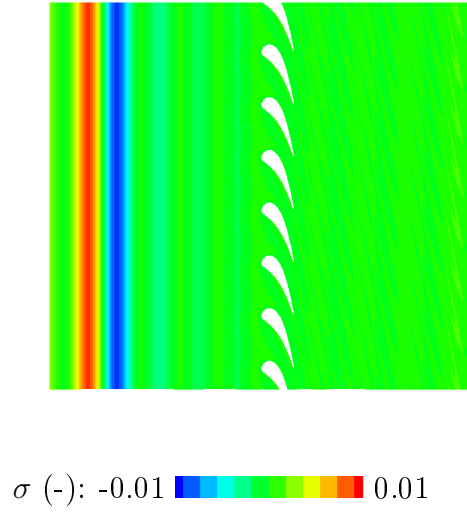


Figure 5.6: Normalised entropy fluctuations simulated with multi-harmonic entropic forcing and the Euler mean flow field.

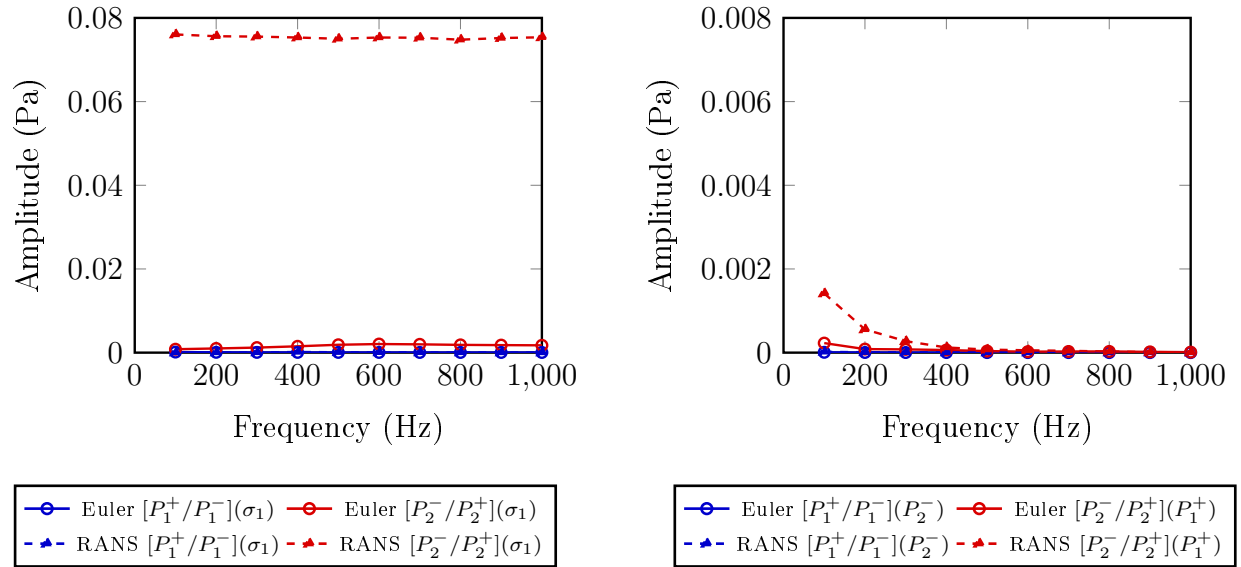


Figure 5.7: Reflection coefficients obtained for the entropy-forced CAA simulation (left) and the two computations with acoustic excitation (right). Euler and RANS mean flow fields are considered and excitation types are given in brackets.

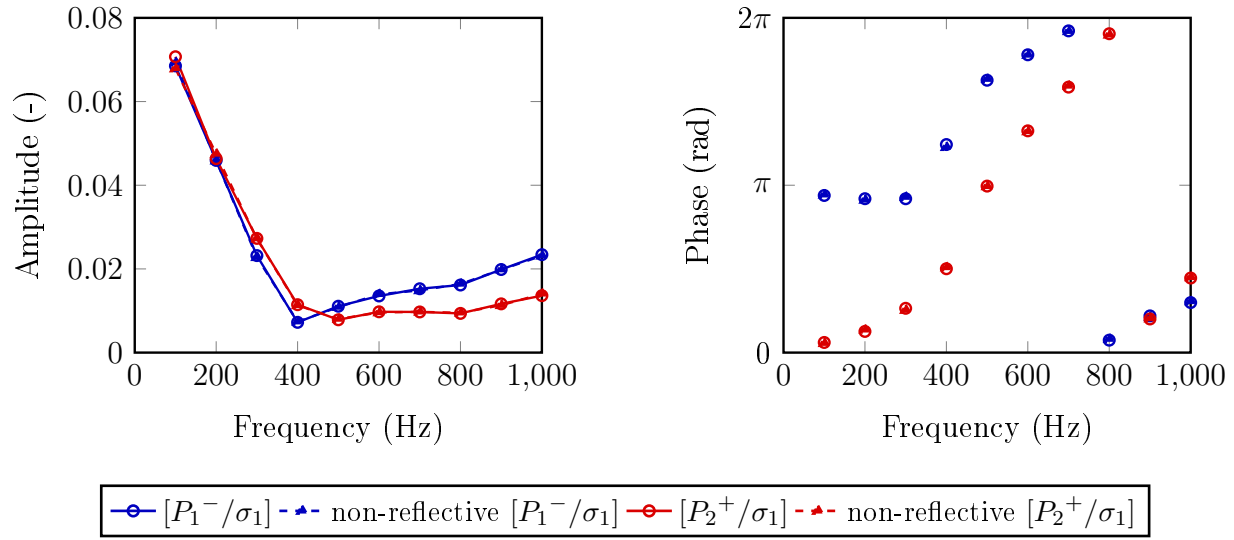


Figure 5.8: Amplitude and phase of transfer functions resulting from entropic excitation with and without non-reflective post-processing and computed with a RANS mean flow.

invariants are used to separate acoustic waves into upstream and downstream propagating components. They are applied in combination with section-averaging and use of several axial positions in the ducts to filter possible hydrodynamic components of fluctuations and to reduce error. The entropy and acoustic waves obtained with this post-processing are used to evaluate the transfer functions of the stator as well as the reflection coefficients on the domain boundaries. Reflection coefficients are evaluated in Fig. 5.7 to verify the importance of reflection in the domain with both Euler and RANS mean flow. The downstream reflection coefficient  $[P_2^-/P_2^+]$  is close to 8% at all frequencies considered in the RANS entropy-forced case. However, Fig. 5.8 shows the transfer function  $[P_2^+/\sigma]$  obtained with and without non-reflective post-processing are almost identical, showing this reflection is of little consequence. Such numerical reflection is also negligible in the other cases considered.

### 5.3 Characterisation of noise levels in the 2D stator

Noise levels simulated using CAA are studied in this section, first by analysing entropy and pressure fluctuation maps and focusing on entropy noise, and then by discussing the transfer functions resulting from acoustic as well as entropic excitations.

The normalised entropy fluctuations injected into the domain to generate entropy noise as they are accelerated by the stator are represented in Fig. 5.9 for harmonically forced cases, at 400 Hz and 1,000 Hz. The colour maps show the fluctuations simulated with the Euler mean flow, while the isolines represent those obtained with RANS flow. At 1,000 Hz, half the number of isolines are used compared to the contour levels for clarity. The injected plane entropy wave is directly affected by the mean flow represented by the Mach number in Fig. 5.2. It is uniformly convected in the upstream duct and it is strongly turned and

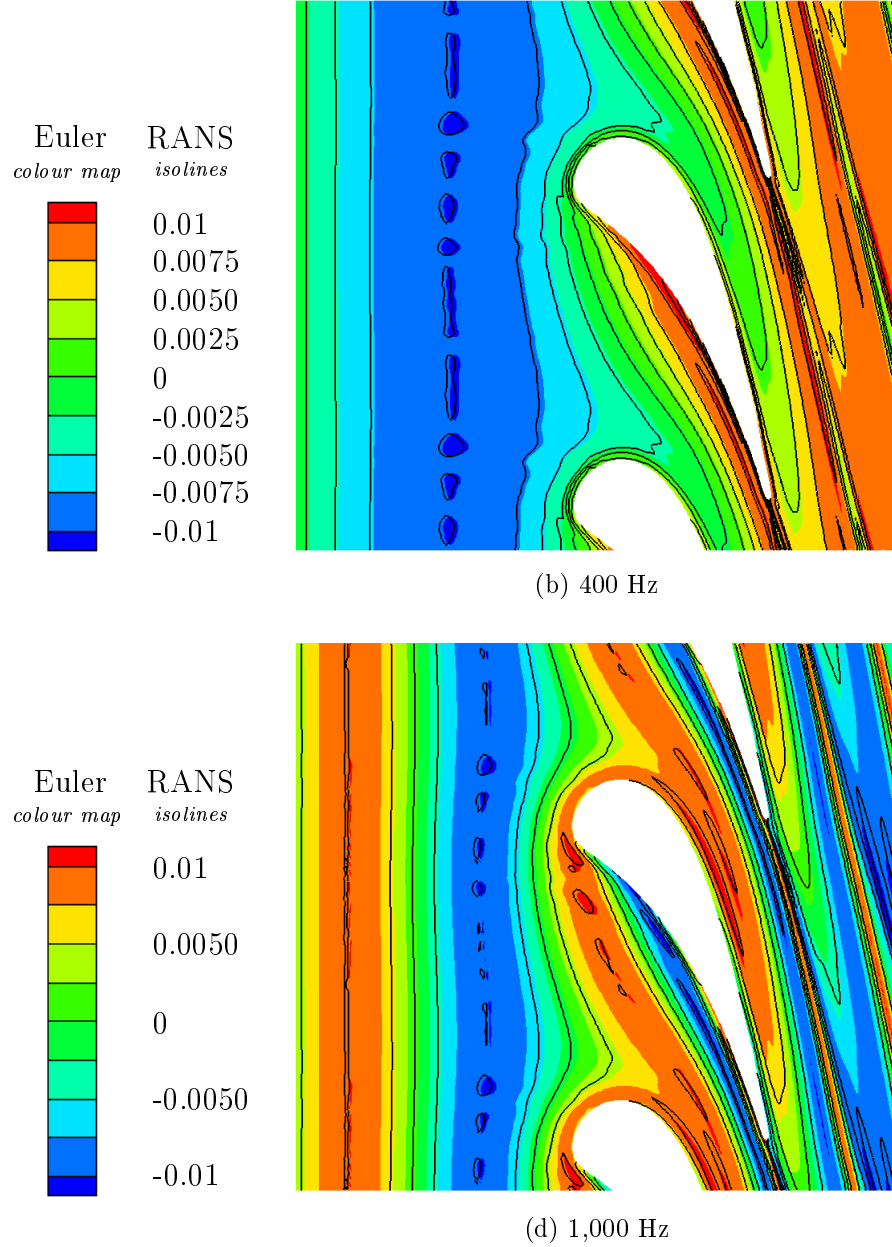


Figure 5.9: Comparison of the shape of the normalised entropy wave  $\sigma$  computed with Euler (colour contour) and RANS (isolines) mean flows at 400 Hz and 1,000 Hz.

chopped by the flow as it is convected through the blade passage. This results in similar behaviour with Euler and RANS mean flows as they are close, as described in section 5.1, but the isolines allow to pin point the differences. They are flush with the colour contour upstream, where the entropy wave is planar, but the perturbations are not accelerated as fast with RANS mean flow, in the presence of boundary layers, than in the Euler case. However, this difference in acceleration appears limited, both at 400 Hz and 1,000 Hz. RANS flow also locally affects the entropy wave deformation because of the boundary layers and the thicker wake than in Euler flow.

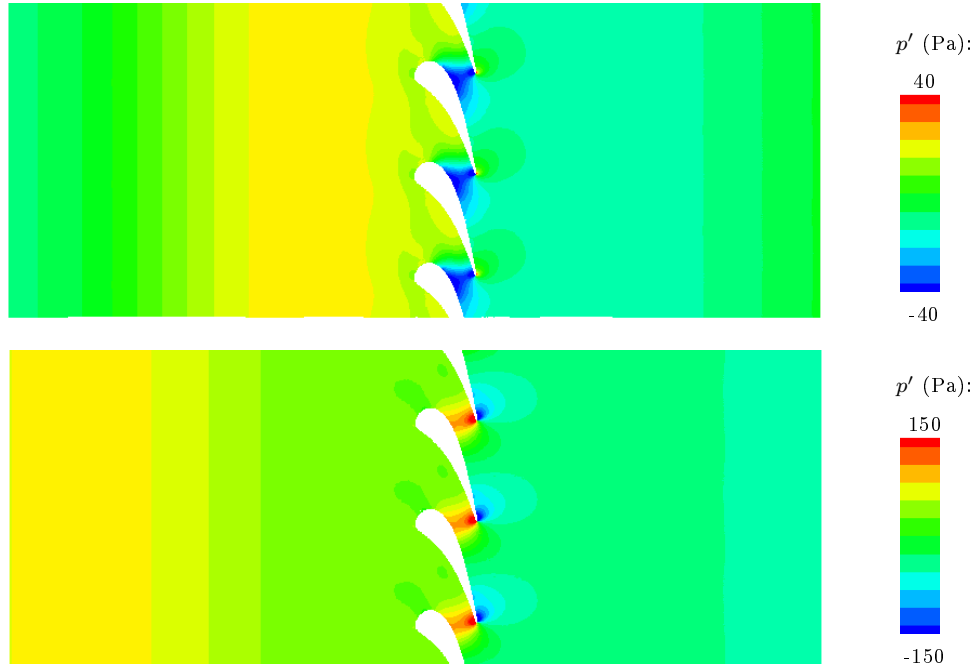


Figure 5.10: Pressure fluctuation  $p'$  colour contours resulting from multi-harmonic entropy-forced simulations with both Euler (top) and RANS (bottom) mean flows.

Pressure fluctuation contours are given in Fig. 5.10 in cases where multi-harmonic entropic perturbations are injected into the domain with Euler and RANS mean flow fields. They show acoustic waves are one-dimensional in the ducts as expected. On the other hand, the stator blade is non-compact and acoustic wave-fronts are perpendicular to the direction of the flow in its vicinity. The colour maps, which represent the same instant in time, display different source shapes with Euler and RANS mean flows. Figure 5.11 provides more information to explain this. It shows both normalised entropy and pressure fluctuations computed using harmonic simulations at 100 Hz, 400 Hz and 1,000 Hz with Euler and RANS mean flows. Each contour corresponds to a different instant in time, chosen close to the peak pressure fluctuation, for them to be comparable. Let's concentrate on the cases with Euler mean flow first. At 100 Hz, the pressure fluctuations are maximal at the trailing edge and in a region covering a large fraction of the suction side of the blade. This is also the case at 400 Hz but along a much smaller portion of the blade, towards the leading edge, which is in accordance with the smaller wavelength at this frequency. At 1,000 Hz, the size of this region is further reduced. It is also the frequency at which the amplitude of  $p'$  is minimal, while it is maximal

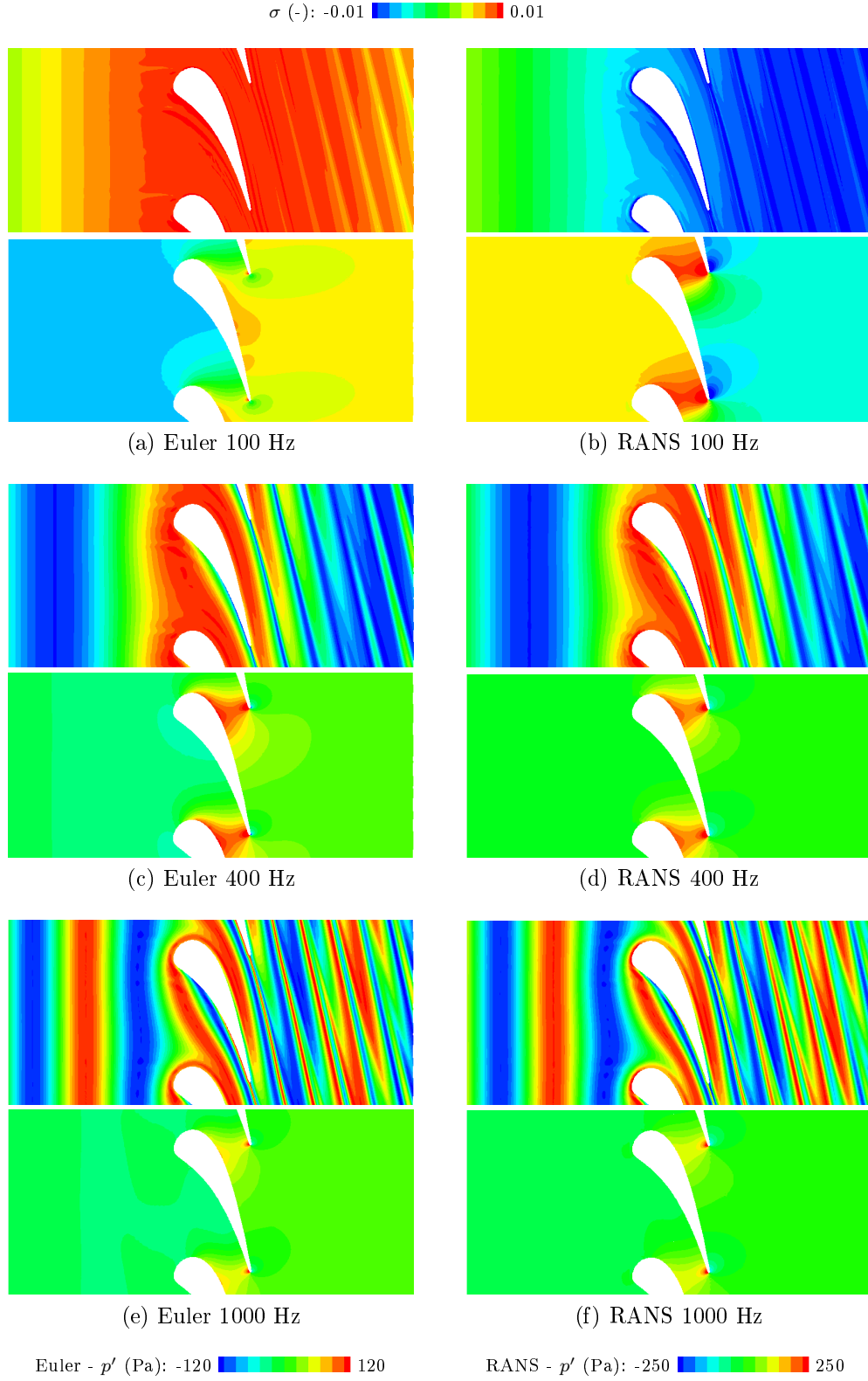


Figure 5.11: Entropy (top) and pressure (bottom) fluctuation contours resulting from harmonic entropy-forced simulations with both Euler and RANS mean flows.

at 400 Hz. A negative pressure fluctuation region is also visible at all three frequencies on the pressure side of the blade. Their absolute amplitude is smaller than positive pressure fluctuations at 400 Hz and 1,000 Hz, but they are of the same order of magnitude at 100 Hz. Pressure fluctuation colour maps obtained with Euler and RANS flows have similar topology at 400 Hz and 1,000 Hz. At 1,000 Hz, the positive  $p'$  region is less spread along the blade's suction side with RANS than with Euler flow and it is only a little larger than the zone of high pressure fluctuations near the trailing edge. At 400 Hz, this effect is only slightly visible. At both frequencies, the pressure fluctuation amplitudes are larger with RANS than with Euler mean flow. Note contour levels are more than twice as high with RANS than with Euler flow. With both mean flow types, the amplitude of  $p'$  is lower at 1000 Hz than 400 Hz. The negative  $p'$  region on the blade's pressure side is not visible on the contour at 400 Hz with RANS mean flow, and only just at 1,000 Hz. It is difficult to compare these regions with the Euler case for which colour map levels are different, but with both mean flow types, the absolute amplitude of the negative pressure fluctuations is low compared to the positive fluctuations at 400 Hz and 1000 Hz.

In the five cases discussed up to now, i.e. 100 Hz, 400 Hz and 1,000 Hz with Euler flow and 400 Hz and 1,000 Hz with RANS (Figs.5.11a-5.11c-f), the normalised entropy wave contours show entropy is positive throughout the blade passage on the suction side. Furthermore, the corresponding pressure fluctuations are also positive on the suction side, which is in accordance with previous studies characterising entropy noise [Bake et al., 2008]. When negative  $\sigma$  crosses the blade passage, the pressure fluctuation region between the leading and trailing edges is also negative and of similar shape as in Fig. 5.11. This synchronisation of  $\sigma$  and  $p'$  indicates the main noise generating mechanism is in fact due to the acceleration of the entropy perturbations. On the other hand, the sixth case shown in Fig. 5.11b displays negative normalised entropy fluctuations and a different pressure fluctuation topology than the other cases, indicating the dominant noise generating mechanism may be different. The acoustic source is of dipolar type around the trailing edge, with significantly larger amplitude than the other cases. The positive  $p'$  region does extend towards the leading edge like for the other cases, which could be due to entropy noise, but it seems noise generated at the trailing edge is predominant at this frequency.

In order to further investigate entropy noise generation, Figure 5.12 shows the evolution of both normalised entropy and pressure fluctuations with time. The case of entropy excitation at 100 Hz with Euler mean flow is chosen, because the high pressure fluctuation region in Fig. 5.11 is the largest at this frequency. The first instant in time corresponds to the smallest pressure fluctuation amplitude, and the last to the iteration used in Fig. 5.11 at which pressure fluctuations are maximal. In Fig. 5.12a, the entropy wave is zero in between the blades, and the pressure fluctuations are small. They are nonetheless non-zero in the region of the trailing edge and of the leading edge in particular. As higher amplitude entropy fluctuations reach the blade (b), the region of positive pressure fluctuations expands in between the leading edge and the trailing edge of the next blade and the amplitude of the pressure fluctuations slowly increases. These pressure fluctuations continue to increase and the high pressure fluctuation region slowly shifts downstream as positive entropy perturbations cross the whole blade passage (c). This effect is amplified as higher entropy fluctuations are convected through the stator, and the pressure fluctuations increase in amplitude and fill most of the blade passage (d-e). The fact the noise sources originate towards the leading edge and at the trailing edge



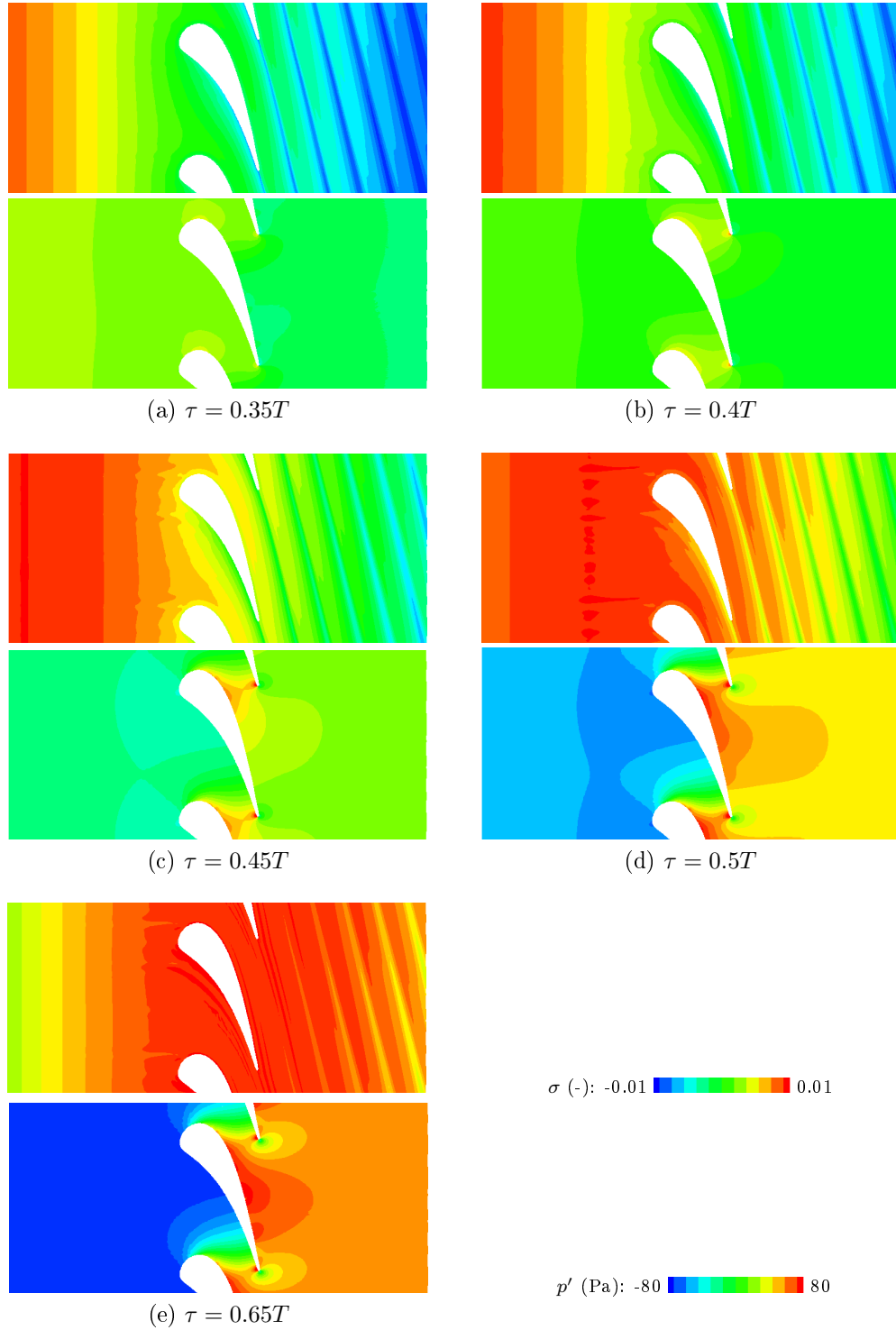


Figure 5.12: Entropy (top) and pressure (bottom) fluctuation contours computed at different instants of an entropy harmonically forced simulation at 100 Hz with Euler mean flow. The time period is noted  $T$ .

is expected, as they are the regions of maximum acceleration (Fig. 5.3), which is responsible for entropy noise. The negative  $p'$  region on the blade's pressure side develops more slowly than its positive counterpart. It is not visible on (b) and it only reaches absolute amplitudes comparable to the pressure fluctuations on the suction side and at the trailing edge when the whole blade passage is filled with large positive entropy fluctuations. Similar evolution of the pressure fluctuations was found at 400 Hz and 1,000 Hz with Euler and RANS mean flows. However, the positive pressure fluctuation regions do not spread as much in these cases, due to smaller wavelengths. Their amplitude reach a maximum at the instants shown in Fig. 5.11c-5.11f, which are closest to Fig. 5.12c, before reducing and following a similar pattern with opposite sign as negative entropy perturbations cross the domain. In these cases, the pressure fluctuations on the pressure side of the blade remain of low absolute amplitude.

Figure 5.13 represents total velocity fluctuation contours resulting from entropy-forced cases at both 100 Hz and 1,000 Hz with the Euler mean flow. Those obtained with RANS are very close and they are not shown for conciseness. Like the pressure fluctuations discussed above, velocity perturbations are one-dimensional upstream of the stator but this is not the case downstream. High amplitude fluctuations appear in the blade passage and are convected downstream in a similar way as for the nozzle in chapter 3. They can be assimilated to vorticity which is generated by the acceleration of entropy perturbations through the stator and, as they are convected downstream, these velocity fluctuations are affected by the turning of the flow in the same way as the entropy perturbations in Fig. 5.9. Recall both DMM and the Riemann invariants are used for pressure fluctuation separation into upstream and downstream propagating waves. The Riemann invariants are only valid under

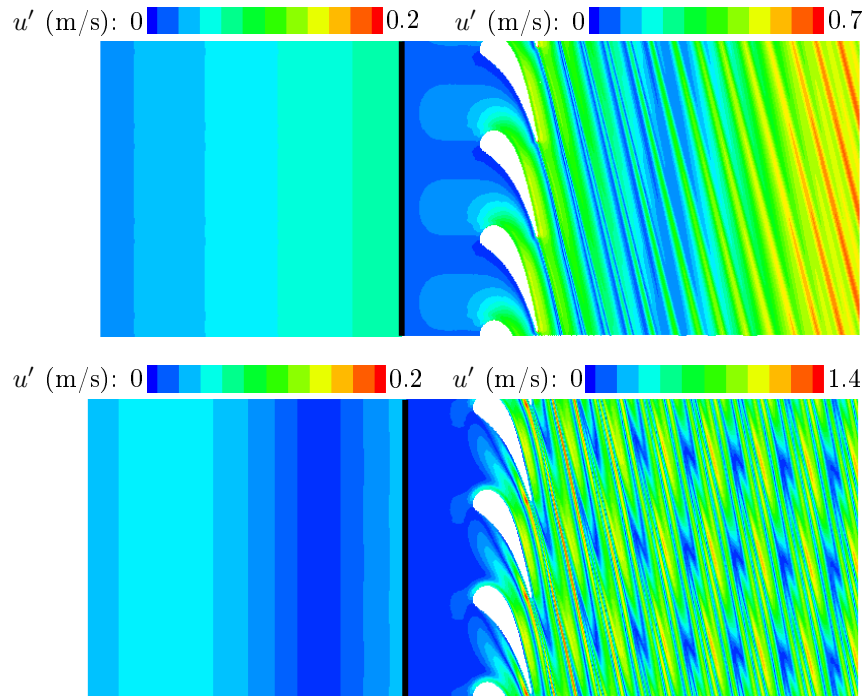


Figure 5.13: Velocity fluctuation fields resulting from harmonic entropic forcing at 100 Hz (top) and 1,000 Hz (bottom) with Euler mean flow.

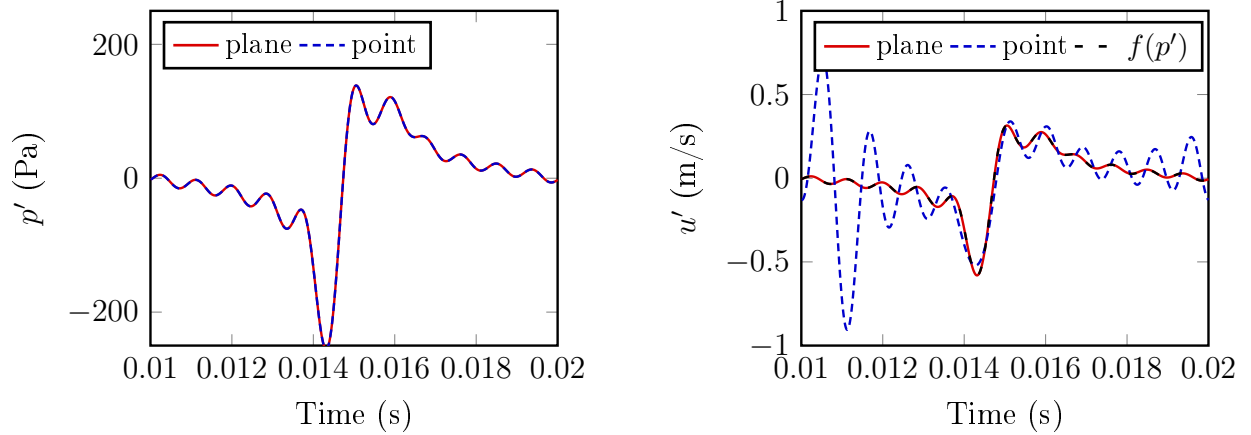


Figure 5.14: Pressure and velocity fluctuations computed as part of the multi-harmonic entropy-forced simulation both at a point of the downstream duct and averaged over the corresponding plane, and acoustic velocity fluctuations computed from the impedance relation for a plane progressive wave  $u' = p' / (\rho_0 c_0)$ .

the assumption both  $p'$  and  $u'$  are purely acoustic, which is not the case here. Filtering of hydrodynamic perturbations during post-processing can be used to overcome this restriction, as in section 3.4.4 in the case of the nozzle. Pressure and velocity fluctuation signals computed both after averaging over a plane downstream of the stator and at a point of the same plane are given in Fig. 5.14. The resulting signals are close for  $p'$ , but  $u'$  signals differ as expected from Fig. 5.13. In order to assess the effect of averaging-filtering, velocity fluctuations are computed from pressure variations using the impedance relation  $u' = p' / (\rho_0 c_0)$ . They are found to be very close to the signal computed from averaged data, indicating hydrodynamic perturbations are cancelled out by this step. It is also verified that computation of the waves  $P_1^\pm$  and  $P_2^\pm$  gives the same values at the different axial positions considered and that DMM and Riemann invariants yield the same results. Either approach can therefore be used to compute transfer functions in this case.

Figures 5.15, 5.16 and 5.17 illustrate the noise levels resulting from upstream acoustic, downstream acoustic and entropic excitations respectively, by showing transfer functions obtained after non-reflective post-processing. The latter are computed using CAA with both Euler and RANS mean flows. The compact solutions formulated by Cumpsty and Marble [1977] from the linearised Euler equations and presented in section 1.1.1.2 are also given for the three forcing types. Although the CAA results could not be computed up to zero Hertz, the Euler transfer functions are in good agreement with those resulting from the compact model in amplitude and in phase, for entropic forcing as well as both cases of acoustic excitation.

Let's concentrate on the acoustic transfer functions given in Figs. 5.15 and 5.16 first. In the case of Euler mean flow, the evolution of the transfer functions with frequency is limited. On the other hand with RANS, the amplitudes follow the same trend but their dependence on frequency is much more pronounced. This leads to the largest differences in

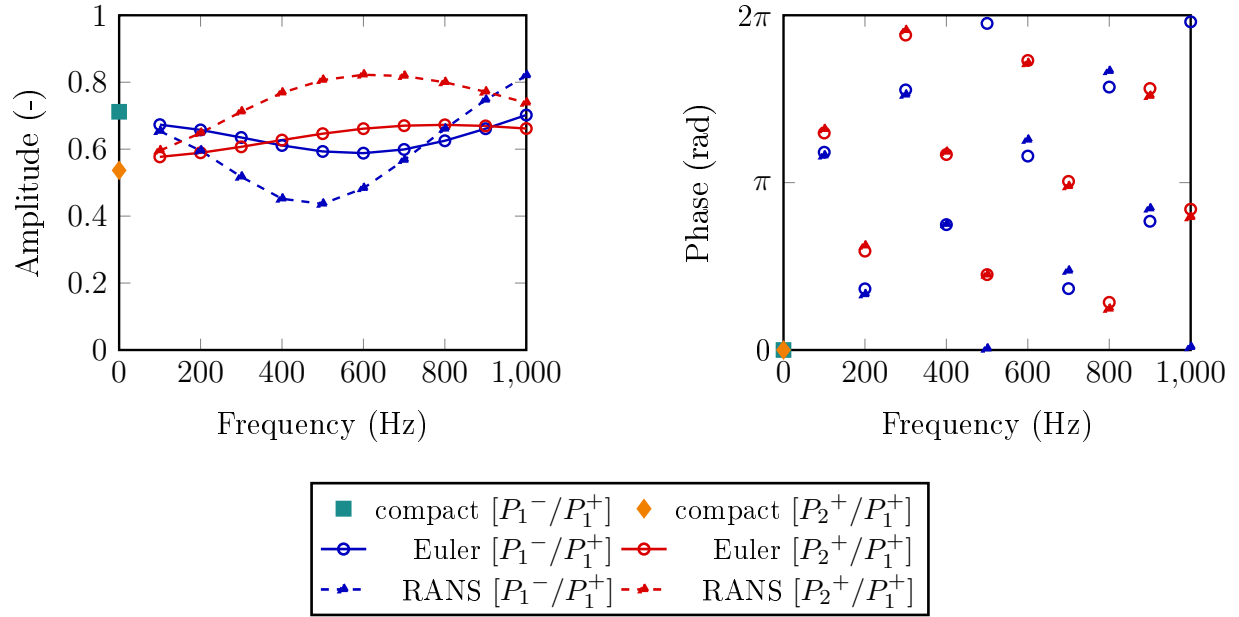


Figure 5.15: Amplitude and phase of the transfer functions resulting from upstream acoustic forcing  $[P_1^-/P_1^+]$  and  $[P_2^+/P_1^+]$ , computed using Cumpsty and Marble's compact solution [1977] and CAA with Euler and RANS mean flow fields.

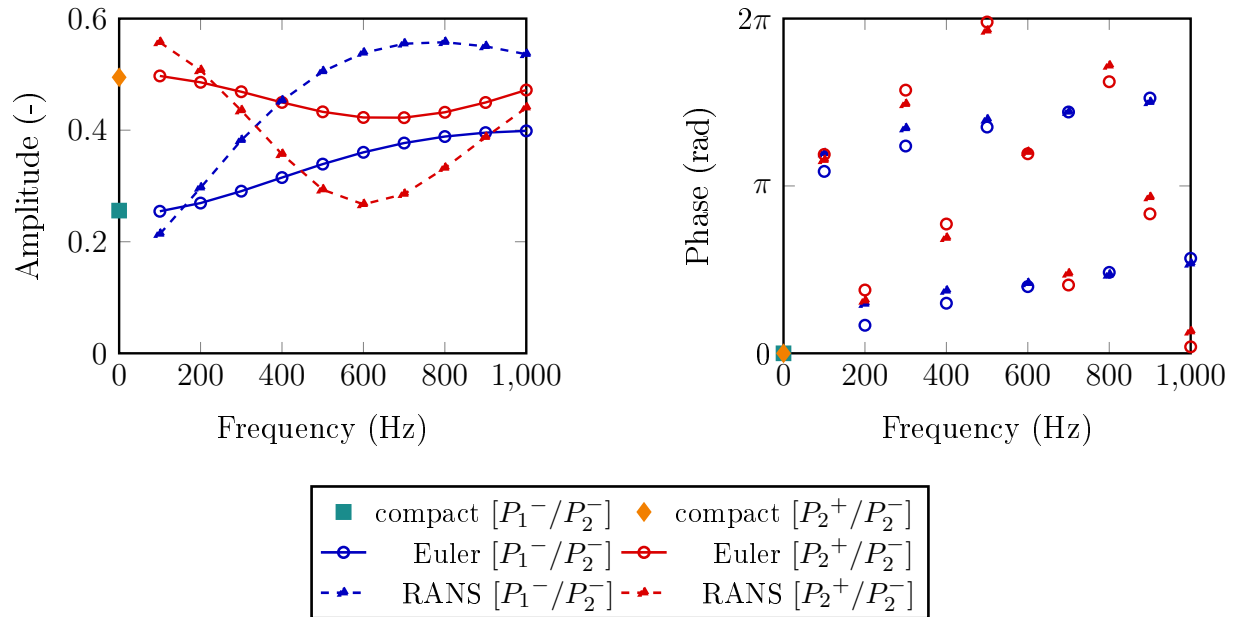


Figure 5.16: Amplitude and phase of the transfer functions resulting from downstream acoustic forcing  $[P_1^-/P_2^-]$  and  $[P_2^+/P_2^-]$ , computed using Cumpsty and Marble's compact solution [1977] and CAA with Euler and RANS mean flow fields.

the mid-frequency range, whereas amplitudes are close below 200 Hz in all cases and the curves tend to join once more towards the upper end of the frequency range. The phases of the acoustic transfer functions are also shown in Figs. 5.15 and 5.16. They are presented in the range  $[0, 2\pi]$  as they are too poorly discretised to be unwrapped. This must be kept in mind as it can lead to misinterpretation when comparing phases in different cases or at different frequencies. The phases of the acoustic transfer functions obtained with Euler and RANS flows are however so close over the whole frequency range that they can be considered in the same  $[0, 2\pi]$  interval. The proximity of these phases could be explained by the large value of the speed of sound compared to the convective axial velocity with both Euler and RANS mean flows.

The thermo-acoustic transfer functions given in Fig. 5.17 represent the acoustic waves generated by the acceleration of entropy perturbations and then scattered as they propagate upstream and downstream. They therefore include the wave reflection and transmission effects outlined by the acoustic transfer functions above. First note the amplitudes of  $[P_1^-/\sigma_1]$  and  $[P_2^+/\sigma_1]$  are similar, in both Euler and RANS cases. With the Euler mean flow, the amplitude of the transfer functions decreases with frequency with approximately constant slope up to about 500 Hz, and more slowly in the upper end of the frequency range. In the RANS case, the amplitude also decreases at lower frequencies but much more sharply. The point where the slope changes is more pronounced and occurs at slightly lower frequency than with the Euler mean flow, near 400 Hz. These slope breaks are in the range of frequencies where the highest differences between acoustic transfer function amplitudes were observed in Figs. 5.15 and 5.16. Moreover, contrary to the Euler case, the amplitude of the transfer

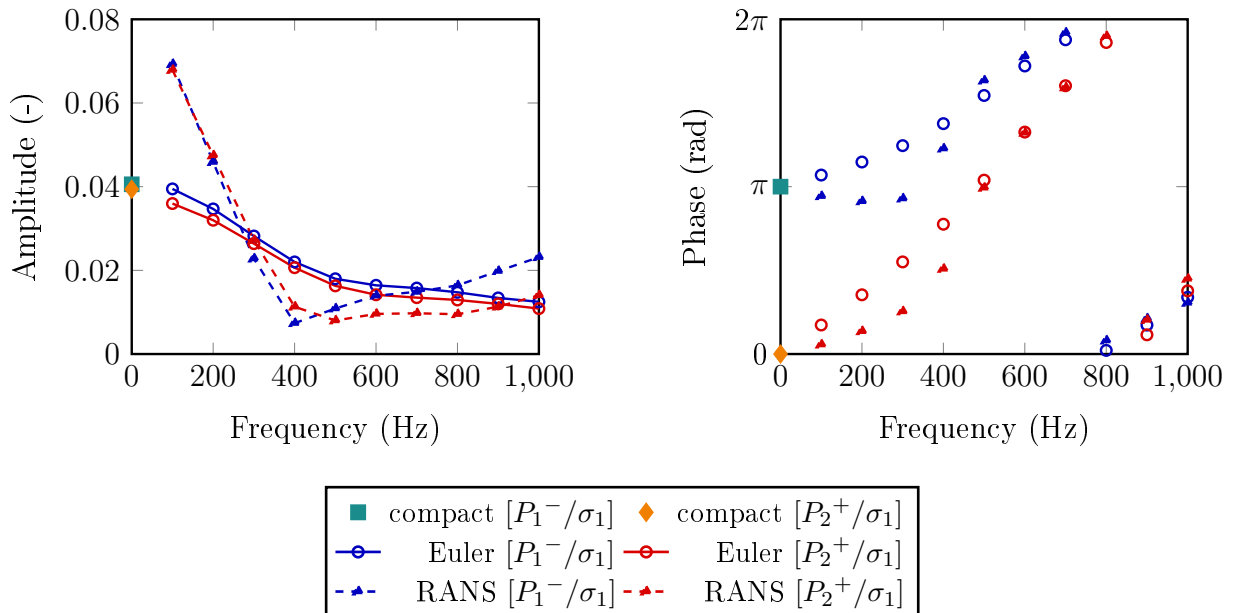


Figure 5.17: Amplitude and phase of the transfer functions resulting from entropic forcing  $[P_1^-/\sigma_1]$  and  $[P_2^+/\sigma_1]$ , computed using Cumpsty and Marble's compact solution [1977] and CAA with Euler and RANS mean flow fields.

functions then slowly increases with frequency up to the end of the range considered. In the upper half of the frequency range, the phases of the Euler and RANS transfer functions are close, like the phases of the acoustic transfer functions. However, these phases differ in the lower half of the frequency range, which also displays the largest differences in amplitude. The latter can be explained by Fig. 5.11 in which the pressure fluctuation generation was found to be driven by the trailing edge at 100 Hz with RANS mean flows, unlike the Euler case. On the other hand, this may not explain the differences in phase found at low frequency, as they seem significant up to 400 Hz, at which the role of the trailing edge in the generation of noise is different than at 100 Hz and the evolution of pressure fluctuations seems globally comparable to the Euler case. Care must be taken with the data resulting from simulations with the RANS mean flow as no point of comparison like the compact solution is available and the CAA mesh is poorly discretised in the boundary layers. It is also less consistent than the Euler mean flow with the CAA code, which solves the Euler equation. Nonetheless, RANS flow is classically used with sAbrinA\_v0 and it has given accurate results in previous studies [Cader et al., 2018, Clair et al., 2013, Reboul et al., 2017], notably to simulate turbulence-aerofoil noise or rotor-stator interaction noise. Further investigations and validation would allow to be confident in the transfer functions obtained with RANS flow and to better understand the differences with the Euler case.

## 5.4 Comparison of analytical and numerical transfer functions

In this section, the noise levels computed in the 2D stator using CHEOPS-Stator are compared to those obtained through CAA simulations, which are described in the previous section and act as a reference case. Cumpsty and Marble's compact solution is also used to understand the differences between CAA and CHEOPS-Stator better. The objective is to determine whether the model is physically accurate, and in doing so to investigate its assumptions, which are stronger than those made by the CAA code.

The same Euler and RANS mean flows are used for the numerical and analytical approaches, limiting the possibility of error. As in previous sections, entropic forcing from upstream, acoustic excitation from the inlet and acoustic forcing from downstream are considered. CHEOPS-Stator is run up to 1,000 Hz, like CAA, but low computational costs, which are independent of frequency, allow the transfer functions to be computed at a much larger number of frequencies with CHEOPS-Stator and up to the compact limit at 0 Hz. The frequency step is set to 10 Hz to fully capture transfer function dependence on frequency.

Let's first compare the entropy waves obtained with CHEOPS-Stator and with CAA, the acceleration of which is the source of entropy noise. Recall it is computed by CHEOPS-Stator from the mean velocity prior to the resolution of its equations, as described in section 4.2. Figure 5.18 represents normalised entropy fluctuations in the stator at 1,000 Hz, computed with both Euler and RANS mean flows and using CAA and CHEOPS-Stator. It shows the entropy waves computed numerically and with the 2D model are in agreement.

Transfer functions resulting from the entropy-forced case and from acoustic excitation from upstream and downstream are presented in Figs. 5.19-5.21. They illustrate the noise levels computed with both Euler and RANS mean flows using CAA, CHEOPS-Stator and

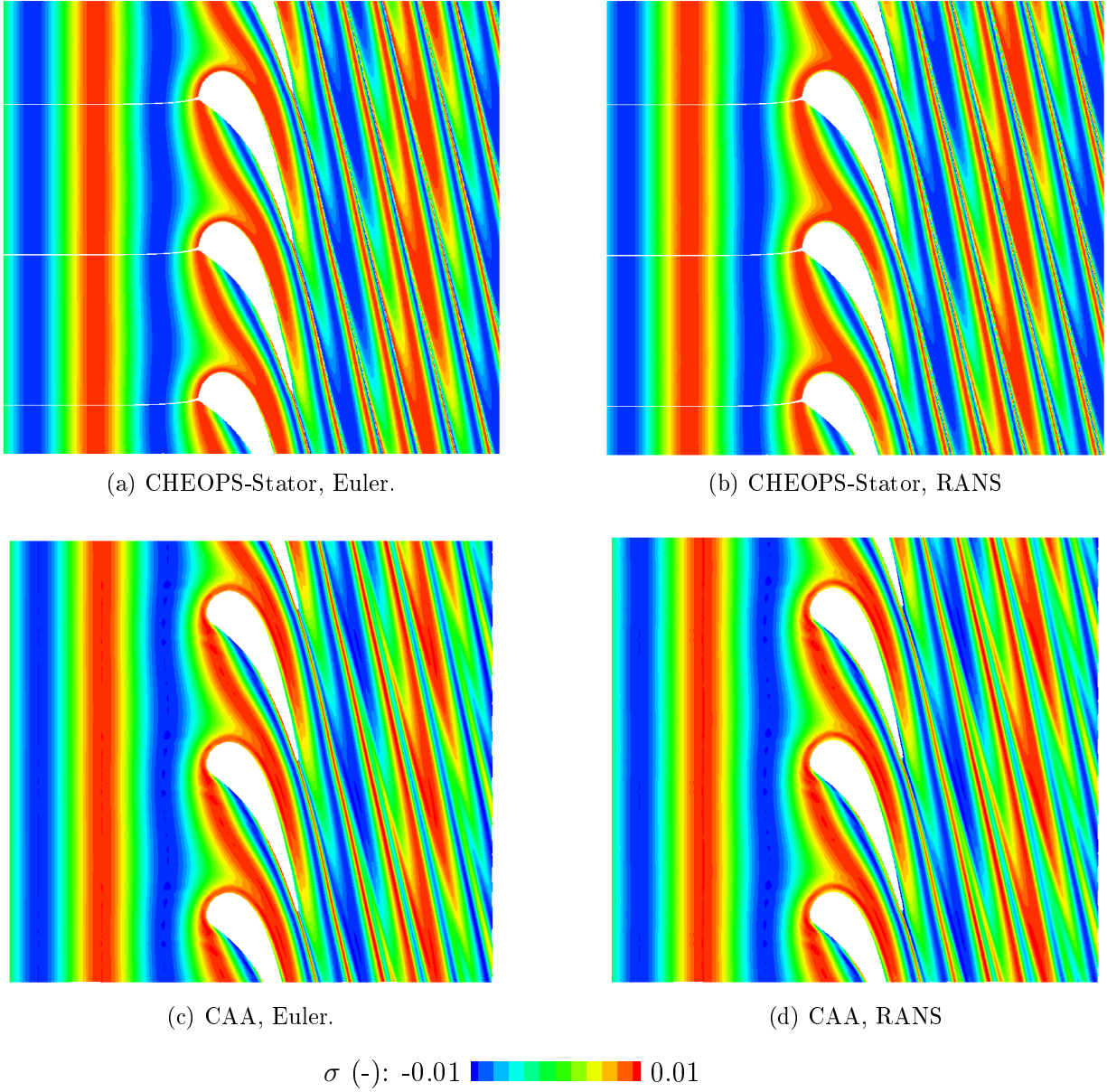


Figure 5.18: Normalised entropy fluctuations computed at 1,000 Hz using both CHEOPS-Stator and CAA, and with Euler and RANS mean flows.

two compact solutions governed by different assumptions. Focusing on the transfer functions obtained with the Euler mean flow and represented by full lines, one can observe the amplitudes obtained with CAA and CHEOPS-Stator differ significantly for the three forcing types. In the entropic case, phases obtained with the two methods seem to be in agreement, but their rapid evolution with frequency makes their comparison difficult. With acoustic excitation, there are errors in the phases of the waves which propagate towards the boundary from which the flow is excited. While these errors are small for  $[P_1^-/P_1^+]$  forcing, they seem significant in the case of  $[P_2^+/P_2^-]$ . Both methods are based on the Euler equations

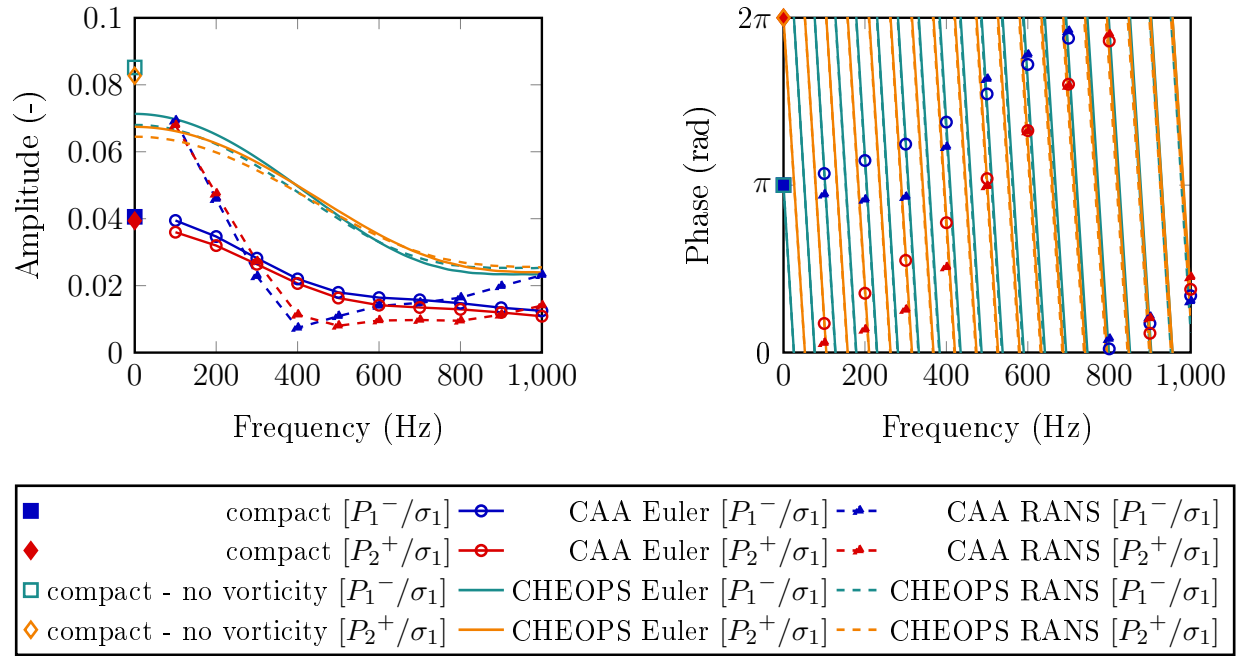


Figure 5.19: Amplitude and phase of the transfer functions resulting from entropic forcing  $[P_1^-/\sigma_1]$  and  $[P_2^+/\sigma_1]$ , computed using Cumpsty and Marble's compact solution [1977], and CHEOPS-Stator and CAA with Euler and RANS mean flow fields.

but the 2D model makes stronger assumptions by neglecting vorticity and assuming acoustic fluctuations are one-dimensional everywhere, including in the blade passage. Analysis of the CAA simulations allowed to establish vorticity is in fact present and that pressure fluctuations are not 1D in the region of the stator. The differences between the transfer functions obtained with CHEOPS-Stator and CAA indicate the model's two additional assumptions are not valid in this case, as they were for the nozzle. It therefore seems vorticity and/or the azimuthal variations of the acoustic waves in the blade passage have a significant impact on noise levels in 2D stator configurations.

Cumpsty and Marble's compact model [1977] is used to isolate the effect of CHEOPS-Stator's two main assumptions. The compact solution is in good accordance with CAA as shown in section 5.3 and in Figs. 5.19-5.21. The latter also show the transfer functions resulting from a version of the compact model which was modified to neglect vorticity, as described in section 4.3.1. The differences in transfer functions between the two compact solutions highlight the effect of vorticity, while those between the modified compact model and CHEOPS-Stator isolate the effect of the one-dimensional acoustic assumption, as both these models neglect vorticity. The two compact solutions result in very different amplitudes for the three forcing types, indicating vorticity cannot be neglected by the models. In the case of  $[P_2^+/P_2^-]$  in Fig. 5.21, neglecting vorticity even modifies the phases obtained with the modified compact model and CHEOPS-Stator. With acoustic excitations, the modified compact model and the 2D model result in transfer functions which are very close in Figs. 5.20 and 5.21, as discussed in section 4.3.2. This indicates the azimuthal variation of acoustic fluctuations in



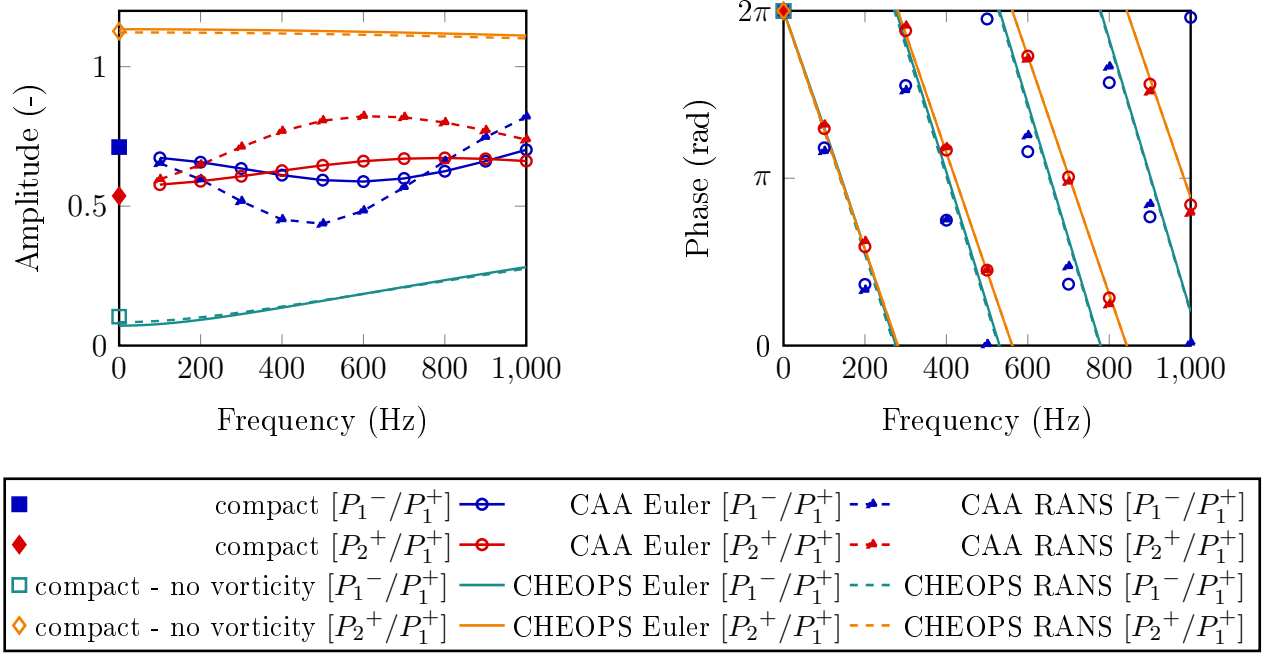


Figure 5.20: Amplitude and phase of the transfer functions resulting from upstream acoustic forcing  $[P_1^-/P_1^+]$  and  $[P_2^+/P_1^+]$ , computed using Cumpsty and Marble's compact solution [1977], and CHEOPS-Stator and CAA with Euler and RANS mean flow fields.

the blade passage has little impact in these cases. On the other hand, Fig. 5.19 suggests they do have an effect on entropy noise. In this case, the error due to the 1D acoustics assumption partly compensates the negligible vorticity error. The difference in amplitudes between the modified compact solution and CHEOPS-Stator is around 30% of the error between the two compact solutions, which indicates that at low frequency, neglecting vorticity is responsible for a larger error than the assumption acoustic waves are independent of the azimuthal direction in the blade passage.

Figures 5.19-5.21 also show the transfer functions resulting from computations with the RANS mean flow. They are very close to those obtained with the Euler flow using CHEOPS-Stator, while significant differences in the evolution of their amplitude with frequency are found using CAA, as discussed in section 5.3. This indicates the different behaviour with RANS flow is due to either the azimuthal variation of acoustic fluctuations or to the presence of vorticity. The latter is most likely to have the most impact.

## 5.5 Conclusions

Entropy noise and its scattering is studied in two-dimensional stator flow in this chapter, considering both Euler and RANS mean flow fields. The use of a CAA code based on the Euler equations allows to make simplifying assumptions. Noise levels generated by entropy, upstream acoustic and downstream acoustic excitations are simulated and presented in the

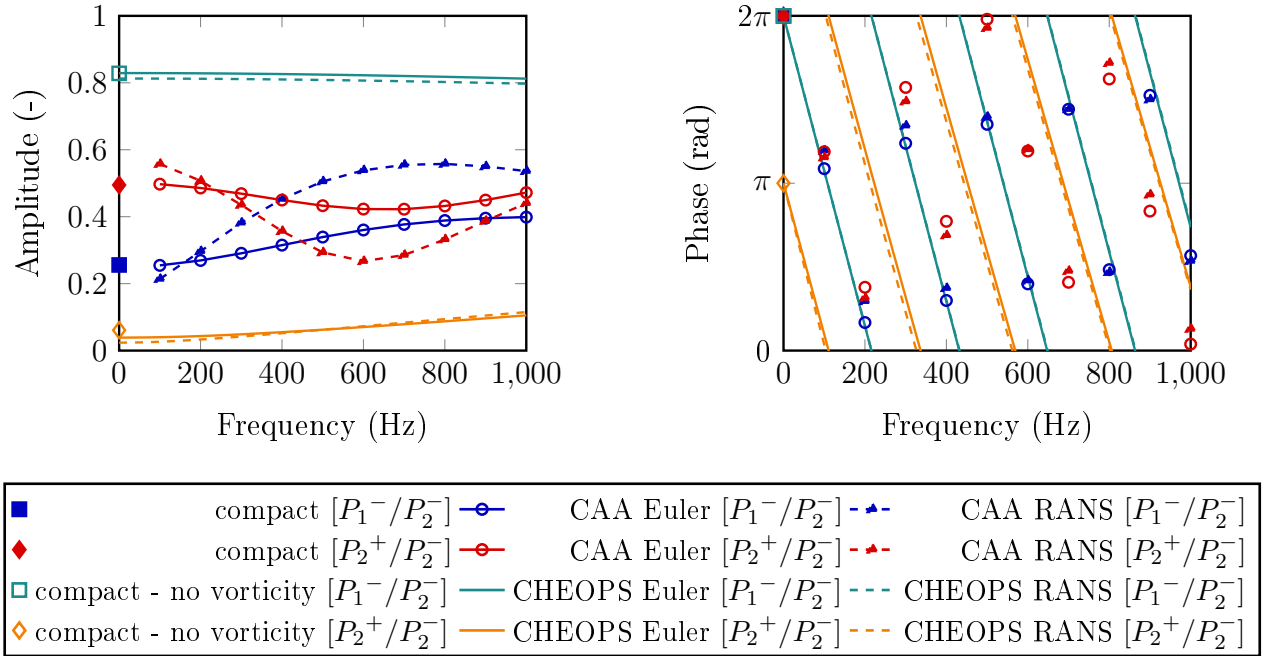


Figure 5.21: Amplitude and phase of the transfer functions resulting from downstream acoustic forcing  $[P_1^-/P_2^-]$  and  $[P_2^+/P_2^-]$ , computed using Cumpsty and Marble’s compact solution [1977], and CHEOPS-Stator and CAA with Euler and RANS mean flow fields.

form of transfer functions. These simulations can be used as a reference case for the two-dimensional model CHEOPS-Stator presented in chapter 4, in the same way as for nozzle flow in chapter 3. Significant differences are found between noise levels resulting from Euler and RANS mean flows for both entropic and acoustic forcing types. The presence of a thick boundary layer at the trailing edge could partly explain this, but further investigations are needed both to validate the noise levels obtained with a RANS flow, and to fully understand the effect of the boundary layer and the wake on the entropy noise source and the scattering of resulting acoustic waves.

These CAA simulations are used as a reference case in comparison to the noise levels estimated with CHEOPS-Stator. The differences in their transfer functions indicate vorticity and the azimuthal variations of acoustic fluctuations play a significant role in the generation of entropy noise and its scattering, and that they cannot be neglected by the model. A version of Cumpsty and Marble’s compact solution [1977] in which vorticity is omitted allows to isolate the effect of each of these assumptions in the compact limit, and it seems vorticity is responsible for the largest part of the error in noise amplitude.

After having clarified the impact of vorticity and the azimuthal variation of acoustic waves in the stator blade passage in two-dimensions, a three-dimensional geometry is considered using ZDES in the next chapter, in order to investigate the impact of three-dimensionality and viscous effects on entropy noise and its scattering.



# Chapter 6

## Investigation of entropy noise in 3D stator flow

*This chapter aims at investigating entropy noise and its scattering through a three-dimensional isolated stator using ZDES. Section 6.1 presents the set-up of the simulations. Next, their aerodynamics are characterised in section 6.2 to verify the coherence of the flow and to evaluate its three-dimensionality and turbulent behaviour. Finally, the aeroacoustics of the flow are presented in section 6.3. The correct filtering of hydrodynamics, the presence of spurious numerical reflections and the signal-to-noise ratio are verified, before discussing the noise levels resulting from an entropy-forced case and simulations excited acoustically from upstream and downstream.*

### Contents

---

<b>6.1</b>	<b>ZDES simulation set-up . . . . .</b>	<b>106</b>
6.1.1	Choice of geometry and mesh construction . . . . .	106
6.1.2	Choice of numerical parameters . . . . .	107
6.1.3	Simulation of the flow . . . . .	109
<b>6.2</b>	<b>Characterisation of aerodynamics . . . . .</b>	<b>112</b>
6.2.1	Characterisation of the baseline flow . . . . .	112
6.2.2	Comparison of the mean flows obtained with different forcing types . . . . .	115
<b>6.3</b>	<b>Investigation of aeroacoustics . . . . .</b>	<b>117</b>
6.3.1	Verification of hydrodynamic filtering . . . . .	117
6.3.2	Assessment of non-reflective post-processing . . . . .	120
6.3.3	Assessment of the signal-to-noise ratio . . . . .	124
6.3.4	Investigation of noise levels . . . . .	125
<b>6.4</b>	<b>Conclusions . . . . .</b>	<b>131</b>

---

## 6.1 ZDES simulation set-up

This section describes the set-up of the ZDES simulations used to compute entropy noise and the scattering of acoustics through a three-dimensional stator channel. The ZDES formulation, detailed in chapter 2, is chosen for its reduced cost compared to LES and because it is well suited to the flow dynamics of this case. The chosen geometry and the characteristics of the mesh are presented in § 6.1.1, an outline of the numerical parameters follows in § 6.1.2, and § 6.1.3 describes the simulations.

### 6.1.1 Choice of geometry and mesh construction

The stator geometry used in the European-FP7 project RECORD [Bake et al., 2016, Knobloch et al., 2016, 2017] is chosen, as for the 2D case in chapter 5. This time the full 3D blade is used and the domain is made of one blade passage as illustrated in Fig. 6.1. Recall the axial chord at 50% blade height is 30.6 mm and the inter-blade spacing is 49.78 mm. The full stator row is made of 22 blades of 50 mm in height, with minimal and maximal radii of 150 mm and 200 mm respectively. Ducts of length 105 mm and 450 mm are appended upstream and downstream of the stator respectively for acoustic post-processing. It is shorter upstream because of computational cost restraints. In the case of entropic forcing, the mesh must be sufficiently refined for accurate convection of entropy perturbations up to the blade, where they are accelerated and entropy noise is generated, whereas only propagation of the resulting acoustic waves is necessary downstream. In addition, the length of the upstream duct is less critical than downstream because acoustic signals are less polluted by the flow, which is uniform with little turbulence and no large scale vortices. This also explains the choice of splitting the domain into two zones shown in Fig. 6.1. Their interface is a little over an axial chord upstream of the blade. Having two zones allows the use of numerical parameters best suited to the flow in each of them. Finally, a short upstream duct reduces distortion of the entropy wave.

The computational domain is discretised into an unstructured mesh using Centaur. It is periodic in the azimuthal direction to suit the boundary conditions set in § 6.1.2. Prisms are used to mesh the domain walls. In the region of the blade, fifty prism layers are used

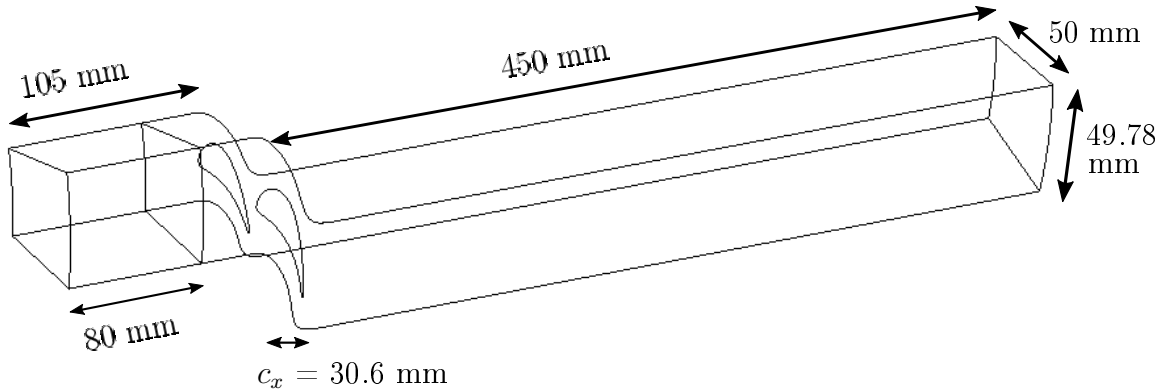


Figure 6.1: Geometry used to simulate the flow in a 3D isolated stator segment.

along the blade wall, the hub and the shroud. In order to obtain values of  $x^+$  and  $z^+$  smaller than 200, their size along the surface is set to 0.5 mm except on the pressure side of the blade near the trailing edge where it is 0.4 mm. The prism initial thickness and stretching from one layer to the next are adjusted between 0.002 and 0.005 mm and between 1.065 and 1.09 respectively to ensure the value of  $y^+$  is lower than one everywhere, while minimising the number of cells. Tetrahedra are used to mesh the rest of the domain, away from the walls. Their size is set to 0.3 mm in the region of the blade and up to about one axial chord downstream, where vortices develop. It is gradually increased in the ducts to reach 1 mm upstream and 6 mm downstream. Thus, the mesh is significantly coarsened in the second half of the downstream duct, which will filter out some hydrodynamic modes and help acoustic post-processing. Additionally, the mesh is refined in the wake region. The size of tetrahedra is reduced to 0.13 mm just downstream of the trailing edge to obtain approximately 20 points across the wake. The final grid contains 147 million nodes, including 2.0 million prisms, 4,000 pyramids and 2.3 million tetrahedra in the upstream zone and 66.6 million prisms, 63,000 pyramids and 76.5 million tetrahedra in the rest of the domain.

### 6.1.2 Choice of numerical parameters

The code used for the ZDES simulations is CEDRE, which is described in section 2.1. The URANS equations are solved in the upstream duct, where there are no large-scale vortices. The Spalart-Almaras turbulence model is chosen because it is a cost-effective solution. The ratio  $\tilde{\nu}/\nu$  is set to 5 at the inlet of the domain and for the initial conditions of the simulations. The ZDES mode II is best suited for the rest of the domain in association with the subgrid scale  $\Delta\omega$  described in section 2.1.1.6. Second-order discretisation is achieved in space and in time, for which an implicit Runge-Kutta scheme is used with 10 sub-iterations. The time step is set to  $3.5 \times 10^{-7}$  s. The objective was initially to reach  $\text{CFL} < 1$  in the region of acoustic sources around the blade, but a compromise had to be made for reasonable computational cost as this is also where the smallest grid sizes are required to accurately simulate the flow. The chosen time step leads to a CFL number which reaches around 5 near the walls, 3 in the refined region of the wake and a maximum of 2 in the rest of the flow, where acceleration affects entropy noise the most. The CFL number is larger than 1 over an axial distance of only about one third of the wavelength of the transmitted acoustic wave at 1000 Hz, which leads to negligible error at the frequencies under consideration. This was verified with a test-case in a duct.

Like in chapter 5, the boundary conditions are chosen according to the subsonic operation point of the RECORD European-FP7 project [Bake et al., 2016, Knobloch et al., 2016, 2017]. The axial velocity is set to 42.99 m/s and temperature to 322 K upstream, while the static pressure is set to 109,216 Pa downstream. Waves are injected into the domain by modifying these boundary conditions, as detailed in section 2.1.2. Like for the nozzle and 2D stator cases studied in previous chapters, entropic, upstream acoustic and downstream acoustic perturbations are injected into the domain in three different simulations, in order to compute entropy noise generation, as well as the scattering of acoustic waves. A baseline case without forcing is also simulated. Frequencies from 100 to 1,000 Hz are considered, with a step of 100 Hz. A multi-harmonic wave regrouping these frequencies is injected with the same amplitude associated to each frequency. Phases are optimised to minimise the peak

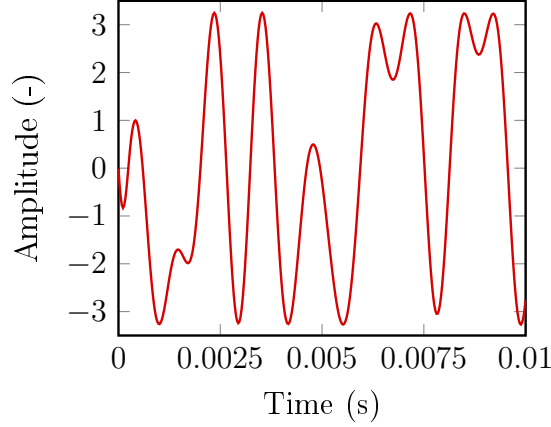


Figure 6.2: Optimised multi-harmonic wave normalised by the amplitude of the harmonics.

amplitude of the multi-harmonic wave using a method based on the Crest Factor minimisation proposed by Guillaume et al. [1991]. This results in the wave presented in Fig. 6.2, which shows the peak amplitude is just over three times the amplitude associated to each of the harmonics. Non-linear effects have been found to be negligible for perturbations up to 10% of the mean variables for both studies of nozzle and turbine applications [Bodony, 2009, Huet and Giauque, 2013a, Mishra and Bodony, 2013]. In order to optimise the signal-to-noise ratio, with a safety margin to avoid non-linear behaviour, the amplitude of the harmonics is set to 2.15% of  $T_0$  for the entropy-forced simulation, leading to a maximum fluctuation amplitude of 7% of  $T_0$  for the multi harmonic wave. With acoustic excitation, optimisation of the signal-to-noise ratio is less critical, as the injected perturbations generate more noise. The amplitudes of the harmonic waves are set to 2% of  $p_0$  for acoustic forcing from the inlet and to 1% of  $p_0$  for downstream forcing. The non-reflective conditions described in section 2.1.3 are also applied at the boundaries. For the baseline case and the first jobs of the transient part of the simulations, boundary conditions based on total variables were used as given by the RECORD project, but the non-reflective boundary conditions affected the injected wave. It is better defined and unaffected by the non-reflective conditions when static variables are used directly, so that the Dirichlet type boundary conditions described above were used for the rest of the simulations.

Computational cost and memory considerations led to a useful signal length which is not a multiple of the time period of the wave injected into the simulations. In the frequency domain, this translates in  $\Delta f \approx 49.9$  Hz instead of 50 Hz for a signal made of two time periods. The results therefore do not exactly correspond to the frequencies at which the simulations are excited, and which are multiples of 100 Hz. The error is of 0.187%, leading to a maximum of 1.87 Hz at 1000 Hz. A test-case was used to reproduce this problem in a duct, and the error in the estimation of the harmonics through Fourier transform of the computed time signal was found to be negligible compared to their theoretical values. Another consequence of the difference in signal length is that the time-average of the variables of excited simulations cannot be achieved over an exact multiple of the time period, with a 2.2% error.

### 6.1.3 Simulation of the flow

The simulations are run on two different machines, one at ONERA and the other at GENCI, the national high-performance computing centre. 1736 processors are used on the first and 2016 on the second. The costs of the different simulations are gathered in Tab. 6.1, as well as the associated physical times. The total cost is 1.25 million CPU hrs, of which 750,000 were computed at ONERA and 500,000 with the GENCI machine.

	Transient	Baseline	$\sigma_1$		$P_1^+$		$P_2^-$	
Physical time (s)	0.091	0.027	transient	useful	transient	useful	transient	useful
			0.017	0.02	0.009	0.02	0.0057	0.02
CPU cost (CPU hr)	340,000	190,000	300,000		220,000		200,000	

Table 6.1: Physical time and cost of the ZDES simulations of the transient flow and the baseline, entropy forced ( $\sigma_1$ ) and acoustically excited ( $P_1^+$ ,  $P_2^-$ ) cases.

The transient part of the simulations was initialised with a RANS computation. The ZDES formulation was then used with a first order implicit time scheme before changing to second order implicit Runge-Kutta, and finally switching from the more robust  $\Delta_{vol}$  subgrid scale to the more accurate  $\Delta\omega$  formulation. Once converged, this simulation was continued without forcing to obtain a baseline case, as well as used to initialise the excited simulations. Injection of the entropic or acoustic waves leads to a second transient phase before the simulation of the useful signal. Two time periods of useful signal are computed in all four cases. Convergence is verified for all simulations. This is illustrated for the baseline computation in Fig. 6.3, which represents the normalised mass flow rate difference and the pressure signal measured at a point close to the pressure side of the stator blade. For clarity, the transient part is shown only from the switch to the second order time scheme. The good behaviour of ZDES in near wall regions of the flow is verified using  $f_d$ . Its value drives the switch

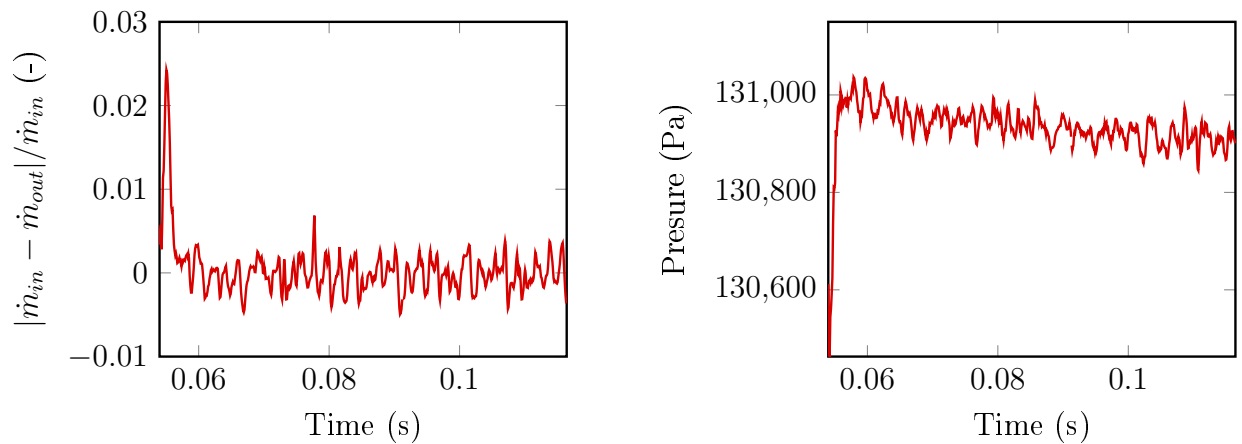


Figure 6.3: Normalised mass flow rate error (left) and pressure signal (right) close to the pressure side of the blade. The signals are computed for the baseline case towards the end of the transient simulations, after the switch to a second order time scheme.



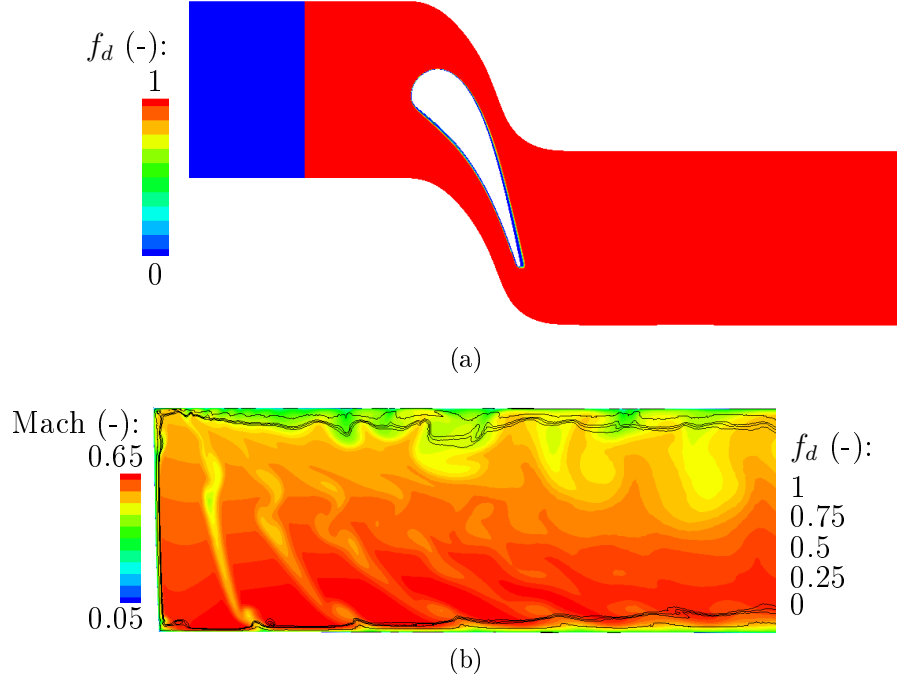


Figure 6.4: Parameter  $f_d$  simulated in the baseline case (a) at mid-span and (b) represented as isolines on a Mach number contour in an azimuthally constant plane downstream of the blade.

between ZDES mode II and mode 0, which amounts to URANS. Figure 6.4a represents this parameter in the mid-span plane. It clearly delimits the URANS zone upstream from the ZDES region, in which the URANS equations are only used close to the blade wall where  $f_d$  is small, as expected. Figure 6.4b represents  $f_d$  as isolines on a Mach number colour map in an azimuthally constant plane downstream of the stator. It indicates that the URANS region correctly follows boundary layers and low energy vortices as they develop along the hub and the shroud. The values of  $x^+$ ,  $y^+$  and  $z^+$  are also verified.  $y^+$  is under 1 in most of the domain as expected, and it reaches 1.6 very locally. Target values are also reached for  $x^+$  and  $z^+$ , as they are smaller than 200 on the blade surface and even below 100 along the hub and shroud in the region of the blade.

The fluctuations and mean variables resulting from the ZDES simulations are post-processed in the same way as data from CAA in chapters 3 and 5. Velocity and pressure fluctuations are decomposed into upstream and downstream propagating waves, using both the Riemann invariants and DMM, while hydrodynamic modes are filtered out through area averaging and characteristic filtering. Non-reflective post-processing is then achieved to reconstruct the transfer functions for the different excitation types. Seven planes are used upstream, where the duct is shorter and the flow is more uniform. Downstream, fluctuations are averaged over 17 planes in the second half of the duct where the mesh is coarsened, which participates in the filtering of hydrodynamic modes.

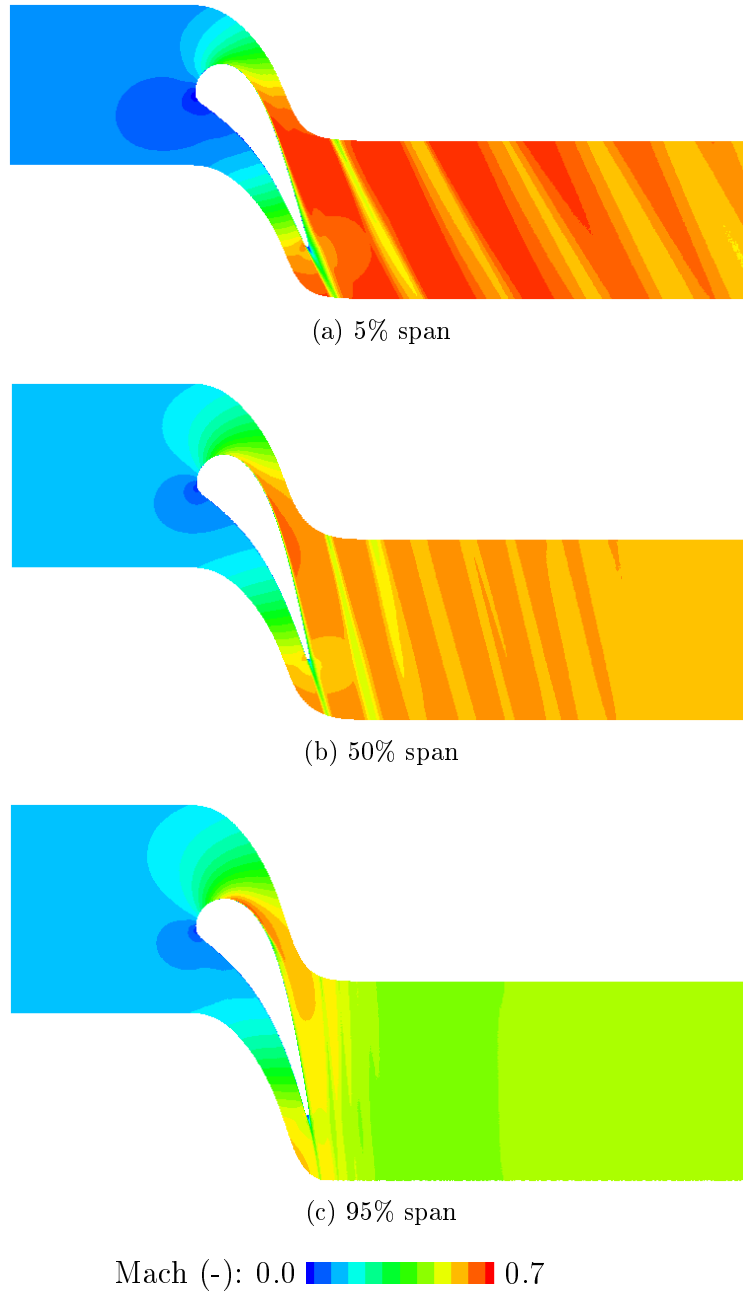


Figure 6.5: Blade-to-blade contours of the mean Mach number computed at 5%, 50% and 95% of the blade's span with the baseline simulation.

## 6.2 Characterisation of aerodynamics

Before discussing the stator's acoustic response in the next section, the aerodynamics of the flow are detailed here. The baseline flow is presented in section 6.2.1, while mean flow fields resulting from simulations with different forcing types are compared in section 6.2.2.

### 6.2.1 Characterisation of the baseline flow

The mass flow rate through the stator channel is  $0.16 \text{ kg.s}^{-1}$ , corresponding to  $3.5 \text{ kg.s}^{-1}$  through the full stator row. Figure 6.5 represents the Mach number in blade-to-blade planes at 5%, 50% and 95% of the blade's height. At mid-span, Fig. 6.5b shows that the acceleration of the flow around the blade is globally comparable to the 2D case discussed in chapter 5 (Fig. 5.2). The Mach number is larger near the hub, in Fig. 6.5a, because of radial equilibrium. This leads to a reduction of the flow angle, which is visible at the wake. The flow separates close to the trailing edge on account of the corner vortex which develops along the suction side of the blade. This also affects the wake which is thicker than at mid-span. Close to the shroud, radial equilibrium has the opposite affect and the Mach number is smaller than at mid-span. Separation occurs around a fifth of the chord, and the wake is not visible for long on Fig. 6.5c, taken over by the trace of large vortical structures. Globally, low-energy fluid fills the near shroud region.

In order to characterise the vortices generated through the stator, static pressure, Mach number and entropy fields are represented in Fig. 6.6, in an axial plane 32% of the axial chord downstream of the trailing edge. They display similar variations to those obtained experimentally at Politecnico di Milano during the RECORD European-FP7 project [Knobloch et al., 2017], although a full turbine stage was considered in this study, with both stator and rotor rows. The evolution of static pressure is significant along the span of the stator, with low pressure at the hub and larger values at the shroud, because of radial equilibrium. The static pressure also varies in the circumferential direction, due to the potential field which forms between the pressure and suction sides of the blade and which is convected downstream. For the same reasons, the Mach number also varies along the radial and circumferential directions. The wake is clearly visible on the contour of entropy, which highlights high loss regions. It also shows vortices induced by secondary flow. The loss regions towards the shroud are displaced mid-span under the influence of radial equilibrium and the blade's three-dimensional geometry. This is also visible on Fig. B.9b of the Mach number, which is reduced in loss cores. The passage vortex, marked I in Fig. 6.6, crosses from the pressure to the suction side in the blade passage, and grows by dragging low energy fluid along the way, making it the largest secondary vortex. Its associated trailing-edge shed vortex is noted II. The strongest vortex on the hub side is the corner vortex III, at the end of the wake, which remains on the suction side as it grows along the blade. There are losses in a thicker region along the shroud than the hub, where the boundary layer remains stuck to the wall due to high Mach number and low pressure. There, the fluid is also swept across the blade passage from pressure to suction side where it accumulates, which is visible on Figs. B.9b and B.9c at IV. Figure 6.6 also gives the same fields in a plane 50% of the axial chord downstream of the trailing edge. The evolution of pressure and Mach number is less affected by the blade than at the more upstream position. Furthermore, the wake and secondary vortices have

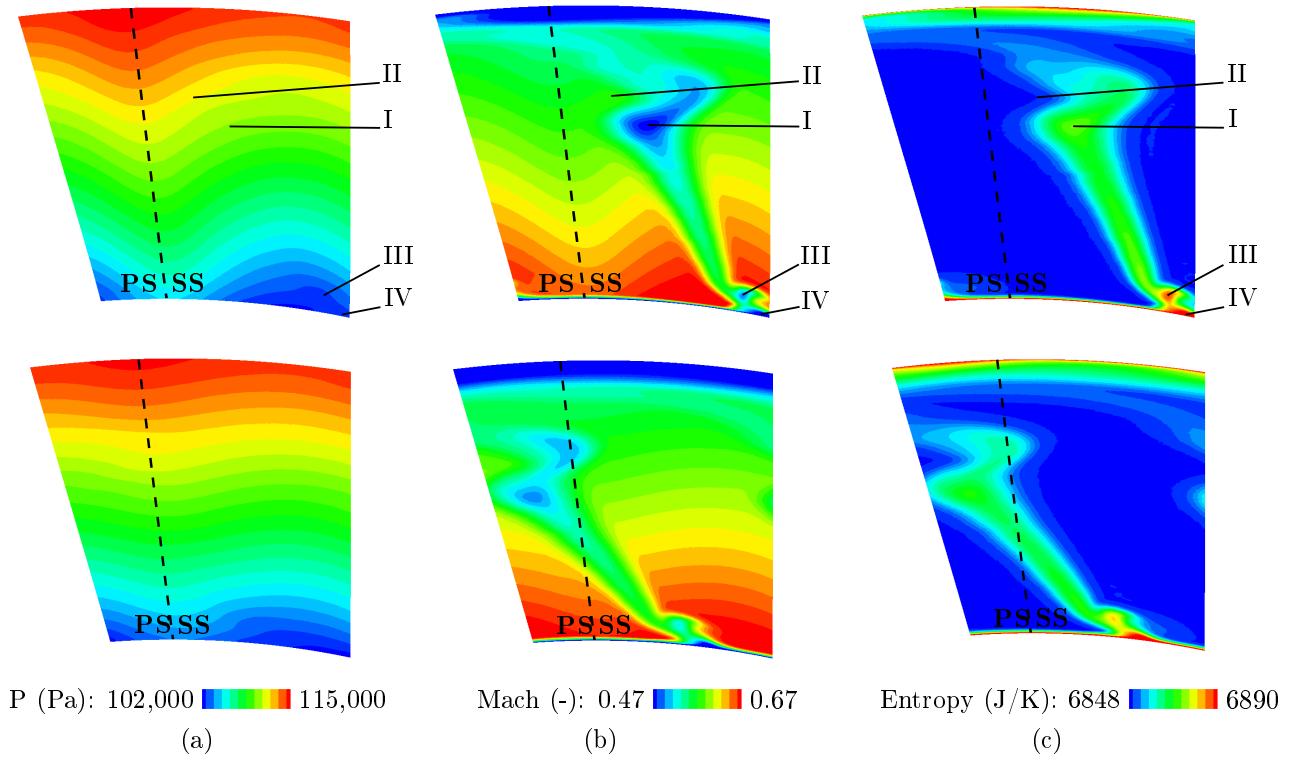


Figure 6.6: Axial contours of the mean Mach number, static pressure and entropy fields, computed with the baseline simulation 32% (top) and 50% (bottom) of the axial chord downstream of the stator's trailing edge.

somewhat dissipated. The wake has slanted, due to a larger velocity towards the hub than the shroud and the passage vortex has shifted further towards mid-span under the influence of the radial pressure gradient.

Next, the instantaneous flow is verified. Figure 6.7a represents the vorticity field in the mid-span plane, which clearly shows the wake and its dissipation as it is convected. However, one would expect small scale turbulence to develop in the wake rapidly after the trailing edge, which is a region treated as LES by the code as previously discussed using Fig. 6.4a. Figure 6.8, which represents the velocity spectrum at a point close to the wake, allows to verify the state of turbulence. As well as not decreasing with a  $-5/3$  slope, as expected for fully developed turbulence [Bailly and Comte-Bellot, 2003], the spectrum displays very low velocity fluctuation amplitudes. The eddy viscosity ratio  $\mu_t/\mu$  presented in Fig. 6.9 reaches approximately 100 in the wake, and the Reynolds based on the axial chord and the velocity in the wake, the values of which are 0.0306 m and 100 m/s respectively, is around 200,000. This makes the effective Reynolds number about 2,000 using  $\mu_t$ , which is quite low. A solution to reproduce small-scale turbulence in the simulation may be to use a different version of the Spalart-Allmaras turbulence model. The formulation used in this study is a variation of the standard model without the  $f_{t2}$  term [Aupoix and Spalart, 2003, Eca et al., 2007]. It is noted 'SA- $f_{v3}$ ' and it includes a  $f_{v3}$  function to prevent negative values of the source

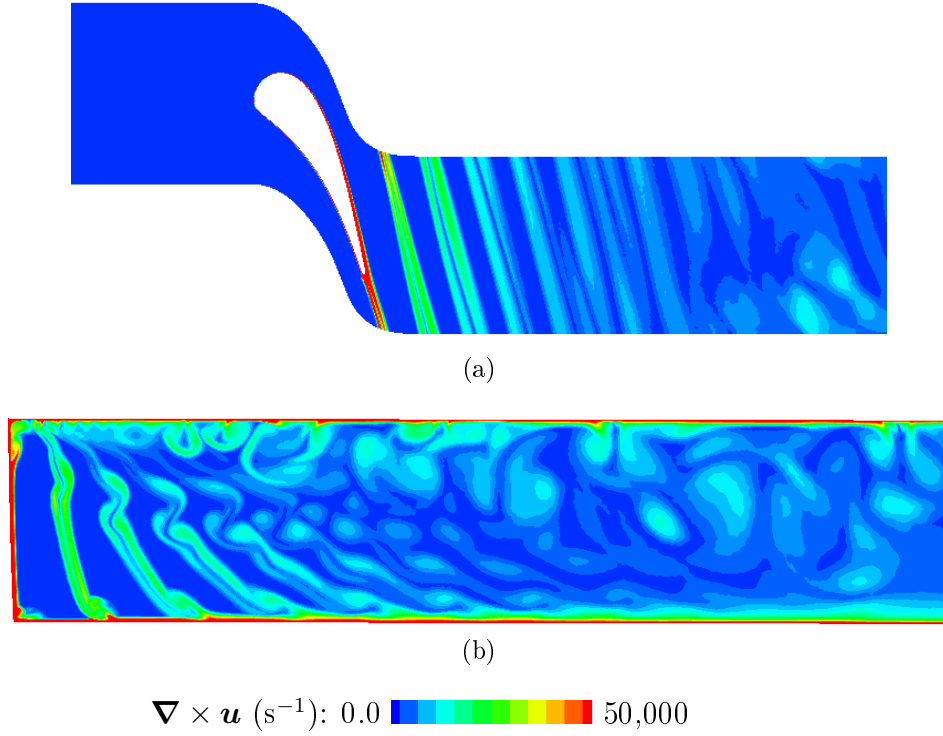


Figure 6.7: Vorticity in (a) the mid-span plane and (b) an azimuthally constant plane downstream of the stator in the baseline case.

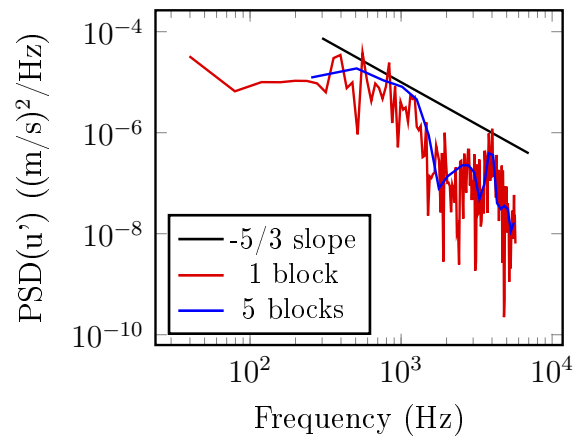


Figure 6.8: PSD of velocity near the wake of the stator. The Welch estimator is used with one and five blocks.

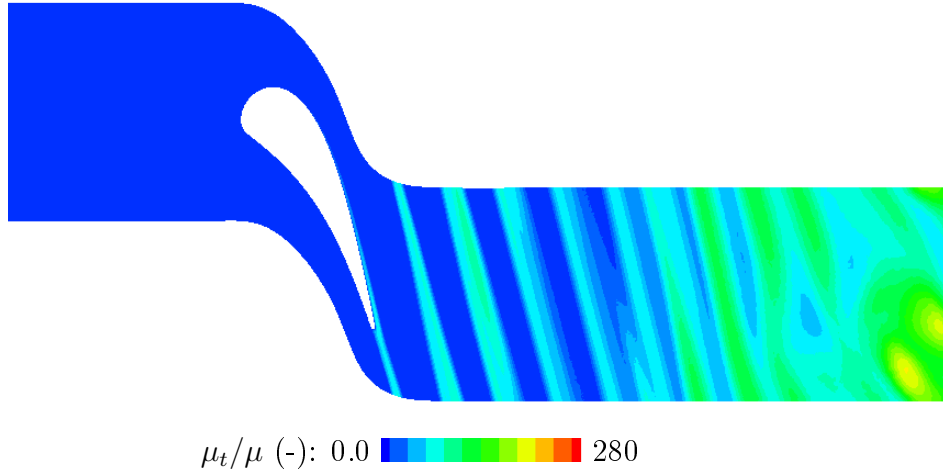


Figure 6.9: Eddy viscosity ratio  $\mu_t/\mu$  in the mid-span plane.

term [Rumsey et al., 2001]. Recent simulations at ONERA in a different context have led to similar behaviour as the present case, with virtually no turbulence. In addition, 'SA- $f_{v3}$ ' is known to display pseudo-transient behaviour [Spalart, 2000], which was verified by De La Puente Cerezo [2017] and Spagnolo [2016], who found the friction coefficient obtained with 'SA- $f_{v3}$ ' was low compared to the standard formulation (without  $f_{t2}$ ), at low-to-medium Reynolds number depending on the  $\tilde{\nu}_\infty/\nu_\infty$  ratio. It seems the standard Spalart-Allmaras model without  $f_{t2}$  would be recommended for future simulations, although the use of a lower  $\tilde{\nu}_\infty/\nu_\infty$  ratio could also be considered with the current model.

Despite the turbulence generation problem, the mean flow field appears to agree with the expected topology. Figure 6.7b represents vorticity in an azimuthally constant plane downstream of the blade. Large scale vortices develop along the hub and shroud. As previously mentioned using Fig. 6.4b, these near-wall vortices originate in the URANS zone. They are much larger at the shroud than at the hub because of radial equilibrium. As they develop, these vortices interact with the wake and participate in its dispersion and dissipation together with viscous effects, and the impact of radial equilibrium is also clearly visible. This highlights the three-dimensionality and viscosity of the flow. Their effect on entropy noise will be discussed in section 6.3 by comparison with CAA data, while the impact of turbulent mixing cannot be considered with the current ZDES simulations.

### 6.2.2 Comparison of the mean flows obtained with different forcing types

The radial profiles presented in Fig. 6.10 give an overview of the flow, which allows to easily compare the mean flows computed with the forced simulations to the baseline case. The pitchwise average of the mean static pressure, the Mach number, the flow angle and total pressure are plotted. They are computed in planes one axial chord upstream and downstream of the stator, as well as 32% of the axial chord away from the trailing edge, like in Fig. 6.6. Radial equilibrium clearly governs the evolution of both static pressure and Mach number

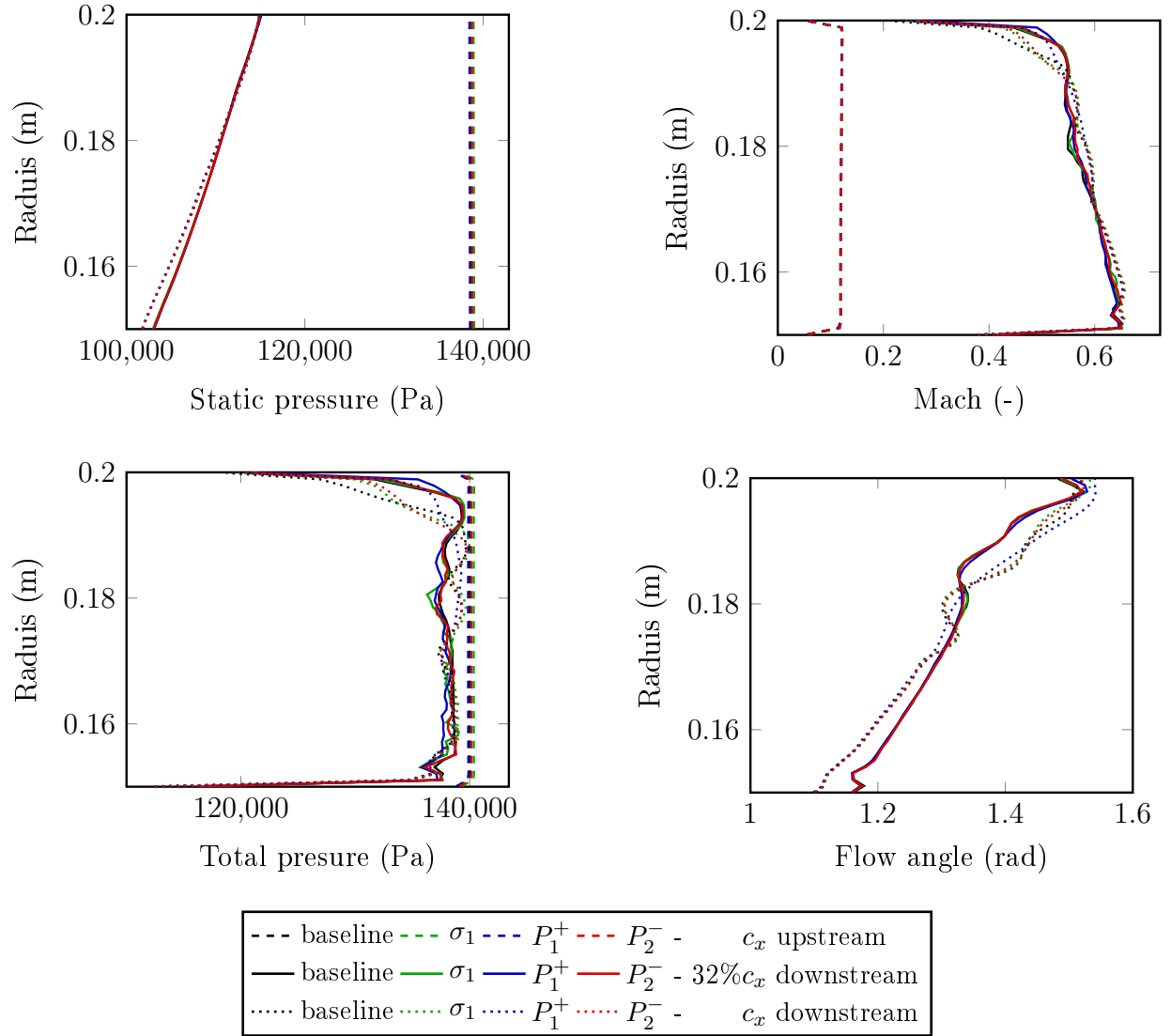


Figure 6.10: Radial profiles of pitchwise-averaged mean flow variables: flow angle, static pressure, Mach number and total pressure. They are computed one axial chord away from the stator blade upstream and downstream, from the baseline, entropy-forced and both upstream and downstream acoustically excited simulations.

for the four simulation types. The flow angle also evolves along the span, increasing as the Mach number is reduced. In addition, the flow angle and Mach number are affected by near-wall viscous effects and vortices. These vortices are also clearly visible with total pressure, since its reduction through the blade passage is due to losses. Close to the hub, where the Mach number is large, the flow is only affected by the wall along 2% of the span in the baseline case, without taking the corner vortex into account, while near the shroud the affected region reaches around 8% and 15% of the blade height 0.32 and one axial chord away from the trailing edge respectively. Secondary flows are also visible in the form of the

corner vortex at the hub and the passage vortex closer to mid-span, especially on the flow angle plot.

The mean flows computed with different forcing types are close overall, in particular upstream, but there are some differences downstream. Static pressure is almost identical for all forcing types. However, the total pressure graph shows excited flows result in more losses and less smooth profiles along the span. This also affects the Mach number, while differences in the flow angle for different forcing types only appear in the upper half of the blade, where fluid is less energetic. The Mach number and flow angle also suggest the passage vortex is more dissipated with acoustic forcing, but discrepancies are very small. There are larger differences towards the shroud one axial chord downstream of the stator. Vortices developing along the shroud appear smaller in forced flow, especially with acoustic excitation from upstream. This effect is also visible 0.32 axial chord downstream from the stator with the latter, unlike with the other two forcing types. The profiles also display smoother evolution with radius with acoustic excitation from upstream, indicating vortices have dissipated. Although the injected pressure fluctuations are well under the 10% limit which ensures linear acoustics, the variations of the aerodynamic field could be due to non-linearities of the flow. Recall the wave injected to force the simulation from upstream has an amplitude twice as large as for acoustic excitation from downstream. This could explain why the variations of the flow are more accentuated with upstream forcing. All-in-all, the differences in mean flow between the baseline and acoustically forced cases remain of low amplitude and localised. They are not likely to have a significant impact on the acoustics of the flow.

## 6.3 Investigation of aeroacoustics

### 6.3.1 Verification of hydrodynamic filtering

The effect of area averaging filtering can be assessed using Figure 6.11. It shows pressure and velocity fluctuations evaluated both after sectional averaging and at a point near the centre of the same plane, in the entropy-forced case. Signals computed both upstream and downstream of the stator are represented. Upstream, both pressure and velocity perturbations computed over the plane and at a point are very close. The velocity fluctuations are also evaluated from the pressure variations using the impedance relation  $u' = -p' / (\rho_0 c_0)$ , which results in only small differences compared to the signal directly computed. Downstream, both pressure and velocity fluctuations evaluated over a plane and at a point are quite different and display higher frequency small-scale disturbances. They are filtered out by averaging, in particular velocity perturbations. The values of  $u'$  computed from pressure fluctuations  $p'$  averaged over a section are also given. The result is much closer to the velocity fluctuations evaluated over the plane than at a point but some differences remain, indicating hydrodynamic perturbations persist, possibly in both  $p'$  and  $u'$ . Nonetheless, area averaging appears very effective in this case, indicating the majority of perturbations are small scale. In addition, these fluctuations decorrelate vorticity and facilitate its filtering.

The next filtering step of the post-processing described in section 6.1.3 is characteristic filtering over several axial positions. Recall that downstream, the planes are chosen in the



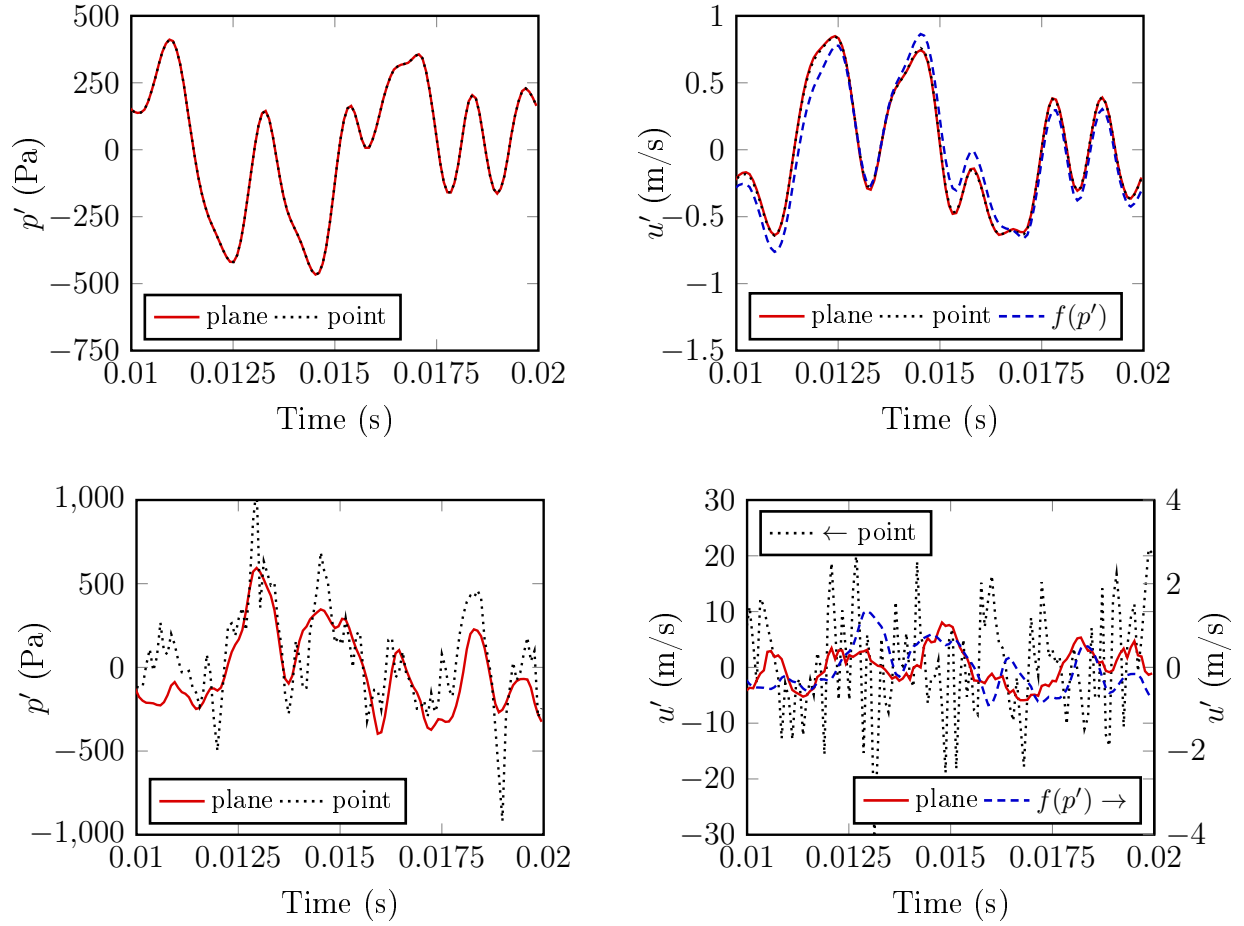


Figure 6.11: Pressure and velocity fluctuations computed both at a point of the upstream (top) and downstream (bottom) duct and averaged over the corresponding plane, and acoustic velocity fluctuations computed from the impedance relation for a plane progressive or regressive wave  $u' = \pm p' / (\rho_0 c_0)$ . Entropy-forced simulation.

second half of the downstream duct in which the mesh is coarsened, providing additional filtering. Figure 6.12 represents the normalised pressure fluctuations  $P^+$  and  $P^-$  computed in the frequency domain after wave separation into upstream and downstream propagating components using both the Riemann invariants and DMM, which are described in § 3.4.3. They are given for all the axial positions considered, both upstream and downstream. Upstream, the amplitudes of the waves  $P^+$  and  $P^-$  are equal over all the planes apart from small differences at 100 Hz with DMM. This shows that area averaging filtered out nearly all the hydrodynamic perturbations, which, additionally, were found to be small initially. On the other hand, there are significant differences between acoustic wave amplitudes computed in different planes downstream, as illustrated in Figs. 6.12c and 6.12d. This shows large scale perturbations remain after area averaging. The differences are more significant with DMM than using the Riemann invariants. This could be due to the fact only  $p'$  is involved in the DMM formulation, while both  $p'$  and  $u'$  appear in the Riemann invariants. Furthermore,

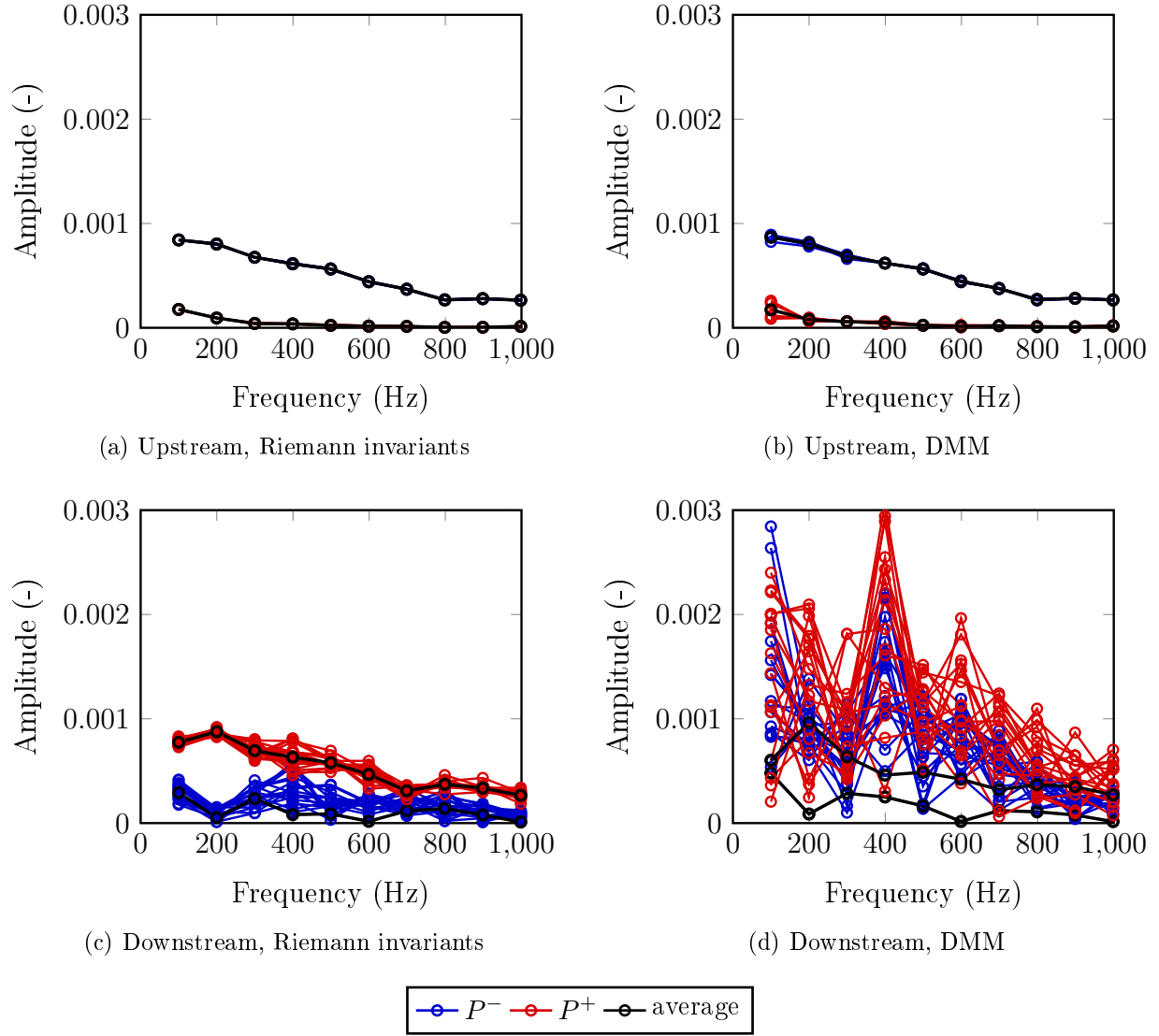


Figure 6.12: Normalised regressive and progressive waves  $P^-$  and  $P^+$  computed in the upstream and downstream ducts in the entropy-forced case, using both the Riemann invariants and the DMM method.

the derivative in the DMM equations could be sensitive to the hydrodynamic perturbations. In either case, characteristic filtering should cancel out all remaining uncorrelated perturbations, leaving acoustic fluctuations. The waves  $P^\pm$  obtained after characteristic filtering with the two wave separation methods are in good agreement, which indicates a sufficient number of axial planes have been used and gives confidence in the results.

### 6.3.2 Assessment of non-reflective post-processing

The non-reflective conditions detailed in § 2.1.3 are used both upstream and downstream in the ZDES simulations. They are effective in reducing spurious reflections but some persist. The objective of this section is to evaluate the effect of these remaining numerical reflections. To do so, reflection coefficients are presented in Fig. 6.13 for the entropy-forced case, as well as simulations with acoustic excitation but not on the side where waves are injected, rendering reflection coefficient unexploitable. Results obtained using both the Riemann invariants and DMM are considered.

With both excitation types and wave separation methods, the upstream reflection coefficient  $[P_1^+/P_1^-]$  is quite low. It is below 0.1 at most frequencies and reaches a maximum at 100 Hz, which corresponds to expectations since the boundary conditions behave like a low-pass filter as explained in section 2.1.3. The downstream reflection coefficient  $[P_2^-/P_2^+]$  is generally larger. In the case of acoustic excitation from upstream, it is equal to about 0.2 at most frequencies. With the Riemann invariants, the maximum is reached at 100 Hz around 0.3, like the upstream reflection coefficient, while using DMM the maximum of 0.45 is found at 200 Hz. The downstream reflection coefficient is larger in the entropic case at most frequencies, although it is lower than 0.1, close to the upstream coefficient, at 200 Hz, 600 Hz and 1,000 Hz. With the Riemann invariants,  $[P_2^-/P_2^+]$  reaches a maximum around 0.4 at 100 Hz, 700 Hz and 800 Hz. Like for the acoustic case, the maximal reflection coefficient is larger using DMM than with the Riemann invariant, since it reaches 0.8 at 100 Hz and nearly 0.55 at 400 Hz. From this it appears numerical reflection could be significant enough to impact the computed noise levels, in particular downstream.

In order to verify this, the transfer functions computed with and without the non-reflective

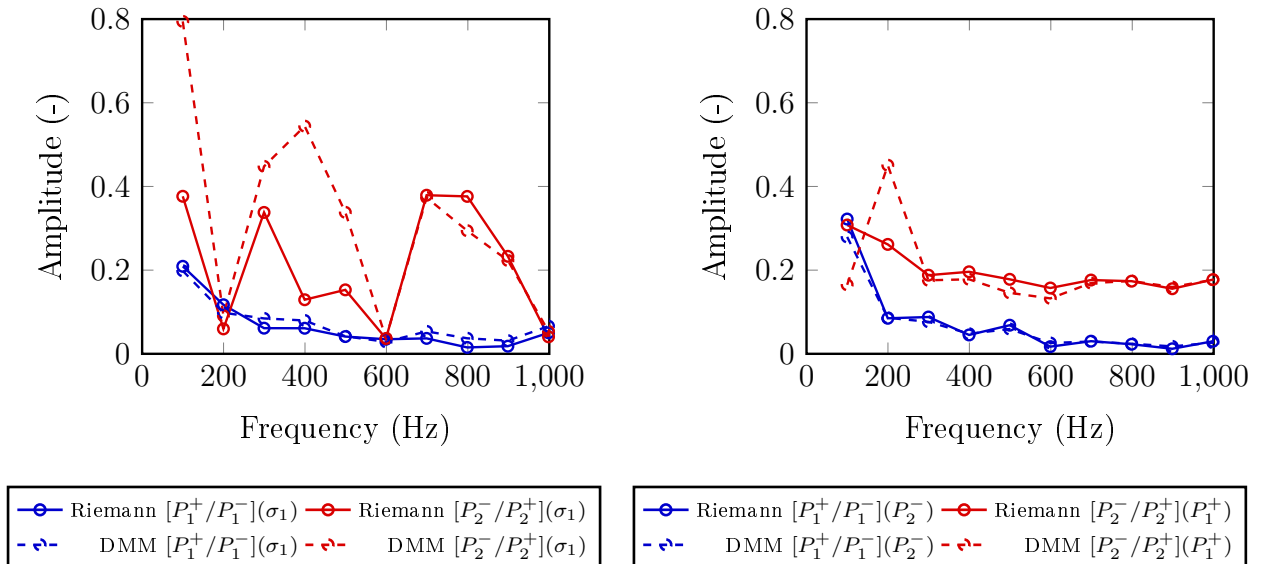


Figure 6.13: Reflection coefficients obtained for the entropy forced ZDES simulation (left) and the two computations with acoustic perturbations (right), with both the Riemann invariants and DMM for post-processing. Excitation types are given in brackets.

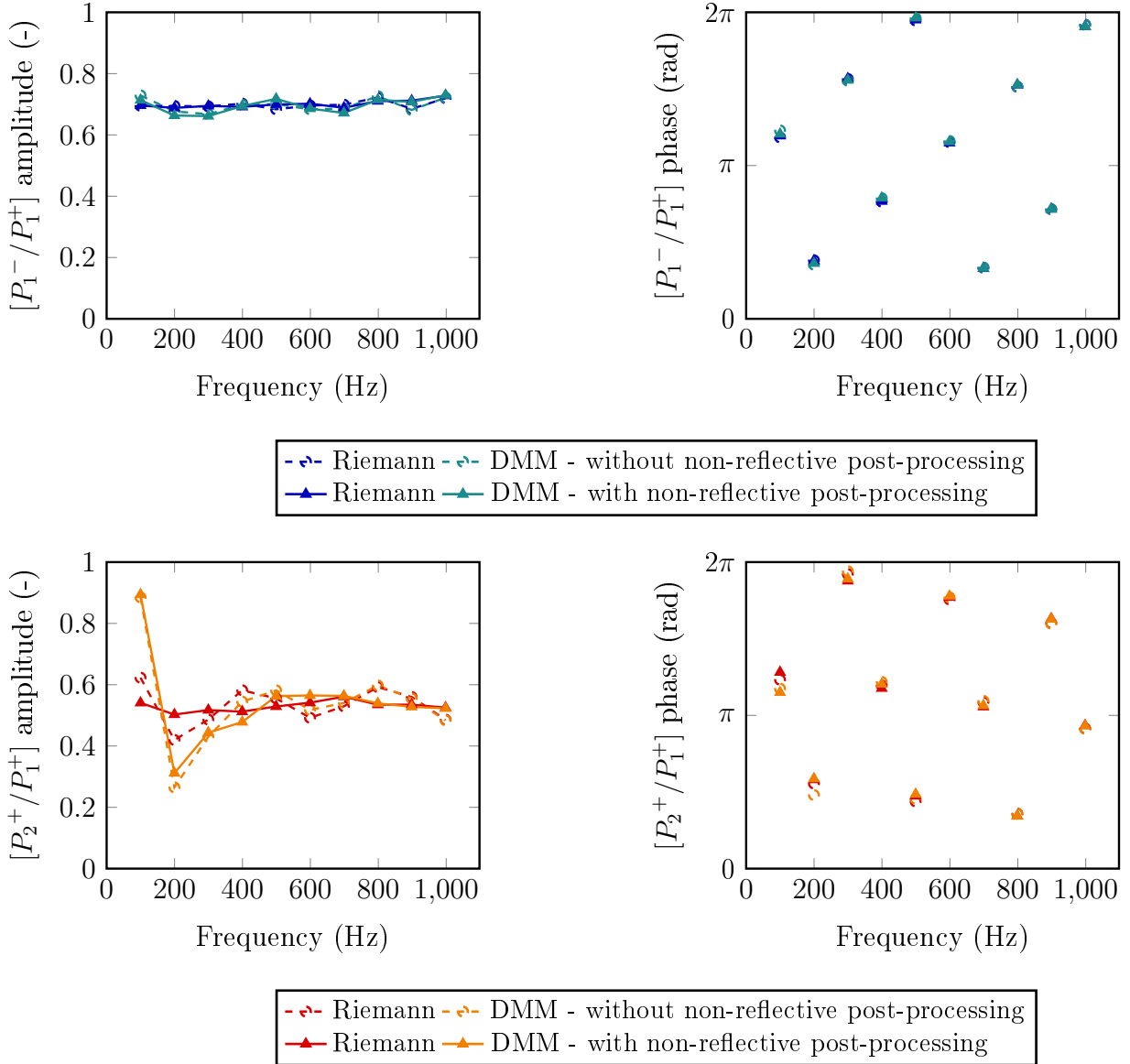


Figure 6.14: Amplitude and phase of the transfer functions resulting from upstream acoustic forcing  $[P_1^-/P_1^+]$  and  $[P_2^+/P_1^+]$ , computed with and without non-reflective post-processing, and using both the Riemann invariants and DMM.

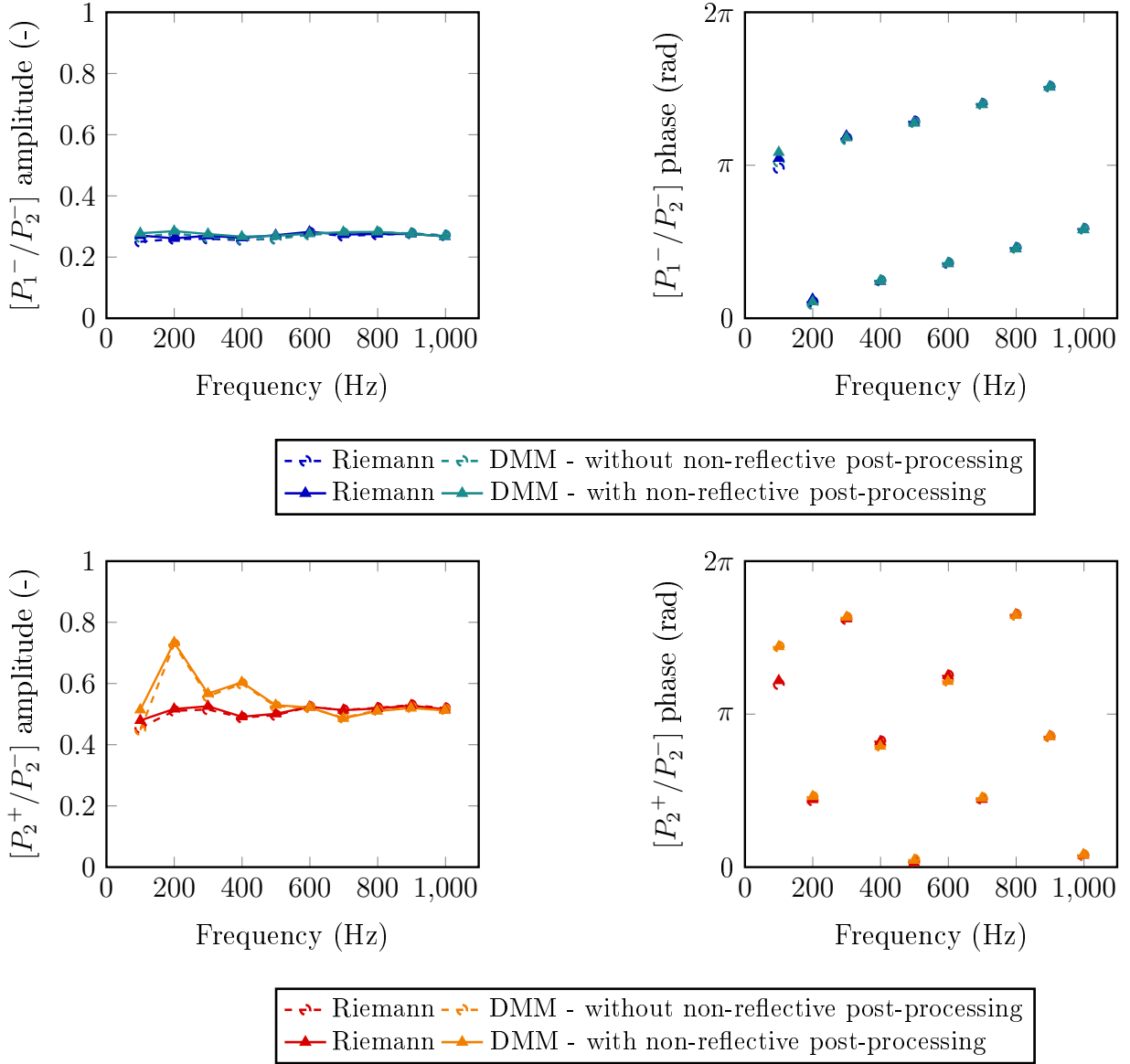


Figure 6.15: Amplitude and phase of the transfer functions resulting from downstream acoustic forcing  $[P_1^-/P_2^-]$  and  $[P_2^+/P_2^-]$ , computed with and without non-reflective post-processing, and using both the Riemann invariants and DMM.

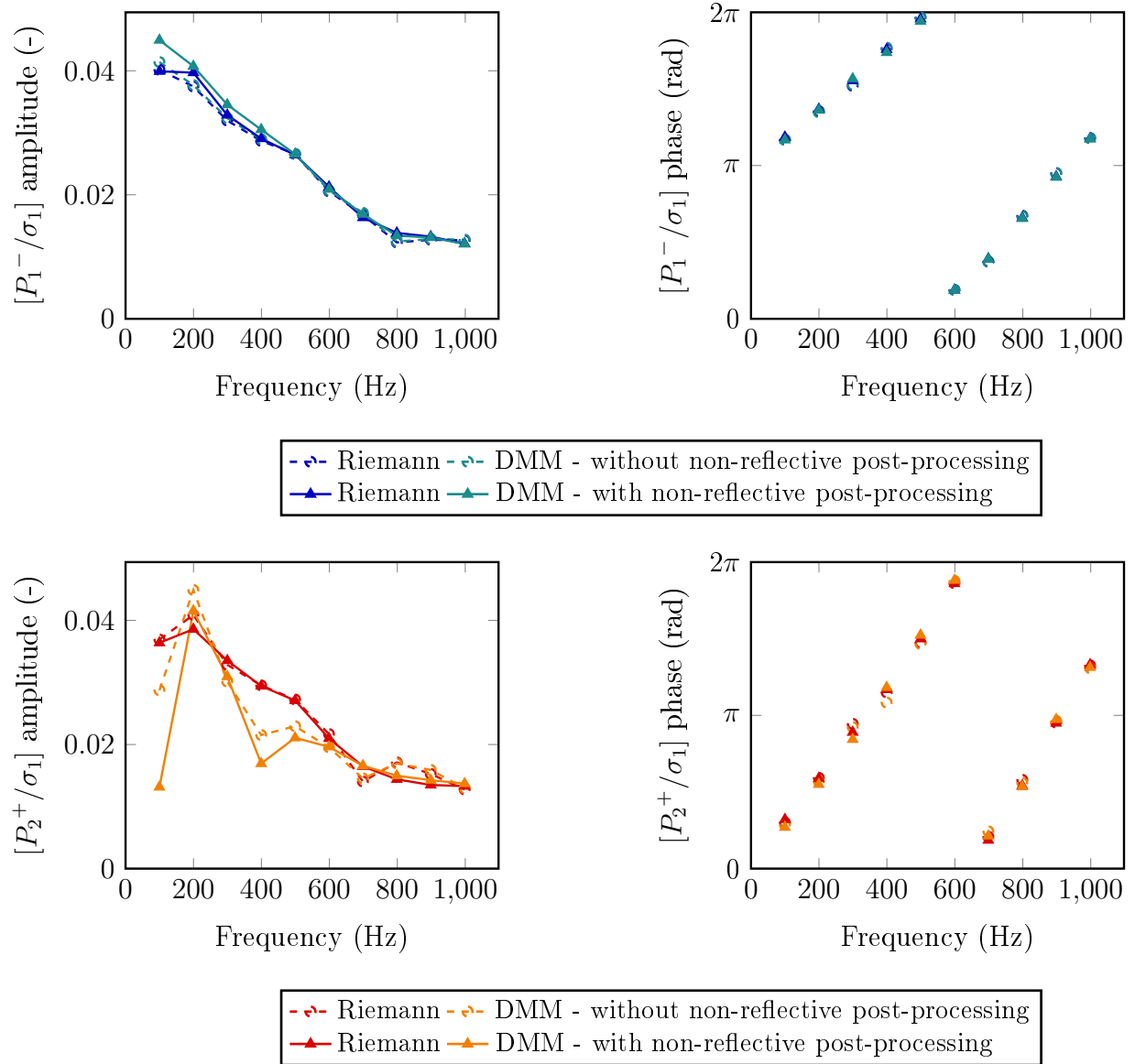


Figure 6.16: Amplitude and phase of the transfer functions resulting from entropic forcing  $[P_1^-/\sigma_1]$  and  $[P_2^+/\sigma_1]$ , computed with and without non-reflective post-processing, and using both the Riemann invariants and DMM.

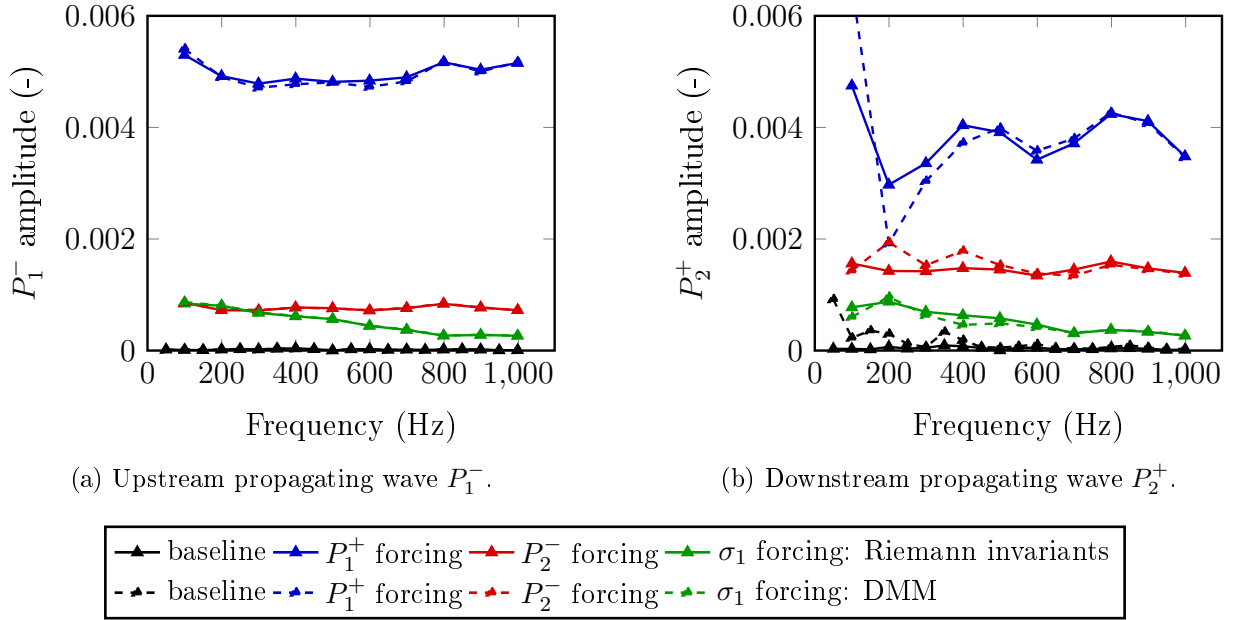


Figure 6.17: Amplitude of the regressive and transmitted acoustic waves  $P_1^-$  and  $P_2^+$  computed in different cases - the baseline simulation, the entropy-forced case, acoustic excitation from the inlet and acoustic forcing from the outlet - and using both the Riemann invariants and DMM for post-processing.

post-processing are given in Figs. 6.14-6.16. The latter correspond to acoustic excitation from upstream, from downstream, and entropic forcing respectively, and they show results obtained with both the Riemann invariants and DMM. There is globally more difference between the amplitudes of transfer functions before and after non-reflective post-processing at low frequency, which is in accordance with the low-pass nature of the non-reflective boundary conditions. Spurious reflections hardly affect the phase. The amplitude error due to reflection is small for the transfer functions of the regressive waves, in particular with acoustic forcing. With excitation from the inlet (Figs. 6.14 and 6.16), non-reflective post-processing has more impact on the amplitude of the downstream transfer functions, which can be explained by the convection of large turbulent structures up to the outlet while the flow is relatively clean upstream. In the upstream acoustically-forced case, non-reflective post-processing smooths out the amplitude of  $[P_2^+/P_1^+]$ , except for the peak that appears at low frequency with DMM. This is also the case with entropic excitation, but the effect of reflection appears more significant in the lower half of the frequency range with DMM. At 100 Hz in particular, the amplitude is doubled. Reflections appear negligible in the case of  $[P_2^+/P_2^-]$ , with pressure fluctuations injected from downstream.

### 6.3.3 Assessment of the signal-to-noise ratio

Figure 6.17 shows the amplitude of the regressive and progressive acoustic waves  $P_1^-$  and  $P_2^+$ . They are represented for simulations with entropic forcing, acoustic excitation from

upstream and acoustic forcing from downstream, on the same graphs as the baseline case without excitation, in order to verify the signal-to-noise ratio of the forced simulations. Note the amplitudes obtained with upstream acoustic forcing are significantly larger than with downstream excitation because the amplitude of the injected wave is twice as high. The pressure fluctuations computed with both the Riemann invariants and DMM are plotted.

Both wave separation methods lead to the same results in Fig. 6.17a for the upstream propagating waves. The amplitude of the latter is negligible in the baseline case, making the signal-to-noise ratio satisfactory for the three simulation forcing types. For the transmitted wave in Fig. 6.17b, there are some differences between the use of DMM or the Riemann invariants for post-processing. The amplitudes computed with the baseline simulation and the Riemann invariants are negligible over the whole frequency range. With DMM, the amplitudes are larger from 50 Hz to 250 Hz and at 350 Hz. At the forced frequencies in this range, 100 Hz and 200 Hz, the noise levels remain low relative to those obtained with entropy forcing, which is the excited case which displays the lowest amplitudes. The other frequencies are less critical as they are not forced, but while the amplitude is also low at 150 Hz and 350 Hz, it is of the same order of magnitude as the entropy-forced signal at 50 Hz. As no such amplitudes are found using the Riemann invariants, the signals could be polluted by hydrodynamic perturbations remaining after the post-processing filtering steps. The amplitudes obtained at frequencies which are not excited in the forced simulations are not displayed for clarity, but it is also verified their amplitudes are negligible compared to those computed at the excited frequencies.

### 6.3.4 Investigation of noise levels

The transfer functions illustrating the regressive and progressive waves obtained following upstream acoustic, downstream acoustic and entropic excitations are represented in Figs 6.18-6.20. They show ZDES results computed using non-reflective post-processing with both the Riemann invariants and DMM. In accordance with the results shown in the previous section, these two methods result in similar regressive transfer functions for the three excitation types considered. For the progressive wave, they agree in the upper-half of the frequency range but there are discrepancies at low frequency. This indicates hydrodynamic perturbations persist downstream at these frequencies. Indeed, the area averaging and characteristic filtering steps detailed in section 3.4.3.1 affect the Riemann invariants and DMM differently, as the first involves both  $p'$  and  $u'$  and the second only  $p'$  and its derivative. The peaks in downstream transfer function amplitudes resulting from DMM at low frequencies seem to indicate it is more sensitive to pollution by hydrodynamic perturbations, but a physical explanation cannot be ruled out. In addition, the signal-to-noise ratio was found to be smaller with DMM at the same frequencies downstream. An error could also be introduced with the Riemann invariant by the presence of the boundary layer which affects velocity fluctuations, although the error appears small. Overall, the good accordance of the two methods in the upper-half of the frequency range and the relative agreement at most low frequencies gives confidence in the transfer function levels.

The amplitude of the acoustic transfer functions represented in Figs. 6.18-6.19 are constant with amplitude, which indicates the stator is acoustically compact. This is in accordance with the wavelength of the injected perturbations, which is about a third larger than the



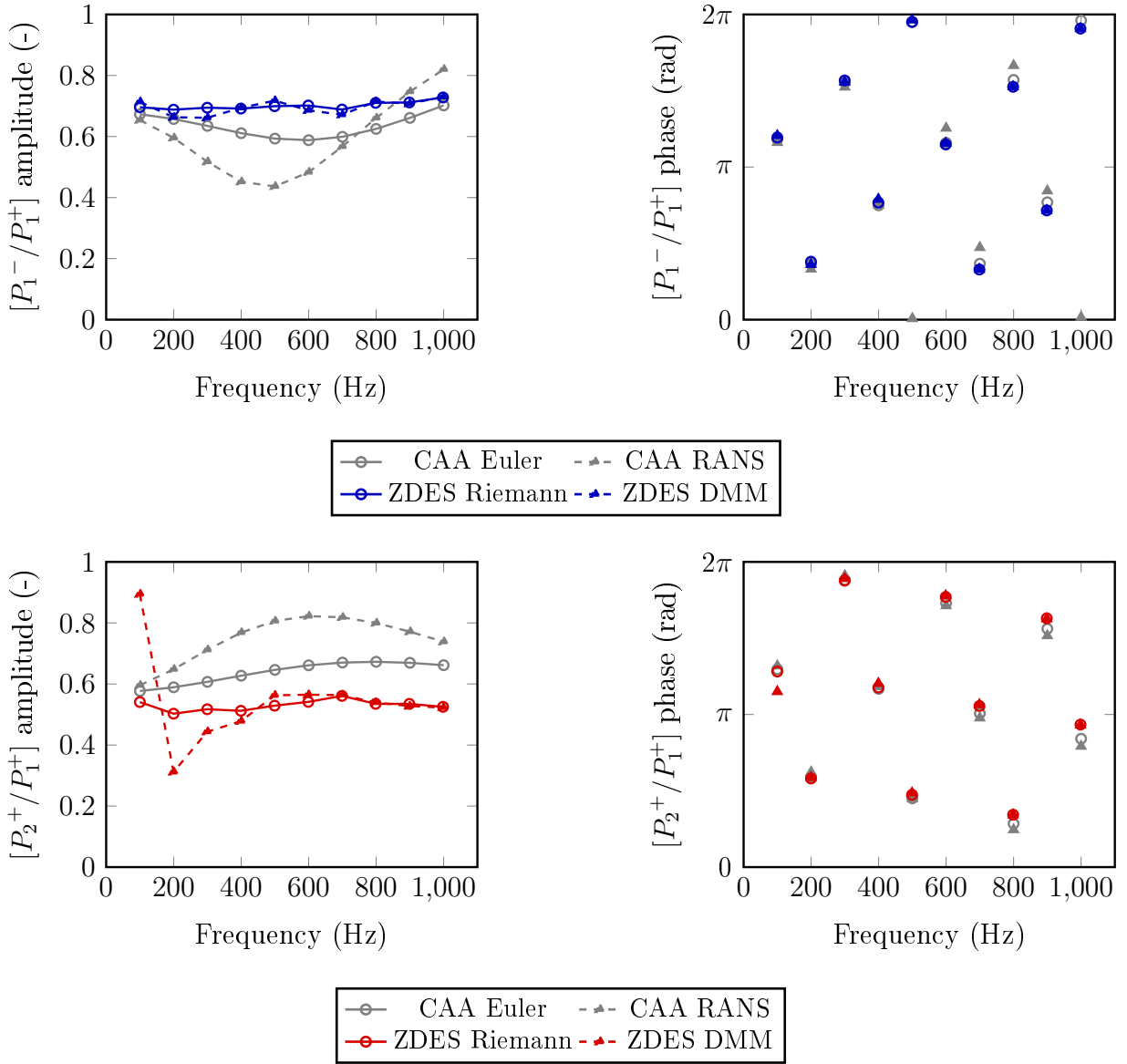


Figure 6.18: Amplitude and phase of the transfer functions resulting from upstream acoustic forcing  $[P_1^-/P_1^+]$  and  $[P_2^+/P_1^+]$ , computed using ZDES with the Riemann invariants and DMM for post-processing, and CAA with Euler and RANS mean flow fields.

blade's axial chord at the largest frequency considered, 1,000 Hz. On the other hand, the noise levels resulting from entropy forcing and represented in Fig. 6.20 display non-compact behaviour, and both regressive and progressive waves get weaker with increasing frequency over the range considered. The normalised entropy fluctuations injected to generate entropy noise are represented in Fig. 6.21. They show the plane wave upstream of the stator and its deformation as it is accelerated through the blade passage. The fluctuations are computed in blade-to-blade planes at different radial positions along the span. The shape of the entropy perturbations at mid-span is similar to the wave computed in two-dimensions using CAA

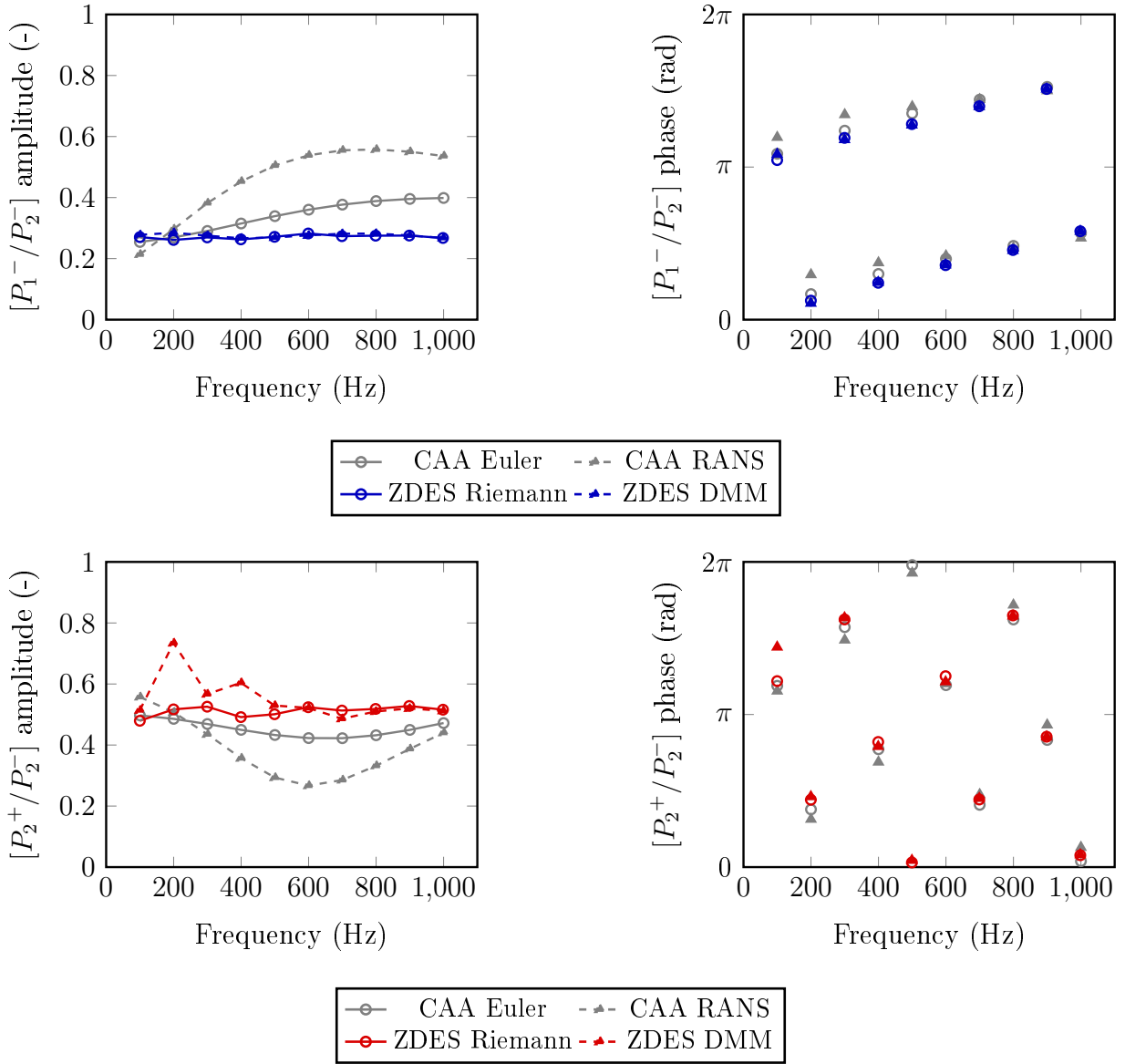


Figure 6.19: Amplitude and phase of the transfer functions resulting from upstream acoustic forcing  $[P_1^-/P_2^-]$  and  $[P_2^+/P_2^-]$ , computed using ZDES with the Riemann invariants and DMM for post-processing, and CAA with Euler and RANS mean flow fields.

in chapter 5 and presented in Fig. 5.9. Note they cannot be compared directly as a multi-harmonic wave is injected into the three-dimensional simulation, while harmonic cases are analysed in chapter 5. The deformation of the entropy wave varies at 5% and 95% span, as can be expected by the differences in mean flow discussed in section 6.2. The shape of the entropy wave is directly affected by the flow angle, which is smaller at the hub and larger at the shroud (cf. Fig. 6.10). It follows that the entropy wave crosses the domain azimuthally less at the hub than towards the blade tip. The large Mach number at the hub and low energy at the shroud also affects the shape of the entropy wave. The latter is quite different

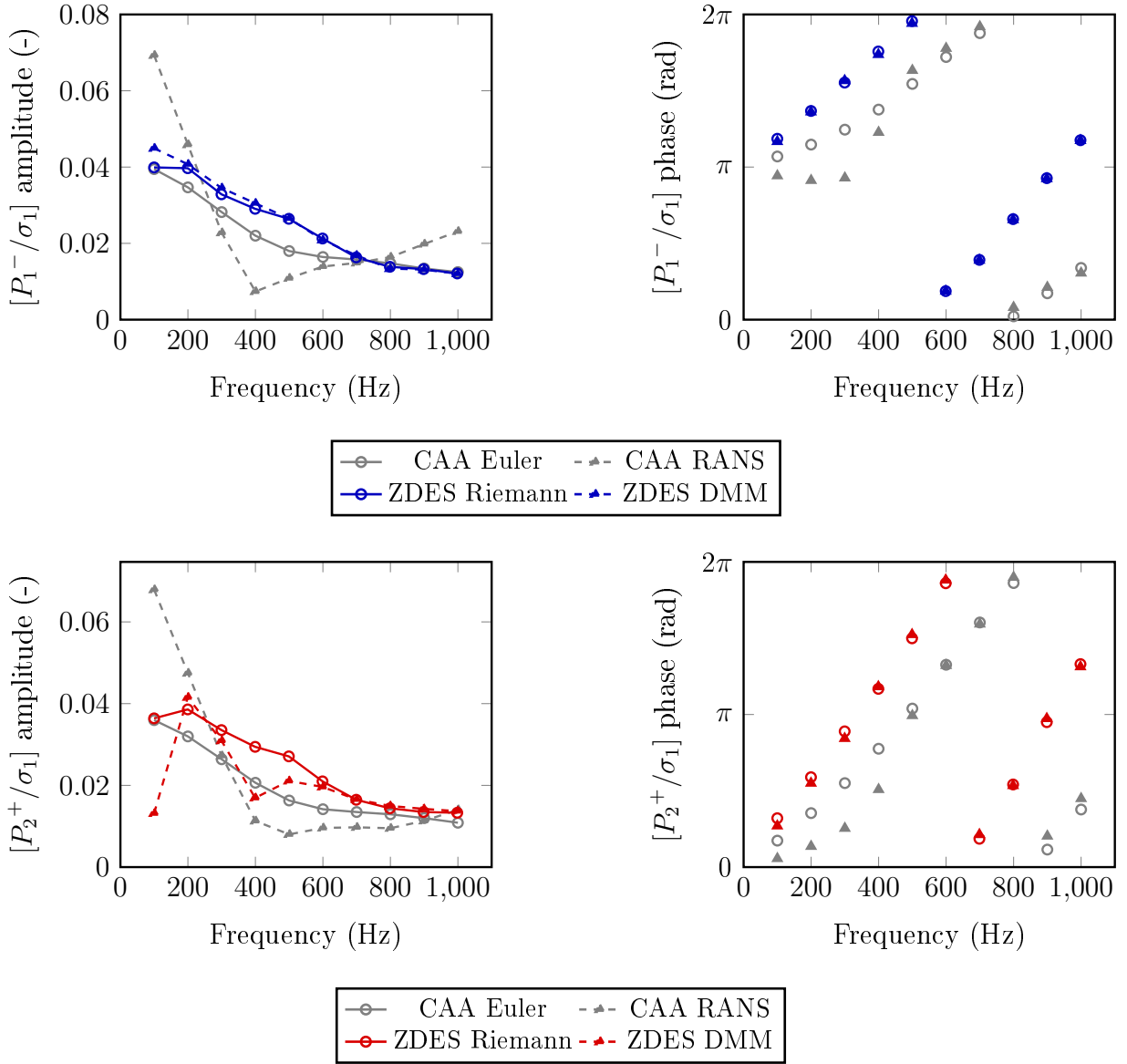


Figure 6.20: Amplitude and phase of the transfer functions resulting from upstream acoustic forcing  $[P_1^-/\sigma_1]$  and  $[P_2^+/\sigma_1]$ , computed using ZDES with the Riemann invariants and DMM for post-processing, and CAA with Euler and RANS mean flow fields.

at the blade tip, where it is deformed by large vortices.

Figures 6.18-6.20 also display the transfer functions obtained in the 2D case using CAA, and discussed in chapter 5. Both results obtained with a Euler and a RANS mean flow are shown. Let's concentrate on the Euler case first. With acoustic forcing from the inlet (Fig. 6.18), the amplitude of the reflected wave's transfer function  $[P_1^-/P_1^+]$  obtained through ZDES are larger than those resulting from CAA at most frequencies and they are close at the extremities of the frequency range. On the other hand, the amplitude of the transmitted wave from the ZDES simulation is smaller than with CAA with the Riemann invariants. This

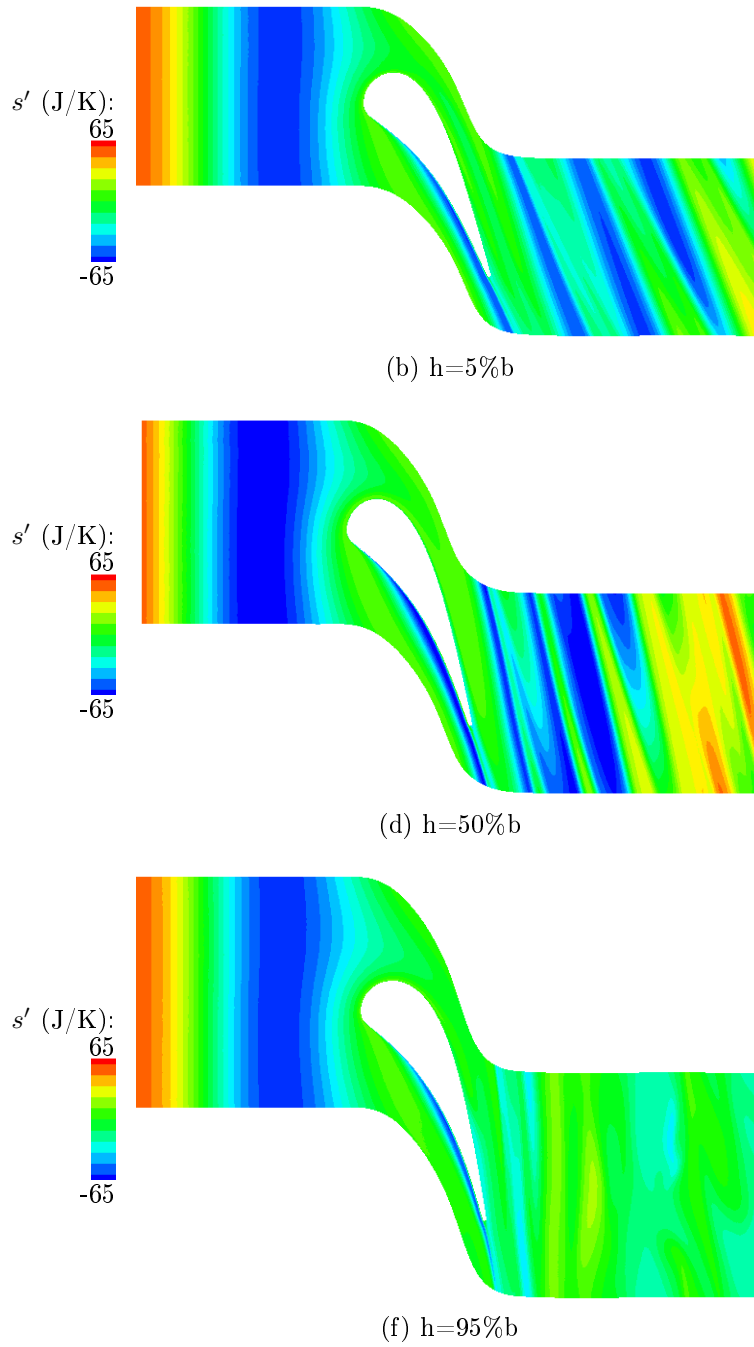


Figure 6.21: Normalised entropy fluctuations computed in the entropy-forced case in blade-to-blade planes at 5%, 50% and 95% of the stator blade's span.

is also true at most frequencies with DMM, except at 100 Hz at which the amplitude is much larger. There is also a negative peak at 200 Hz. Now with DMM, at high frequencies the amplitude does not vary with frequency and it is approximatively constant at all frequencies using the Riemann invariants. With both methods, the amplitude of the regressive wave does not evolve with frequency either. With CAA however,  $[P_1^-/P_1^+]$  decreases with frequency up to 600 Hz where it increases again, and  $[P_2^+/P_1^+]$  increases up to about 800 Hz and slowly decreases. In phase, ZDES and CAA are in good agreement for both reflected and transmitted waves.

The amplitudes of the transfer functions obtained with acoustic excitation from downstream are also close in the case of ZDES and CAA with Euler mean flow. This time,  $[P_1^-/P_2^-]$  is lower with ZDES than with CAA and  $[P_2^+/P_2^-]$  is a little higher, except at low frequencies at which they are equal for both waves. Similarly to the acoustically-forced case from upstream, the amplitudes of both progressive and transmitted waves are nearly constant with frequency, unlike with CAA, with the exception of peaks at 200 Hz and 400 Hz for  $[P_2^+/P_2^-]$  with DMM. The difference between ZDES results obtained with the Riemann invariants and DMM is quite large at these frequencies, and the peak could be explained by an error due to residual hydrodynamic perturbations. The phases computed with the Riemann invariants and DMM are nearly equal at 200 Hz, while there are some differences at 100 Hz. Unlike with acoustic excitation from the inlet, in this case the phases from ZDES and CAA slightly differ for both upstream and downstream propagating waves, but these differences appear negligible.

Finally, the transfer functions resulting from ZDES and CAA entropy-forced simulations are also quite close with a Euler mean flow. The amplitudes of  $[P_1^-/\sigma_1]$  are equal at 100 Hz with the Riemann invariants and from 700 Hz with either post-processing method. They are a little larger with ZDES than CAA at the other frequencies. The evolution of the amplitude is similar for  $[P_2^+/\sigma_1]$  with the Riemann invariants, for which results from ZDES and CAA are equal at 100 Hz and very close from 700 Hz. Processing the data from ZDES with DMM leads to negative peaks at 100 Hz, where the amplitude is twice as small as with CAA, and at 400 Hz at which the noise level is just below that obtained with CAA. The phases of the transfer functions resulting from ZDES and CAA are close at low frequencies but the error increases with frequency due to a phase-shift.

Overall, the transfer functions computed with 3D ZDES and 2D CAA using Euler mean flow fields are very close. This indicates three-dimensionality and viscosity have a relatively low impact on the noise levels resulting from entropy noise and the scattering of acoustic waves through a stator channel.

The transfer functions resulting from CAA simulations with a RANS mean flow are also represented in Figs. 6.18-6.20. As detailed in chapter 5, the evolution of their amplitudes with frequency differs from the Euler case. In the entropy-forced case, some differences in phase were also noted in the lower half of the frequency range. One could expect the transfer functions obtained with ZDES to be closer to those computed with a RANS mean flow, which takes some viscosity into account, but their evolution with frequency is much closer to the Euler case. Before drawing conclusions from this, the simulations involving the RANS mean flow should be validated, as unlike the Euler case, the resulting transfer functions could not be verified in the compact limit.

## 6.4 Conclusions

This chapter presents the simulation of entropy noise and the scattering of acoustic waves through a three-dimensional isolated stator using ZDES. The construction of the mesh, the choice of numerical parameters and the convergence and cost of the simulations are detailed. Then the aerodynamics of the stator are described, highlighting the three-dimensional nature of the flow, before discussing acoustic results. Filtering of hydrodynamic perturbations and non-reflective post-processing are verified, and the satisfactory signal-to-noise ratio of the three forced simulations is confirmed. Finally, the noise levels resulting from the injection of entropy, an acoustic wave from upstream and an acoustic wave from the outlet are discussed. The two wave separation methods used for post-processing lead to similar transfer functions, giving confidence in the results. The stator is found to be acoustically compact, while entropic forcing results in non-compact transfer functions, with decreasing amplitude with frequency. Comparison of noise levels obtained using ZDES and the CAA simulations with Euler mean flow detailed in chapter 5 yield to small differences in amplitude and phase. This suggests three-dimensional and viscous effects of the flow have little impact on entropy noise in the isolated stator. The three-dimensional results were also compared to those from CAA with RANS mean flow in order to investigate the role of viscous effects in the mean flow, in particular boundary layers. This time, entropy noise and acoustic scattering displayed different levels. Further study is needed to validate the CAA simulations with RANS mean flow and to explain these differences.



# Discussion

Entropy noise is first investigated in nozzle flow, which is the simplest geometry, in chapter 3. To do so, a CAA approach is set-up under simplifying assumptions, which allow more straightforward analysis of the flow. This also makes for a pertinent reference case for analytical tools governed by similar assumptions. Indeed, the simulations allowed the rigorous verification of the noise levels obtained by the two-dimensional semi-analytical model CHEOPS-Nozzle developed by Zheng [Zheng, 2016, Zheng et al., 2015]. Comparison of these 2D methods to existing 1D models highlighted the significance of two-dimensional effects on entropy noise. Furthermore, the relevance of the distortion of entropy perturbations was underlined. However, only radial variations are taken into account, while studies have indicated they may also be significant in the circumferential direction [Dowling and Mahmoudi, 2015]. In addition, only Euler mean flow has been considered, which simplifies analysis but is not realistic. In the future, the deformation of the entropy wave should be considered in both circumferential and radial directions, and viscous effects and turbulence of the flow should be taken into account to evaluate their effect on entropy noise in nozzle flow.

Following the validation of CHEOPS-Nozzle, the two-dimensional model is extended to isolated stator flow in chapter 4, using a mobile curvilinear reference frame. This is a first attempt at a fully non-compact solution for such geometries. However, some assumptions inherited from the model for nozzle flow should be relaxed. Noise levels estimated with the model are compared to those obtained with CAA, Cumpsty and Marble's compact solution [1977] and a formulation of the latter neglecting vorticity. This shows that both vorticity and the azimuthal variation of acoustic waves in the blade passage have a significant impact on entropy noise and therefore cannot be neglected. The latter only seems to affect entropy noise, but the presence of vorticity also has a strong impact on the scattering of acoustic waves. In addition, vorticity has the largest effect on entropy noise levels for the geometry considered. Further developments are therefore required to obtain a working version of the model for entropy noise in 2D stator flow, taking into account vorticity and azimuthal variations of acoustic waves in the blade passage.

As well as being investigated analytically, entropy noise in isolated 2D stator flow is analysed using CAA in chapter 5. The noise generation mechanism is highlighted under the CAA's simplifying assumptions. For most cases considered, pressure and entropy fluctuations are found to be synchronised, indicating entropy noise is the main noise source. Furthermore, pressure fluctuations seem to originate from regions near the leading and trailing edges where acceleration, which drives entropy noise, is maximal. High pressure fluctuation areas are found to spread with time until the entropy perturbations crossing the blade passage on the suction side change sign. This spreading is more and more limited as the forcing frequency is



increased, because the wavelength and the residence time of entropy perturbations of the same sign in the blade passage are reduced. This could explain the larger amplitudes computed at low frequency. Noise levels obtained using Euler and RANS mean flows are also compared. In the RANS case, the topology of the pressure fluctuation contour is quite different from the other cases. It is not synchronised with entropy perturbations, indicating entropy noise may not be the dominant noise source. Most pressure fluctuations appear to be generated at the trailing edge at this frequency, which could be due to additional interactions with the boundary layer compared to the Euler case. While noise levels obtained with Euler flow seem to compare well with Cumpsty and Marble's compact solution [1977], no such data is available for the RANS case, not even in the compact limit. In addition, the noise levels resulting from three-dimensional ZDES simulations in chapter 6 are closer to those obtained with the Euler mean flow than with RANS, even though the latter takes some viscous effects into account. The simulations with the RANS flow therefore require validation before conclusions can be drawn from their results, and to explain their differences compared to both the 2D Euler case and the 3D ZDES simulations.

The objective of chapter 6 is to evaluate the impact of three-dimensionality and viscous effects on entropy noise in isolated stator flow using ZDES. Mean aerodynamic fields obtained from baseline, entropy-forced and acoustically-forced simulations are compared. They display differences from about mid-span towards the shroud, but these remain quite close and it seems they do not have a significant effect on noise levels. Acoustic post-processing of the ZDES simulations is more challenging than with CAA in chapters 3 and 5, because of secondary flows and the wake, which make filtering of hydrodynamic modes more difficult. This could lead to inaccurate values of pressure and velocity fluctuations, which would not be purely acoustic. This is a necessary condition for the Riemann invariants to be valid. The latter are used for wave separation during acoustic post-processing, as well as the DMM method, which seems to be sensitive to error because of the derivative involved in its equations. Nevertheless, despite the different sources of error faced using the two methods, they provide noise levels which are very close at most frequencies, giving confidence in acoustic post-processing. Comparing the transfer functions resulting from ZDES and CAA simulations with the Euler mean flow, described in chapter 5, gives indications of the effects of three-dimensionality and viscosity. For acoustic excitations from both upstream and downstream, the amplitudes obtained with ZDES evolve even less with frequency than those from CAA, and the flow seems acoustically compact. Phases computed with the two methods are in agreement. In the entropy-forced case, the amplitudes resulting from ZDES and CAA are very close at high frequency, and somewhat underestimated by CAA compared to ZDES over most of the rest of the frequency range. There are also some differences in phase, although they appear to be small. Overall, for the three forcing types, the transfer functions resulting from ZDES and CAA with Euler mean flow are close, which suggests three-dimensionality and viscous effects have limited impact on entropy noise in isolated stator flow. In the future, the aerodynamics of 3D stator flow could be further analysed, in particular to determine whether small-scale turbulence and unsteady flow affect entropy noise in this case. In the present study, large forcing amplitudes were chosen to guarantee adequate signal-to-noise ratios while remaining in the linear domain. It would also be interesting to simulate entropy noise and acoustic scattering using realistic forcing amplitudes, as well as entropy perturbation shapes typical of those convected downstream of a combustion chamber instead of plane waves. Finally, the fact

that transfer functions obtained using ZDES and CAA with Euler mean flow are close gives confidence in the results, but experimental data would be necessary to fully validate the simulations.



# General conclusions

Entropy noise is gaining in relative importance in modern engines, for which the dominant fan and jet noise sources have been greatly reduced. It also affects  $NO_x$  emissions and the risk of combustion instabilities. In order to reduce its contribution to the perceived aircraft noise and  $NO_x$  emissions, entropy noise needs to be better understood and tools adapted to an industrial context are required. This study aims at increasing understanding of entropy noise in turbine stator flow and at extending a two-dimensional non-compact model for entropy noise in nozzle flow to stator configurations.

In chapter 3, the 2D model for entropy noise in nozzle flow is validated using a CAA approach under assumptions similar to those of the model. This study also confirms the significance of two-dimensional effects on entropy noise in nozzle flow.

Once rigorously validated for nozzle flow, the two-dimensional, non-compact model is extended to isolated stator flow in a mobile curvilinear reference frame in chapter 4. Among other assumptions, the model CHEOPS-Stator neglects all vorticity terms and assumes acoustic waves are independent of the azimuthal direction. However, these assumptions are found to have a significant impact on the entropy noise computed in chapter 5 using a similar CAA approach as for the nozzle, and the model requires further work to relax them. Cumpsty and Marble's compact solution [1977] and a formulation of this model in which vorticity is neglected are used to isolate the effect of azimuthal variations of acoustic waves and vorticity.

As well as underlining the significance of vorticity and azimuthal evolution of acoustics on entropy noise, the CAA simulations presented in chapter 5 allow to highlight the entropy noise generation mechanism under simplifying assumptions. The differences obtained with Euler and RANS mean flow fields are identified in both noise levels and the behaviour of acoustic waves. However, the RANS results require validation before conclusions can be drawn.

The analysis is then extended to a 3D geometry using ZDES simulations. Comparison of the mean flow fields show minor differences between the baseline and acoustically forced cases, which are close globally. Furthermore, the noise levels simulated with ZDES and two-dimensional CAA are in agreement, which indicates that three-dimensionality and viscous effects have a limited impact on the entropy noise generated in an isolated stator.

As discussed in more detail in the previous section, these conclusions open the following perspectives for future study. Regarding the nozzle case, the model CHEOPS-Nozzle for entropy noise in axisymmetric nozzles could be extended to take circumferential modes and vorticity into account. In addition, viscous mean flow fields should be considered.

Further work is required on the non-compact model CHEOPS-Stator for entropy noise in stator flow. It needs to be extended to take both vorticity and azimuthal variations of

acoustic waves in the blade passage into account.

The findings of the CAA study in two-dimensional stator flow using RANS mean flow fields need to be verified and further investigated before the differences found with the Euler case can be confirmed. URANS simulations could be an interesting tool for this.

The ZDES simulation of a three-dimensional stator channel could also benefit from further validation, although the agreement of its noise levels with CAA gives confidence in its results. While the objective during this study was to insure good signal-to-noise ratios, it could be interesting to inject perturbation with more realistic amplitudes into the simulation. Entropy perturbations of more complex shape than plane waves could also be injected, and their characterisation downstream of the stator could be useful for the investigation of entropy noise in rotor flow.

The study of the isolated stator is a first step towards the investigation of entropy noise in a full turbine stage. The next step is to extend the model and numerical methods to rotor configurations, with the added challenge of rotation, while the rotor-stator interface and interactions will need to be taken into account to model a turbine stage.

# Appendix A

## Derivation of the Euler equations in a streamline-attached reference frame

The objective of this appendix is to express the Euler equations in the streamline-attached coordinate system  $(\mathbf{e}_s, \mathbf{e}_n, \mathbf{e}_z)$  illustrated in Fig. A.1 and used in the formulation of the semi-analytical model for entropy noise in two-dimensional stator flow, CHEOPS-Stator. The orthogonal curvilinear mobile reference frame follows a streamline of local angle  $\varphi$  relative to the x-axis of the Cartesian coordinate system  $(\mathbf{e}_x, \mathbf{e}_y, \mathbf{e}_z)$ . In this coordinate system, an infinitesimal displacement can be formulated  $d\mathbf{r} = h_s dq_s \mathbf{e}_s + h_n dq_n \mathbf{e}_n + h_z dq_z \mathbf{e}_z$ , with the following expressions for the metric coefficients:

$$h_s = \frac{ds}{dq_s} \quad (\text{A.1})$$

$$h_n = \frac{dn}{dq_n} \quad (\text{A.2})$$

$$\text{and } h_z = 1 \quad (\text{A.3})$$

because there is no curvature in the z-direction. The radii of curvature in the  $s$  and  $n$ -constant lines are expressed:

$$R_s = \frac{1}{K_s} = \frac{\partial s}{\partial \varphi} \quad (\text{A.4})$$

$$R_n = \frac{1}{K_n} = \frac{\partial n}{\partial \varphi} \quad (\text{A.5})$$

where curvatures are noted  $K_s$  and  $K_n$ .

In order to express the Euler equations in the  $(\mathbf{e}_s, \mathbf{e}_n, \mathbf{e}_z)$  coordinate system, they are written in vectorial form:

$$\frac{\partial \rho}{\partial t} + \nabla \cdot (\rho \mathbf{u}) = 0 \quad (\text{A.6})$$

$$\frac{\partial \mathbf{u}}{\partial t} + (\mathbf{u} \cdot \nabla) \mathbf{u} = -\frac{1}{\rho} \nabla p \quad (\text{A.7})$$

Then, relations for the divergence and gradient operators are required in the  $(\mathbf{e}_s, \mathbf{e}_n, \mathbf{e}_z)$

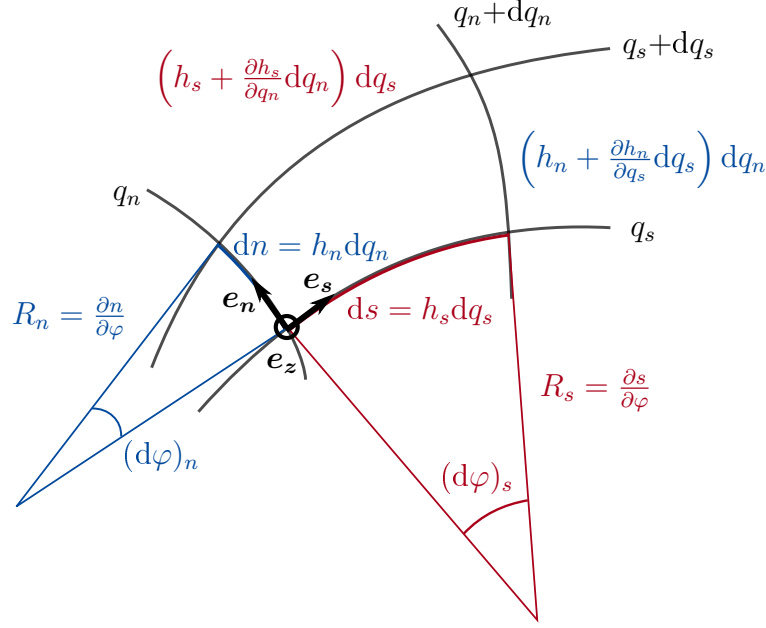


Figure A.1: Sketch of the coordinate system  $(\mathbf{e}_s, \mathbf{e}_n, \mathbf{e}_z)$ .

coordinate system. The divergence theorem states:

$$\int_V \nabla \cdot \mathbf{f} dV = \int_{\partial V} \mathbf{f} d\mathbf{S} \quad (\text{A.8})$$

where  $V$  is a volume and  $\partial V$  the surface of  $V$ . For an infinitesimal volume,

$$\int_V \nabla \cdot \mathbf{f} dV = \nabla \cdot \mathbf{f} dV \quad (\text{A.9})$$

The right-hand side term of Eq. A.8 is the net flux of the field  $\mathbf{f}$  through the surface  $\partial V$ , noted  $\phi$ . Considering an hexahedral element such as the one represented in Fig. A.2, the net flux can be expressed:

$$\begin{aligned} \int_{\partial V} \mathbf{f} d\mathbf{S} &= ([\phi_s(q_s + dq_s, q_n, q_z)] \mathbf{e}_s - [\phi_s(q_s, q_n, q_z)] \mathbf{e}_s) \mathbf{e}_s \\ &+ ([\phi_n(q_s, q_n + dq_n, q_z)] \mathbf{e}_n - [\phi_n(q_s, q_n, q_z)] \mathbf{e}_n) \mathbf{e}_n \\ &+ ([\phi_z(q_s, q_n, q_z + dq_z)] \mathbf{e}_z - [\phi_z(q_s, q_n, q_z)] \mathbf{e}_z) \mathbf{e}_z \end{aligned} \quad (\text{A.10})$$

and using the Taylor series:

$$\begin{aligned} \int_{\partial V} \mathbf{f} d\mathbf{S} &= \frac{\partial \phi_s}{\partial q_s}(q_s, q_n, q_z) dq_s \\ &+ \frac{\partial \phi_n}{\partial q_n}(q_s, q_n, q_z) dq_n \\ &+ \frac{\partial \phi_z}{\partial q_z}(q_s, q_n, q_z) dq_z \end{aligned} \quad (\text{A.11})$$

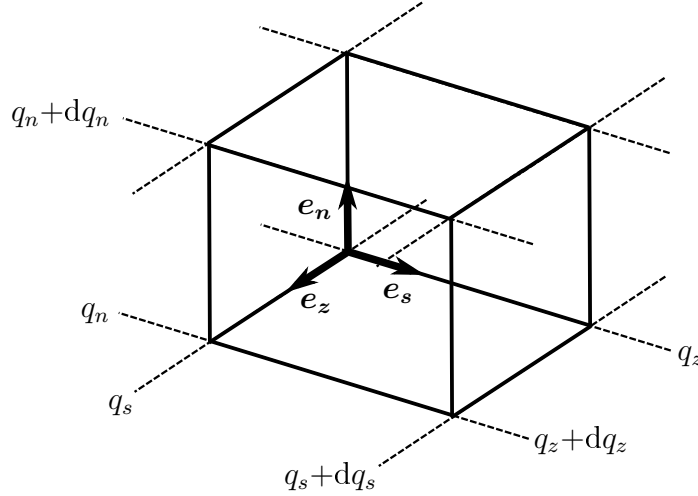


Figure A.2: Sketch of an hexahedral element.

where the flux components write:

$$\phi_s(q_s, q_n, q_z) = f_s(q_s, q_n, q_z) h_n h_z dq_n dq_z \quad (\text{A.12})$$

$$\phi_n(q_s, q_n, q_z) = f_n(q_s, q_n, q_z) h_s h_z dq_s dq_z \quad (\text{A.13})$$

$$\phi_z(q_s, q_n, q_z) = f_z(q_s, q_n, q_z) h_s h_n dq_s dq_n \quad (\text{A.14})$$

Deriving  $\phi_s$ ,  $\phi_n$  and  $\phi_z$  in directions  $q_s$ ,  $q_n$  and  $q_z$  respectively and observing  $dV = h_s h_n h_z dq_s dq_n dq_z$ , it comes:

$$\frac{\partial \phi_s}{\partial q_s} dq_s = \frac{dV}{h_s h_n h_z} \frac{\partial}{\partial q_s} (f_s h_n h_z) \quad (\text{A.15})$$

$$\frac{\partial \phi_n}{\partial q_n} dq_n = \frac{dV}{h_s h_n h_z} \frac{\partial}{\partial q_n} (f_n h_s h_z) \quad (\text{A.16})$$

$$\frac{\partial \phi_z}{\partial q_z} dq_z = \frac{dV}{h_s h_n h_z} \frac{\partial}{\partial q_z} (f_z h_s h_n) \quad (\text{A.17})$$

Divergence can then be expressed in a curvilinear coordinate system as follows:

$$\begin{aligned} \nabla \cdot \mathbf{f} &= \frac{1}{h_s h_n h_z} \left( \frac{\partial}{\partial q_s} (f_s h_n h_z) + \frac{\partial}{\partial q_n} (f_n h_s h_z) + \frac{\partial}{\partial q_z} (f_z h_s h_n) \right) \\ &= \frac{1}{h_s h_n} \left( h_n \frac{\partial f_s}{\partial q_s} + f_s \frac{\partial h_n}{\partial q_s} + h_s \frac{\partial f_n}{\partial q_n} + f_n \frac{\partial h_s}{\partial q_n} + h_s h_n \frac{\partial f_z}{\partial q_z} \right) \end{aligned} \quad (\text{A.18})$$

recalling  $h_z = 1$ . Then, expressions for  $\partial h_n / \partial q_s$  and  $\partial h_s / \partial q_n$  are required. From Fig. A.1:

$$\left( h_s + \frac{\partial h_s}{\partial q_n} dq_n \right) dq_s = R_s d\varphi + h_n dq_n d\varphi \quad (\text{A.19})$$

$$R_s = h_s \frac{\partial q_s}{\partial \varphi} = \frac{1}{K_s} \quad (\text{A.20})$$



Substituting Eq. A.20 into Eq. A.19, it finally comes:

$$\frac{\partial h_s}{\partial q_n} = h_n \frac{d\varphi}{dq_s} = h_s h_n K_s \quad (\text{A.21})$$

Proceeding similarly in the  $n$ -direction:

$$\frac{\partial h_n}{\partial q_s} = h_s h_n K_n \quad (\text{A.22})$$

The expression for divergence in the  $(\mathbf{e}_s, \mathbf{e}_n, \mathbf{e}_z)$  coordinate system becomes:

$$\nabla \cdot \mathbf{f} = \frac{\partial f_s}{\partial s} + K_n f_s + \frac{\partial f_n}{\partial n} + K_s f_n + \frac{\partial f_z}{\partial z} \quad (\text{A.23})$$

Combining Eqs. A.6 and A.23, the continuity equation then writes:

$$\frac{\partial \rho}{\partial t} + \frac{\partial \rho u_s}{\partial s} + \frac{\partial \rho u_n}{\partial n} + \frac{\partial \rho u_z}{\partial z} + \rho (K_n u_s + K_s u_n) = 0 \quad (\text{A.24})$$

Next, the momentum equation is also expressed in the  $(\mathbf{e}_s, \mathbf{e}_n, \mathbf{e}_z)$  coordinate system. The right-hand side of Eq. A.7, involving the gradient operator, is expressed:

$$\nabla p = \frac{1}{h_s} \frac{\partial p}{\partial q_s} \mathbf{e}_s + \frac{1}{h_n} \frac{\partial p}{\partial q_n} \mathbf{e}_n + \frac{1}{h_z} \frac{\partial p}{\partial q_z} \mathbf{e}_z \quad (\text{A.25})$$

$$= \frac{\partial p}{\partial s} \mathbf{e}_s + \frac{\partial p}{\partial n} \mathbf{e}_n + \frac{\partial p}{\partial z} \mathbf{e}_z \quad (\text{A.26})$$

Then focusing on the second term on the left-hand side of Eq. A.7, it writes:

$$(\mathbf{u} \cdot \nabla) \mathbf{u} = u_s \frac{\partial \mathbf{u}}{\partial s} + u_n \frac{\partial \mathbf{u}}{\partial n} + u_z \frac{\partial \mathbf{u}}{\partial z} \quad (\text{A.27})$$

Recalling  $\mathbf{u} = u_s \mathbf{e}_s + u_n \mathbf{e}_n + u_z \mathbf{e}_z$ , expressions for unit vector derivatives are required. In the following, the expression for  $\partial \mathbf{e}_s / \partial q_s$  is detailed as an example. For its evaluation, it is convenient to consider  $\partial h_s \mathbf{e}_s / \partial q_s$  first, using properties of the scalar product:

$$\frac{\partial h_s \mathbf{e}_s}{\partial q_s} = \frac{1}{h_s} \left( \frac{\partial h_s \mathbf{e}_s}{\partial q_s} \right) \cdot (h_s \mathbf{e}_s) \mathbf{e}_s + \frac{1}{h_n} \left( \frac{\partial h_s \mathbf{e}_s}{\partial q_s} \right) \cdot (h_n \mathbf{e}_n) \mathbf{e}_n + \frac{1}{h_z} \left( \frac{\partial h_s \mathbf{e}_s}{\partial q_s} \right) \cdot (h_z \mathbf{e}_z) \mathbf{e}_z \quad (\text{A.28})$$

Expanding the first term on the right-hand side of Eq. A.28, and noting the derivative  $\partial \mathbf{e}_s / \partial q_s$  is perpendicular to  $\mathbf{e}_s$ :

$$\left( \frac{\partial h_s \mathbf{e}_s}{\partial q_s} \right) \cdot (h_s \mathbf{e}_s) = h_s \frac{\partial h_s}{\partial q_s} \quad (\text{A.29})$$

To express the second term of Eq. A.28, the orthogonality of the  $s$  and  $n$ -axes is used. It leads to  $(h_s \mathbf{e}_s) \cdot (h_n \mathbf{e}_n) = 0$ , thus:

$$\frac{\partial (h_s \mathbf{e}_s) \cdot (h_n \mathbf{e}_n)}{\partial q_s} = \left( \frac{\partial h_s \mathbf{e}_s}{\partial q_s} \right) \cdot (h_n \mathbf{e}_n) + (h_s \mathbf{e}_s) \cdot \left( \frac{\partial h_n \mathbf{e}_n}{\partial q_s} \right) = 0 \quad (\text{A.30})$$

A property of orthogonal mobile reference frames is that the tensor of the derivative of the unit vectors is symmetric, so that:

$$\frac{\partial h_n \mathbf{e}_n}{\partial q_s} = \frac{\partial h_s \mathbf{e}_s}{\partial q_n} \quad (\text{A.31})$$

This equality is used to take advantage of the orthogonality between a unit vector and its derivative in the following, by substitution into Eq. A.30:

$$\left( \frac{\partial h_s \mathbf{e}_s}{\partial q_s} \right) \cdot (h_n \mathbf{e}_n) = -(h_s \mathbf{e}_s) \cdot \left( \frac{\partial h_s \mathbf{e}_s}{\partial q_n} \right) \quad (\text{A.32})$$

$$= -(h_s \mathbf{e}_s) \cdot \left( \frac{\partial h_s}{\partial q_n} \mathbf{e}_s + h_s \frac{\partial \mathbf{e}_s}{\partial q_n} \right) \quad (\text{A.33})$$

$$= -h_s \frac{\partial h_s}{\partial q_n} \quad (\text{A.34})$$

Noting  $\mathbf{e}_z$  is perpendicular to  $\mathbf{e}_s$ , its derivative and  $\mathbf{e}_n$ , the third term of Eq. A.28 yields to:

$$\left( \frac{\partial h_s \mathbf{e}_s}{\partial q_s} \right) \cdot (h_z \mathbf{e}_z) = 0 \quad (\text{A.35})$$

Then, substituting Eqs. A.29, A.34 and A.35 into Eq. A.28:

$$\frac{\partial h_s}{\partial q_s} \mathbf{e}_s + h_s \frac{\partial \mathbf{e}_s}{\partial q_s} = \frac{\partial h_s}{\partial q_s} \mathbf{e}_s - \frac{h_s}{h_n} \frac{\partial h_s}{\partial q_n} \mathbf{e}_n \quad (\text{A.36})$$

Rearranging and using Eq. A.21:

$$\frac{\partial \mathbf{e}_s}{\partial q_s} = -\frac{1}{h_n} \frac{\partial h_s}{\partial q_n} \mathbf{e}_n = -h_s K_s \mathbf{e}_n \quad (\text{A.37})$$

The derivative of  $\mathbf{e}_s$  finally writes:

$$\frac{\partial \mathbf{e}_s}{\partial s} = -K_s \mathbf{e}_n \quad (\text{A.38})$$

Following the same method, the other unit vector derivatives are expressed:

$$\frac{\partial \mathbf{e}_s}{\partial q_n} = \frac{1}{h_s} \frac{\partial h_n}{\partial q_s} \mathbf{e}_n \Rightarrow \frac{\partial \mathbf{e}_s}{\partial n} = K_n \mathbf{e}_n \quad (\text{A.39})$$

$$\frac{\partial \mathbf{e}_s}{\partial q_z} = 0 \Rightarrow \frac{\partial \mathbf{e}_s}{\partial z} = 0 \quad (\text{A.40})$$

$$\frac{\partial \mathbf{e}_n}{\partial q_s} = \frac{1}{h_n} \frac{\partial h_s}{\partial q_n} \mathbf{e}_s \Rightarrow \frac{\partial \mathbf{e}_n}{\partial s} = K_s \mathbf{e}_s \quad (\text{A.41})$$

$$\frac{\partial \mathbf{e}_n}{\partial q_n} = -\frac{1}{h_s} \frac{\partial h_n}{\partial q_s} \mathbf{e}_s \Rightarrow \frac{\partial \mathbf{e}_n}{\partial n} = -K_n \mathbf{e}_s \quad (\text{A.42})$$

$$\frac{\partial \mathbf{e}_n}{\partial q_z} = 0 \Rightarrow \frac{\partial \mathbf{e}_n}{\partial z} = 0 \quad (\text{A.43})$$

$$\frac{\partial \mathbf{e}_n}{\partial q_s} = 0 \Rightarrow \frac{\partial \mathbf{e}_z}{\partial s} = 0 \quad (\text{A.44})$$

$$\frac{\partial \mathbf{e}_n}{\partial q_n} = 0 \Rightarrow \frac{\partial \mathbf{e}_z}{\partial n} = 0 \quad (\text{A.45})$$

$$\frac{\partial \mathbf{e}_n}{\partial q_z} = 0 \Rightarrow \frac{\partial \mathbf{e}_z}{\partial z} = 0 \quad (\text{A.46})$$

It follows the momentum equations in the s, n and z-directions can be written:

$$\frac{\partial u_s}{\partial t} + u_s \frac{\partial u_s}{\partial s} + u_n \frac{\partial u_s}{\partial n} + u_z \frac{\partial u_s}{\partial z} + u_n(u_s K_s - u_n K_n) = -\frac{1}{\rho} \frac{\partial p}{\partial s} \quad (\text{A.47})$$

$$\frac{\partial u_n}{\partial t} + u_s \frac{\partial u_n}{\partial s} + u_n \frac{\partial u_n}{\partial n} + u_z \frac{\partial u_n}{\partial z} + u_s(u_s K_s - u_n K_n) = -\frac{1}{\rho} \frac{\partial p}{\partial n} \quad (\text{A.48})$$

$$\frac{\partial u_z}{\partial t} + u_s \frac{\partial u_z}{\partial s} + u_n \frac{\partial u_z}{\partial n} + u_z \frac{\partial u_z}{\partial z} = -\frac{1}{\rho} \frac{\partial p}{\partial z} \quad (\text{A.49})$$

The continuity and momentum equations expressed in this section are used in chapter 4 to develop the two-dimensional model CHEOPS-Stator. In the two-dimensional coordinate system  $(\mathbf{e}_s, \mathbf{e}_n)$ , Eqs. A.24 and A.47-A.49 reduce to:

$$\frac{\partial \rho}{\partial t} + \frac{\partial \rho u_s}{\partial s} + \frac{\partial \rho u_n}{\partial n} + \rho(K_n u_s + K_s u_n) = 0 \quad (\text{A.50})$$

$$\frac{\partial u_s}{\partial t} + u_s \frac{\partial u_s}{\partial s} + u_n \frac{\partial u_s}{\partial n} + u_n(u_s K_s - u_n K_n) = -\frac{1}{\rho} \frac{\partial p}{\partial s} \quad (\text{A.51})$$

$$\frac{\partial u_n}{\partial t} + u_s \frac{\partial u_n}{\partial s} + u_n \frac{\partial u_n}{\partial n} + u_s(u_s K_s - u_n K_n) = -\frac{1}{\rho} \frac{\partial p}{\partial n} \quad (\text{A.52})$$

# Appendix B

## Abstract in French

La question de la pollution sonore autour des aéroports devient de plus en plus urgente à mesure que le trafic aérien augmente. D'après l'ICAO (International Civil Aviation Organisation), le nombre de passagers-kilomètres a augmenté de 70% entre 2007 et 2017 [ICAO, 2017]. L'ACARE (Advisory Council for Aeronautics Research in Europe) a été mis en place pour guider et encourager la recherche aéronautique en Europe, avec des objectifs ambitieux pour 2050. L'organisation vise en particulier la réduction de 65% du niveau de bruit aérien perçu par rapport à l'année 2000 [ACARE, 2017]. Plusieurs sources de bruit sont présentes au niveau des réacteurs, qui sont la cause d'une partie conséquente du bruit d'un avion. Les bruits de soufflante et de jet sont les sources principales, mais elles ont été réduites de façon significative ces dernières années, de sorte que la contribution relative des sources internes au moteur a augmenté.

En plus de contribuer au bruit émis par un moteur en champs lointain, ces sources internes peuvent interagir avec la flamme dans la chambre de combustion, ce qui peut participer au déclenchement d'instabilités thermo-acoustiques. Des marges de sécurité importantes permettent de les éviter, mais c'est au prix d'une augmentation des émissions du moteur, notamment d'oxydes d'azote ( $\text{NO}_x$ ), qui réduisent la qualité de l'air et sont à l'origine de pluies acides. Leur effet particulièrement néfaste sur l'environnement et la santé explique l'objectif ACARE de réduire leur émission de 90 % d'ici 2050. Une meilleure compréhension des sources de bruit internes du moteur pourrait permettre de réduire le risque d'instabilité de combustion ainsi que les émissions de  $\text{NO}_x$ .

Une des sources principales de bruit interne est le bruit de combustion qui est composé de deux phénomènes distincts : les bruits direct (BCD) et indirect (BCI). Le BCD est dû à la fluctuation du flux de chaleur au niveau de la flamme dans la chambre de combustion [Candel et al., 2009, Hassan, 1974]. Le BCI quant à lui est généré par l'accélération d'hétérogénéités résultant de la combustion à travers le reste du moteur. Ce peut être des fluctuations de composition, de vorticit  ou de température, qui sont responsables du bruit de composition, de vorticit  et du bruit entropique respectivement. Cette th se porte sur ce dernier.

L' tude des m canismes   l'origine du bruit entropique est donc motiv e   la fois par la r duction du bruit  mis et la meilleure compr hension des instabilit s de combustion. La prise en compte du bruit entropique dans un contexte industriel pendant les phases de conception d'un r acteur n cessite aussi le d veloppement d'outils pr cis et   bas co t. En effet, les m thodes exp rimentales et num riques disponibles sont co teuses et complexes   cause

de conditions de fonctionnement extrêmes, de réactions chimiques, d'échanges de chaleur, d'écoulements complexes et de réflexions acoustiques. Expérimentalement, ces difficultés conduisent en particulier à des problèmes de séparation des bruits de combustion direct et indirect ou de mesures de température, alors que le coût des simulations permettant de capturer les fluctuations acoustiques est limitant numériquement. Ces enjeux motivent le développement de méthodes semi-analytiques qui sont un outil complémentaire intéressant pour mieux comprendre les mécanismes du bruit entropique, et qui pourraient devenir une alternative performante pour des développements industriels.

Dans les années 1970, l'étude du bruit entropique a abouti à des modèles compacts de référence à la fois pour des tuyères et des turbines. Plus récemment, des travaux expérimentaux [Bake et al., 2009b, De Domenico et al., 2017] et numériques [Leyko et al., 2011, Moreau et al., 2018, Mühlbauer et al., 2009] ont permis une meilleure compréhension du bruit entropique dans le cas de la tuyère, et des études sont en cours pour mieux comprendre cette source de bruit complexe. Plusieurs modèles 1D ont été développés [Durán and Moreau, 2013b, Giauque et al., 2012, Goh and Morgans, 2011, Huet and Giauque, 2013a, Moase et al., 2007, Stow et al., 2002], ainsi que des modèles 2D, à la fois dans la direction radiale [Zheng, 2016, Zheng et al., 2015] et circonférentielle [Dowling and Mahmoudi, 2015, Durán and Morgans, 2015]. Zheng a mis en évidence l'impact des variations radiales de l'écoulement sur le bruit entropique, mais son modèle requiert une validation plus poussée. Une fois validé, le modèle pourrait être étendu au cas de la turbine, qui a été moins étudiée que la tuyère à cause de la complexité de l'écoulement, bien que la turbine soit responsable de la majeure partie du bruit entropique généré. Il y a eu peu d'études analytiques de la turbine, qui se limitent actuellement au cas compact, mais plusieurs projets numériques [Becerril Aguirre, 2017, Ceci et al., 2019, Wang et al., 2016] et expérimentaux [Beard et al., 2009, Persico et al., 2012] ont commencé ces dernières années, avec pour objectif de mieux comprendre les mécanismes de génération du bruit entropique dans des étages de turbines.

Dans ce contexte, l'objectif de cette étude est de mieux comprendre les mécanismes de génération du bruit entropique dans un stator de turbine, ainsi que d'étendre le modèle 2D développé par Zheng pour la tuyère au cas du stator.

Pour cela, cette thèse est articulée comme suit. Tout d'abord, une étude bibliographique ainsi que les méthodes numériques utilisées sont présentées dans les chapitres 1 et 2 respectivement. Le chapitre 3 concerne l'étude du bruit entropique dans une tuyère. Un cas de référence CAA (Computational AeroAcoustics) est mis en place pour comparaison avec des modèles analytiques, afin de mettre en évidence les effets bi-dimensionnels sur le bruit entropique et de valider le modèle 2D CHEOPS-Nozzle développé par Zheng. Dans le chapitre suivant, ce modèle est étendu au cas du stator de turbine. Les niveaux de bruit entropique obtenus sont comparés à ceux résultant de simulations CAA 2D dans le chapitre 5, de la même manière que pour la tuyère. Ceci permet de mettre en évidence les limites de certaines hypothèses du modèle dans le cas du stator et d'investiguer le bruit entropique dans de telles géométries. Enfin, l'impact des effets tridimensionnels et visqueux sur le bruit entropique dans un stator est vérifié grâce à un calcul ZDES (Zonal Detached Eddy Simulation), dans le chapitre 6.

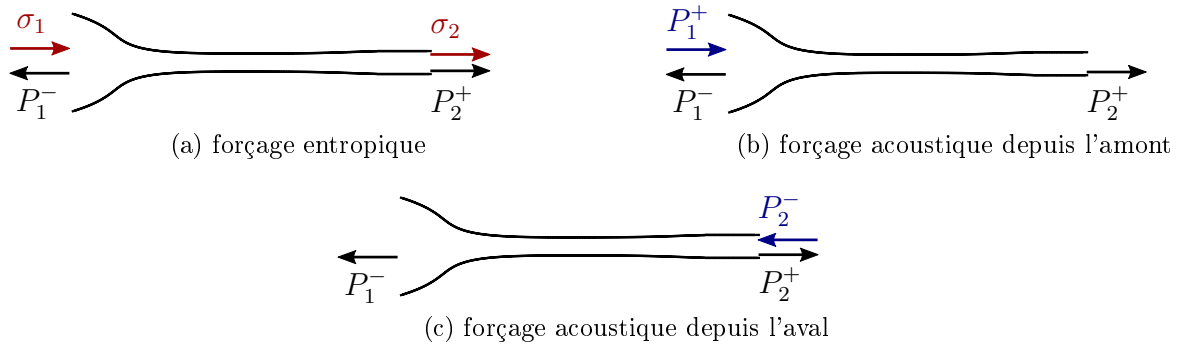


Figure B.1: Schémas des ondes présentes pour chacun des forçages étudiés en subsonique.

L'étude bibliographique présentée dans le chapitre 1 s'intéresse à l'état de l'art des études analytiques pour la prédiction du bruit entropique dans un premier temps, puis aux avancées vers une meilleure compréhension des mécanismes physiques à l'origine de ce bruit. L'évolution de modèles compacts développés dans les années 1970 jusqu'à des modèles 1D puis 2D est présentée, et les solutions compactes pour la tuyère [Marble and Candel, 1977] et la turbine [Cumpsty and Marble, 1977], le modèle 1D MARCAN [Giauque et al., 2012, Huet et al., 2016] et le modèle 2D CHEOPS-Nozzle [Zheng, 2016], tous utilisés dans cette thèse, sont détaillés. L'état de l'art sur la génération de bruit entropique est ensuite brièvement présenté, en se focalisant sur l'atténuation des perturbations entropiques, des campagnes d'essais de référence, les mécanismes fondamentaux du bruit entropique, et en particulier les effets d'interaction avec la vorticit , de tridimensionnalit  et d' coulement de turbine complexes.

Deux types de simulations num riques sont utilis s dans cette th se : la CFD, pour le calcul de champs porteurs Euler et RANS ainsi que pour un calcul 3D ZDES, et la CAA, pour la propagation d'ondes acoustiques et la convection de perturbations hydrodynamiques. La description des m thodes utilis es dans ces deux cas fait l'objet du chapitre 2. Celles associ es au code de CFD CEDRE [Refloch et al., 2011], qui est d velopp    l'ONERA, sont pr sent es en premier. Les  quations de Navier-Stokes, d'Euler et RANS sont rappel es, mais aussi les particularit s des simulations LES, DES97 et DDES, avant de pr senter les  quations utilis es pour la ZDES. Les m thodes permettant l'injection de fluctuations entropiques ou acoustiques dans le domaine, et les conditions de non-r flexion aux fronti res sont  galement d taill es. Dans une seconde partie, les  quations du code CAA sAbrinA\_v0 [Redonnet, 2010, Redonnet et al., 2001],  galement d velopp    l'ONERA, sont d crites, ainsi que les conditions limites qui permettent   la fois l'injection de fluctuations et la non-r flexion aux fronti res.

Le bruit entropique dans la tuy re est  tudi  dans le chapitre 3. Des simulations CAA sont mises en place pour  tudier l'effet de la bidimensionnalit  de l' coulement sur le bruit entropique dans ces g om tries, ainsi que pour servir de r f rence en comparaison   des mod les semi-analytiques et pour valider le mod le 2D CHEOPS-Nozzle en particulier. La CAA est particuli rement bien adapt e   cela parce qu'elle permet de prendre des hypoth ses simpli-

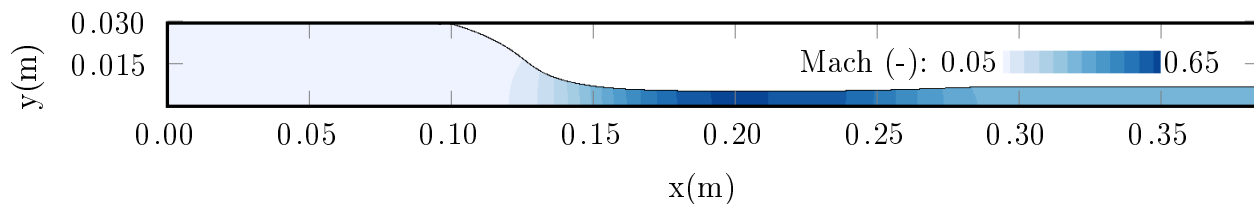


Figure B.2: Nombre de Mach dans la tuyère.

ficatrices similaires à celles des modèles. On s'intéresse à une tuyère convergente-divergente subsonique, dans laquelle trois types de fluctuations, illustrés Fig. B.1, sont injectées. Dans le premier cas, des perturbations entropiques sont injectées par l'amont afin de calculer le bruit entropique résultant de leur accélération à travers la tuyère. Comme il existe d'autres sources de bruit dans un turboréacteur, on s'intéresse aussi à la dispersion d'ondes acoustiques à travers la tuyère. Pour les deux autres cas étudiés, des fluctuations acoustiques sont donc injectées par l'amont ou par l'aval du domaine, comme le montrent les Figs. B.1b et B.1c respectivement. Une coupe axi-symétrique de la tuyère DISCERN, conçue pour maximiser le bruit entropique, est utilisée avec des conduits à l'amont et à l'aval de celle-ci pour le post-traitement acoustique. Suite à la construction d'un maillage non-structuré, les équations Euler sont résolues avec le code CEDRE afin d'obtenir des champs porteurs qui serviront d'entrée à la fois à la CAA et aux modèles. Celui-ci est représenté par le contour du nombre de Mach sur la Fig. B.2.

Les champs fluctuants sont d'abord estimés avec le modèle bidimensionnel CHEOPS-Nozzle, qui prend en compte les variations radiales de l'écoulement. Un maillage 2D structuré est construit et les champs moyens  $y$  sont interpolés. Des ondes planes sont utilisées dans les trois cas étudiés : l'injection de perturbations entropiques par l'amont et le forçage acoustique soit par l'entrée du domaine, soit par l'aval. Les fréquences de forçages sont fixées entre 0 et 1000 Hz avec un pas de 10 Hz. On obtient des fonctions de transfert, donnant le niveau de bruit obtenus pour chacun des forçages, et leur convergence avec la taille du maillage et le nombre de tubes de courant utilisés notamment pour modéliser la convection des fluctuations d'entropie est vérifiée. Les niveaux de bruit sont également simulés grâce à la CAA, dont les hypothèses sont similaires à celles du modèle 2D. Pour cela, un maillage structuré est construit dans la tuyère 3D divisée en 5 domaines. Il est dimensionné pour avoir au moins 16 points par longueur d'onde. Les champs moyens 2D-axisymétriques sont interpolés sur ce maillage. Les conditions limites non-réfléchissantes de Tam et al. [Tam and Dong, 1996, Tam and Webb, 1993] sont appliquées afin de limiter la pollution par des réflexions numériques aux frontières du domaine. Ces conditions limites permettent également d'injecter des fluctuations par l'amont ou par l'aval du domaine, excitant ainsi l'écoulement. Pour les trois forçages étudiés, les fréquences sont fixées entre 100 et 1000 Hz avec un pas de 100 Hz. La CAA permet des simulations multi-harmoniques, et l'écoulement peut être excité à toutes ces fréquences en même temps. Les équations d'Euler linéarisées sont résolues avec un pas de temps de  $8.10^{-8}$  secondes, de sorte que le nombre de CFL atteint 0.73 au maximum. 220 processeurs sont utilisés pour ces simulations. Le post-traitement de ces calculs est fait en plusieurs étapes. D'abord, les perturbations entropiques sont calculées. Les fluctuations de pression doivent ensuite être séparées en deux parties, se propageant vers l'amont et l'aval respectivement,

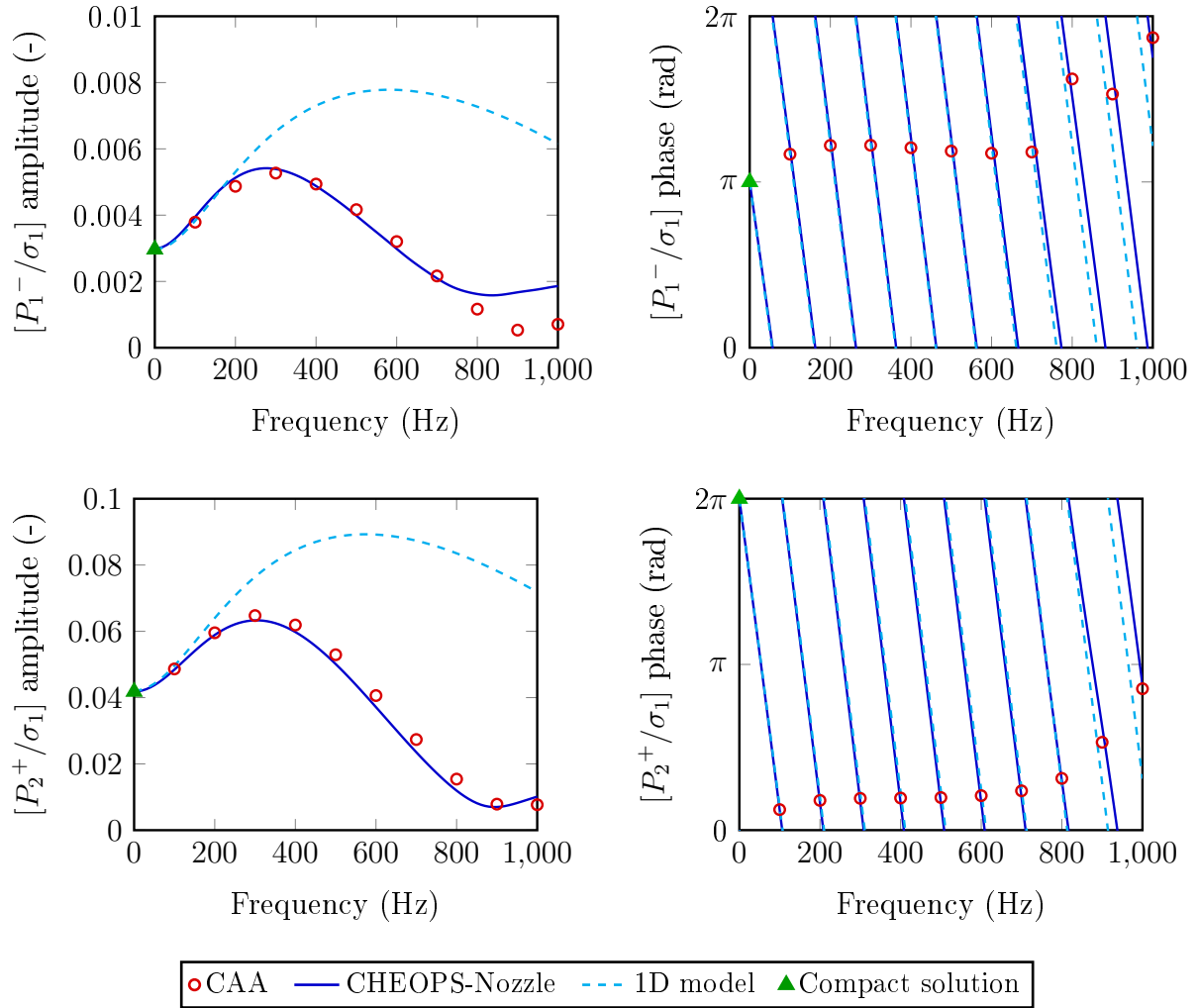


Figure B.3: Amplitude et phase des fonctions de transfert entropiques  $[P_1^-/\sigma_1]$  (haut) et  $[P_2^+/\sigma_1]$  (bas) obtenues par la CAA, CHEOPS-Nozzle, le modèle 1D MARCAN [Giauque et al., 2012, Huet et al., 2016] et la solution compacte de Marble and Candel [Marble and Candel, 1977].





Suite à la validation du modèle 2D pour la tuyère CHEOPS-Nozzle, celui-ci peut être

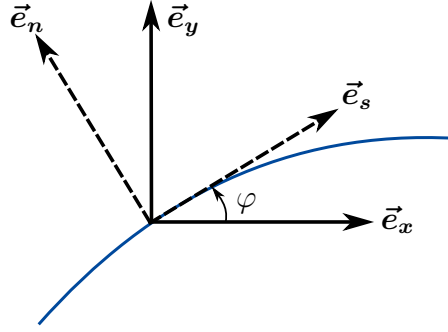


Figure B.5: Vecteurs unitaires du système de coordonnées cartésien ( $\vec{e}_x, \vec{e}_y$ ) et du système de coordonnées mobile ( $\vec{e}_s, \vec{e}_n$ ) en un point le long d'une ligne de courant.

étendu au cas du stator de turbine. C'est l'objectif du chapitre 4. Afin de dériver les équations du modèle, ses hypothèses doivent d'abord être adaptées. On suppose un écoulement 2D plan et non visqueux, pour lequel les fluctuations de pression et de vitesse sont purement acoustiques, négligeant la vorticité, et les ondes acoustiques sont 1D et orientées selon la direction  $x$ . Enfin, on admet que les perturbations sont petites, de sorte que les équations peuvent être linéarisées. Le système de coordonnées utilisé est ensuite redéfini, le système de coordonnées cylindrique de CHEOPS-Nozzle n'étant pas adapté aux configurations 2D planes. Un système de coordonnées mobile qui suit les lignes de courant est adopté. Il est illustré par la Fig. B.5. Comme par la suite les équations sont appliquées dans les tubes de courant, ce référentiel permet des simplifications. Les coordonnées sont projetées dans le repère cartésien, qui correspond au repère privilégié des ondes acoustiques qui sont 1D et se propagent dans la direction axiale, et la matrice jacobienne est construite. Les équations du modèle peuvent alors être dérivées. Les équations d'Euler dans le repère mobile sont linéarisées. Les fluctuations d'entropie sont ensuite substituées aux termes de masse volumique correspondants aux termes sources du modèle. Puis, les équations sont écrites dans le domaine fréquentiel, en supposant un régime harmonique, ce qui permet d'éliminer les dérivées temporelles. Enfin, les équations sont moyennées dans chaque section pour pouvoir les résoudre.

En plus des équations du modèle, sa méthode de résolution doit aussi être adaptée au cas du stator. Tout d'abord, comme pour la tuyère, un champ porteur doit être interpolé sur un maillage structuré bidimensionnel et à plans  $x$  constant, afin de pouvoir moyenner les équations. Des lignes de courant sont ensuite obtenues, soit par génération par le modèle, soit à l'aide d'un logiciel tierce. En plus de permettre la simplification des équations, ces lignes de courants facilitent le calcul de fluctuations entropiques dans la prochaine étape. Une fois ces perturbations entropiques calculées en 2D, les variables moyennes et fluctuantes peuvent être moyennées pour pouvoir résoudre les équations. Un schéma d'ordre 2 est ensuite utilisé pour la discrétisation spatiale. Enfin, deux conditions limites sont nécessaires pour fermer le système d'équations. Celles-ci décrivent les réflexions acoustiques aux frontières du domaine. Une fois les équations résolues, les fonctions de transfert sont calculées.

Le modèle est ensuite appliqué au stator de turbine utilisé dans le projet européen FP7 RECORD. Deux types de champs porteurs sont simulés avec le code CEDRE, en résolvant les

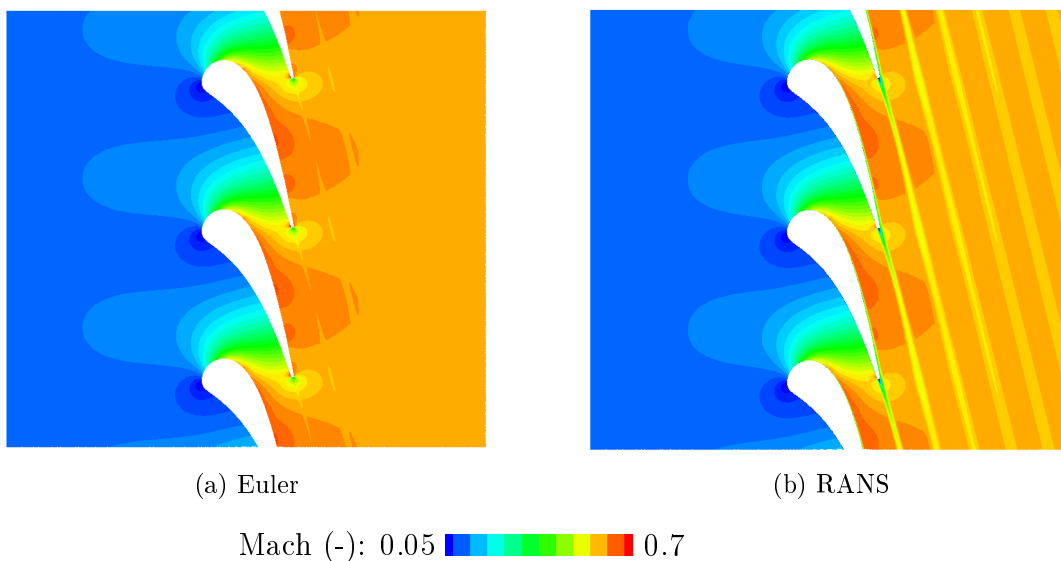


Figure B.6: Nombre de Mach moyen.

équations d'Euler et RANS respectivement. Ils font l'objet de la Fig. B.6. La convergence des résultats est vérifiée en maillage et en nombre de tubes de courant. Les niveaux de bruit entropique obtenus sont aussi comparés à ceux estimés avec une version du modèle de Cumpsty and Marble [1977] modifiée pour négliger la vorticit . Ceux-ci sont en bon accord avec les for ages acoustiques, mais ils sont sous-estim s par le mod le 2D dans le cas entropique. Ceci peut  tre expliqu  par l'hypoth se d'acoustique 1D, ce qui est d taill  dans le chapitre suivant.

L'objectif du chapitre 5 est d' tudier le bruit entropique dans un stator de turbine 2D et de construire un cas de r f rence pour la comparaison avec le mod le CHEOPS-Stator d crit au chapitre pr c dent. Pour cela, des simulations CAA sont mises en place, comme au chapitre 3 pour la tuy re. Les m mes champs porteurs que ceux pr sent s Fig. B.6 sont utilis s en entr e, apr s interpolation sur un maillage acoustique structur . Comme pour la tuy re, les conditions limites de Tam et al. [Tam and Dong, 1996, Tam and Webb, 1993] sont utilis es   la fois pour injecter des fluctuations acoustiques ou entropiques et comme conditions non-r fl chissantes, et le m me post-traitement est appliqu . Les simulations sont lanc es en parall le sur 12 processeurs. Le bruit simul  est d'abord analys , puis compar  aux niveaux estim s par le mod le CHEOPS-Stator.

Afin d' tudier le bruit r sultant des simulations CAA, on s'int resse d'abord aux perturbations entropiques. Les diff rences obtenues avec des champs porteur Euler ou RANS, qui sont locales au niveaux des couches limites et du sillage, sont isol es. L' volution des fluctuations de pression   travers le stator est ensuite  tudi e dans diff rents cas. On note que les ondes acoustiques sont 1D dans les conduits   l'amont et   l'aval de la pale, ce qui correspond   nos attentes. En revanche, cette hypoth se ne tient pas   proximit  de l'aube, qui est non-compacte. Les fluctuations de pression varient dans la direction perpendiculaire   l' coulement. Les contours de fluctuations d'entropie et de pression sont compar es   dif-

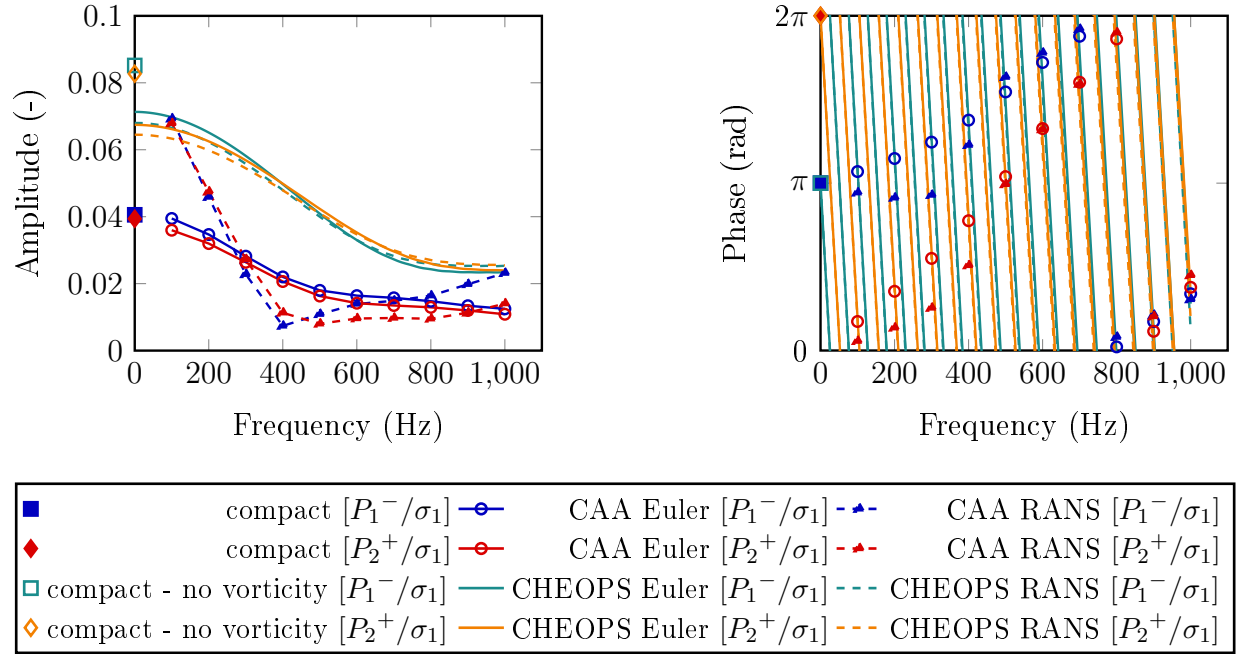


Figure B.7: Amplitude et phase des fonctions de transfert entropiques  $[P_1^-/\sigma_1]$  et  $[P_2^+/\sigma_1]$ , obtenues avec CHEOPS-Stator et la CAA avec des champs Euler et RANS, ainsi que la solution compacte de Cumpsty and Marble [1977].

férentes fréquences et avec les deux champs porteur étudiés. Dans le cas du champs Euler, on note en particulier que l'instant auquel des perturbations entropiques positives remplissent le canal inter-aube correspond au maximum des fluctuations de pression. Celles-ci se concentrent sur la première partie de la face en dépression et au bord de fuite, et elles sont plus élevées à 400 Hz qu'à 100 ou 1000 Hz. De plus, plus la fréquence est basse, plus la longueur d'onde est importante et plus la région de fluctuations de pression positives s'étend le long de la face en dépression du stator. On retrouve le même comportement avec le champs RANS, sauf à 100 Hz. En effet, à cette fréquence, l'instant auquel les fluctuations de pression sont maximales ne correspond pas à un instant auquel des perturbations entropiques positives sont dans le canal inter-aube. Par ailleurs, l'analyse des fluctuations de vitesse indique la présence de vorticit   à l'aval du stator. Bien que l'utilisation des invariants de Riemann implique l'hypoth  se d'acoustique 1D, ils donnent les m  me niveaux de bruit qu'en utilisant la DMM, ce qui indique le bon fonctionnement du filtrage des fluctuations post-trait  es et valide les deux m  thodes de s  paration des signaux. Les niveaux de bruit obtenus sont ensuite pr  sent  s sous forme de fonctions de transfert.

Ces r  sultats peuvent   tre compar  s    ceux du mod  le 2D CHEOPS-Stator. Le bon accord entre les perturbations entropiques mod  lis  es et simul  es est v  rifi   dans un premier temps. Les niveaux de bruit obtenus sont ensuite compar  s en   tudiant les fonctions de transfert. Elles sont repr  sent  es Fig B.7 dans le cas d'un for  age entropique. Concentrons nous d'abord sur les r  sultats de la CAA. Pour les deux champs moyens   tudi  s, les ondes transmises et r  fl  chies ont des amplitudes proches. Bien que la CAA ne permette pas

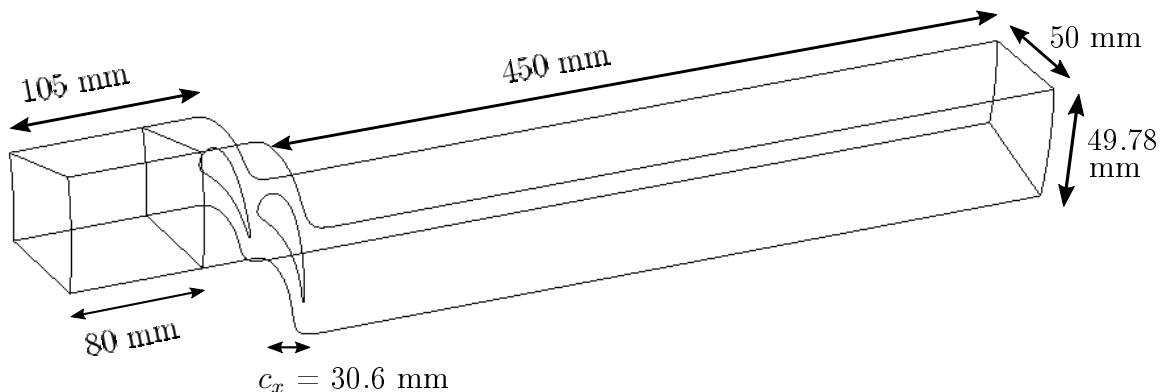


Figure B.8: Géométrie utilisée pour simuler le bruit dans un canal de stator isolé de turbine.

de forcer la tuyère jusqu'à 0 Hz, les fonctions de transfert obtenues avec des champs Euler sont en bon accord avec la solution compacte de Cumpsty and Marble [1977], à la fois en amplitude et en phase. L'amplitude des fonctions de transfert diminue quand la fréquence augmente, avec une pente plus lente à partir d'environ 500 Hz. Ce changement de pente est plus marqué avec un champ porteur RANS, pour lequel les amplitudes suivent la même tendance qu'avec les champs Euler, mais avec de plus fortes variations. C'est aussi le cas pour les forçages acoustiques dont les résultats ne sont pas représentés dans ce résumé. Pour les trois types de forçages, les amplitudes obtenues avec le modèle 2D CHEOPS-Stator sont surestimées par rapport à la CAA. On rappelle que les hypothèses des deux méthodes sont similaires, à l'exception des hypothèses d'acoustique 1D et de vorticit  négligeable prises par le modèle. L'analyse des simulations numériques a montré que ces hypothèses ne sont pas vérifiées dans le stator, ce qui peut expliquer les différences de niveau de bruit obtenues. Une version du modèle de Cumpsty and Marble [1977] modifiée pour négliger la vorticit  est utilisée pour dissocier l'effet des deux hypothèses du modèle 2D. Les amplitudes obtenues sont fortement surestimées par rapport à celles issues de la solution compacte complète. Avec un forçage acoustique, ces niveaux correspondent à ceux obtenus avec CHEOPS-Stator à 0 Hz, de sorte que la vorticit  semble  tre la principale responsable des différences entre les résultats du modèle 2D et de la CAA. Néanmoins, les amplitudes issues de CHEOPS-Stator sont inférieures à la solution compacte modifiée dans le cas du forçage entropique, comme l'illustre la Fig. B.7. Ceci indique que les différences entre le modèle 2D et la CAA dans ce dernier cas seraient dues à la fois à l'hypothèse de vorticit  néglig e et d'acoustique 1D. Enfin, on note que ces deux effets semblent aussi  tre à la source des différences entre les résultats obtenus par la CAA avec des champs Euler et RANS, comme les niveaux de bruit estimés avec le modèle sont très proches avec ces deux types de champs.

Après avoir étudi  la g n ration de bruit entropique dans un stator 2D dans le chapitre 5, on s'int resse au cas 3D dans le chapitre 6. Pour cela, un calcul ZDES est effectu , ce qui permet aussi de prendre en compte l'effet visqueux. La m me aube de stator que dans les chapitres pr c dents est utilis e, cette fois compl te en 3D, et des canaux sont ajout s à l'amont et à l'aval de la pale comme le montre la Fig. B.8. Un maillage non-structur  de 147 million de points est construit. La simulation est r alis e avec le code CEDRE et le domaine

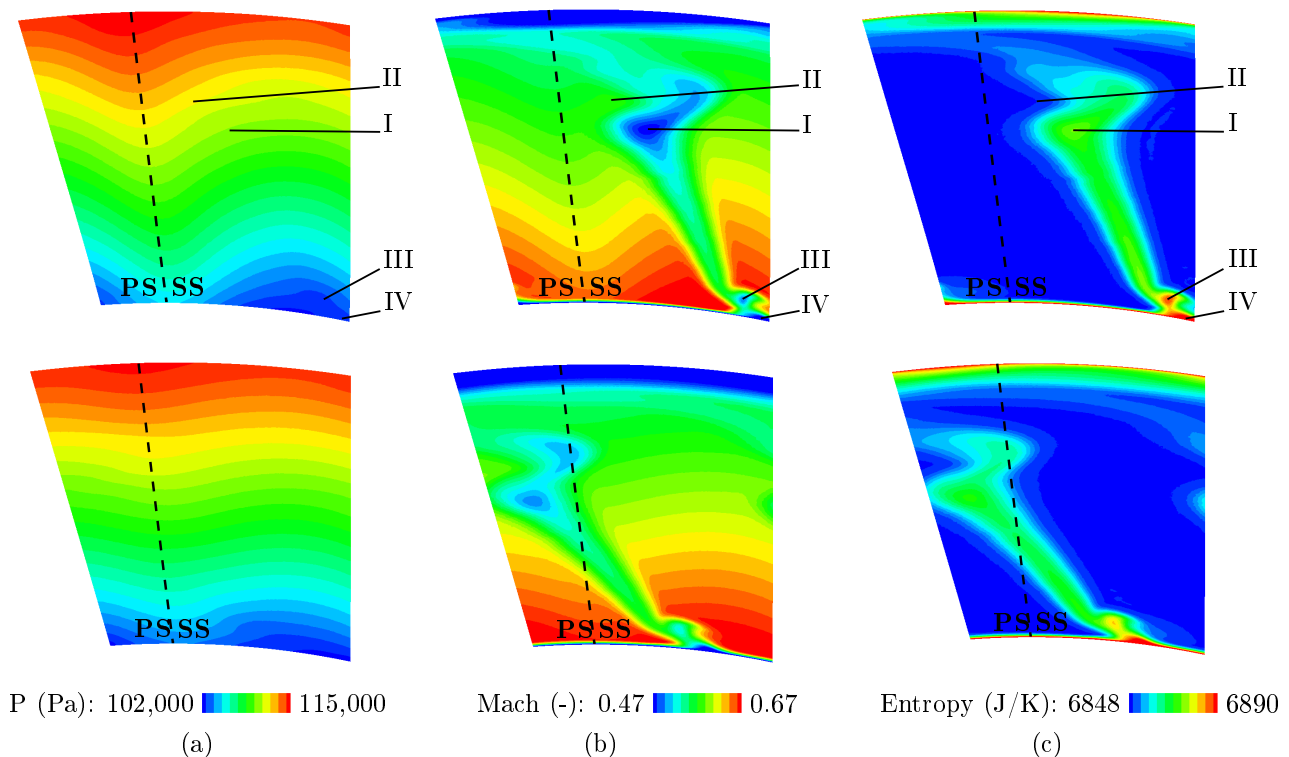


Figure B.9: Champs moyens simulés avec le calcul sans forçage et représentés dans des coupes axiales à 32% (haut) et 50% (bas) d'une corde axiale à l'aval du bord de fuite.

de calcul est séparé en deux zones. Les équations URANS sont résolues dans la première zone, qui occupe le conduit amont jusqu'à environ une corde axiale à l'amont de l'aube et dans laquelle l'écoulement est uniforme. La seconde zone correspond au reste du domaine et les équations ZDES mode II y sont résolues. Le modèle de turbulence de Spallart-Almaras est choisi et les schémas de discrétisation en temps et en espace sont d'ordre 2. Des conditions limites non-réfléchissantes et permettant d'injecter des perturbations entropiques ou acoustiques sont utilisées. Une onde multi-harmonique est injectée afin d'exciter l'écoulement sur une gamme de fréquence de 100 à 1000 Hz avec un pas de 100 Hz. Comme pour les cas de la tuyère et du stator 2D, trois types d'ondes sont étudiées dans trois simulations différentes : des perturbations entropiques injectées par l'amont et des fluctuations acoustiques se propageant vers l'aval et vers l'amont respectivement. De plus, un calcul de référence, sans forçage, est simulé. 1736 et 2016 processeurs ont été utilisés pour ces calculs sur une machine de l'ONERA et du GENCI respectivement, pour un total de 1,25 million d'heures CPU.

Avant d'étudier la réponse acoustique du stator, l'écoulement est décrit du point de vue aérodynamique. On s'intéresse d'abord à l'écoulement moyen. L'effet de l'équilibre radial et des tourbillons de coin est mis en évidence grâce à des coupes aube-à-aube du stator à mi-hauteur de pale, proche moyeu et proche carter. Des coupes axiales à deux positions à l'aval du stator permettent quant à elles de décrire l'évolution des tourbillons secondaires

et du sillage. Elles sont représentées Fig. B.9. L'équilibre radial et les tourbillons sont également visibles sur les profils radiaux de champs moyennés suivant l'azimut. Ces derniers permettent de comparer les champs moyens obtenus avec le calcul de référence et les trois simulations forcées. On note des différences, notamment vers le carter, mais celles-ci sont locales et d'amplitude assez faible pour qu'on s'attende à ce qu'elles aient un impact limité sur l'acoustique. Les champs instantanés permettent aussi de mettre en évidence les tourbillons et leur dissipation à mesure qu'ils sont convectés. La turbulence n'est pas déclenchée dans ces simulations, ce qui semble provenir de la version du modèle de turbulence utilisée. L'impact de cet écoulement hautement tridimensionnel et visqueux est étudié par la suite par comparaison aux simulations CAA présentées dans le chapitre précédent.

D'abord, différents éléments des simulations sont vérifiés. L'effet du filtrage hydrodynamique est étudié. Il est effectué de la même manière que pour les simulations CAA dans les chapitres 3 et 5, en moyennant sur chaque section puis en appliquant un filtrage aux caractéristiques. L'effet du post-traitement non-réfléchissant et la présence de réflexions numériques sont ensuite investigués. Enfin, on vérifie le bon rapport signal sur bruit des simulations. Suite à ces vérifications, le bruit généré est étudié. L'évolution du champ de fluctuations entropiques est analysé à différentes hauteurs de pale. Les fonctions de transfert obtenues pour un forçage entropique sont représentées Fig. B.10. Celle-ci montre les courbes obtenues au chapitre précédent grâce à la CAA, à la fois avec des champs porteur Euler et RANS, ainsi que les résultats de la ZDES obtenus soit avec les invariants de Riemann, soit par la DMM pour séparer les ondes acoustiques. Ces deux méthodes donnent des résultats en bon accord pour l'onde réfléchie, mais on note des écarts à basse fréquence pour l'onde transmise vers l'aval où des tourbillons perturbent l'écoulement. Des pics apparaissent avec la DMM, ce qui semble indiquer que cette approche est plus sensible aux perturbations hydrodynamiques. Leur bon accord sur le reste de la gamme de fréquence donne confiance dans les niveaux de bruit obtenus. Les fonctions de transfert résultant de la ZDES et de la CAA avec des champs Euler sont globalement très proches, à la fois en amplitude, un peu plus élevée avec la ZDES aux moyennes fréquences, et en phase pour laquelle on note un léger déphasage. Les niveaux obtenus avec les calculs 3D sont plus proches de ceux résultant des simulations CAA avec des champs Euler que RANS. La poursuite de cette étude permettrait de comprendre ces différences et de valider les résultats de la CAA avec des champs moyens RANS. Les conclusions sont similaires pour les fonctions de transfert acoustiques, qui permettent également de mettre en évidence la compacité acoustique du stator.

Après une discussion des conclusions de chacun des chapitres, les conclusions générales de la thèse sont présentées. On rappelle son objectif d'améliorer la compréhension du bruit entropique dans les stators de turbine et d'étendre le modèle 2D non-compact pour la tuyère CHEOPS-Nozzle au cas du stator. Pour cela, un cas de référence CAA est mis en place pour la tuyère et le modèle est validé dans le chapitre 3. Il peut alors être étendu au stator dans le chapitre 4. Cette nouvelle version du modèle est comparée à des simulations CAA dans le chapitre suivant, qui permet de caractériser le bruit entropique dans un stator 2D et de discuter des hypothèses du modèle. Enfin, le chapitre 6 montre que les effets 3D et visqueux ont un impact limité sur les niveaux de bruit obtenus.

Cette thèse mène à de nombreuses perspectives de poursuite d'étude. Les variations circonférentielles de l'écoulement et la viscosité pourraient être prises en compte dans le cas

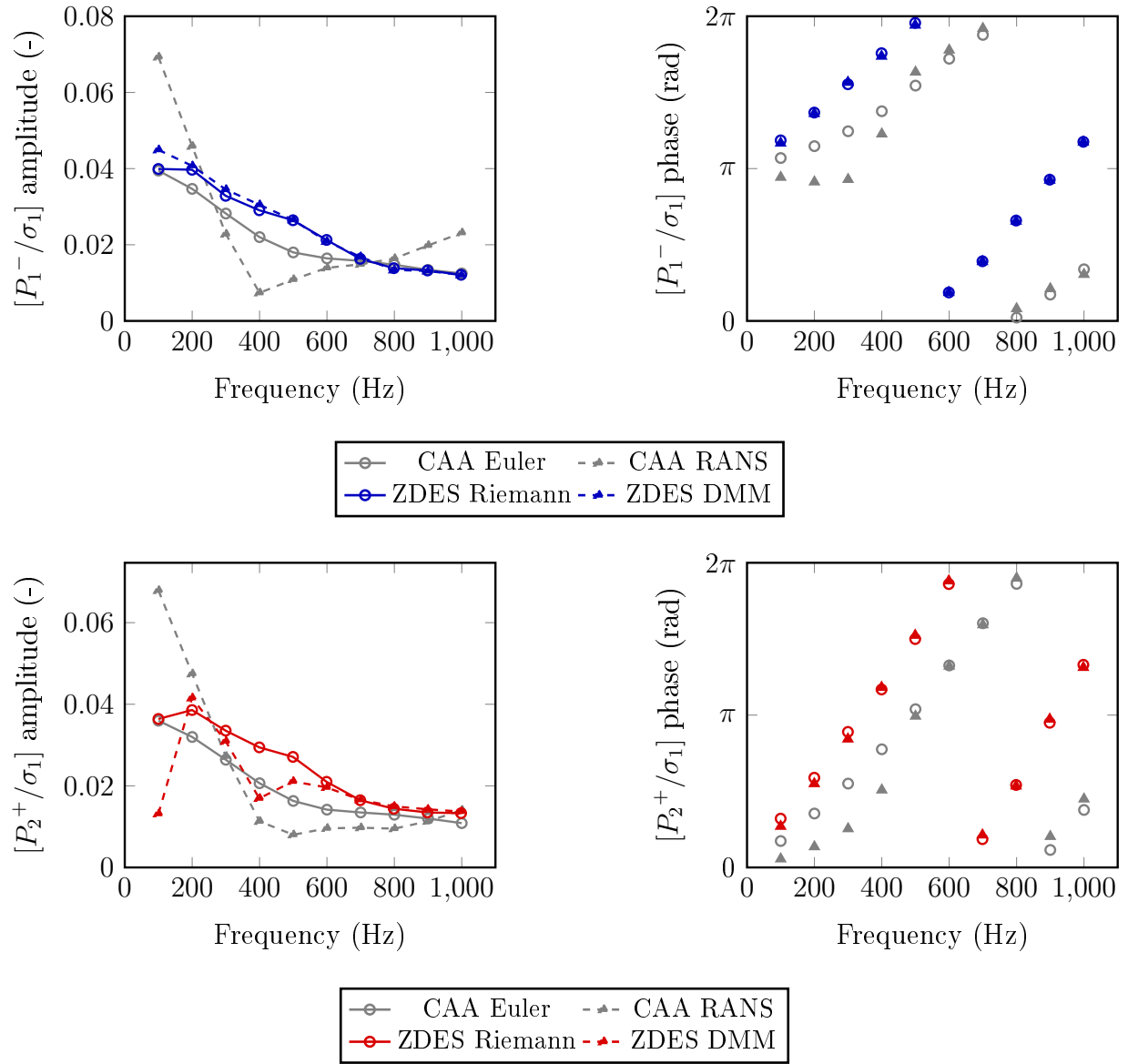


Figure B.10: Amplitude et phase des fonctions de transfert entropiques  $[P_1^-/\sigma_1]$  et  $[P_2^+/\sigma_1]$ , obtenues par des simulations ZDES post-traitées soit avec les invariants de Riemann soit avec la DMM, et par des calculs CAA avec des champs Euler ou RANS.

de la tuyère. Le modèle CHEOPS-Stator doit aussi être étendu pour prendre en compte la vorticit  et les variations azimutales des ondes acoustiques. De plus, les simulations CAA avec des champs RANS devraient  tre valid es et leur analyse approfondie. Concernant l' tude 3D du bruit entropique dans un stator de turbine, il pourrait  tre int ressant d'injecter des ondes plus r alistes en entr e,   la fois en amplitude et de part la forme des perturbations. Enfin, cette  tude est une premi re  tape vers l' tude du bruit entropique dans un  tage complet de turbine, en passant par l' tude d'un rotor isol .





# List of Figures

1.1	Sketch of the configuration considered in Cumpsty and Marble's [1977] compact model. This figure is adapted from Leyko et al. [2014]. . . . .	10
1.2	Resolution process of CHEOPS-Nozzle. . . . .	19
1.3	Contours of reduced entropy concentration, $S$ , on a symmetry plane of $z = 0$ , at four time instants after the impulsive entropy source injection into the time-varying combustor flow-field [Xia et al., 2018]. . . . .	21
1.4	Sketches of the (a) EWG [Bake et al., 2007] and (b) HAT [Knobloch et al., 2015a] test-facilities at DLR. . . . .	23
1.5	Snapshot showing the pressure field generated as an entropy line pulse is convected through a fixed turbine blade. In this figure, red is compression (high pressure) and blue is rarefaction (low pressure). [Tam and Parrish, 2014] . .	24
1.6	$\ \nabla\rho\ /\rho$ of an instantaneous solution at mid-span without (a) and with (b) an entropy pulse. [Papadogiannis et al., 2016, Wang et al., 2016] . . . . .	26
2.1	Classification of flow problems associated with ZDES modes. I: separation fixed by the geometry, II: separation induced by a pressure gradient on a curved surface, III: separation strongly influenced by the dynamics of the incoming boundary layer [Deck, 2012]. . . . .	34
2.2	Amplitude and phase error over the distance convected and for a range of entropy wave spatial discretisation [Huet and Vuillot, 2017]. . . . .	36
3.1	Diagrams of the waves involved for each forcing type in the subsonic case. . .	43
3.2	Contour of the Mach number in the nozzle. . . . .	44
3.3	Amplitude of the transfer function $[P_2^+/\sigma_1]$ computed using CHEOPS-Nozzle for a varying mesh size or number of streamlines. . . . .	45
3.4	CAA geometry and structured mesh. (b) and (c) have different scales. . . . .	46
3.5	Density fluctuations injected into the computational domain in the entropy-forced case. . . . .	48
3.6	Pressure fluctuations measured in the entropic forcing case on the nozzle axis in the exit plane. . . . .	48
3.7	Contour of normalised entropy fluctuations in an axial plane in the multi-harmonic entropy-forced case. . . . .	49
3.8	RMS values of pressure and velocity fluctuations $p'$ and $u'$ in upstream and downstream ducts. . . . .	50

3.9	Amplitude of the transfer functions resulting from entropic forcing $[P_1^-/\sigma_1]$ (left) and $[P_2^+/\sigma_1]$ (right) computed using CAA with a baseline 2.2 million node mesh, a mesh 1.5 times finer in all directions with 7.5 million elements and harmonic simulations. . . . .	52
3.10	Amplitude of the transfer functions resulting from entropic forcing $[P_1^-/\sigma_1]$ (left) and $[P_2^+/\sigma_1]$ (right) computed using CAA and both the Riemann invariants and DMM for acoustic wave separation. . . . .	53
3.11	Pressure and velocity fluctuations computed as part of the multi-harmonic entropy-forced simulation both at a point of the nozzle axis in the middle of the downstream duct and averaged over the plane, and acoustic velocity fluctuations computed from the impedance relation for a plane progressive wave $u' = p'/(\rho_0 c_0)$ . . . . .	53
3.12	Reflection coefficients obtained for the (a) entropy-forced simulation and (b) the two computations with acoustic forcing. Excitation types are given in brackets. . . . .	54
3.13	Amplitude of the transfer functions $[P_2^+/\sigma_1]$ , $[P_2^+/P_1^+]$ and $[P_2^+/P_2^-]$ computed with and without non-reflective post-processing. . . . .	54
3.14	Amplitude and phase of the transfer functions resulting from entropic forcing $[P_1^-/\sigma_1]$ (top) and $[P_2^+/\sigma_1]$ (bottom) computed using CAA, CHEOPS-Nozzle, the one-dimensional model MARCAN [Giauque et al., 2012, Huet et al., 2016] and Marble and Candel's compact solution [1977]. . . . .	56
3.15	Mean axial velocity (left) and pressure (right) profiles used by the 2D model CHEOPS-Nozzle after sectional averaging and by the 1D model MARCAN [Giauque et al., 2012, Huet et al., 2016]. . . . .	57
3.16	Contour of the normalised entropy fluctuations $\sigma$ inside the nozzle in 1D (top) and 2D (bottom) for harmonic forcing at 1000 Hz. . . . .	57
3.17	Amplitude and phase of the transfer functions resulting from upstream acoustic forcing $[P_1^-/P_1^+]$ (top) and $[P_2^+/P_1^+]$ (bottom) computed using CAA, CHEOPS-Nozzle, the 1D model MARCAN [Giauque et al., 2012, Huet et al., 2016] and Marble and Candel's compact solution [1977]. . . . .	58
3.18	Amplitude and phase of the transfer functions resulting from downstream acoustic forcing $[P_1^-/P_2^-]$ (top) and $[P_2^+/P_2^-]$ (bottom) computed using CAA, CHEOPS-Nozzle, the 1D model MARCAN [Giauque et al., 2012, Huet et al., 2016] and Marble and Candel's compact solution [1977]. . . . .	60
3.19	Pressure fluctuation contours in an axial plane with entropic excitation at 100 and 1,000 Hz respectively. Figures (b) and (d) show the convergent regions of the nozzle with reduced colour contour range. . . . .	61
3.20	Axial velocity fluctuation contours in an axial plane of the nozzle with entropic excitation at 100 and 1,000 Hz. Different colour contour ranges are used upstream and downstream. . . . .	61
4.1	Unit vectors of the Cartesian coordinate system $(\vec{e}_x, \vec{e}_y)$ and the mobile coordinate system $(\vec{e}_s, \vec{e}_n)$ at a point along a streamline. . . . .	65
4.2	Sketch showing the radii of curvature $R_s$ and $R_n$ in the $s$ and $n$ directions respectively. . . . .	66

4.3	Resolution process of CHEOPS-Stator. . . . .	68
4.4	Velocity interpolated by CHEOPS-Stator onto a mesh made of five streamtubes delimited by streamlines (grey lines). The blade and stagnation streamlines are represented by thicker black lines. . . . .	69
4.5	Amplitude and phase of the transfer functions $[P_1^-/P_1^+]$ and $[P_n^+/P_1^+]$ computed using CHEOPS-Nozzle for a varying number of streamlines and mesh size with Euler mean flow. Transfer functions obtained using Cumpsty and Marble's compact solution [1977] assuming negligible vorticity are also represented. . . . .	74
4.6	Amplitude and phase of the transfer functions $[P_1^-/P_n^-]$ and $[P_n^+/P_n^-]$ computed using CHEOPS-Nozzle for a varying number of streamlines and mesh size with Euler mean flow. Transfer functions obtained using Cumpsty and Marble's compact solution [1977] assuming negligible vorticity are also represented. . . . .	75
4.7	Amplitude and phase of the transfer functions $[P_1^-/\sigma_1]$ and $[P_n^+/\sigma_1]$ computed using CHEOPS-Nozzle for a varying number of streamlines and mesh size with Euler mean flow. Transfer functions obtained using Cumpsty and Marble's compact solution [1977] assuming negligible vorticity are also represented. . . . .	76
4.8	Amplitude and phase of the transfer functions $[P_1^-/P_1^+]$ and $[P_n^+/P_1^+]$ computed using CHEOPS-Nozzle for a varying number of streamlines and mesh size with RANS mean flow. . . . .	78
4.9	Amplitude and phase of the transfer functions $[P_1^-/P_n^-]$ and $[P_n^+/P_n^-]$ computed using CHEOPS-Nozzle for a varying number of streamlines and mesh size with RANS mean flow. . . . .	79
4.10	Amplitude and phase of the transfer functions $[P_1^-/\sigma_1]$ and $[P_n^+/\sigma_1]$ computed using CHEOPS-Nozzle for a varying number of streamlines and mesh size with RANS mean flow. . . . .	80
5.1	Geometry used to simulate two-dimensional isolated stator flow with computational domain dimensions. . . . .	84
5.2	Mach number contours of Euler and RANS mean flow fields. . . . .	85
5.3	Acceleration contours of Euler and RANS mean flow fields. . . . .	85
5.4	Sketch of the domains used for CAA and zoom of the mesh at the intersection of the domains on the suction side of the blade, showing both unfiltered (black) and filtered (blue) meshes. . . . .	86
5.5	Pressure fluctuations measured over two time periods $T$ at a point near the exit of the domain in the entropic forcing case with both Euler and RANS mean flows. . . . .	87
5.6	Normalised entropy fluctuations simulated with multi-harmonic entropic forcing and the Euler mean flow field. . . . .	88
5.7	Reflection coefficients obtained for the entropy-forced CAA simulation (left) and the two computations with acoustic excitation (right). Euler and RANS mean flow fields are considered and excitation types are given in brackets. . . . .	88

5.8	Amplitude and phase of transfer functions resulting from entropic excitation with and without non-reflective post-processing and computed with a RANS mean flow. . . . .	89
5.9	Comparison of the shape of the normalised entropy wave $\sigma$ computed with Euler (colour contour) and RANS (isolines) mean flows at 400 Hz and 1,000 Hz.	90
5.10	Pressure fluctuation $p'$ colour contours resulting from multi-harmonic entropy-forced simulations with both Euler (top) and RANS (bottom) mean flows. .	91
5.11	Entropy (top) and pressure (bottom) fluctuation contours resulting from harmonic entropy-forced simulations with both Euler and RANS mean flows. . .	92
5.12	Entropy (top) and pressure (bottom) fluctuation contours computed at different instants of an entropy harmonically forced simulation at 100 Hz with Euler mean flow. The time period is noted $T$ . . . . .	94
5.13	Velocity fluctuation fields resulting from harmonic entropic forcing at 100 Hz (top) and 1,000 Hz (bottom) with Euler mean flow. . . . .	95
5.14	Pressure and velocity fluctuations computed as part of the multi-harmonic entropy-forced simulation both at a point of the downstream duct and averaged over the corresponding plane, and acoustic velocity fluctuations computed from the impedance relation for a plane progressive wave $u' = p'/(\rho_0 c_0)$ . . . . .	96
5.15	Amplitude and phase of the transfer functions resulting from upstream acoustic forcing $[P_1^-/P_1^+]$ and $[P_2^+/P_1^+]$ , computed using Cumpsty and Marble's compact solution [1977] and CAA with Euler and RANS mean flow fields. . .	97
5.16	Amplitude and phase of the transfer functions resulting from downstream acoustic forcing $[P_1^-/P_2^-]$ and $[P_2^+/P_2^-]$ , computed using Cumpsty and Marble's compact solution [1977] and CAA with Euler and RANS mean flow fields.	97
5.17	Amplitude and phase of the transfer functions resulting from entropic forcing $[P_1^-/\sigma_1]$ and $[P_2^+/\sigma_1]$ , computed using Cumpsty and Marble's compact solution [1977] and CAA with Euler and RANS mean flow fields. . . . .	98
5.18	Normalised entropy fluctuations computed at 1,000 Hz using both CHEOPS-Stator and CAA, and with Euler and RANS mean flows. . . . .	100
5.19	Amplitude and phase of the transfer functions resulting from entropic forcing $[P_1^-/\sigma_1]$ and $[P_2^+/\sigma_1]$ , computed using Cumpsty and Marble's compact solution [1977], and CHEOPS-Stator and CAA with Euler and RANS mean flow fields. . . . .	101
5.20	Amplitude and phase of the transfer functions resulting from upstream acoustic forcing $[P_1^-/P_1^+]$ and $[P_2^+/P_1^+]$ , computed using Cumpsty and Marble's compact solution [1977], and CHEOPS-Stator and CAA with Euler and RANS mean flow fields. . . . .	102
5.21	Amplitude and phase of the transfer functions resulting from downstream acoustic forcing $[P_1^-/P_2^-]$ and $[P_2^+/P_2^-]$ , computed using Cumpsty and Marble's compact solution [1977], and CHEOPS-Stator and CAA with Euler and RANS mean flow fields. . . . .	103
6.1	Geometry used to simulate the flow in a 3D isolated stator segment. . . . .	106
6.2	Optimised multi-harmonic wave normalised by the amplitude of the harmonics.	108

6.3	Normalised mass flow rate error (left) and pressure signal (right) close to the pressure side of the blade. The signals are computed for the baseline case towards the end of the transient simulations, after the switch to a second order time scheme. . . . .	109
6.4	Parameter $f_d$ simulated in the baseline case (a) at mid-span and (b) represented as isolines on a Mach number contour in an azimuthally constant plane downstream of the blade. . . . .	110
6.5	Blade-to-blade contours of the mean Mach number computed at 5%, 50% and 95% of the blade's span with the baseline simulation. . . . .	111
6.6	Axial contours of the mean Mach number, static pressure and entropy fields, computed with the baseline simulation 32% (top) and 50% (bottom) of the axial chord downstream of the stator's trailing edge. . . . .	113
6.7	Vorticity in (a) the mid-span plane and (b) an azimuthally constant plane downstream of the stator in the baseline case. . . . .	114
6.8	PSD of velocity near the wake of the stator. The Welch estimator is used with one and five blocks. . . . .	114
6.9	Eddy viscosity ratio $\mu_t/\mu$ in the mid-span plane. . . . .	115
6.10	Radial profiles of pitchwise-averaged mean flow variables: flow angle, static pressure, Mach number and total pressure. They are computed one axial chord away from the stator blade upstream and downstream, from the baseline, entropy-forced and both upstream and downstream acoustically excited simulations. . . . .	116
6.11	Pressure and velocity fluctuations computed both at a point of the upstream (top) and downstream (bottom) duct and averaged over the corresponding plane, and acoustic velocity fluctuations computed from the impedance relation for a plane progressive or regressive wave $u' = \pm p'/(\rho_0 c_0)$ . Entropy-forced simulation. . . . .	118
6.12	Normalised regressive and progressive waves $P^-$ and $P^+$ computed in the upstream and downstream ducts in the entropy-forced case, using both the Riemann invariants and the DMM method. . . . .	119
6.13	Reflection coefficients obtained for the entropy forced ZDES simulation (left) and the two computations with acoustic perturbations (right), with both the Riemann invariants and DMM for post-processing. Excitation types are given in brackets. . . . .	120
6.14	Amplitude and phase of the transfer functions resulting from upstream acoustic forcing $[P_1^-/P_1^+]$ and $[P_2^+/P_1^+]$ , computed with and without non-reflective post-processing, and using both the Riemann invariants and DMM. . . . .	121
6.15	Amplitude and phase of the transfer functions resulting from downstream acoustic forcing $[P_1^-/P_2^-]$ and $[P_2^+/P_2^-]$ , computed with and without non-reflective post-processing, and using both the Riemann invariants and DMM. . . . .	122
6.16	Amplitude and phase of the transfer functions resulting from entropic forcing $[P_1^-/\sigma_1]$ and $[P_2^+/\sigma_1]$ , computed with and without non-reflective post-processing, and using both the Riemann invariants and DMM. . . . .	123

6.17	Amplitude of the regressive and transmitted acoustic waves $P_1^-$ and $P_2^+$ computed in different cases - the baseline simulation, the entropy-forced case, acoustic excitation from the inlet and acoustic forcing from the outlet - and using both the Riemann invariants and DMM for post-processing. . . . .	124
6.18	Amplitude and phase of the transfer functions resulting from upstream acoustic forcing $[P_1^-/P_1^+]$ and $[P_2^+/P_1^+]$ , computed using ZDES with the Riemann invariants and DMM for post-processing, and CAA with Euler and RANS mean flow fields. . . . .	126
6.19	Amplitude and phase of the transfer functions resulting from upstream acoustic forcing $[P_1^-/P_2^-]$ and $[P_2^+/P_2^-]$ , computed using ZDES with the Riemann invariants and DMM for post-processing, and CAA with Euler and RANS mean flow fields. . . . .	127
6.20	Amplitude and phase of the transfer functions resulting from upstream acoustic forcing $[P_1^-/\sigma_1]$ and $[P_2^+/\sigma_1]$ , computed using ZDES with the Riemann invariants and DMM for post-processing, and CAA with Euler and RANS mean flow fields. . . . .	128
6.21	Normalised entropy fluctuations computed in the entropy-forced case in blade-to-blade planes at 5%, 50% and 95% of the stator blade's span. . . . .	129
A.1	Sketch of the coordinate system $(\mathbf{e}_s, \mathbf{e}_n, \mathbf{e}_z)$ . . . . .	140
A.2	Sketch of an hexahedral element. . . . .	141
B.1	Schémas des ondes présentes pour chacun des forçages étudiés en subsonique. . . . .	147
B.2	Nombre de Mach dans la tuyère. . . . .	148
B.3	Amplitude et phase des fonctions de transfert entropiques $[P_1^-/\sigma_1]$ (haut) et $[P_2^+/\sigma_1]$ (bas) obtenues par la CAA, CHEOPS-Nozzle, le modèle 1D MARCAN [Giauque et al., 2012, Huet et al., 2016] et la solution compacte de Marble and Candel [Marble and Candel, 1977]. . . . .	149
B.4	Fluctuations d'entropie normalisées $\sigma$ dans la tuyère 1D (haut) et 2D (bas) pour un forçage harmonique à 1000 Hz. . . . .	150
B.5	Vecteurs unitaires du système de coordonnées cartésien $(\vec{\mathbf{e}}_x, \vec{\mathbf{e}}_y)$ et du système de coordonnées mobile $(\vec{\mathbf{e}}_s, \vec{\mathbf{e}}_n)$ en un point le long d'une ligne de courant. . . . .	151
B.6	Nombre de Mach moyen. . . . .	152
B.7	Amplitude et phase des fonctions de transfert entropiques $[P_1^-/\sigma_1]$ et $[P_2^+/\sigma_1]$ , obtenues avec CHEOPS-Stator et la CAA avec des champs Euler et RANS, ainsi que la solution compacte de Cumpsty and Marble [1977]. . . . .	153
B.8	Géométrie utilisée pour simuler le bruit dans un canal de stator isolé de turbine. . . . .	154
B.9	Champs moyens simulés avec le calcul sans forçage et représentés dans des coupes axiales à 32% (haut) et 50% (bas) d'une corde axiale à l'aval du bord de fuite. . . . .	155
B.10	Amplitude et phase des fonctions de transfert entropiques $[P_1^-/\sigma_1]$ et $[P_2^+/\sigma_1]$ , obtenues par des simulations ZDES post-traitées soit avec les invariants de Riemann soit avec la DMM, et par des calculs CAA avec des champs Euler ou RANS. . . . .	157

# List of Tables

2.1	Variables imposed at the boundaries of the domain using CILEPI for three fluctuation types: entropic at the inlet, acoustic at the inlet, acoustic at the outlet. . . . .	36
2.2	Amplitude and phase of the acoustic transfer functions at the inlet and at the outlet, with $\omega_* = 2\omega/\tilde{f}$ where $\tilde{f}$ is the relaxation frequency of the variables not imposed at the boundary. . . . .	37
3.1	Number of nodes in the axial and radial directions for the different scales considered for mesh convergence in the semi-analytical model. . . . .	45
4.1	Cost of the computation of transfer functions by CHEOPS-Stator, for one forcing type and 101 frequencies, using different mesh sizes and numbers of streamtubes. . . . .	77
6.1	Physical time and cost of the ZDES simulations of the transient flow and the baseline, entropy forced ( $\sigma_1$ ) and acoustically excited ( $P_1^+$ , $P_2^-$ ) cases. . . . .	109





# Bibliography

- ACARE. Strategic Research and Innovation Agenda, 2017. URL <https://www.acare4europe.org/sria/flightpath-2050-goals>. 3, 145
- B. An, J. Liu, and H. Jiang. Numerical Investigation on Unsteady Effects of Hot Streak on Flow and Heat Transfer in Turbine Stage. *Journal of Turbomachinery*, 131(3):031015, 2009. 27
- B. Aupoix and P. R. Spalart. Extensions of the Spalart-Allmaras Turbulence Model to Account for Wall Roughness. *International Journal of Heat and Fluid Flow*, 24(4):454–462, 2003. 113
- C. Bailly and G. Comte-Bellot. *Turbulence*. CNRS éditions, 2003. 113
- F. Bake, U. Michel, and I. Roehle. Investigation of Entropy Noise in Aero-engine Combustors. *Journal of Engineering for Gas Turbines and Power*, 129(2):370–376, 2007. 22, 23, 159
- F. Bake, N. Kings, and I. Roehle. Fundamental Mechanism of Entropy Noise in Aero-engines: Experimental Investigation. *Journal of Engineering for Gas Turbines and Power*, 130(1):11202, 2008. 22, 93
- F. Bake, N. Kings, A. Fischer, and I. Röhle. Experimental Investigation of the Entropy Noise Mechanism in Aero-engines. *International Journal of Aeroacoustics*, 8(1):125–141, 2009a. 22
- F. Bake, C. Richter, B. Mühlbauer, N. Kings, I. Röhle, F. Thiele, and B. Noll. The Entropy Wave Generator (EWG): a Reference Case on Entropy Noise. *Journal of Sound and Vibration*, 326(3-5):574–598, 2009b. 5, 22, 24, 25, 146
- F. Bake, P. Gaetani, G. Persico, L. Neuhaus, and K. Knobloch. Indirect Noise Generation in a High Pressure Turbine Stage. In *22nd AIAA/CEAS Aeroacoustics Conference*, number AIAA 2016-3001, 2016. 5, 23, 43, 72, 84, 106, 107
- M. Bauerheim, I. Durán, T. Livebardon, G. Wang, S. Moreau, and T. Poinot. Transmission and Reflection of Acoustic and Entropy Waves through a Stator-rotor Stage. *Journal of Sound and Vibration*, 374:260–278, 2016. 4, 17, 21, 59
- P. T. Beard, T. Povey, and K. S. Chana. Turbine Efficiency Measurement System for the Qinetiq Turbine Test Facility. *Journal of Turbomachinery*, 132(1):011002, 2009. 5, 23, 146

- C. Becerril Aguirre. *Simulation of noise emitted by a reactive flow*. PhD thesis, INP Toulouse, 2017. 5, 21, 22, 23, 25, 26, 59, 146
- D. J. Bodony. Scattering of an Entropy Disturbance into Sound by a Symmetric Thin Body. *Physics of Fluids*, 21(9):096101, 2009. 108
- M. S. Bohn. Response of a Subsonic Nozzle to Acoustic and Entropy Disturbances. *Journal of Sound and Vibration*, 52(2):283–297, 1977. 22
- M. S. Bohn. *Noise Produced by the Interaction of Acoustic Waves and Entropy Waves with High-speed Nozzle Flows*. PhD thesis, California Institute of Technology Pasadena, 1979. 22
- A. Cader, C. Polacsek, and T. Le Garrec. Numerical prediction of rotor-stator interaction noise using 3D CAA with synthetic turbulence injection. In *2018 AIAA/CEAS Aeroacoustics Conference, AIAA AVIATION Forum*, number AIAA 2018-4190, 2018. 99
- S. Candel, D. Durox, S. Ducruix, A. L. Birbaud, N. Noiray, and T. Schuller. Flame dynamics and combustion noise: progress and challenges. *International Journal of Aeroacoustics*, 8(1):1–56, 2009. 3, 145
- S. M. Candel. *Analytical Studies of Some Acoustic Problems of Jet Engines*. PhD thesis, California Institute of Technology, Pasadena, California, 1972. 8, 20
- A. Ceci, R. Gojon, and M. Mihaescu. Large Eddy Simulations for Indirect Combustion Noise Assessment in a Nozzle Guide Vane Passage. *Flow, Turbulence and Combustion*, 102(2): 299–311, 2019. 5, 27, 146
- S. Chandramouli, R. Gojon, J. Fridh, and M. Mihaescu. Numerical Characterization of Entropy Noise with a Density Based Solver. In *12th European Conference on Turbomachinery Fluid dynamics & Thermodynamics*, number ETC2017-143, 2017. 27
- B. Chu and L. S. G. Kovásznyai. Non-linear Interactions in a Viscous Heat-conducting Compressible Gas. *Journal of Fluid Mechanics*, 3(5):494–514, 1958. 24
- V. Clair, C. Polacsek, T. Le Garrec, and G. Reboul. Experimental and Numerical Investigation of Turbulence-Airfoil Noise Reduction Using Wavy Edges. *AIAA Journal*, 51(11): 2695–2713, 2013. 99
- L. Crocco. Supercritical Gaseous Discharge with High Frequency Oscillations. *Aerotechnica*, 33(1):46–53, 1953. 8
- N. A. Cumpsty. Excess Noise from Gas Turbine Exhausts. In *ASME International Gas Turbine Conference and Products Show*, number 75-GT-61 in 1A, 1975. 8
- N. A. Cumpsty and F. E. Marble. The Interaction of Entropy Fluctuations with Turbine Blade Rows; A Mechanism of Turbojet Engine Noise. *Proceedings of the Royal Society of London A*, 357:323–344, 1977. 4, 6, 8, 10, 17, 63, 72, 73, 74, 75, 76, 77, 81, 83, 96, 97, 98, 101, 102, 103, 133, 134, 137, 147, 152, 153, 154, 159, 161, 162, 164

- F. De Domenico, E. O. Rolland, and S. Hochgreb. Detection of Direct and Indirect Noise Generated by Synthetic Hot Spots in a Duct. *Journal of Sound and Vibration*, 394:220–236, 2017. 5, 23, 146
- F. De Domenico, S. M. Lowe, L. Fan, S. Hochgreb, P. Shah, B. A.O. Williams, and P. Ewart. High Frequency Measurement of Temperature and Composition Spots with LITGS. *Journal of Engineering for Gas Turbines and Power*, 141(3):031003, 2018. 23
- F. De Domenico, E. Rolland, and S. Hochgreb. A Generalised Model for Acoustic and Entropic Transfer Function of Nozzles with Losses. *Journal of Sound and Vibration*, 440:212–230, 2019. 13, 23
- F. De La Puente Cerezo. *Aeroacoustic Simulations of Landing Gears with Unstructured Grids and a ZDES Turbulence Model*. PhD thesis, Université Pierre et Marie Curie - Paris VI, 2017. 115
- S. Deck. Recent Improvements in the Zonal Detached Eddy Simulation (ZDES) formulation. *Theoretical and Computational Fluid Dynamics*, 26(6):523–550, 2012. 34, 159
- A. P. Dowling and Y. Mahmoudi. Combustion Noise. *Proceedings of the Combustion Noise Institute*, 35(1):65–100, 2015. 3, 5, 17, 43, 133, 146
- I. Durán and S. Moreau. Study of the Attenuation of Waves Propagating Through Fixed and Rotating Turbine Blades. In *18th AIAA/CEAS Aeroacoustics Conference*, number AIAA2012-2133, 2012. 21
- I. Durán and S. Moreau. Numerical Simulation of Acoustic and Entropy Waves Propagating through Turbine Blades. In *19th AIAA/CEAS Aeroacoustics Conference, AIAA Aviation*, number AIAA 2013-2102, 2013a. 4
- I. Durán and S. Moreau. Solution of the Quasi-one-dimensional Linearized Euler Equations Using Flow Invariants and the Magnus Expansion. *Journal of Fluid Mechanics*, 723:190–231, 2013b. 5, 13, 17, 22, 146
- I. Durán and A. S. Morgans. On the Reflection and Transmission of Circumferential Waves Through Nozzles. *Journal of Fluid Mechanics*, 773:137–153, 2015. 5, 17, 25, 59, 146
- I. Durán, M. Leyko, S. Moreau, F. Nicoud, and T. Poinsot. Computing Combustion Noise by Combining Large Eddy Simulations with Analytical Models for the Propagation of Waves through Turbine Blades. *Comptes Rendus Mécanique*, 341(1-2):131–140, 2013. 4
- L. Eca, M. Hoekstra, A. Hay, and D. Pelletier. A Manufactured Solution for a Two-Dimensional Steady Wall-Bounded Incompressible Turbulent Flow. *International Journal of Computational Fluid Dynamics*, 21(3-4):175–188, 2007. 113
- A. Emmanuelli, M. Huet, T. Le Garrec, and S. Ducruix. CAA Study of Entropy Noise in Nozzle Flow for the Validation of a 2D Semi-Analytical Model . In *ASME Turbo Expo*, number GT2017-63640 in 2C, 2017. 41

- A. Emmanuelli, M. Huet, T. Le Garrec, and S. Ducruix. Study of Entropy Noise through a 2D Stator using CAA. In *2018 AIAA/CEAS Aeroacoustics Conference*, number AIAA 2018-3915, 2018. 86
- A. Emmanuelli, J. Zheng, M. Huet, A. Giauque, T. Le Garrec, and S. Ducruix. Description and Application of a 2D-axisymmetric Model for Entropy Noise in Nozzle Flows. *Journal of Sound and Vibration*, 472(115163), 2020. 17, 41
- P. Gaetani and G. Persico. Hot Streak Evolution in an Axial HP Turbine Stage. *International Journal of Turbomachinery Propulsion and Power*, 2(2):6, 2017. 5, 23, 27
- P. Gaetani, G. Persico, V. Dossena, and C. Osnaghi. Investigation of the Flow Field in a High-Pressure Turbine Stage for Two Stator-Rotor Axial Gaps – Part I: Three-Dimensional Time-Averaged Flow Field. *Journal of Turbomachinery*, 129(3):572–579, 2007a. 5
- P. Gaetani, G. Persico, V. Dossena, and C. Osnaghi. Investigation of the Flow Field in a High-Pressure Turbine Stage for Two Stator-Rotor Axial Gaps – Part II: Unsteady Flow Field. *Journal of Turbomachinery*, 129(3):580–590, 2007b. 5
- P. Gaetani, G. Persico, and C. Osnaghi. Effects of Axial Gap on the Vane-Rotor Interaction in a Low Aspect Ratio Turbine Stage. *Journal of Propulsion and Power*, 26(2):325–334, 2010. 5
- P. Gaetani, G. Persico, and A. Spinelli. Entropy Wave Generator for Indirect Combustion Noise Experiments in a High-Pressure Turbine. In *11th European Turbomachinery Conference*, number ETC2015-025, 2015. 23
- A. Giauque, M. Huet, and F. Cléro. Analytical Analysis of Indirect Combustion Noise in Subcritical Nozzles. *Journal of Engineering for Gas Turbines and Power*, 134(11):111202, 2012. 4, 5, 13, 22, 56, 57, 58, 60, 62, 146, 147, 149, 150, 160, 164
- A. Giauque, M. Huet, F. Cléro, S. Ducruix, and F. Richecoeur. Thermoacoustic Shape Optimization of a Subsonic Nozzle. *Journal of Engineering for Gas Turbines and Power*, 135(10):102601, 2013. 13, 43
- A. Giusti, N. A. Worth, E. Mastorakos, and A. P. Dowling. Experimental and Numerical Investigation into the Propagation of Entropy Waves. *AIAA Journal*, 55(2):446–458, 2017. 20
- C. S. Goh and A. S. Morgans. Phase Prediction of the Response of Choked Nozzles to Entropy and Acoustic Disturbances. *Journal of Sound and Vibration*, 330(21):5184–5198, 2011. doi: 10.1. 5, 13, 146
- P. Guillaume, J. Schoukens, R. Pintelon, and I. Kollár. Crest-Factor Minimisation using Nonlinear Chebyshev Approximation Methods. *IEEE Transactions on Instrumentation and Measurement*, 40(6):982–989, 1991. 108
- J. Guzmán-Iñigo, A. Morgans, and I. Durán. A Model for the Sound Generated by Entropy Disturbances Interacting with Isolated Blades. In *2018 AIAA/CEAS Aeroacoustics Conference, AIAA AVIATION Forum*, number AIAA 2018-2958, 2018. 17

- H. A. Hassan. Scaling on Combustion-generated Noise. *Journal of Fluid Mechanics*, 66(3): 445–453, 1974. 3, 145
- A. Holewa, S. Lesnik, G. Ashcroft, and S. Guérin. CFD-Based Investigation of Turbine Tonal Noise Induced by Steady Hot Streaks. *International Journal of Turbomachinery Propulsion and Power*, 2(1):3, 2017. 5, 23, 27
- S. M. Hosseinalipour, A. Fattahi, H. Afshari, and N. Karimi. On the Effects of Convecting Entropy Waves on the Combustor Hydrodynamics. *Applied Thermal Engineering*, 110: 901–909, 2017. 21
- M. Howe. Indirect Combustion Noise. *Journal of Fluid Mechanics*, 659:267–288, 2010. 22, 25, 26, 59
- M. Huet. Extension du Code MarCan pour l’Évaluation des Fonctions de Transfert de Tuyère aux Écoulements Supersoniques sans et avec Choc. Technical Report RT 7/18759, ONERA, 2013b. 13
- M. Huet. Nonlinear Indirect Combustion Noise for Compact Supercritical Nozzle Flows. *Journal of Sound and Vibration*, 374:211–227, 2016. 10, 13
- M. Huet. Budgets of Disturbances Energy for Nozzle Flows at Subsonic and Choked Regimes. *Journal of Engineering for Gas Turbines and Power*, 140(11):112602, 2018. 59
- M. Huet and B. Courbet. Évaluation Analytique et Numérique de la Non-réflexion des Conditions aux Limites dans le code CEDRE. Technical report, ONERA, 2016. 36, 37
- M. Huet and A. Giauque. A Nonlinear Model for Indirect Combustion Noise Through a Compact Nozzle. *Journal of Fluid Mechanics*, 733:268–301, 2013a. 4, 5, 12, 108, 146
- M. Huet and F. Vuillot. Évaluation de la Précision des Schémas Numériques du Code CEDRE pour la Propagation de Perturbations Entropiques en Maillage Tétraédrique. Technical report, ONERA, 2017. 35, 36, 159
- M. Huet, F. Vuillot, N. Bertier, M. Mazur, N. Kings, W. Tao, P. Scoufflaire, F. Richecoeur, S. Ducruix, C. Lapeyre, and T. Poinot. Recent Improvements in Combustion Noise Investigation: from the Combustion Chamber to Nozzle Flow. *Aerospace Lab*, 11(10), 2016. 3, 56, 57, 58, 60, 62, 147, 149, 150, 160, 164
- ICAO. Annual Report of the Council, 2017. URL <https://www.icao.int/annual-report-2017/>. 3, 145
- M. Ihme. Combustion and Engine-Core Noise. *Annual Review of Fluid Mechanics*, 49:277–310, 2017. 3
- N. Kings. *Indirect Combustion Noise: Experimental Investigation of the Vortex Sound Generation in Nozzle Flows*. PhD thesis, Technischen Universität Berlin, 2014. 3, 25

- N. Kings and F. Bake. Indirect Combustion Noise: Noise Generation by Accelerated Vorticity in a Nozzle Flow. *International Journal of Spray and Combustion Dynamics*, 2(3):253–266, 2010. 25
- N. Kings, W. Tao, P. Scoufflaire, F. Richecoeur, and S. Ducruix. Experimental and Numerical Investigation of Direct and Indirect Combustion Noise in a Lean Premixed Laboratory Swirled Combustor. In *ASME Turbo Expo*, number GT2016–57848 in 4B, 2016. 25
- K. Knobloch, T. Werner, and F. Bake. Entropy Noise Generation and Reduction in a Heated Nozzle Flow. In *21st AIAA/CEAS Aeroacoustics Conference, AIAA AVIATION Forum*, number AIAA 2015–2818, 2015a. 22, 23, 24, 159
- K. Knobloch, T. Werner, and F. Bake. Noise Generation in Hot Nozzle Flow. In *ASME Turbo Expo*, number GT2015-43702, 2015b. 22, 24
- K. Knobloch, A. Holewa, S. Guérin, Y. Mahmoudi., T. Hynes, and F. Bake. Noise Transmission Characteristics of a High Pressure Turbine Stage. In *22nd AIAA/CEAS Aeroacoustics Conference*, number AIAA 2016-3001, 2016. 5, 23, 43, 72, 84, 106, 107
- K. Knobloch, L. Neuhaus, F. Bake, P. Gaetani, and G. Persico. Experimental Assessment of Noise Generation and Transmission in a High-pressure Transonic Turbine Stage. In *ASME Turbo Expo*, number GT2016-57209, 2017. 5, 23, 43, 72, 84, 106, 107, 112
- J. Kopitz, E. Bröcker, and W. Polifke. Characteristics-based Filter for Identification of Planar Acoustic Waves in Numerical simulation of Turbulent Compressible Flows. *International Congress of Sound and Vibration*, pages 3913–3920, 2005. 50
- M. Leyko, F. Nicoud, and T. Poinso. Comparison of Direct and Indirect Combustion Noise Mechanisms in a Model and Combustor. *AIAA Journal*, 47(11):2709–2716, 2009. 22
- M. Leyko, S. Moreau, F. Nicoud, and T. Poinso. Waves Transmission and Generation in Turbine Stages in a Combustion-Noise Framework. In *16th AIAA/CEAS AeroAcoustics Conference*, number AIAA 2010-4032, 2010. 4, 17, 21
- M. Leyko, S. Moreau, F. Nicoud, and T. Poinso. Numerical and Analytical Modelling of Entropy Noise in a Supersonic Nozzle with a Shock. *Journal of Sound and Vibration*, 330(16):3944–3958, 2011. 5, 22, 26, 146
- M. Leyko, S. Moreau, F. Nicoud, and T. Poinso. Simulation and Modelling of the Waves Transmission and Generation in a Stator Blade Row in a Combustion-Noise Framework. *Journal of Sound and Vibration*, 333(23):6090–6106, 2014. 4, 10, 12, 159
- T. Livebardon, S. Moreau, L. Gicquel T. Poinso, E. Bouty Combustion, and Flame. Combining LES of Combustion Chamber and an Actuator Disk Theory to Predict Combustion Noise in a Helicopter Engine. *Combustion and Flame*, 165:272–287, 2016. 17, 21
- J. M. Lourier, A. Huber, B. Noll, and M. Aigner. Numerical analysis of indirect combustion noise generation within a subsonic nozzle. *AIAA Journal*, 52(10Time Domain Simulations of Non-linear Thermoacoustic Stability of a Model Combustor):2114–2126, 2014. 22

- W. Magnus. On the Exponential Solution of Differential Equations for a Linear Operator. *Communications on pure and applied mathematics*, 7(4):649–673, 1954. 13
- L. Magri, J. O’Brien, and M. Ihme. Compositional Inhomogeneities as a Source of Indirect Combustion Noise. *Journal of Fluid Mechanics*, 799(R4), 2016. 3
- Y. Mahmoudi, A. Giusti, E. Mastorakos, and A. P. Dowling. Low-Order Modeling of Combustion Noise in an Aero-Engine: The Effect of Entropy Dispersion. *Journal of Engineering for Gas Turbines and Power*, 140(1):011502, 2018. 21
- F. E. Marble. Acoustic Disturbance from Gas Non-uniformities Convecting through a Nozzle. *Symposium on Transportation Noise*, 1973. 8, 20
- F. E. Marble and S. M. Candel. Acoustic Disturbance from Gas Non-uniformities Convected Through a Nozzle. *Journal of Sound and Vibration*, 55(2):225–243, 1977. 4, 8, 12, 13, 17, 24, 55, 56, 58, 59, 60, 62, 147, 149, 150, 160, 164
- F. R. Menter. Two-equation Eddy-viscosity Turbulence Models for Engineering Applications. *AIAA Journal*, 32(8):1598–1605, 1994. 32
- J. H. Miles. Time Delay Analysis of Turbofan Engine Direct and Indirect Combustion Noise Sources. *Journal of Propulsion and Power*, 25(1):218–227, 2009. 23
- J. H. Miles. Separating Direct and Indirect Engine Combustion Noise using the Correlation Function. *Journal of Propulsion and Power*, 26(5):1144–1152, 2010. 23
- A. Mishra and D. J. Bodony. Evaluation of Actuator Disk Theory for Predicting Indirect Combustion Noise. *Journal of Sound and Vibration*, 332(4):821–838, 2013. 12, 108
- W. Moase, M. J. Brear, and C. Manzie. The Forced Response of Choked Nozzles and Supersonic Diffusers. *Journal of Fluid Mechanics*, 585:281–304, 2007. 4, 5, 10, 13, 16, 146
- S. Moreau, C. Becerril Aguirre, and L. Gicquel. Large-eddy-simulation Prediction of Indirect Combustion Noise in the Entropy Wave Generator Experiment. *International Journal of Spray and Combustion Dynamics*, 10(2):154–168, 2018. 5, 21, 22, 146
- C. L. Morfey. Amplification of Aerodynamic Noise by Convected Flow Inhomogeneities. *Journal of Sound and Vibration*, 31(4):391–397, 1973. 8, 20
- A. S. Morgans and I. Durán. Entropy Noise: A review of Theory, Progress and Challenges. *International Journal of Spray and Combustion Dynamics*, 8(4):285–298, 2016. 3, 20
- A. S. Morgans, C. S. Goh, and J. A. Dahan. The Dissipation and Shear Dispersion of Entropy Waves in Combustor Thermodynamics. *Journal of Fluid Mechanics*, 733(R2), 2013. 20
- B. Mühlbauer, A. Wiedenhorn, M. Liu, B. Noll, and M. Aigner. Numerical Investigation of the Fundamental Mechanism of Entropy Noise Generation in Aero-engines. *Acta Acustica united with Acustica*, 95(3):470–478, 2009. 5, 22, 25, 146



- M. Muthukrishnan. *An Experimental Study of the Separation of Combustion Entropy Noise*. PhD thesis, Gorgia Institute of Technology, 1977. 22
- D. Papadogiannis, G. Wang, S. Moreau, F. Duchaine, L. Gicquel, and F. Nicoud. Assessment of the Indirect Combustion Noise Generated in a Transonic High-pressure Turbine Stage. *Journal of Engineering for Gas Turbines and Power*, 138(4):041503, 2016. 23, 26, 159
- B. Pardowitz, U. Tapken, K. Knobloch, F. Bake, E. Bouty, I. Davis, and G. Bennett. Core Noise Identification of Broadband Noise Sources of a Turbo-shaft Engine. In *20th AIAA/CEAS Aeroacoustics Conference, AIAA Aviation*, number AIAA 2014-3321, 2014. 23
- G. Persico, A. Mora, P. Gaetani, and M. Savini. Unsteady aerodynamics of a low aspect ratio turbine stage: Modeling Issues and Flow Physics. *Journal of Turbomachinery*, 134(6):061030, 2012. 5, 23, 146
- L. Pinelli, F. Poli, A. Arnone S. Guérin, A. Holewa, J. R. F. Aparicio, R. Puente D. Torzo, C. Favre, P. Gaetani, and G. Persico. On the Numerical Evaluation of Tone Noise Emissions Generated by a Turbine Stage: An In-Depth Comparison Among Different Computational Methods. In *ASME Turbo Expo*, number GT2015-42376, 2015. 5, 23
- Wolfgang Polifke, Clifton Wall, and Parviz Moin. Partially Reflecting and Non-reflecting Boundary Conditions for Simulation of Compressible Viscous Flow. *Journal of Computational Physics*, 213(1):437–449, 2006. 49
- G. Reboul, A. Cader, C. Polacsek, and T. Le Garrec. CAA Prediction of Rotor-Stator Interaction Using Synthetic Turbulence: Application to a Low-Noise Serrated OGV. In *23rd AIAA/CEAS Aeroacoustics Conference, AIAA AVIATION Forum*, number AIAA 2017-3714, 2017. 99
- S. Redonnet. Numerical Study of Acoustic Installation Effects with a Computational Aeroacoustics Method. *AIAA Journal*, 48(5):929–937, 2010. 37, 147
- S. Redonnet, E. Manoha, and P. Sagaut. Numerical Simulations of Propagation of Small Perturbations Interacting with Flows and Solid Bodies. In *7th AIAA/CEAS Aeroacoustics Conference, Aeroacoustics Conferences*, number AIAA 2001-0222, 2001. 37, 147
- A. Refloch, B. Courbet, A. Murrone, P. Villedieu, C. Laurent, P. Gilbank, J. Troyes, L. Tessé, G. Chaineray, J. B. Dargaud, E. Quémerais, , and F. Vuillot. Cedre software. In *CFD Platforms and coupling, Aerospace Lab*, volume 2, 2011. 30, 147
- N. Renard and S. Deck. Improvements in Zonal Detached Eddy Simulation for Wall Modeled Large Eddy Simulation. *AIAA Journal*, 53(11):3499–3504, 2015. 35
- E. Rolland, F. De Domenico, and S. Hochgreb. Theory and Application of Reverberated Direct and Indirect Noise. *Journal of Fluid Mechanics*, 819:435–464, 2017. 23
- E. Rolland, F. De Domenico, and S. Hochgreb. Direct and Indirect Noise Generated by Entropic and Compositional Inhomogeneities. *Journal of Engineering for Gas Turbines and Power*, 140(8):082604, 2018. 3, 23

- C. L. Rumsey, D. O. Allison, R. T. Biedron, P. G. Buning, T. G. Gainer, J. H. Morrison, S. M. Rivers, and D. P. Witkowski. CFD Sensitivity Analysis of a Modern Civil Transport Near Buffet-Onset Conditions. Technical Report TM-2001-211263, NASA, 2001. 115
- P. Sagaut, S. Deck, and M. Terracol. *Multiscale and Multiresolution Approaches in Turbulence*. Imperial College Press, 2013. 33
- T. Sattelmayer. Influence of the Combustor Aerodynamics on Combustion Instabilities from Equivalence Ratio Fluctuations. *Journal of Engineering for Gas Turbines and Power*, 125: 11–19, 2003. 20
- J. Smagorinsky. General Circulation Experiments with the Primitive Equations. *Monthly Weather Review*, 91(3):99–164, 1963. 33
- S. Spagnolo. *Unsteady Aerodynamic Loads on Aircraft Landing Gear*. PhD thesis, University of Southampton, 2016. 115
- P. Spalart, W. Jou, M. Strelets, and S. Allmaras. Comments on the feasibility of LES for wings and on a hybrid RANS/LES approach. In *Proceedings of the 1st AFSOR International Conference on DNS/LES, Ruston*, pages 137–147, 1998. 33
- P. Spalart, S. Deck, M. Shur, K. Squires, M. Strelets, and A. Travin. A New Version of Detached-eddy Simulation, Resistant to Ambiguous Grid Densities. *Theory of Computational Fluid Dynamics*, 20:181–195, 2006. 33
- P. R. Spalart. Trends in Turbulence Treatments. In *Fluids 2000 Conference and Exhibit*, number AIAA 2000-2306, 2000. 115
- P. R. Spalart and S. R. Allmaras. A One-equation Turbulence Model for Aerodynamic Flows. *La Recherche Aerospatiale*, 1:5–21, 1994. 32
- S. R. Stow, A. P. Dowling, and T. P. Hynes. Reflection of circumferential modes in a choked nozzle. *Journal of Fluid Mechanics*, 467:215–239, 2002. 5, 13, 17, 146
- C. K. W. Tam. Advances in Numerical Boundary Conditions for Computational Aeroacoustics. *Journal of Computational Aeroacoustics*, 1998. 39
- C. K. W. Tam and Z. Dong. Radiation and Outflow Boundary Conditions for Direct Computation of Acoustic and Flow Disturbances in a Nonuniform Mean Flow. *Journal of Computational Acoustics*, 4(2):175–201, 1996. 39, 47, 87, 148, 152
- C. K. W. Tam and S. A. Parrish. On the Generation of Indirect Combustion Noise. In *20th AIAA/CEAS Aeroacoustics Conference, AIAA Aviation*, number AIAA 2014-3315, 2014. 17, 24, 159
- C. K. W. Tam and S. A. Parrish. Noise of High-performance Aircraft at Afterburner. *Journal of Sound and Vibration*, 352:103–128, 2015. 23
- C. K. W. Tam and S. A. Parrish. The Physical Processes of Indirect Combustion Noise Generation. *International Journal of Aeroacoustics*, 17(2):22–35, 2018. 24

- C. K. W. Tam and J. Webb. Dispersion-Relation-Preserving Finite Difference Schemes for Computational Acoustics. *Journal of Computational Physics*, 107(2):262–281, 1993. 39, 47, 87, 148, 152
- C. K. W. Tam, S. A. Parrish, J. Xu, and B. Schuster. Indirect Combustion Noise of Auxiliary Power Units. *Journal of Sound and Vibration*, 332:4004–4020, 2013. 17
- H. S. Tsien. The Transfer Function of Rocket Nozzles. *Journal of the American Rocket Society*, 22:139–143, 1952. 8
- W. C. Ullrich, J. Gikadi, C. Jörg, and T. Sattelmayer. Acoustic-entropy Coupling Behavior and Acoustic Scattering Properties of a Laval Nozzle. In *20th AIAA/CEAS Aeroacoustics Conference, AIAA Aviation*, number AIAA 2014-3193, 2014a. 22
- W. C. Ullrich, M. Schulze, and T. Sattelmayer. Fundamental Indirect Noise Generation by Interactions between Entropy, Vorticity and Acoustic Waves in the Context of Aero Engine Applications. In *Inter.noise (43rd Int. Congress on Noise Control Engineering)*, 2014b. 25
- G. Wang, M. Sanjose, S. Moreau, D. Papadogiannis, F. Duchaine, and L. Gicquel. Noise Mechanisms in a Transonic High-pressure Turbine Stage. *International Journal of Aeroacoustics*, 15(1-2):144–161, 2016. 5, 23, 26, 146, 159
- Y. Xia, I. Durán, A. Morgans, and X. Han. Dispersion of Entropy Perturbations Transporting through an Industrial Gas Turbine Combustor. *Flow Turbulence and Combustion*, 100(2): 481–502, 2018. 20, 21, 159
- J. Zheng. *Analytical and Numerical Study of the Indirect Combustion Noise Generated by Entropy Disturbances in Nozzle Flows*. PhD Thesis, Université Paris Saclay, 2016. 4, 5, 6, 17, 26, 42, 133, 146, 147
- J. Zheng, M. Huet, A. Giauque, F. Cléro, and S. Ducruix. A 2D-axisymmetric Analytical Model for the Estimation of Indirect Combustion Noise in Nozzle Flows. In *21st AIAA/CEAS Aeroacoustics Conference, AIAA Aviation*, number AIAA 2015-2974, 2015. 4, 5, 17, 133, 146
- E. E. Zukoski and J. M. Auerbach. Experiments Concerning the Response of Supersonic Nozzles to Fluctuating Inlet Conditions. *Journal of Engineering for Power*, 98(1):60–64, 1976. 22



**Titre :** Simulation numérique et modélisation du bruit entropique à travers une tuyère et un stator de turbine

**Mots clés :** aéroacoustique, bruit de combustion, modèle d'ordre réduit, CAA, ZDES.

**Résumé :** L'étude du bruit de combustion est motivée par l'augmentation de sa contribution relative au bruit émis par les moteurs aéronautiques actuels, ainsi que par son impact sur la conception de chambres de combustion à basse émission de  $\text{NO}_x$ . Le bruit entropique est une source de bruit de combustion indirect générée par l'accélération de perturbations entropiques à travers les tuyères et les étages de turbine à l'aval de la chambre de combustion. Cette étude porte sur la simulation numérique et la modélisation du bruit entropique à travers une tuyère et un stator de turbine. Dans un premier temps, le bruit entropique est simulé dans une tuyère avec un code CAA (Computational AeroAcoustics) afin de valider un modèle 2D existant sous des hypothèses similaires. Les niveaux de bruit entropique et de diffusion acoustique obtenus par les deux méthodes sont en accord. Leur comparaison au bruit estimé par des modèles compacts et 1D montre que les effets bi-dimensionnels sont significatifs. De plus, de la vorticit  induite par l'accélération de perturbations entropiques est identifi e, mais celle-ci ne contribue pas significativement au bruit g n r . Une g om trie de stator de turbine haute pression est ensuite  tudi e en 2D. Le mod le pour les tuy res 2D

est  tendu   ces configurations, h ritant de certaines de ses hypoth ses. L' tude de celles-ci montre que l'impact de la vorticit  et des variations azimutales des fluctuations acoustiques, n glig es par le mod le, est significatif. Ces hypoth ses devront  tre relax es lors de d veloppements futurs. Les calculs CAA permettent  galement de caract riser la g n ration de bruit entropique sous hypoth ses simplificatrices avec   la fois des champs porteurs Euler et RANS. Une  tude plus approfondie du cas RANS est n cessaire pour sa validation, ainsi que pour mieux comprendre le r le de la couche limite dans la g n ration du bruit entropique. Enfin, un canal de stator est  tudi  par des calculs ZDES (Zonal Detached Eddy Simulation) afin d'examiner les effets 3D et visqueux sur le bruit g n r . La tri-dimensionnalit  de l' coulement est mise en  vidence et les perturbations sont post-trait es en portant une attention particuli re au filtrage des fluctuations hydrodynamiques et aux r flexions en parois. Les r sultats obtenus par la CAA et la ZDES sont comparables, ce qui indique que la tri-dimensionnalit  et la viscosit  de l' coulement ont un effet limit  sur le bruit entropique g n r  dans un stator de turbine.

**Title :** Numerical simulation and modelling of entropy noise in nozzle and turbine stator flows

**Keywords :** aeroacoustics, combustion noise, reduced order modeling, CAA, ZDES.

**Abstract :** The investigation of combustion noise is motivated by its growing relative contribution to the noise emitted by modern turbofan engines overall, as well as its effect on low  $\text{NO}_x$  emission combustor design. Entropy noise is a source of indirect combustion noise, which is generated by the acceleration of heterogeneities, in this case entropy, downstream of the combustion chamber. This study consists of the investigation of entropy noise in nozzle and turbine stator flow using both analytical and numerical methods. Nozzle flow is considered first. A Computational AeroAcoustics (CAA) reference case is built for the validation of an existing two-dimensional semi-analytical model developed under similar assumptions. The levels of entropy noise and acoustic scattering estimated using both methods are in good agreement. Two-dimensional effects on entropy noise are highlighted, notably by comparison with compact and 1D models. In addition, vorticity induced by the acceleration of entropy noise is evidenced, but it yields negligible vortex sound. Next, the focus is shifted to a 2D high-pressure turbine stator. The 2D model for nozzle flow is exten-

ded to this configuration, inheriting some of its main assumptions. Their investigation, using CAA in particular, sets the path for future developments and allows insight to be gained into the role of both vorticity and azimuthal variation of acoustics, which are neglected by the model. CAA also allows to characterise entropy noise generation in 2D stator flow under simplifying assumptions, using Euler and RANS mean flows. Further investigation is needed to validate the RANS case and to fully understand the effect of boundary layers on entropy noise generation. Finally, entropy noise is simulated using Zonal Detached Eddy Simulation (ZDES) in a stator channel in order to investigate 3D and viscous effects on entropy noise. The three-dimensionality of the flow is highlighted and acoustic signals are carefully post-processed, ensuring hydrodynamic perturbations are correctly filtered and boundary reflections are minimised. The closeness of noise levels obtained using CAA and ZDES suggest three-dimensional and viscous effects have a limited impact on the entropy noise generated in turbine stator flow.

